INVESTIGATION OF UNSTABLE FAILURE IN UNDERGROUND COAL MINING USING THE DISCRETE ELEMENT METHOD

by

Evan M. C. Kias

A thesis submitted to the Faculty and the Board of Trustees of the Colorado School of Mines in partial fulfillment of the requirements for the degree of Doctor of Philosophy (Mining and Earth Systems Engineering).

Golden, Colorado

Date _____

Signed: _____
Evan M. C. Kias

Signed: _____
Dr. Ugur Ozbay
Thesis Advisor

Golden, Colorado

Date _____

Signed: _____
Dr. Hugh Miller
Associate Professor and Interim Department Head
Department of Mining Engineering

ABSTRACT

Unstable failure in underground coal mining is the sudden and violent ejection of coal from mine walls and pillars into the mine opening. This thesis demonstrates the use of the discrete element method to simulate stable and unstable modes of compressive failure of a western U.S. coal. Two discrete element models are evaluated for their ability to simulate unstable and stable compressive failure using the discrete element program Particle Flow Code in Two Dimensions (PFC2D): the bonded particle model and the displacement softening model. Compressive strength tests show that the displacement softening model is better suited for unstable failure studies based on consistent behavior in stable and unstable modes of failure and a post-peak softening characteristic that is independent of the loading rate.

A set of model behaviors, called indicators, are analyzed on their ability to distinguish the stability of failure in a series of unconfined compression tests and then a series slender pillar compressive strength tests. Generally, the indicators show consistent values for stable failures and increasing magnitude with increasing levels of instability. A grid based measurement technique is used to observe indicator behavior and model damage spatially.

The work by the damping mechanism, kinetic energy, and the mean unbalanced force are used to analyze pillar edge failure in a model with excavation induced loading conditions. The indicators reveal unstable failure events, and a comparison between stable and unstable mining steps show that the indicators can be used to detect local instabilities on, such as pillar rib failure. Grid based measurements show that the unstable failure is initiated due to a single mining step and that failure occurred along a diagonal failure plane originating from the mine face similar to that seen in practice. Unstable failures show highly localized planes of failure while stable pillar failure is more dispersed. Future application of the techniques developed in this thesis include more in depth study of factors influencing unstable failures in coal mines including the mine/coal seam contact condition and depth.

TABLE OF CONTENTS

LIST OF FIGURES

LIST OF TABLES

LIST OF SYMBOLS

Effective Stiffness . . . . . K

Particle Stiffness . . . . . k

Normal Contact Stiffness . . . . . k_n

Shear Contact Stiffness . . . . . k_s

Parallel Bond Shear Strength . . . . . τ_s

Parallel Bond Shear Force . . . . . F_s

Parallel Bond Normal Force . . . . . F_n

Parallel Bond Cross Sectional Area . . . . . A

Parallel Bond Moment . . . . . M

Parallel Bond Radius . . . . . R

Parallel Bond Moment of Inertia I

Displacement Softening Contact Strength Components . . . . . F_c^k

Displacement Softening Contact Force Components . . . . . F^k

Displacement Softening Contact Resultant Force . . . . . F

Displacement Softening Contact Bond Strength . . . . . F_{cmax}

Displacement Softening Contact Elastic Displacement . . . . . U_e^k

Displacement Softening Contact Plastic Displacement . . . . . U_p^k

Displacement Softening Contact Resultant Plastic Displacement . . . . . U_p

Displacement Softening Contact Plastic Displacement Limit . . . . . U_{pmax}

Minimum Disc Radius . . . . . R_{min}

Maximum Disc Radius . . . . . R_{max}

Specimen Generation Vessel Pressure . . . . . σ_o^t

Number of Floaters . . . . . n_f

Number of elements . . . . . N_b

Bulk Density of Elements . . . . . ρ_{bulk}

Elastic Modulus . . . . . E

Contact Friction Coefficient . . . . . μ

All Force in Bonds Flag . . . . . B_{pball}

Moment Contribution Factor . . . . . $\bar{\beta}$

Parallel Bond Radius Multiplier . . . . . $\bar{\lambda}$

Parallel Bond Elastic Modulus . . . . . $\bar{E_c}$

Parallel Bond Normal Contact Stiffness . . . . . $\bar{k_n}$

Parallel Bond Shear Contact Stiffness . . . . . $\bar{k_s}$

Parallel Bond Tensile Strength . . . . . $\bar{\sigma}_c$

Parallel Bond Cohesion . . . . . $\bar{c}$

Parallel Bond Friction Angle . . . . . $\bar{\phi}$

Poisson's Ratio . . . . . ν

Unconfined Compressive Strength . . . . . σ_c

Parallel Bond Friction Angle . . . . . ϕ

Post-peak Elastic Modulus . . . . . E_{pp}

Displacement Softening Contact Bond Friction Coefficient . . . . . μ_{ds}

Displacement Softening Contact Bond Tensile Strength . . . . . F_{tmax}

Displacement Softening Contact Bond Shear Strength . . . . . F_{smax}

Displacement Softening Contact Bond Compressive Stiffness . . . . . k_{nc}

Displacement Softening Contact Bond Tensile Stiffness . . . . . k_{nt}

Displacement Softening Contact Bond Residual Friction Coefficient . . . . . μ_{rds}

Particle/Loading Velocity v

Coupling Segment Length Ratio . . . . . ξ

Particle Position Vector . . . . . $\bar{r}$

Control Gridpoint Position Vector x

Coupling Segment Length l

Segment Orientation Unit Vector . . . . . $\hat{t}$

Platen Elastic Modulus . . . . . E_{plat}

Damping Force . . . . . F_d

Unbalanced Force . . . . . F_{unbal}

Time Step . . . . . t

Damping Moment . . . . . M_d

Kinetic Energy . . . . . KE

Particle Mass . . . . . m

Cumulative Kinetic Energy . . . . . KE

Instantaneous Mean Unbalanced Force . . . . . F_μ

Unbalanced Force Sum . . . . . $\mathbb{F}$

Cumulative Mean Unbalanced Force . . . . . $F_{\mu c}$

Maximum Instantaneous Maximum Unbalanced Force . . . . . F_{max}

Maximum Instantaneous Maximum Unbalanced Force . . . . . F_{max_c}

Contact Softening Ratio . . . . . U_{rat}

Total Number of Contacts C

Change in Force Exerted on Roof/Floor . . . . . ΔF_p

Change in Roof/Floor Displacement . . . . . ΔD

Slender Pillar Compressive Strength Model Width . . . . . M_W

Slender Pillar Compressive Strength Pillar Width . . . . . P_W

Failure Time Step Interval . . . . . dT

Pillar Post-peak Stiffness . . . . . K_{pp}

Lateral Earth Pressure Coefficient . . . . . K_E

Excavation Half-Span . . . . . l_e

Shear Modulus . . . . . G

In Situ Vertical Stress . . . . . σ_v

Abutment Vertical Stress . . . . . σ_z

Position Inside the Excavation . . . . . x_e

Position Inside the Abutment . . . . . x_a

LIST OF ABBREVIATIONS

Discrete Element Method	DEM
Particle Flow Code in 2/3 Dimensions	PFC2D/3D
Fast Lagrangian Analysis of Continua in 2/3 Dimensions	FLAC2D/3D
Unconfined Compressive Strength	UCS
Multiple Seams/Non-linear	MULSIM/NL
Laminated Model	LaModel
Analysis of Retreat Mining Pillar Stability	ARMPS
Analysis of Longwall Mining Pillar Stability	ALPS
Analysis System	ANSYS
Finite Element Method	FEM
Realistic Failure Process Analysis in 2 Dimensions	RFPA2D
Local Energy Release Rate	LERR
Finite Difference Method	FDM
Universal Distinct Element Code	UDEC
3 Dimensional Universal Distinct Element Code	3DEC
Synthetic Rock Mass	SRM
Triaxial Compressive Strength	TCS
Elastic Platen Compression	EPC
Loading Rate Compression	LRC
An native programming language accompanying Itasca C.G. codes	FISH

Adaptive Continuum/Discontinuum . . . . . AC/DC

Bonded Particle Model . . . . . BPM

Displacement Softening Model . . . . . DSM

Transmission Control Protocol/Internet Protocol . . . . . TCP/IP

Slender Pillar Compressive Strength . . . . . SPCS

In Situ Pillar . . . . . ISP

ACKNOWLEDGMENTS

I would like to first acknowledge my thesis advisor, Ugur Ozbay. Guided by your kind wisdom I have learned much about myself and life in general. Each time I arrived at new stages of realization throughout my studies, I also gained a greater appreciation for the efforts you afforded me. To put it mildly, I owe you one, and thank you.

My peers Ray Gu and Ryan Garvey spent many hours with me discussing topics of research. These conversations, which inevitably made their way towards more esoteric subjects, helped keep a flame of inspriation flickering in my mind when my way forward was murky. Thanks gents!

Graham Mustoe, who helped to provide much needed support with questions regarding nuances of the DEM. You've always sent me on my way with new ideas and possible pathways to explore. Cheers!

To my friends in Golden and Albuquerque. It's been a blessing having such friends that have always made me feel loved and at home. And a special shout out for my canine compainion, Roofis. That little guy has been through it all with me. Love ya buddy!

To my family back in the midwest. Barbara and Kevin, I owe you debt of gratitude for your advice to turn my sights on the Ph.D. at CSM. Without you I would have never taken this route. Also to the Rowlands, Dale, Charlie, and Grandma. I can't say enough about having a loving family to come back to.

To the esteemed faculty at the Colorado School of Mines who have gone great lengths to make the last four years a life changing experience. In particular Juan Lucena, John Berger, and Christian Frenzel. I strive everyday to emulate your confidence and professionalism.

This thesis is dedicated to my family: Susan, Mike, and Lauren. I find my motivation in our support for one another.

CHAPTER 1

INTRODUCTION

An underground mine is constructed as a system of hallways, or entries, that are kept open by pillars and abutments comprised of the in-situ material that is left behind. This primary support system is accompanied by a secondary support system composed of wood, steel, and hydraulic props that provide the additional support necessary to ensure stability of the working areas. A greater burden is put onto the support system as activity in the mine advances and more material is removed. Ideally, the support system will gradually fail under the increasing load and then these areas will be sealed permanently. However, the rock doesn't always fail in a controlled manner. In some cases, large amounts of rock are suddenly ejected with great velocity from mine walls resulting in injury or death of mine workers and suspension of operations. This sudden, violent failure of rock is called rockburst, or is more generally referred to as unstable failure.

Unstable failure is common in underground coal mining operations. The magnitude of unstable failures in underground coal mining can range from audible readjustment of mine stress to ejection of material from mine walls in a localized area to collapse of entire panels of coal pillars. In coal mining terminology, localized unstable failures are typically referred to not as rockburst but bumping or bouncing. While much effort has been dedicated to understanding the physical mechanism of unstable failure of rock in general, and the concepts have been applied to the coal mining situation, mining operations still are unable to predict the time and intensity of bumps.

Recent advances in numerical modeling have allowed for research into the physical mechanism of unstable failure that has potential to aid existing theoretical and experimental methods. An increase in computer processing power has allowed for models with increased complexity and size to be practical. More specifically, the discrete element method (DEM)

shows promise in capturing the micro-mechanical behavior of rock during failure that may be a crucial part in understanding the unstable failure of underground coal. An attractive feature of the DEM is the property of having emergent rock like behavior despite no explicit assignment of specific rock properties. For example, the ability of DEM to allow for crack propagation, a realistic Poisson effect, and increased strength with confinement. This thesis describes the development of improved numerical tools in DEM for analysis of the problem of unstable failure in an underground coal mining situation.

1.1 Problem Statement

In underground mining conditions, it is currently impossible to reliably predict when, where and with what intensity an unstable failure will occur. By studying the failure mechanism and factors that affect unstable failures, improvements can be made towards assessing the probability of intense, unstable failure. However, studying the mechanism of unstable failures in underground coal mines is a challenging task for two reasons. The unpredictable nature of unstable failures makes observation of the events problematic. Aside from a few case studies, anecdotes from the surviving mine workers are the only data available to describe the failure. And, due to the nature of the failure, evidence of the failure mechanism is lost because it is unsafe or impossible to access the failed area of the mine.

A recent occurrence of a series of unstable failures at the Crandall Canyon Mine, Utah in 2007 illustrates the devastation potentially associated with unstable failures in coal mining. The Mine Safety and Health Administration (MSHA) coordinated an investigation of the incident that included the participation of the mine operator, MSHA investigators and consultants Stricklin [80]. The initial collapse failed highly stressed pillars throughout a distance of approximately one half mine and registered as a magnitude 3.9 seismic event. This failure entombed six miners, and three were subsequently killed during a second failure while performing a rescue excavation operation. Figure 1.1 is a picture of the entry in which rescue miners were working to rescue the trapped miners after the second failure. The coal ejected from the entry walls in this area of the mine rendered this entry impassable and in

the process inflicted fatal damage.

Figure 1.1: Crandall Canyon mine entry filled with rubble after the second failure incident

The discrete element modeling technique has been successful in recreating poignant features of rock failure mode including softening post-peak curves with increasing confinement, crack propagation, and ejection of material during failure. By applying the discrete element method to the problem of underground unstable failure, an investigation on the effect of geological characteristics and mine geometry can be conducted in greater detail compared to continuum models. The ability of numerical models, including DEM, to simulate unstable failure is not well established. It is necessary to test DEM's abilities in simulating unstable failure and develop any tools or techniques necessary to utilize these capabilities. In this study, the discrete element code Particle Flow Code in Two Dimensions (PFC2D) is utilized in simulating unstable compressive failure and developing a method of distinguishing between stable and unstable failure [43].

1.2 Research Objectives and Methodology

The objectives of this research are to implement a DEM model appropriate for studying unstable compressive failure that utilizes the state of the art techniques in DEM modeling and knowledge of the mechanism of unstable failure. This goal is achieved by accomplishing a series of tasks listed below.

- Calibrate candidate contact models in PFC2D to approximate an in situ western U.S. coal.
- Implement advanced techniques in DEM modeling to facilitate appropriate model characteristics, e.g. apply appropriate confinement via boundary forces, utilize mechanical coupling algorithm to apply realistic and computationally efficient loading via continuum model, and construction of large DEM assemblies using a periodic material generation procedure.
- Test candidate models in a variety of compressive tests to determine poignant model behaviors and assess their applicability to studying compressive unstable failure.
- Validate the ability of the calibrated DEM model to simulate unstable and stable failure modes in compression.
- Identify a series of potential numerical indicators for distinguishing between stable and unstable failure.
- Analyze performance of indicators in cases of known failure stability.
- Develop a method for calculating and displaying indicator values so that spatial and magnitude attributes can be observed.
- Test identifier performance in a mine model with realistic loading applied by in situ stress and excavation.

1.3 Thesis Organization

Chapter 2 is a review of previous research found in the literature. Topics included are the rock mechanics of unstable failure, coal minig methods, and unstable failure in underground coal mining. The subject of numerical modeling in coal mining is discussed thoroughly by introducing numerical methods used in analyzing underground mining, some applications to study unstable failure, and special attention is given to the discrete element method to establish context for the DEM models used in this research.

Chapter 3 describes the calibration and comparison of two discrete element models, a widely used bonded particle model and a model that uses the so called displacement softening contact model. The specimens are failed in compression in four separate test types to evaluate the characteristic material behavior under rigid loading, the effect of confinement on stress to determine the Mohr-Coulomb friction angle, a test designed to reveal model behavior in stable and unstable failure modes, and a test to determine the effect of loading velocity on material behavior. Based on the results of these tests, the more appropriate DEM is chosen for further use in the thesis.

Chapter 4 introduces several failure stability indicators and applies them to two sets of compressive strength tests. One test set is the failure stability test from chapter three and the other is a compressive strength test for a series of slender coal pillars. Indicator behavior is evaluated in the the context of failure intensity and also the size of the model. A grid based indicator measurement technique that was developed for this study is explained and a selection of indicators are used to analyze the stable and unstable slender pillar failures.

Chapter 5 describes the implementation of a complex hybrid model designed to simulate a realistic mining situation. In situ stresses are installed and the coal material, as modeled in PFC, is incrementally mined and the stress distribution in the model is allowed to readjust after each mining increment. Failure stability is difficult to detect when failure is local, so the successful indicators from chapter two are used to closely analyze a situation of suspected instability. The analysis is then supported with grid grid based measurements of

two prominent indicators.

Chapter 6 then concludes the thesis by summarizing the conclusions from chapters three through five. A series of studies is suggested for future work using the current models and also additional research outside the scope of this thesis.

CHAPTER 2
BACKGROUND INFORMATION ON UNSTABLE FAILURE IN UNDERGROUND COAL MINING

Since the inception of underground mining, miners have dealt with unstable failures. However, before the nineteen sixties, mitigation for this danger has depended upon miner's intuition and rules of thumb. Improvements have been made in dealing with unstable failures by increasing the understanding of the physical mechanisms associated with unstable failure and by applying sophisticated technologies to mitigate dangerous mining situations, augment mining practices, and further study the problem. This chapter presents a background of the progression of research on unstable failure in underground mining in the context of rock mechanics and numerical modeling.

First, the rock mechanics of unstable failure are introduced. Then a background of underground coal mining is given and the geological conditions that are widely understood to influence unstable failure are presented. A review of noteworthy modeling tools in underground mining is also presented, with special attention paid to those focused on modeling unstable failure. Finally, a brief history of application of the discrete element method for rock mechanics is presented, with special attention given to applications in underground mining.

2.1 The Rock Mechanics of Unstable Failure

Due to the nature of underground mining methodology, rock structures in mines are often subjected to stresses high enough to cause failure. In order to formulate a theory to explain the mode of rock failure it is necessary to describe the behavior of rock after failure. Although, up until the 1960's, no theoretical basis was available to describe the behavior of rock after failure. The two prevailing theories in solid mechanics, linear elasticity and Mohr-Coulomb yield with perfect plasticity were insufficient to describe the state of equilibrium

within a fractured rock mass [54]. In 1965, N. G. W. Cook provided a lasting contribution which improved our ability to describe rock behavior after failure. He theorized that rock behavior after failure is governed by the formation of crack surfaces from stored strain energy. The process of forming cracks from the available strain energy results in a non linear path from peak stress to residual stress [17].

An set of laboratory compressive strength test tests are also presented in [17]. The results demonstrate the implications of a non linear post peak curve. The theory implies that if there is additional energy supplied by the loading system, the crack formation will not be capable of absorbing the additional energy and failure will occur unstably, along with a considerable release of excess energy. In the tests, similar rock specimens were failed with two different compression machines. One machine was very stiff and one had lower stiffness, capable of storing a larger amount of energy and hence failing the specimen unstably. The non linear post peak theory was confirmed when the soft testing machine failed the specimen unstably, as evinced by a loud shock, and the stiff machine failed the specimen stably with no noticeable shock. Cook's theoretical work and laboratory study together provided a tenant of failure stability that will be echoed throughout this thesis. That is, when the stiffness of the loading system is lower than the post peak stiffness of the failing material, there will be excess energy available that cannot be absorbed during the failure process, and failure will be unstable. Figure 2.1 is a stress strain plot that illustrates the concept of failure stability due to the effect of loading system stiffness. The solid line represents a UCS specimen's characteristic behavior that is only obtainable under perfectly rigid loading conditions. The dotted lines represent the load lines of a soft and a stiff loading system. When the loading system is stiff as compared to the post-peak stiffness of the specimen, the material is capable of absorbing the energy stored in the loading system through the failure process. When the loading system is soft, there is an excess of energy stored in the loading system, with magnitude dependent upon the angle theta, which the specimen is unable to absorb during failure process. For unstable failure two conditions must be met. The material must fail and

the loading system stiffness must be less than the post-peak stiffness of the material.

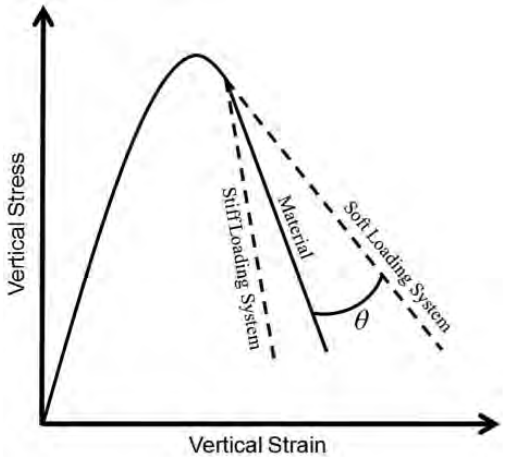

Figure 2.1: UCS failure stability stiffness criteria, after Kias *et al.* [49]

Other researchers followed in Cook's footsteps by performing laboratory testing exploring the post peak behavior of rock using stiff testing machines. These experiments both improved our understanding of the post peak behavior of rock and made advances in the technology required to investigate it. In 1967, Z. T. Bieniawski conducted a broad set of experiments to study various stages of rock failure, including post peak crack growth [9]. He obtained the first complete stress-strain curves of hard rock and verified the dependence of failure stability on loading system stiffness. W. Wawersik and C. Fairhurst in 1970 used a uniquely designed machine to study the post peak behavior of rock failure [88]. Six rock types were tested: two types of granite, marble, slate, basalt, and sandstone. They presented results for two types of post peak behavior, Class I and Class II. Figure 2.2 shows examples of stress strain curves of Class I and Class II behavior. Class I behavior is post peak behavior exhibiting increasing vertical compressive strain with decreasing load, a negative slope, while Class II post peak curves have a positive slope.

Wawersik and Fairhurst related the slope of the post peak curve to the amount of available strain energy in the rock specimen itself to cause failure. Class II failure indicates that additional energy must be supplied by the system to create additional crack surfaces and

progress failure. The negative slope of the Class I specimen indicates that an excess of strain energy is available in the specimen and the loading platens must be retracted to sustain a stable failure process. The vertical line between Class I and Class II, as shown in Figure 2.2 denotes the boundary in which precisely the exact amount of energy required for failure is supplied by the loading system and the specimen. The lettered regions of the Class I curve indicate different stages of failure discussed in [88].

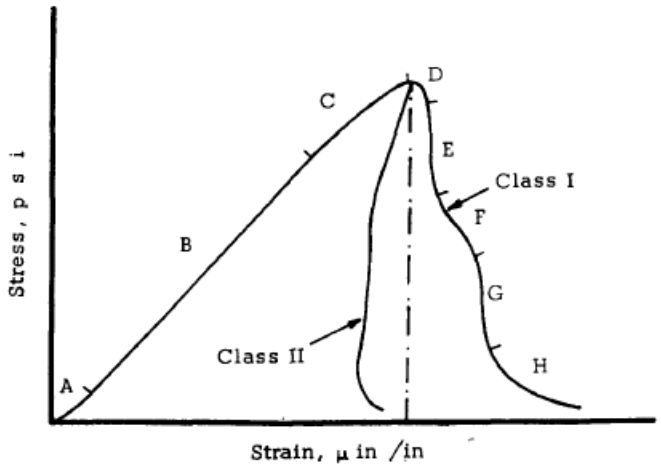

Figure 2.2: Class I and Class II post peak behavior, after Wawersik & Fairhurst [88]

Another careful study of post peak behavior using a stiff testing machine was published in 1971 by Wawersik and Brace [89]. The authors inspected crack patterns in specimens at various levels of confinement with Class I and Class II behavior. They concluded that the fracture mechanisms in rock were highly dependent upon confinement pressure and therefore a single failure criterion could not be used to describe failure of rock. Concerning unstable failure, they observed that small distributed cracking was more prominent in stable failures while unstable failures where coincident with the formation of longer and spatially focused fractures. Different fracture patterns suggest different failure mechanisms are in effect for stable versus unstable failure.

Additional, notable contributions to the study of rock post peak behavior were made in the following years. They include the introduction of a testing machine with a servo

controlled loading mechanism that was based on a a lateral strain gauge feedback measurement system [36]. This machine paved the way for modern testing machines with elaborate electronic systems designed to provide stress controlled loading schemes. A review of the progress in rock testing technology to date was provided in [35]. Then, the time dependent nature of rock behavior using advanced servo controlled testing equipment was presented by Peng in 1973 [63]

Elastic theory predicts a release of seismic energy simultaneous to the enlargement of an underground excavation, a theory for the mechanism of rockburst. Elastic theory was even used to propose a mechanism for collapse of room and pillar mines [76]. However, the energy release predicted by elastic theory is far greater than that measured during rockburst events [16]. With a better description of the post peak behavior of rock and a theoretical explanation of unstable failure in place, progress was made towards understanding this discrepancy by means of a possible mechanism for rockburst. Immediately following his seminal paper in 1965 Cook published a paper, aptly titled, *A Note on Rockburst Considered as a Problem of Instability*. In this paper, he explains that as a mining face advances a region of failed rock precedes it. This failed region is created by transfer of energy from the loading system, releasing available elastic energy in a less violent fashion than supposed by elastic theory. Furthermore, due to the mechanism of instability proposed in his previous paper a *'crudely periodic'* series of instabilities can result as the relative stiffnesses of the loading system and failing rock change during the mining process.

It was later pointed out that unstable failure could generally be grouped as either compressive or shear failures. Cook's failure stability stiffness criteria was applied to discontinuities by Salamon [77]. Ortlepp claimed that compressive and shear unstable failure could manifest in a variety of forms including pillar crushing, buckling, shear rupture in intact rock, and fault slip [61]. The work in this thesis deals only with the compressive type of unstable failure. Therefore, the term unstable failure is used in this thesis to refer to general compressive unstable failure, and not as distinguishing between types of compressive failure

as defined by Ortlepp.

Additional theories for the basic mechanism of rockburst have been proposed [74][86][83]. However Cook's mechanism is widely accepted as the leading theory for unstable failure in both rock and coal. So, the advances made by Cook on the understanding of failure stability and post peak behavior form the foundation for the physical mechanism of failure this research is based upon. The following section presents context for the application of these concepts to a coal mining situation.

2.2 Unstable Failure in Underground Coal Mining

The study of unstable failure of rock originated in response to the violent and often deadly failures that occur in underground mining situations. Throughout the history of underground mining practices, unstable failures have remained a pervasive danger that are not well understood, still to this day. While it is generally understood what conditions make unstable failures likely, predicting the precise moment and intensity of these failures is not possible. The mechanics of rock failure provide us with an insight to how rock fails, but the conditions in a particular mining situation add a layer of complexity and uniqueness. The characteristics of underground coal mining that influence unstable failures are discussed here.

Unstable failure in coal mining is often referred to as a coal bump or bounce in reference to the deep sound of shifting Earth reported during these failures. These failures range in intensity and volume depending on the location and nature of the failure. For example, a bump can result in nothing more than an audible sound in the roof or floor in the coal mine due to slip along joints or bedding planes. It can also cause the expulsion of tons of coal from mining faces or entry walls with fragment velocities up to the order of 10 m/s, entirely filling the mined out area with coal and burying mine employees and equipment. It can even result in a series of pillar failures, resulting in the complete destruction of entire mine panels. In each of these cases, the basic mechanism for unstable failure discussed above is in effect, but it is important to note that unique conditions for each case trigger instability

or determine the extent or intensity of failure.

The unpredictable and potentially fatal nature of coal bumps renders their in situ study not only dangerous but also impractical from a logistical standpoint. Coal bump researchers are forced to rely on mine incident reports for data and case studies that contain first hand accounts of bump incidents. A limited amount of seismic, load and displacement data is also available. Together, these sources help to provide information in establishing factors that influence the frequency and intensity of coal bumps.

Two basic mining methods are used in mining coal. They are the room and pillar mining method and longwall mining. The type of mining method can have an effect on the occurrence of coal bumps. In both types of mining, coal pillars are developed by mining away surrounding coal to create transport hallways, or entries. The remaining coal pillars and secondary support provide the ground control necessary for safe mining conditions. The sizing of pillars is important depending on the function they are designed to serve. Abutment pillars are large pillars that are capable of withstanding the total overburden stress. Abutment pillars typically have a pillar width to pillar height ratio greater than 10. Yield pillars are designed with failure in mind, so they fail gradually during the mining process and provide the loading system a stable means of releasing of strain energy. Yield pillars typically have a width to height ratio less than 5. Pillars sized in between abutment pillars and yield pillars are potential coal bump hazards as they are too large to yield stably and too small to withstand the total overburden stress [50]. These pillars are called critical pillars. Figure 2.3 is a diagram of the performance of gate road pillars for longwall mining that illustrates the effect of pillar size on stability. Note that the yield pillars fail while the abutment pillars do not, but they are both considered stable in their ground control performance.

2.2.1 Coal Mining Methods

In room and pillar mining, a panel of coal pillars is developed by first removing coal in a grid of hallways, also called entries. The pillar sizes in these developed panels can range widely in side and shape about 100 feet in width on each side. Upon completion of

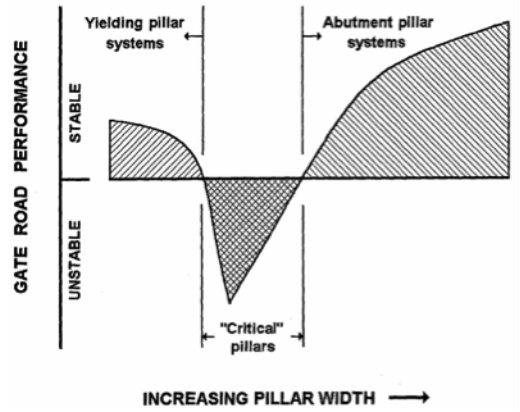

Figure 2.3: Pillar size versus stability

development, the pillars are removed in a process referred to as retreat mining. Starting from edge of the developed panel furthest from the mine's main transport area, the pillars are then mined out moving towards the opening of the mine. The roof of the mine is allowed to cave in after the pillars are removed. Due to safety, pillars are not always retreated in room and pillar mines, but it is often desired in order to maximize production.

Unstable failures are more likely to occur during retreat mining in room and pillar mines than during development [33]. This is due to the stress concentrations at pillar lines that can provide the load necessary to fail the pillar and then facilitate unstable failure. Pillars that are highly stressed yet not failed can also fail unstably during the retreat process. During the retreat mining process, pillars should yield as the pillar line approaches. The yielding process allows stress in the roof and floor to redistribute to larger load bearing structures or to facilitate caving inby the pillar line. If a pillar has yet to yield, a considerable amount of energy can be stored at the core of the pillar, acting as a critical pillar.

A method of pillar removal, called pillar splitting, is used to section a pillar into smaller, mineable parts to allow stress to redistribute safely. A bump can occur if an attempt is made to split a critical pillar [40]. The bump can occur when the highly stressed core of the pillar is suddenly deconfined. Sudden deconfinement results in a reduction in strength of the pillar core, and if the loading condition is unstable, a bump can result [12]. High stresses in

critical pillars can be due to inadequate caving. In any retreat mining operation continuous caving of the roof is desired. If roof rock remains intact, the cantilevered rock can impart additional load onto the pillar line. Suggestions for mitigating high occurrences of bumps near pillar extraction lines include taking preventative bump cuts ahead of the pillar line, pillar sequencing, and complete removal of pillars to promote adequate caving [38][39][94].

In extreme cases, entire panels of pillars can fail in a chain reaction as load is quickly shed from one failing pillar to the other and the potential energy in the loading system is abundant enough to propagate failure. A notorious example of such a failure is the Coalbrook North Colliery in South Africa 1960. Thousands of 12 by 12 by 4.2 meter pillars failed in a matter of minutes, destroying a mining area around 750 acres in size, killing 437 people [10]. Numerous other examples have been documented and studied to determine key factors of failure and possible mitigations procedures [13]. The effect of loading system stiffness in these failures in discussed separately by Salamon and Zipf, stating similarly that if the local mine stiffness is lower than the post peak stiffness of the failing pillars, the failure will be unstable [76][93].

The longwall mining method involves the use of a technologically advanced machine that moves mechanically back and forth along a wide panel of coal. A rotating drum attached to the machine scrapes coal from the mining face. The coal then drops onto a moving conveyor which transports the coal to a nearby entry and then to the mine opening. In the United States, the panel of coal being mined is typically 300 to 400 meters in width, 1.5 to 3 meters in height, and 3 to 4 kilometers in length or even longer. The coal shearer machine advances throughout the length of the panel under the protection of mechanized roof supports that advance with the mining face. The unsupported ground behind the supports is allowed to cave. In order to mine an entire coal seam, a series of longwall panels are developed alongside one another. These panels are mined in succession, and the entry on the trailing edge of the mined panels is named the tailgate while the entry on leading edge of the current panel is named the headgate.

In comparison to the room and pillar method, longwall mining is seen as a safe underground mining method due to the highly mechanized nature of the process. However, severe coal bump incidents are encountered. Similar to room and pillar mining, high stress areas are located along boundaries where mining has recently occurred and the overburden is unsupported. If material is not caving properly, cantilevered overburden leads to high stress on these mining boundaries. This increase in stress, called abutment stress, occurs in two locations in longwall mining, along the mining face and in the tailgate entries. So, the abutment stress increase is magnified at the tailgate side of the mining face. The likelihood of bumping occurs when highly stressed material is unconfined by the mining process. Therefore, increased bumping activity occurs when the coal shearer approaches and changes direction at the tailgate side of the panel. The pillars in the gate road entries serve an important roll in providing safe travel for mine workers, conveyance of materials, and proper ventilation. Much importance is placed on the design of gate road pillar systems [39]. Bumping in tailgate pillars is a common problem that often leads modern mines to discontinue mining on problematic panels [1][7]. In addition to the mining method, the frequency of coal bumps can be attributed to geological conditions in the mine, discussed in detail in the following section.

2.2.2 Geological Conditions Contributing to Coal Bumps

The geological conditions in a coal mine contribute to the frequency of bump incidents. For example, the presence of thick competent rock in the immediate roof and floor is a prominent feature of bump prone mines. The thick competent roof, usually sandstone, can contribute to the likelihood of bump incidents in multiple ways. First, the sandstone roof can resist fracture when underlying material is mined out and create cantilevered mass thereby increasing the load on critical structures such as a pillar line or the longwall face [70][29][30]. For this reason, sand stone members in the roof of a coal mine contribute to the inadequate caving seen in problematic mines. The competent sand stone also prevents an alternative mode of failure in the mine called punching. Punching is the failure of the immediate roof

and floor cause by the penetration of the still intact pillar into the roof or floor material [47]. The presence of the competent roof and floor ensure that, given a sufficient load, pillar failure will occur rather than the floor and could then possibly facilitate a bump by means of Cook's unstable failure mechanism.

An additional consideration associated with competent roof and floor rock is the contact condition. Iannacchione has suggested that a sudden slip along the coal rock interface would result in sudden deconfinement of the stressed coal [37]. Deconfinement would lead to a simultaneous drop in strength and lead to failure and a possible bump. This mechanism was earlier demonstrated in the laboratory by [3]. This experiment showed that similar coal specimens would fail stably or unstably depending on the confinement condition.

More traditional geological features such as faults or dykes contribute to bumping by augmenting the stress field when mining approaches these features. Dykes are channels of rock formed within the crack of another rock formation. Sandstone can be one such dyke material that when overlaying a coal seam can lead to increased stress as a result of the high stiffness [1]. Faults are preexisting zones of shear failure that allow shear movement more freely than intact or fractured rock. Depending on the orientation of a fault, approaching a fault by mining can lead to unstable slip along the fault. If the fault is dipping downward from the approach perspective then mining activity can unload the fault in the roof and lead to unstable roof failure. While heaving floor is possible when approaching upward dipping faults, the risk is not as severe.

One of the foremost factors in coal bumps is the depth of the mining activity. It is widely understood that deeper mines are at greater risk for bumping. The simple reason for this is that for coal bumps to occur, failure must occur, and failure is pervasive in deep mines as opposed to shallow ones. In U.S. coal mines 'deep cover' is defined as being greater than 1500 ft (457 m), but mines at depths greater than 1000 ft (305 m) are at risk [57].

Coal is a brittle rock, which means that it fragments upon failure and has little ductile deformation capacity. The brittleness of coal makes it susceptible to bumping in contrast

to more ductile materials such as salt. Complete stress strain curves for in situ coal pillars have been obtained of by Wagner and by Van Heerden [85]Van Heerden [84]. These tests results show an in situ coal behavior that has a defined post peak softening characteristic that decreases in slope as the width to height ratio of the specimen increases. The brittleness of rock is key to fulfillment of the Cook failure stability mechanism, in so far as for unstable failure the loading system stiffness must be less than the coal's post peak stiffness. It has also been proposed that pre-peak stiffness of coal is relevant to the intensity of failure [64]

2.3 Numerical Models and Unstable Failure

Due to the cost and logistical issues associated with experimentation, numerical models have become a popular means for investigating the failure of rock. The behavior of rock in mining situations requires an understanding of how the rock mass will behave prior to failure. As explained above, the mining process necessarily leads to the failure of surrounding rock. The surrounding rock is an agglomeration of layered, jointed material that behaves according to the properties of the joints and rock itself at all stages of stress and strain. Numerical models provide a tool to understand the key mechanisms at work on the process in question. The methodology by which one investigates such processes using numerical models is an area of contention. For example, it may seem desirable to build a complex model that contains all of the geological features of a rock mass. Although, Starfield and Cundall argue that simplification is needed in order to allow for comprehension of model results and thoughtful iteration of the experimentation process [79].

In this section, I will discuss a range of numerical modeling tools that have been used for modeling stress and strain in underground mining and discuss their capability to capture unstable failure. Then, I will present a set of important studies that are focused on simulating unstable failure. Using these examples as a basis, I will demonstrate that there is a well defined need for improving the ability of numerical models to simulate stable and unstable failure modes. The discrete element method is a proven method for modeling realistic features of rock failure and as this thesis will show, it is capable of capturing stable and unstable

modes of failure. So, a thorough review of rock failure simulated using the discrete element method and advanced techniques and capabilities are presented.

2.3.1 Underground Mine Models

Modeling stress and displacements in underground mining is a difficult task due to unknown geological features and properties. Through simplifications of the model such as idealized geometry and assumptions on material behavior, key features of mine behavior can be satisfactorily to allow for study. It is important to be aware of assumptions and limitations of each model in order to prevent erroneous interpretation of results.

A variation on the boundary element method called the displacement discontinuity method has been used in various programs. The program MULSIM/NL uses this method to model up to four parallel seams with optional non-linear behavior and elastic non seam material [92]. Another displacement discontinuity method program similar in structure, LaModel, is seen as having surpassed MULSIM/NL [32]. LaModel uses a lamination formulation that allows for more closure in excavated areas and matches subsidence observations better. These programs do not allow failure in any of the non seam regions.

The company Rocscience offers a series of programs for simulating stress and strain around underground openings. The boundary element programs Examine2D and Examine3D are boundary element programs that use the elasto-plastic material models and the modified Hoek-Brown failure criterion to simulate rock behavior [71][72]. The finite element program Phase2 utilizes the same material models but allows for polygonal material zones for customized geometries and multi stage calculations in order to simulate excavation processes [73]. Due to their explicit nature, these programs are incapable of converging on a solution if a physical instability occurs.

Including accurate simulation of failure stability in a mine model is not always a priority. However, such a model could aid in the preventative design of less bump prone mines. Mark provided an alternative to complex mechanical models with the programs Analysis of Retreat Mining Pillar Stability (ARMPS) and Analysis of Longwall Pillar Stability (ALPS)

[55][56]. These programs use empirical relationships to determine a pillar stability factor which indicates the likelihood of unstable failure. The sophistication of these programs lies in the extensive collection of case histories of pillar failures in U.S. underground coal mines.

The finite difference programs FLAC2D and FLAC3D, are highly versatile in definition of geometry, boundary conditions, and material properties [41, 42]. Each program includes numerous material models suitable for simulating a variety of geomaterials. Notable for rock is the strain softening plasticity model, which has been used to simulate yielding coal pillars in longwall mining [4]. The program has also been used to model stable and unstable failure modes in laboratory and in situ conditions [26].

2.3.2 Simulating Unstable Failure in Underground Mining

Specific to the problem of failure mode in underground mining, several sources can be cited that deal with unstable failure. In 1983, Zubelewicz and Mroz used a finite element model to study the violent failure of rock in various underground situations [95]. First, the static equilibrium is achieved, then the full equations of motion are solved explicitly after a disturbance is applied to the system. Kinetic energy is monitored, and if the energy increases drastically, the failure is considered to be unstable. Bardet created a finite element model to investigate surface buckling as a trigger for unstable failure [6]. These researchers claimed, by citing bifurcation theory, that instability can be detected when the stiffness matrix of the finite element grid becomes singular. The moment of instability was determined by finding the time step when eigenvalues of the stiffness matrix become negative. Muller followed up this study in 1991 with a comparison of explicit and implicit numerical methods in modeling unstable failure [59]. The author performed simulations in ANSYS, an explicit finite element program, and FLAC, an implicit finite difference program. Muller concluded that ANSYS was unable to represent the instability, but FLAC was successful by responding to instabilities with increases in local unbalanced force [2]. In their 1996 publication, Oelfke et al. presented a combined DEM-FEM code applicable to underground mine deformability [60]. The authors introduced the concept of mine instability as a function of local mine

stiffness and noted that the program could detect unstable failure as a divergence of the solution. Another group of researchers investigated the effect of a fractured rock mass as a loading system [14]. In this study, Chen et al. used a finite element model, called RFPA2D, to study the behavior of microseismicity during unstable failure [19]. They loaded a double rock sample in displacement control and monitored acoustic emission events. The authors claim that unstable failure can be detected as sudden changes in the microseismic rate, and demonstrated this with a realistic loading system with finite strength. In a 2009 study, Tan et al. suggested that unstable failure of pillars could be modeled using a discrete element model composed of two dimensional circular elements [81] These researchers used particle velocity to describe the intensity of failure. In a study using the program FLAC3D, Jiang et al. defined a term called the local energy release rate (LERR) that they claim can be used to describe the intensity of failure [46]. The LERR is the difference in stored strain energy in an element before and after failure. The authors compared LERR computed from simulations to known cases of unstable failure and showed that comparisons of magnitude of LERR were the same as the comparisons of intensity for the observed cases. Although, they stated that it is not possible to determine at what value of LERR an unstable failure occurs.

A publication by Larson and Whyatt reviewed available stress analysis tools for underground coal mining [53]. They compared the use of three numerical models in simulating a deep western coal mine with strong, stiff overlying strata: ALPS, an empirical model, LaModel, a boundary element method program, and FLAC2D, a finite difference method program (FDM). In their study, they showed that FLAC2D was able to model the sudden collapse of the mine entry due to failure in the roof and floor while LaModel and ALPS do not possess this ability due to the assumption of elastic overlying strata. Following this, Esterhuizen et al. presented a method to determine the ground response curve in FLAC models, and showed that the span to depth ratio has a notable effect on the ground response curve [23].

In some cases, strong consideration is given to how the structure of the rock mass is an integral part of its material behavior. Typically, the addition of joints, joint sets, and bedding planes brings an element of realism to the model. The computer programs UDEC and 3DEC allow the user to insert joints and joint sets with a variety of joint constitutive behaviors in 2d or 3d geometries respectively [45]. Barton 1995 presents an evaluation of the influence of joint properties on rock mass models that contain systems of joints [8].

2.3.3 Discrete Element Modeling Techniques and Applications

One other popular method of modeling rock is the discrete element method or DEM [18]. The two-dimensional method uses a collection of discs to simulate a granular material by detecting contact between the discs and calculating subsequent motion due to contact forces. Spheres can be substituted for discs to create a three-dimensional model, and if the elements are bonded together a solid material can be simulated [68]. DEM is powerful as a numerical modeling method because the user does not input a constitutive material law. Rather, the user specifies a set of micro-parameters that define stiffness and strength of the discs and bonds.

Calibration of material behavior by selecting the appropriate micromechanical parameters is an area that has widely been explored, but still needs much improvement. When calibrating a DEM model it is advantageous to understand the effects of changing micro-parameters on macro behavior. Potyondy and Cundall provided the initial guidance for choosing micro-parameters in their seminal paper [68]. Since then, several researchers have published papers on material calibration and sensitivity of macroscopic behavior on various micro-parameters. Kulatilake et al. demonstrated an iterative calibration scheme for rock behavior up to the strength at various levels of confinement [52]. Initial stiffness values were calculated from equations provided by the PFC3D manual and adjusted after testing the sample based on results for overall sample strength, elastic modulus, and Poisson's ratio [44].

A pervasive drawback of modeling rock failure with DEM is the underestimated angle of internal friction and the low compressive to tensile strength ratio. Fakhimi attempted to calibrate these behaviors by using a technique where the particle assembly is slightly overlapped at all contacts and then normal forces are zeroed [24]. It is thought that the increased contact frictional force in absence of the normal contact force would increase the overall internal friction angle. While the internal friction angle and compressive to tensile strength ratio both improved, the modified DEM still yielded unrealistic values. In 2007, Fakhimi and Villegas published a dimensional analysis of DEM micro-parameters that reinforced the importance of the sample genesis pressure to the material failure envelope [25]. Koyama and Jing showed the effect of model scale and particle size on the macro behavior of the sample and outlined a method to determine the representative elementary volume for a given set of micro-parameters [51]. Cho et al. introduced the idea that by clumping particles together into irregular shapes, one can improve the simulation of failure behavior in terms of the failure envelope and tensile to strength ratio [15]. Yoon suggested that by selective design of experiment, Plackett-Burman in this case, one can optimize the micro-parameters using sensitivity analysis [91]. This method results in reliable parameter selection for rock materials within ranges not applicable to the study of coal and only up to the point of failure.

Hsieh et al. demonstrated the effect that complex arrangements of various types of particles with particularly defined contact parameters can affect deformability and strength behavior [34]. Wang and Tonon produced a sensitivity analysis that developed equations relating micro-parameters to sample deformability and strength [87]. Shopfer et al. showed the effect of sample porosity and initial crack density on material behavior up to peak strength [78]. Up to this point no researchers had dealt with the calibration of the post-peak behavior until 2011 when Garvey and Ozbay offered a method to calibrate deformability, strength, and post-peak modulus [27].

Despite difficulties in calibration, it has been demonstrated in numerous papers that with proper micro-parameter calibration, realistic rock properties emerge [31, 58]. Some

of these properties are elasticity, fracturing, anisotropy with accumulated damage, dilation, strength increase with increased confinement, post-peak softening and hysteresis. Modeling rock behavior with DEM has three limitations worth noting. The measured Mohr-Coulomb friction angle is roughly half of its expected value, the Mohr-Coulomb failure envelope is linear, and the compressive to tensile strength ratio of the material is lower than the real rock [21, 67, 68]. It has been proposed that by introducing non-circular elements, the effects of these limitations are greatly reduced [15].

Many strategies are available to tailor a DEM model to most efficiently achieve its goal. Within bonded particle models, user defined contact laws have a notable effect on the overall behavior of the model. Resulting macro behaviors include time-dependent stress corrosion and sliding along pre-existing joints [58, 66]. Also, heterogeneity in rock can be modeled by enclosing groups of similarly strong or stiff particles with smooth contacts to create a larger grain [69]. The grain-based model is well suited for modeling cases that involve spalling or for instances where inter-granular and intra-granular cracking are pertinent features of the failure process. The method of modeling a rock mass by embedding a system of joints can be achieved in DEM by replacing bonds with smooth contacts along predetermined joint planes. The synthetic rock mass (SRM) approach was developed by Mas Ivars et al [58]. Pierce et al. showed that it satisfactorily predicted rock mass brittleness by validating fracturing in a case study block cave mine Pierce *et al.* [65]. The SRM approach has also been used to address scaling issues associated with using DEM to model rock masses. When DEM material is calibrated to intact rock properties, the well-known effect of strength degradation due to increased scale does not occur. Deisman et al. and Esmaieli et al. showed that an SRM model can simulate the scale dependency of macroscopic behaviors in a coal bed methane reservoir and an underground metals mine in Canada [20][22].

DEM models are well suited to model micro-mechanical behavior of rock such as notching [68]. Although, DEM is notorious for high run times, so it is unreasonable to construct large models out of relatively small particles. One reason is that equilibrating such large a system

can be problematic, especially if they contain regions with varying material behavior. One alternative is to construct a large model using a continuum modeling software and embed a DEM section in the appropriate area. The commercial programs FLAC2D and PFC2D are capable of using a mechanical coupling algorithm to communicate forces and velocities to one another via socket connection [68]. Aside from the verification studies provided by the makers of the program, uses of this facility include an acoustic emissions detector adjacent to a large underground excavation [11] and a model of a blast induced damage zone inside a tunnel [75].

CHAPTER 3

EVALUATION OF TWO DEM MODELS FOR SIMULATING UNSTABLE FAILURE IN COMPRESSION

In order to simulate unstable failure using a numerical model, the post-peak behavior of the simulated material must have a softening characteristic. In this chapter, two different discrete element models are compared to determine which is better suited for simulating unstable failure in compression. The two models are described in detail then subjected to a series of compression tests. In each test, the same geometry of specimen is brought to failure under compressive loading. The suite of tests was chosen to investigate the effect of key loading conditions imposed on the DEM by in situ models of later chapters.

Four different test procedures are used to investigate the behavior of each DEM. The first test is used to establish the so-called characteristic material behavior, which refers to the rock specimen deforming incrementally under gradually increased loading. The uniaxial compressive strength test, UCS, is used to establish characteristic material behavior for the purpose of this research. The other three tests that are used to investigate the effect of three separate loading conditions include: triaxial compressive strength test (TCS), elastic platen compression test (EPC), and loading rate compression test (LRC).

The UCS and TCS model tests use a constant velocity boundary condition to load the specimen where no strain energy is available from the loading system to affect the specimen's failure mode. To investigate the performance of DEM and also the failure modes of rocks, elastic end platens are placed on top and bottom of the specimen. In this series, the platens can store strain energy, which can be released during specimen failure in a gradual or sudden manner depending on the rock's failure mode. In a specific test series called elastic platen compression, EPC, the platen stiffness is gradually reduced to observe the failure mode changing from being stable to unstable. Lastly, a test is implemented to investigate the

effect of loading rate on the characteristic material behavior of the DEM code. A series of UCS tests is conducted in which the loading rate is changed to a different value for each test. By comparing the resulting stress-strain curves, the effect of loading rate on elastic behavior, strength and post-peak behavior is analyzed.

3.1 Particle Flow Code in Two Dimensions (PFC2D)

In this study, the DEM modeling studies are performed by using the commercially available discrete element code PFC2D [43]. These codes allow for model customization via an embedded programming language called FISH. PFC2D comes with a collection of FISH functions that allow the user to accomplish complicated tasks with a moderate amount of background knowledge in discrete element modeling. The authors of PFC2D call the preinstalled collection of fish functions the Fishtank. The Fishtank contains a series of functions that generates a discrete element model of a bonded rock-like material and performs tests to determine material properties. Templates are provided in the Fishtank that link together steps in a study such as material generation, testing, then data display. Templates can be run as examples or by providing custom inputs to the template, user specific tasks can be easily performed. Fishtank version 1-115 was used in this research. It is often necessary to modify the provided test procedures and functions for user specific purposes. Template files used in material generation, testing or function definition will be referenced along with customized inputs. Files containing modified test procedures or custom functions will be provided in the appendices.

3.2 Material Generation and Calibration

This study utilizes the material generation procedure described in the PFC2D manual within the section entitled PFC Fishtank. Circular elements, or particles, are created within a vessel and element radii are varied until a target isotropic stress is achieved. Then "floating" particles (particles with a number of contacts below a predefined threshold) are deleted and the elements are bonded using either parallel or contact bonds. Here, periodic boundaries are

used to create a square vessel, resulting in square blocks of material that can be connected seamlessly to create a larger assembly. This so called pbrick method is decried in detail in the PFC2D manual under the topic of adaptive continuum/discontinuum (AC/DC) logic. For material generation and specimen assembly, the Fishtank template `acdc-2d` is used. The file `acdc-pbr.dvr` is used to generate the pbrick, and the file `acdc-bv.dvr` is used to assemble pbricks into the specimen.

The behavior of the generated material is largely determined by behavior of particle contacts, called the contact model, and the type of bond used to attach the particles to one another. The combination of contact model and bonding scheme make up the constitutive model of the discrete element model. Both the contact model and the bond are defined by a set of microparameters governing stiffness and strength properties. For this study an appropriate constitutive model must be chosen and calibrated for the purpose of simulating unstable failure. It is necessary that the constitutive model is capable of simulating a softening post-peak characteristic. Two constitutive models available to PFC2D users that are capable of simulating a softening post-peak characteristic are the parallel bonded particle model and the displacement softening model.

Figure 3.1 shows the components of a discrete element model constitutive model. The contact model can contain a bond in the form of a contact bond and a parallel bond can be added. Elastic contact behavior in both constitutive models described below is the same. Figure 3.2 shows a schematic of the components of stiffness between two particles that are in contact. Each particle is assigned a value for normal stiffness, k_n, and shear stiffness, k_s. Force between the particles is calculated using Hooke's law, Equation 3.1, where i represents values associated with either the normal or shear direction. The stiffness coefficient, K_i, is calculated by assuming the element stiffnesses to act in series. Therefore, contact stiffness is calculated using Equation 3.2, where A and B represent the particles involved in the contact.

$$F_i = K_i dx_i \tag{3.1}$$

$$K_i = \frac{k_i^A k_i^B}{k_i^A + k_i^B} \tag{3.2}$$

The differing behavior between the two models evaluated in this chapter have to do with definition of strength and behavior after failure. These differences and calibration of the models is described below.

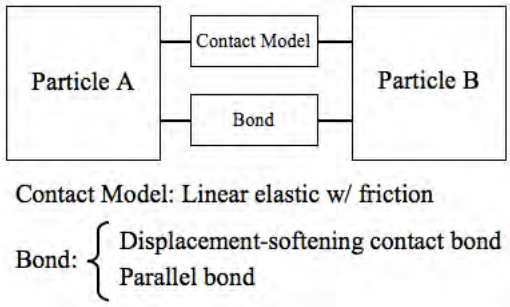

Figure 3.1: Components of a DEM constitutive model

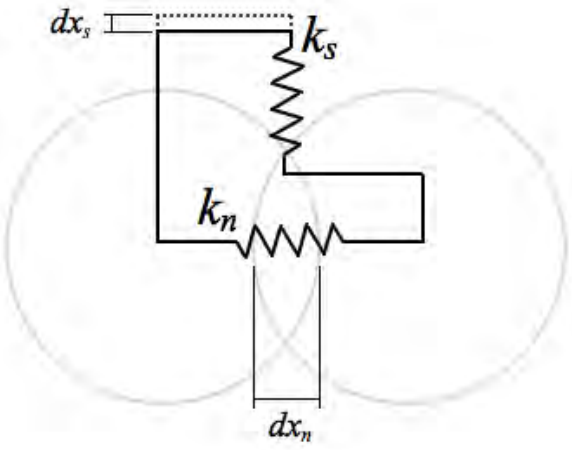

Figure 3.2: Contact stiffness and displacement between DEM particles

3.2.1 Bonded Particle Model

The bonded particle model (BPM) includes a parallel bond in addition to the linear elastic contact model described above. A parallel bond behaves as an elastic beam joining bonded particles. The parallel bond can resist tension, compression and bending, but can

also fail in direct tension or due to bending. After a bond breaks, newly detected contacts obey the laws of the contact model.

Failure in the parallel bond is dependent upon the geometry of the contacting particles and the cross sectional area of the bond. According to beam theory, the maximum shear and tensile stresses that can exist in the bond are Equation 3.3 and Equation 3.4 respectively.

$$\tau_{max} = \frac{F_s}{A} \tag{3.3}$$

$$\sigma_{max} = \frac{-F_n}{A} - \frac{|M|\,R}{I} \tag{3.4}$$

F_s and F_n are the shear and normal forces on the bond, M is the moment, and $A = 2R$, the cross-sectional area of the bond with unit thickness and I is the bond moment of inertia.

In this study, success of the calibration of the BPM relied on achieving a softening post-peak characteristic. Until recently, no information existed in the literature on calibration of post-peak behavior in bonded DEM models. Garvey & Ozbay [27] introduced an iterative calibration method that uses an elitist-selection, genetic algorithm and an unconfined compression test to discover a set microparameters that achieve a target stress-strain behavior. For this research, the method was modified to utilize a two dimensional specimen assembled using the pbrick method. Table 3.1 shows the resulting microparameters necessary to reproduce the BPM material used in this study. Parameters not listed are set to the default values, which can be found in the PFC manual.

3.2.2 Displacement Softening Model

The displacement softening model (DSM) in PFC2D is a constitutive model composed of a bonded contact model without a parallel bond. Figure 3.3 shows the force versus displacement curve for the DSM. The DSM behaves as described above in the elastic region. When initial contact bond strength, F_c^n, is reached, the contact behavior begins to follow a linear strength softening curve. If unloaded during softening, the bond can rebound along the elastic path. When the user defined plastic displacement limit is reached, U_{pmax}, the

Table 3.1: BPM microparameters

Parameter	Description	Value
PFC2D Material (parallel bonded)		
Associate with disk size distribution		
R_{min} [m]	Minimum Disk Radius	0.005
(R_{max}/R_{min})	Particle Size Ratio w/ uniform distribution	1.636
Associated with material generation		
$\sigma_o{}^t$ [MPa]	Vessel Pressure	-0.1
n_f/N_b	Remaining Floater Ratio	0
Associated with particles		
ρ_{bulk} [kg/m^3]	Bulk Density	1313
E [GPa]	Elastic Modulus	3.143
(k_n/k_s)	Stiffness Ratio	0.533
μ	Friction Coefficient	0.399
Associated with parallel bonds		
B_{pb_all}	All load in pbonds flag	0
$\overline{\beta}$	Moment Contribution Factor	0
$\overline{\lambda}$	Bond Radius Multiplier	1
$\overline{E}_c$ [GPa]	Modulus	3.143
$(\overline{k}_n/\overline{k}_s)$	Stiffness Ratio	0.96
$\overline{\sigma}_c$ [MPa]	Tensile Strength	6.741
$\overline{c}$ [MPa], $\overline{\phi}$ [deg]	Cohesion, Friction Angle	5.34, 0

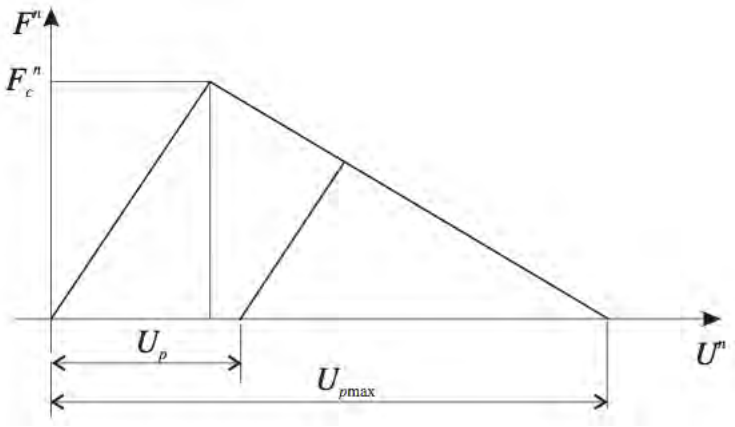

Figure 3.3: Displacement-softening constitutive model behavior

bond is inactive.

The contact yields in tension when the resultant contact force, Equation 3.5, is greater than the contact strength, Equation 3.6. Here, the plastic displacement is in the direction of the resultant force.

$$F = \sqrt{F^{n^2} + F^{s^2}} \tag{3.5}$$

$$F_{cmax} = \left(1 - \frac{2\alpha}{\pi}\right) \cdot F_c^n + \frac{2\alpha}{\pi} \cdot F_c^s \tag{3.6}$$

If the contact is in compression, failure can occur due to shear. The strength of the contact, Equation 3.7, is dependent upon the coefficient of friction and the normal force, and plastic displacement is in the shear direction.

$$F_{cmax} = \mu \left|F^n\right| + F_c^s \tag{3.7}$$

During yield, the elastic displacment increments in the normal and shear directions are a function of only the portion of resultant force up to the strength and the contact stiffness, Equation 3.8, where $k = n, s$, and the plastic displacement increments are given by Equation 3.9.

$$\triangle F^k = K^k \triangle U_e^k \tag{3.8}$$

$$\triangle U_p^k = \triangle U^k - \triangle U_e^k \tag{3.9}$$

The contact normal and shear strengths are decreased depending upon the amount of softening experienced by the contact, where U_p is the sum of plastic displacement increments in the direction of the contact force:

$$F_c^k = F_c^k \left(1 - \frac{U_p}{U_{pmax}}\right) \tag{3.10}$$

The particle assembly in the DSM is generated with a linear contact law, then displacement softening contact model microparameters are assigned and the model is cycled to achieve equilibrium. Table 3.2 shows the set of microparameters that are needed to reproduce the DSM material used in this thesis. Parameters not listed are set to the default values.

Table 3.2: DSM microparameters

Parameter	Description	Value
PFC2D Material (displacement-softening)		
Associate with disk size distribution		
R_{min} [m]	Minimum Disk Radius	0.005
(R_{max}/R_{min})	Particle Size Ratio w/ uniform distribution	1.66
*Associated with material generation**		
$\sigma_o{}^t$ [MPa]	Vessel Pressure	-0.1
n_f/N_b	Remaining Floater Ratio	0
Associated with particles		
ρ_{bulk} [kg/m^3]	Bulk Density	1313
E [GPa]	Elastic Modulus*	3
(k_n/k_s)	Stiffness Ratio*	2.5
μ	Friction Coefficient*	0.5
Associated with d.s. contact model		
μ_{ds}	Friction Coefficient	1.75
$F_{t\max}$ [kPa]	Tensile Strength	6.5
$F_{s\max}$ [kPa]	Shear Strength	6.5
k_{nc} [GN/m]	Compressive Stiffness	6.0
k_{nt} [GN/m]	Tensile Stiffness	6.0
k_s [GN/m]	Shear Stiffness	2
μ_{rds}	Residual Friction Coeff.	0.5
U_{pmax}	Plastic Displacement Limit	0.007

The calibration of the DSM can be performed iteratively by the user in a short period of time due to the intuitive response of macro behavior due to changes in microparameters. Material generation is performed once. The resulting particle assembly is used to test various combinations of microparameters. The UCS test is used to determine the stress-strain behavior. First, desired elastic behavior is achieved by varying contact stiffness. Then the plastic displacement limit is varied to change the post-peak softening behavior of the specimen. By increasing U_{pmax}, the post-peak modulus decreases and the strength of the specimen increases. To achieve an appropriate UCS and post-peak modulus, the tensile and shear strengths of the contact are decreased. Some iteration is necessary to achieve the desired behavior. The following section presents results for UCS tests on the calibrated BPM and DSM.

3.3 Unconfined Compressive Strength Test (UCS)

The DEM material properties necessary for study of unstable failure in compression can be found using a simulation of compressive strength tests. The UCS is used in this research to calibrate the DEM by approximating a target set of characteristic material properties. The target characteristic behavior is representative of an in situ western United States coal.

The UCS test specimen is a one meter wide by two meter high assembly of two blocks of either DSM or BPM material. The specimen is loaded passed the point of failure until an adequate assessment of post-peak behavior can be determined. The Fishtank template, direct tension test with reversed platen displacement is used to perform this test. It is necessary to use "grip particles" in order to compress the specimen due to the roughness of the specimen ends. Table 3.3 shows UCS test template filenames and necessary inputs. For the DSM, all contacts are assigned the displacement softening contact model with microproperties listed in Table 3.2 after the specimen is restored. Stress in the sample is calculated by summing particle forces in each grip respectively, dividing by the width of the specimen, and then averaging the two grip stresses. Strain is calculated by determining the change in specimen height using grip displacement. The test is terminated in the post-peak region when the

measured axial stress in the sample is lower than half of the UCS. After half of the peak stress has been dissipated due to failure, a sufficient range of post-peak softening can be observed in order to quantify the material post-peak modulus.

Table 3.3: UCS test parameters

Parameter	Description	Value
Associated with `sW_mL_tA-tw.dvr`		
dt dscale	differential density scaling option	set on
Associated with `tAtt_param.dat`		
`mt_tt`	Grip Thickness (m)	0.02
`mt_psr`	Platen Strain Rate	0.05
`mt_code`	Test Termination Criteria	2
`mt_alpha`	Test Termination Value	-1
`p_close`	Close Platens Flag	1
`mv_H`	Specimen Height (m)	2

Figure 3.4 shows the stress-strain curves from UCS testing on the BPM and DSM. Table 3.4 lists the elastic properties and post-peak modulus of each model and for a target material. The target material is set to approximate an in situ, western United States coal. Both curves reflect a post-peak softening characteristic that is approximately equal in magnitude to the pre-peak modulus. Each material is within an acceptable range from the target material properties. While it is beyond the scope of this thesis, improvements in the calibration of both the BPM and DSM warrant further investigation. This would involve an in-depth look at the genetic algorithm used to calibrate the BPM or comprehensive sensitivity analysis of DSM microparameters respectively.

Table 3.4: DEM and target characteristic material properties

	Target	BPM	DSM
E (GPa)	4.0	5.3	6.0
ν	0.2	0.1	0.4
σ_c (MPa)	7.6	7.6	8.7
E_{pp} (GPa)	4.0	7.9	3.0

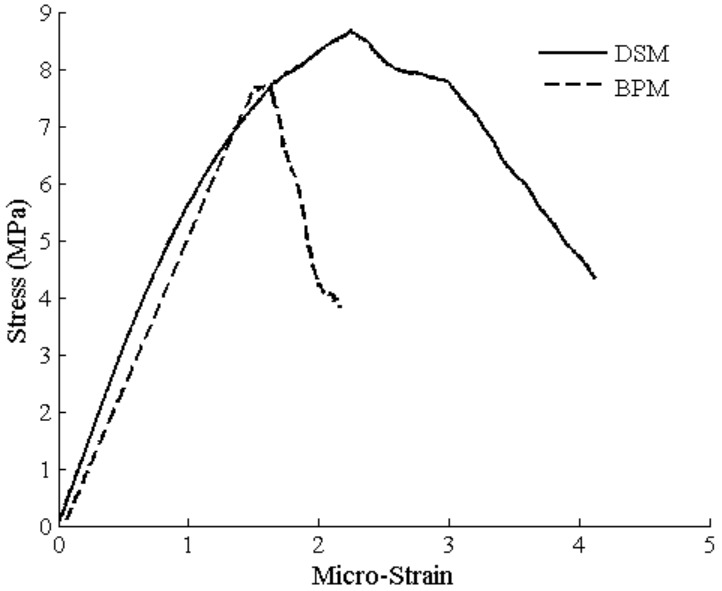

Figure 3.4: UCS stress-strain curves for the BPM and DSM

3.4 Biaxial Compressive Strength Test (BCS)

Consider an axially loaded rock specimen shown in Figure 3.5 under a constant confinement stress σ_3 and deviatoric stress σ_1. According to the Coulomb failure criterion, failure will occur along a plane oriented at an angle β. In this failure criterion, the strength is linearly proportional to the normal stress on the failure plane. Equation 3.11 shows the relationship between the shear strength, τ, the cohesion, c, the normal stress, σ_n, and the internal friction angle, ϕ.

$$\tau = c + \sigma_n tan\phi \tag{3.11}$$

Similar to what is observed in the laboratory, when confinement stresses are applied to bonded discrete element models, strength of the material increases. Strength increase in the presence of a confining stress is an emergent property of the DEM that is not directly calibrated. By performing BCS tests on the specimens described above, the internal friction angle of the DEM material can be calculated and compared to that of real rock.

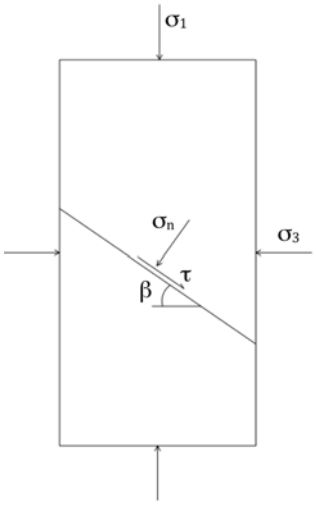

Figure 3.5: Coulomb shear failure plane and stresses

A constant confining pressure is applied to the specimen using the so called spanning chain algorithm included in the Fishtank. The spanning chain algorithm detects particles that lie along a boundary and applies forces to the particles to simulate a constant boundary pressure. The advantage of using this technique is that it allows for displacements on the boundary preventing stress concentrations that would be caused by a rigid boundary such as a wall. Custom functions were introduced in order to adapt the algorithm to the UCS specimen. These custom functions are shown in Listing A.1. The test template used for the UCS tests above was modified to include the spanning chain and pressure functionality. This file is shown in Listing A.2. The test parameters listed in Table 3.3 are also used in this set of tests. Figure 3.6 shows a screen shot of the specimen. The yellow marks are the disk shaped elements, and the red circles attached by black lines make up the spanning chain used to apply the confining stress.

BCS tests were performed using 1, 2, 4 and 6 MPa confining stress on both the BPM and DSM DEMs. The tests were terminated post-failure when the axial stress decreased to ninety percent of the strength. Figure 3.7 and Figure 3.8 show stress versus axial strain curves for the BPM and DSM. The dotted lines are the horizontal stresses and the solid lines are the axial stresses. The dotted lines show that the spanning chain confinement method

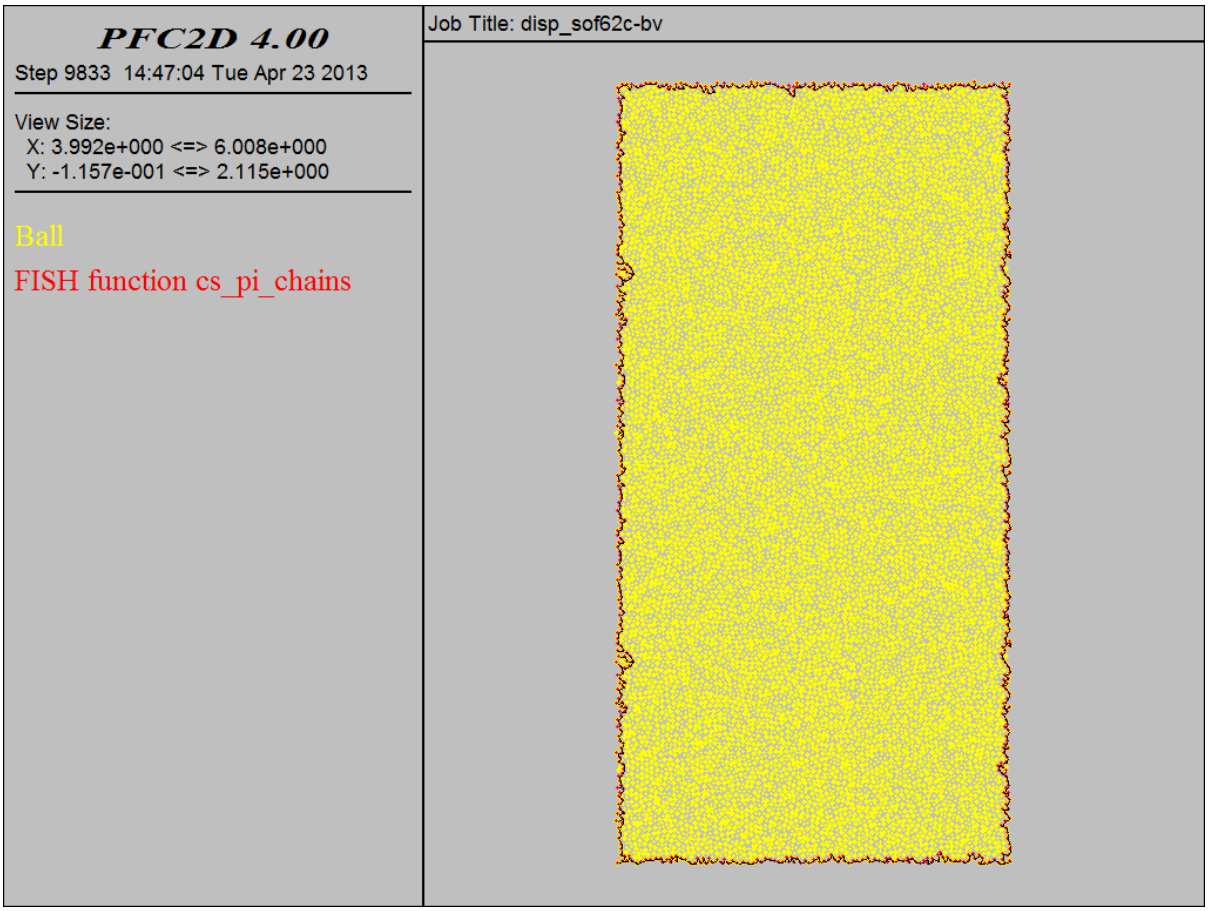

Figure 3.6: PFC2D specimen and spanning chain

provided more consistent confinement stress during the BPM tests than in the DSM tests. Horizontal stress increased approximately 1 MPa throughout each of the DSM tests and

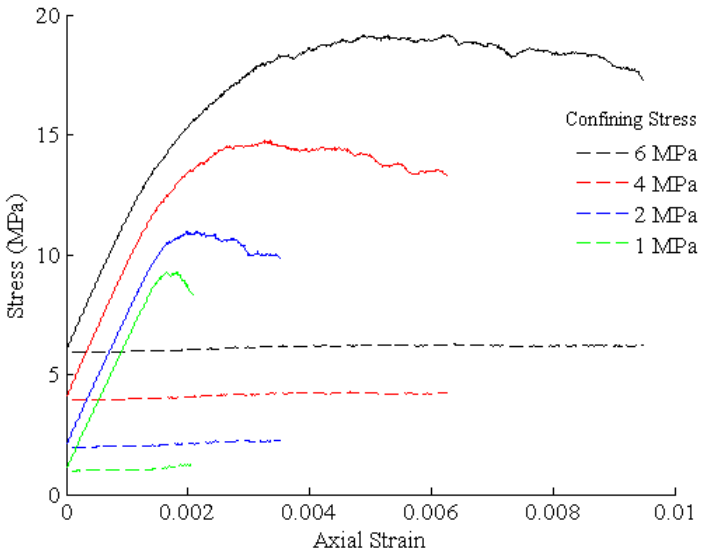

Figure 3.7: BPM confined compression test stress versus strain curves

only approximately 0.1 MPa for the BPM tests. Peak axial stress, σ_1, and the prescribed confinement stress, σ_3, were used to calculate the shear and normal stresses on the failure plan in order to determine the friction angle.

Figure 3.9 shows a shear stress versus normal stress plot using each test result for both discrete element models. The plot also shows the internal friction angle for each model. The friction angle for the DSM is significantly higher than the BPM. The friction angle of real coal is approximately 30 degrees. So, the BPM will simulate the coal as being weaker under confined conditions than reality while the DSM will simulate the coal as being stronger under confined conditions. Considering the increase in horizontal stress during the DSM tests, a slightly lower friction angle can be attributed to the DSM material. By considering the horizontal stress at failure rather than the prescribed confining stress as the true confining stress the friction angle of the DSM material decreases slightly to 42 degrees. The effect of confining stress on strength will determine the strength of the rock during compressive

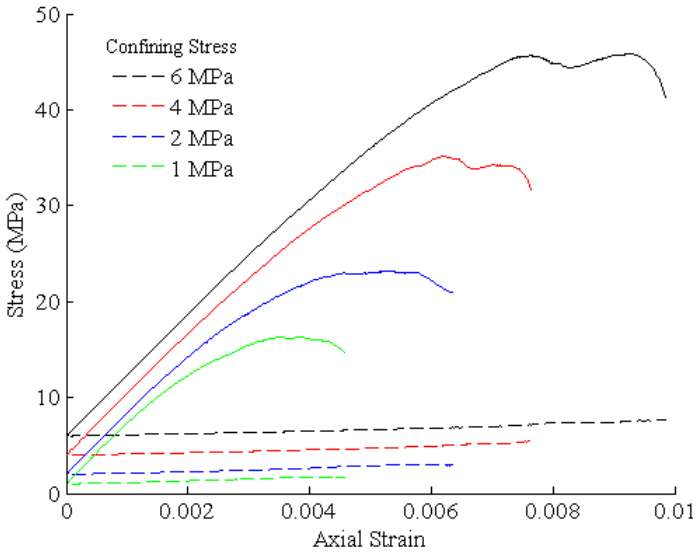

Figure 3.8: DSM confined compression test stress versus strain curves

failure but it will not effect the failure mode of the rock. So, while a study on the mechanisms underlying unstable failure will not be directly affected by the friction angle the BCS test provides supplementary information on the accuracy of DEM simulation of rock behavior.

3.5 Elastic Platen Compression Test (EPC)

By varying the stiffness of the loading system, the DEM specimen can be failed in a stable or unstable mode of failure. A mechanical coupling method is used to fail the DEM models under elastic platens simulated using the finite-difference, continuum code FLAC2D. Here, first the coupling method will be explained and then results from the compression tests will be presented and discussed.

The mechanical coupling of FLAC2D and PFC2D relies on the exchange of gridpoint velocities and particle forces at the coupling boundary via a socket connection like that used in TCP/IP transmission over the internet. The coupling boundary consists of a layer of discs in the PFC model which overlaps the FLAC grid and the gridpoints associated with the FLAC grid on that boundary. The particles on the boundary are called control particles and the gridpoints that are on the FLAC coupling boundary are called control gridpoints.

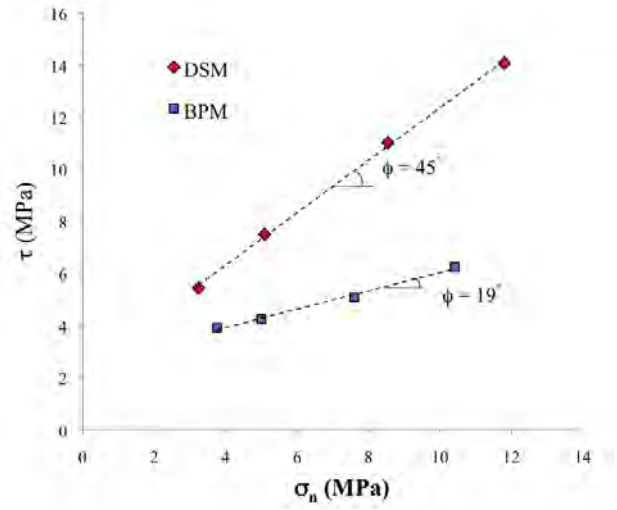

Figure 3.9: Shear stress versus normal stress results from the confined compression tests

Figure 3.10 shows a diagram of the coupled model calculation cycle. The red arrows indicate communication between FLAC2D and PFC2D. PFC2D uses Fish functions provided in the Fishtank to update boundary conditions before every cycle. With these functions, PFC2D uses control gridpoint velocities to calculate and then apply velocities to control particles. Following a calculation cycle in PFC2D, updated forces on the control particles are used to calculate and then send control gridpoint forces to FLAC2D. Following a calculation cycling in FLAC2D, updated control gridpoint velocities are sent back to PFC and the coupled model cycle repeats.

Each control particle is associated with a FLAC2D segment, which is defined by two control gridpoints Figure 3.11 shows a diagram of two control gridpoints, 0 and 1, and one control particle, P. In order to apply the velocity boundary condition to PFC2D, control particle velocity is determined by linear interpolation of control gridpoint velocities. The relationship between control particle velocity, v, and control gridpoint velocities, v_0 and v_1 is shown using Equation 3.12

$$v\left(\xi\right) = v_0 + \xi(v_1 - v_0) \tag{3.12}$$

where,

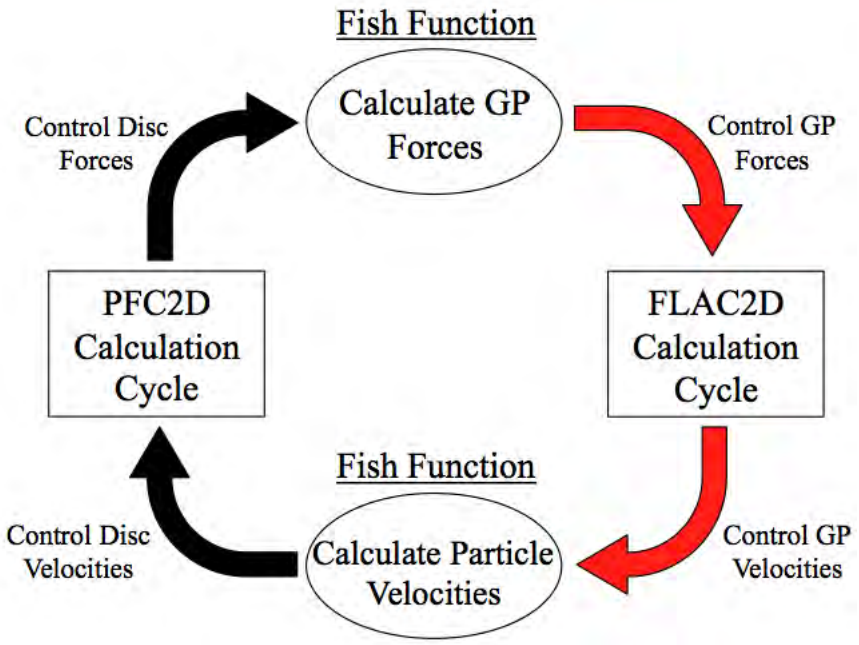

Figure 3.10: Mechanically coupled model calculation cycle

$$\xi = \frac{r \cdot \hat{t}}{l},\ \bar{r} = x_p - x_0,\ \hat{t} = \frac{x_p - x_0}{l}$$

Figure 3.12 shows a close up of a PFC2D/FLAC2D coupling boundary in PFC2D. The yellow circles are the discs, the black circles are the locations of control gridpoints and the discs with red circles are the control discs. The blue arrows are velocity vectors. The velocities of the control particles are assigned directly via the coupling relationship shown in Equation 3.12 while the velocities of the other particles are calculated by PFC2D as usual. Control gridpoint forces are calculated by distributing control particle forces to control gridpoints in the segment with which they are associated. The control gridpoint forces, $\overrightarrow{F_0}$ and $\overrightarrow{F_1}$, are calculated by distributing the shear stress on each control particle based on nearness, conserving the moment about x_0 and ensuring that the sum of the forces on the control gridpoints equal the sum of the forces on the control particles. Figure 3.13 shows a close up of a coupling boundary as seen in FLAC2D. The white lines are grid zone boundaries

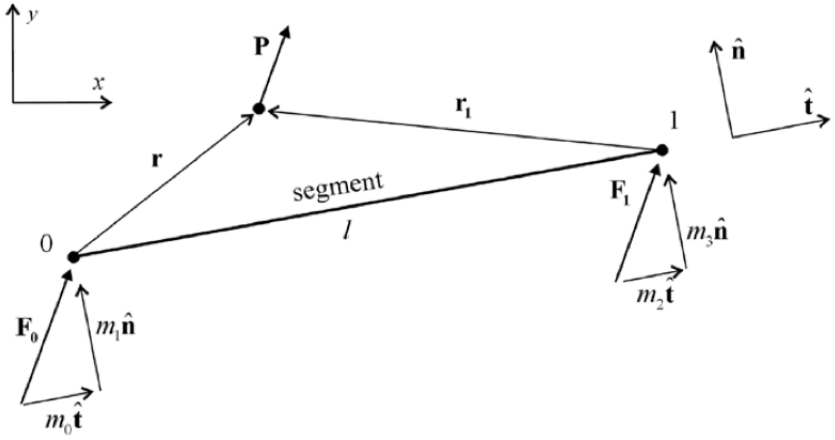

Figure 3.11: PFC2D/FLAC2D coupling mechanism diagram

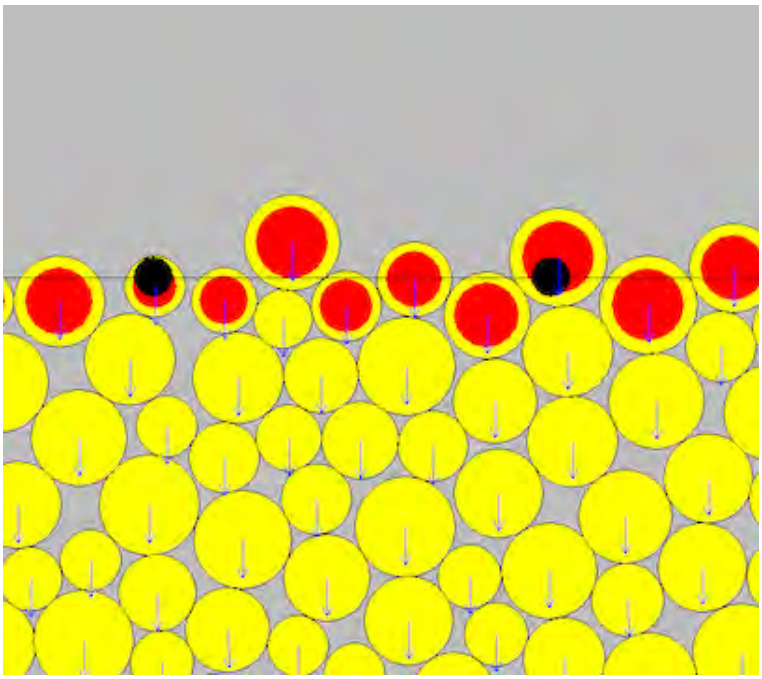

Figure 3.12: Coupling boundary as shown in PFC2D

and the blue arrows are forces applied to control gridpoints via the coupling mechanism.

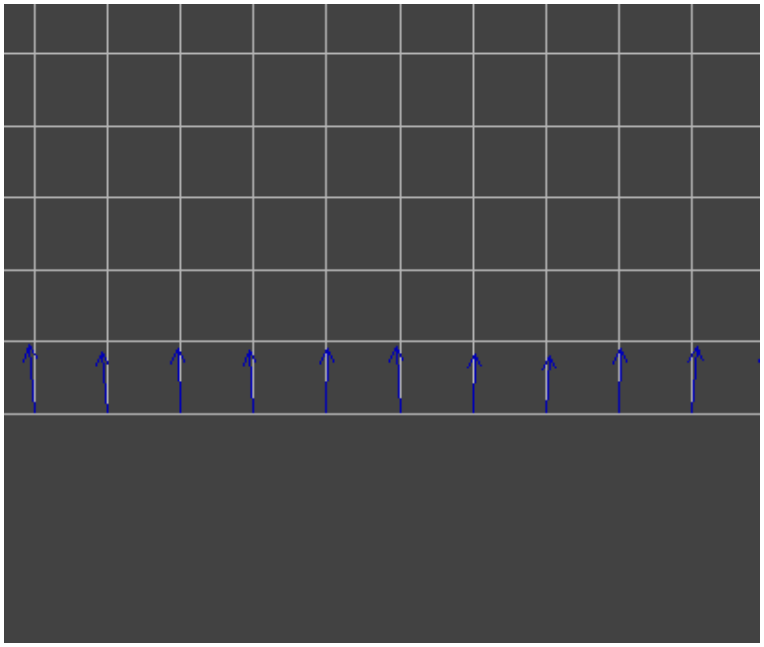

Figure 3.13: Coupled model boundary as shown in FLAC2D

Default functions provided with PFC2D used for coupled simulation are found in the files `cpflib.fis` and `cpplib.fis` and are located in the Fishtank. For FLAC2D, seven custom files were used in the unstable compression test and they are provided in Appendix A. Each file is presented as a listing of the lines of code. Listing A.3 shows the front end file for the FLAC2D simulation. Here, the user specifies the elastic modulus to be used for the test, then the simulation is initiated. The main driver file in Listing A.4 issues all of the commands to load necessary functions [Listing A.5] and initiate functionality by calling the functions at the appropriate times. This includes defining custom fish functions for controlling the coupling mechanism, [Listing A.6], defining model specific functions that control geometry, material properties and boundary conditions, [Listing A.7 and Listing A.8], and defining model state measurement functions and recorded data, [Listing A.9].

For PFC, five custom files are used, they are shown in the appendices. These files are structured similarly to the FLAC2D EPC files in that a front end file, Listing A.10, controls the initiation of the test by restoring the DEM specimen and calling the main driver

file, [Listing A.11]. PFC2D acts as the master program and controls coupling by issuing commands to cycle the two codes one calculation step at a time. This is done in the main driver file, along with loading default functions for control of the coupling boundary and custom functions used to initialize the system, [Listing A.12 and Listing A.13]. Functions used for measuring model state variables and recording data are also called from the driver file, [Listing A.14].

Figure 3.14 shows the test geometry and boundary conditions for the coupled simulation. The upper and lower platens are moved inward at the velocity used for calibration. It was expected that the specimen would fail in a stable manner when the loading system modulus was higher than than the specimen post-peak modulus and unstable when the loading system modulus is lower than the specimen's post-peak modulus. A series of tests for each DEM were run in which only the platen elastic modulus was varied. A range of moduli were chosen for each model so as to clearly depict the transition from stable to unstable failure as platen moduli decreases.

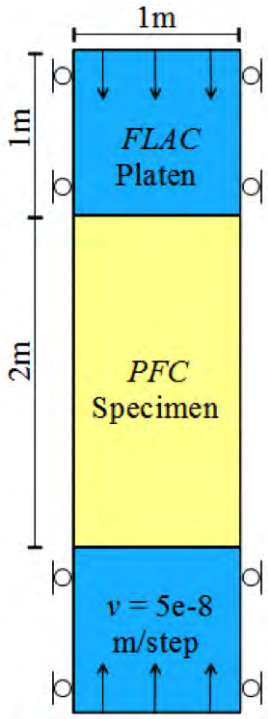

Figure 3.14: Mechanically coupled compression geometry and boundary conditions

Figure 3.15 and Figure 3.16 show stress strain curves for the EPC simulations using the BPM and DSM respectively. BPM simulations were conducted using ten different platen moduli: 0.5, 1, 2, 3, 5, 10, 15, 20, 35, and 50 GPa. DSM simulations were conducted using seven different moduli: 1, 1.5, 2.5, 5, 10, 20, and 35 GPa. In both plots, the unconfined compressive strength stress-strain curve is included to provide a reference to the calibrated characteristic material behavior. Both plots show that for tests with stiff platens as compared to the material post-peak modulus the post-peak behavior follows the slope of the characteristic material curve from the UCS test. Tests with soft platens show a deviation in specimen post-peak behavior from the characteristic material post-peak behavior.

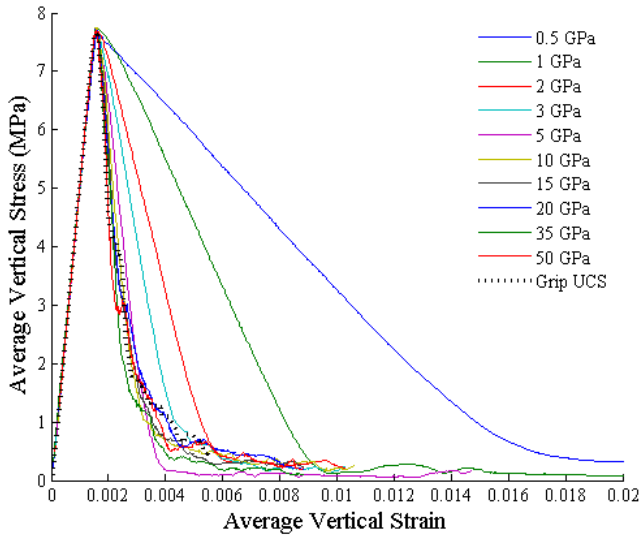

Figure 3.15: BPM coupled simulation stress-strain curves

A determination of failure stability is possible by comparing the assigned loading system modulus and the specimen modulus determined from observed post-peak behavior. The specimen post-peak modulus is determined by measuring the post-peak slope of the specimen stress-strain curve. During stable failure, the specimen fails according to its characteristic material properties. So, the post-peak modulus equals the calibrated characteristic post-peak modulus, E_{pp}. During unstable failure, all load bearing capacity of the specimen is lost. Without the resistance of the specimen, the platens rebound according to the elastic

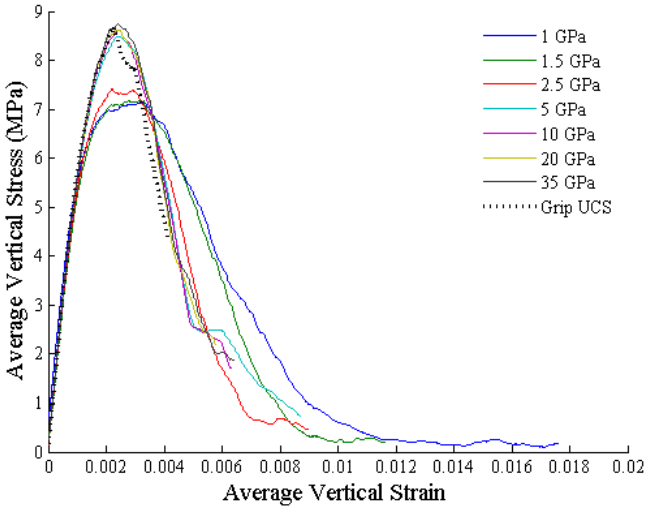

Figure 3.16: DSM coupled simulation stress-strain curves

properties. So, it appears that the specimen post-peak modulus changes to equal the modulus of the loading system.

Table 3.5 and Table 3.6 show the specimen post-peak modulus measured from each test and the strength of each specimen for the BPM and DSM respectively. The characteristic material behavior is also included, labeled as "UCS Grip". The shaded area indicates tests that resulted in unstable failures. Figure 3.17 shows a scatter plot of E_{pp} and E_{plat} from each EPC test, the measured specimen post-peak modulus and the assigned loading system modulus respectively. The vertical lines are E_{pp} from the "Grip UCS" tests, which are the calibrated specimen post-peak moduli for the BPM and DSM.

Table 3.5 and Table 3.6 show numerically that when E_{plat} becomes larger than the characteristic E_{pp} the EPC E_{pp} begins to deviate from E_{plat}. This is shown graphically in Figure 3.17 as a asymptotic trend to the right of the vertical lines marking characteristic E_{pp}. Ideally, each model should transition immediately to stable failure as loading system modulus increases beyond this value. The trend in the DSM post-peak modulus values indicate that a fairly sharp transition from unstable to stable failure occurs. This is reflected in the consistency of values in Table 3.6 that are not shaded. On the other hand, the post-peak behavior

Table 3.5: BPM EPC post-peak modulus and strength values

E_{plat} (GPa)	E_{pp} (GPa)	σ_c (MPa)
0.5	0.51	7.64
1	1.06	7.74
2	1.93	7.70
3	2.74	7.68
5	3.86	7.67
10	5.14	7.74
15	6.59	7.72
20	6.83	7.72
35	7.49	7.69
50	7.06	7.69
Grip UCS	7.90	7.70

Table 3.6: DSM EPC post-peak modulus and strength values

E_{plat} (GPa)	E_{pp} (GPa)	σ_c (MPa)
1	1.05	7.13
1.5	1.43	7.18
2.5	2.04	7.41
5	2.95	8.49
10	2.94	8.61
20	3.07	8.63
35	2.95	8.74
Grip UCS	3.00	8.70

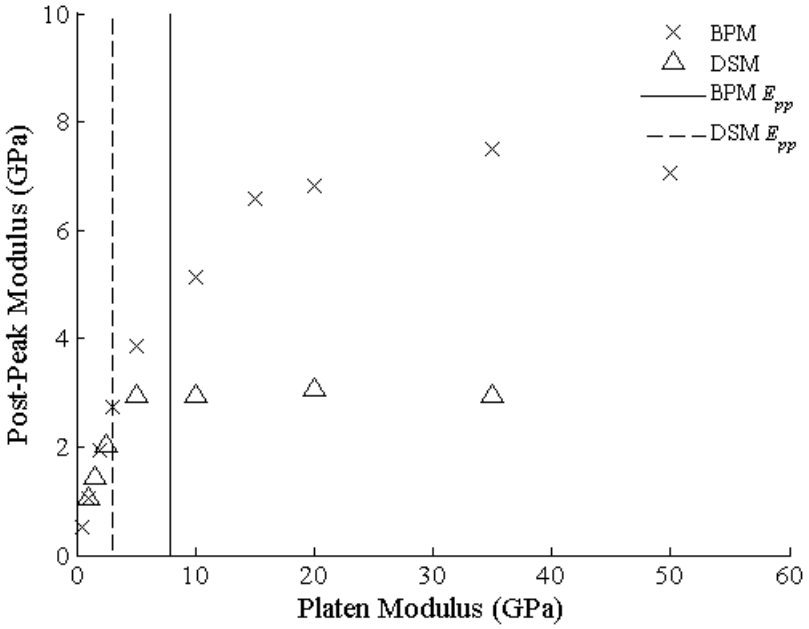

Figure 3.17: Loading system and specimen post-peak moduli in EPC tests

of stable BPM failure has a range of values. This is shown in Figure 3.17 as a slow transition toward stability in terms of EPC E_{pp} and inconsistent values for high moduli tests. The stability transition behavior for the BPM indicates that other factors are in effect. This so called quasi-stable behavior in the BPM tests could be caused by micro-mechanical behavior that is not visible in this type of analysis. For example variation in failure progression could lead to a change in the post-peak characteristic during the process of the failure, leading to a E_{pp} different from the characteristic E_{pp} or E_{plat}. This effect is not noticeable in the DSM results. Additionally, the DSM has consistent E_{pp} for each stable test while the BPM E_{pp} for the high modulus tests (more likely to be stable than the quasi-stable moduli tests) varies slightly and remains below characteristic E_{pp}.

In the EPC tests, the effect of loading system stiffness on the mode of failure of two DEMs was investigated by changing the modulus of elasticity of the loading platens between different tests. The stability transition behavior of the two DEM models is important to the current research in so far as we are able to reliably detect unstable failure. According

to the stability transition behavior presented above, in a situation where the loading system stiffness is similar to the characteristic material post-peak stiffness, the DSM more clearly distinguishes between stable and unstable failure. The BPM behaves in a quasi stable manner when the loading system stiffness is similar to the characteristic material post-peak stiffness. The quasi-stable behavior is more difficult to discern as stable or unstable because the post-peak behavior is equal to neither the characteristic post-peak behavior nor the loading system stiffness.

A difference arrises between the DSM and BPM model behavior during the EPC test when examining the strength. Figure 3.16 show a change in specimen strength for the three softest DSM EPC tests while in the strength in the BPM EPC tests remains fairly consistent. Table 3.5 and Table 3.6 show the strength of each specimen for each test. These results indicate that the strength of the DSM material decreases when subjected to unstable loading conditions. The BPM model does not experience this change. A possible reason for this reduction in strength could be the sudden onset of localized, unstable crack growth. Contact bond failure associated with material yielding could be prematurely accelerated if a large amount of stored strain energy is available. In the case of soft, elastic loading systems, this is possible. Additional work would be needed to confirm this hypothesis. Local measurements of material stiffness could provided evidence for this micromechanical process. Regardless, when using this DEM, a reduction in strength of the DSM material should be expected when loading system stiffness is less than material post-peak stiffness.

3.6 Loading Rate Compression Test (LRC)

In the final test of DSM and BPM behavior in compression, the UCS test is revisited with different loading rates, referred to as LRC. Four loading rates are chosen, including the loading rate used for the previous tests. As in the UCS test, grip particles are moved inward to load the specimen. Vertical stress and strain measurements are taken using the grip particles and the stress-strain curves for each test are compared.

Figure 3.18 shows the stress strain curves for four LRC tests of the BPM. Figure 3.19 shows the stress-strain curves for the same tests using the DSM. **??** and Table 3.8 show the loading velocity (v), the post-peak modulus (E_{pp}) and the strength (σ_c) for the BPM and DSM tests. Due to the shape of the DSM curves in the post-peak region, some liberty had to be taken to choose a representative section of each curve in Figure 3.19 to describe the post-peak behavior as linear. The straight portions of the curves ranging from 50% to approximately 80% of peak strength were used to calculate E_{pp}.

Table 3.7: LRC BPM loading velocity, post-peak modulus and strength values

v (m/s x 10^{-9})	E_{pp} (GPa)	σ_c (MPa)
1.2	121	7.58
30	13	7.6
60	10	7.7
90	7	7.92

Table 3.8: LRC DSM loading velocity, post-peak modulus and strength values

v (m/s x 10^{-9})	E_{pp} (GPa)	σ_c (MPa)
1.2	3.6	8.02
30	3.0	8.29
60	3.1	8.67
90	3.6	8.99

Figure 3.18 and Figure 3.19 show that there is no noticeable effect of loading rate on the elastic region of the stress-strain curve. As loading rate increases, the strength of both DEMs increases. The effect is more prominent in the DSM model than in the BPM model. In the post-peak region, a change in material behavior emerges as the loading rate is changed. Figure 3.18 and Table 3.5 show that the E_{pp} of the BPM increases as the loading rate is decreased. The change in post-peak stiffness is so drastic, that the material entirely looses the calibrated post-peak softening characteristic. Figure 3.19 shows that the change in loading rate has an effect on DSM post-peak stiffness. As loading rate decreases the stress-strain curve reveals abrupt changes in vertical stress as the material fails. Despite changes to the

slope, enumerated in Table 3.6, it can be seen in Figure 3.19 that the material retains its softening post-peak characteristic.

A possible explanation for the changes in DEM post-peak behavior under various loading rates is the interaction between increased confinement with increasing loading rate and specimen strain energy. The release of stored strain energy in the DEM specimen can result in unstable failure if the material cannot absorb the energy during failure. Although, this effect can be masked by a high loading rate, giving the impression of a definite post-peak material characteristic for a given loading rate. Additional work to support this claim is presented in Appendix B. The conclusion that can be drawn from the supplementary study is that the BPM model characteristic E_{pp} is unknown, but is likely a value greater than the elastic modulus. The DSM model is mostly unaffected by the loading rate because the material is capable of absorbing the specimen strain energy during failure. When modeling situations where the loading velocity is controlled, the BPM can be calibrated to have a definite post-peak characteristic at that specific loading velocity. The UCS, BCS, and EPC tests in this chapter are examples of cases where the BPM model is used successfully due to a constant loading rate. Although, when modeling in situ conditions, the loading velocity is not controlled by the user and the material will experience changes in the post-peak softening behavior. The DSM is expected to retain a consistent softening characteristic with varying loading velocity and hence will behave more consistently in the post-peak region in situ.

3.7 Summary of Results and Conclusions

The four tests in this chapter were implemented to investigate the properties of two DEMs during compressive failure. The UCS tests showed that calibrating a softening post-peak characteristic behavior is possible for both models, and that the material properties could be set to approximate a western United States in situ coal. The micromechanical softening aspect of the DSM seems to allow for a direct calibration of macro-scale post peak material softening, however additional work would be required to understand the complexities of this relationship.

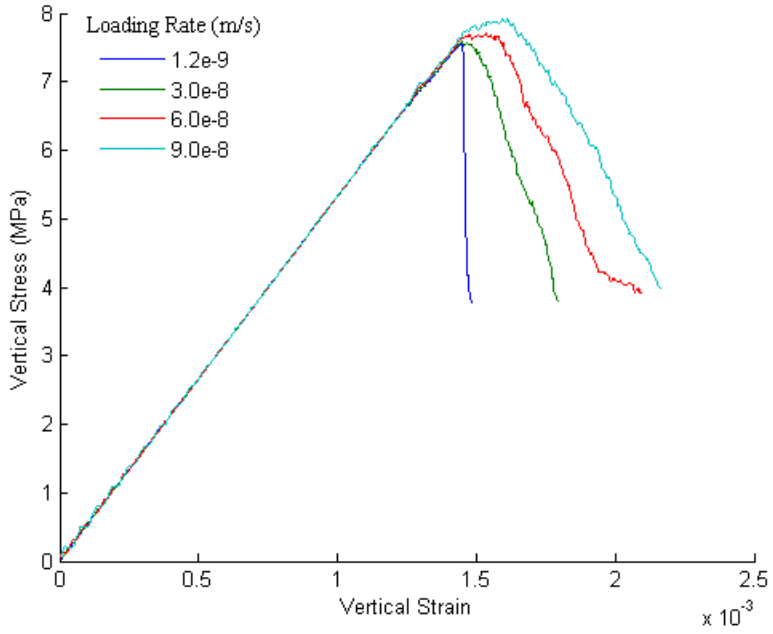

Figure 3.18: BPM variable loading rate unconfined compression stress-strain curves

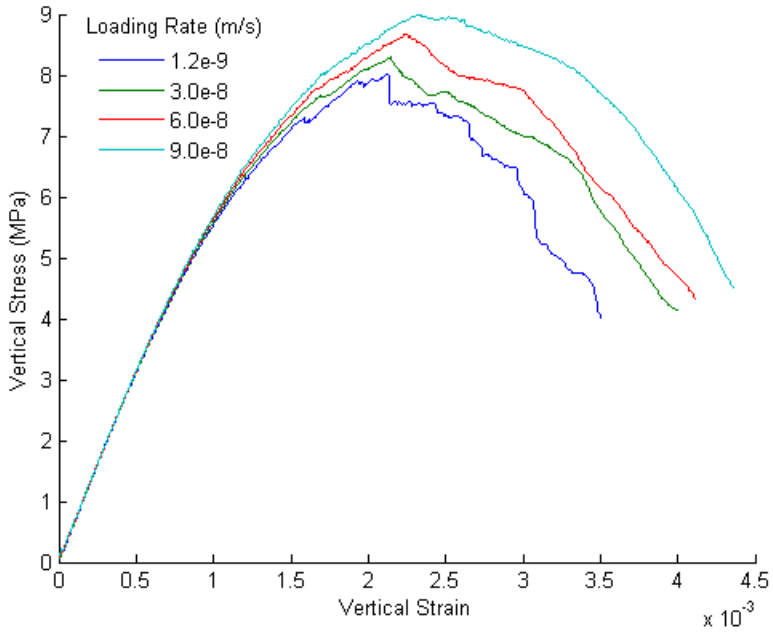

Figure 3.19: DSM variable loading rate unconfined compression stress-strain curves

BCS tests showed a stark difference in the effect of confinement on strength between the two models. The DSM has an internal friction angle that is higher than the approximate internal friction angle of coal and the BPM's internal friction angle is too low. The low internal friction angle of the BPM is a known shortcoming of the model [68]. The higher than desired internal friction angle of the DSM is an unexpected result.

EPC test results showed that failure stability in the DEMs could be determined by comparing loading system and material post-peak stiffnesses. Using this comparison as an indicator of unstable failure, when platen modulus increased beyond the material post-peak stiffness the DSM transitioned more quickly than the BPM from unstable to stable failure. LRC tests revealed changes in post-peak behavior in both models. In the BPM, as loading rate decreased the post-peak stiffness increased drastically. While in the DSM, the slowest loading rate resulted in abrupt changes in stress during failure, but overall the material retained its post-peak softening characteristic.

The results from the EPC and the LRC tests provide important model behavior characteristics that suggest that the DSM is more appropriate for the studies of unstable failure in underground coal mining. The DSM's sudden transition from unstable to stable failure seen in Figure 3.17 indicate that the expression of unstable failure is more ambiguous in models using the BPM. It was important in this chapter to show that the chosen DEMs could satisfactorily simulate unstable failure, but in work in later chapters it will be shown that detecting instances of unstable failure in larger models is crucial to studying the effects of local mine conditions on instability.

In a later chapter, an underground mine model will be introduced that uses in situ stresses to load the PFC2D coal. Rather than applying a consistent loading velocity, gradual mining steps will redistribute stresses in the model resulting in increased load on material near the excavation. The velocity by which the model applies the load is not controlled by the user and will vary from the velocity used to calibrate the PFC2D material. Figure 3.18 showed drastic changes in the post-peak softening characteristic of the BPM material as loading

velocity decreased. If the loading velocities imposed during simulated mining are of similar magnitude, the BPM will experience a change in post-peak behavior. Although, the DSM retains its post-peak softening characteristic despite changes in loading velocity. A consistent post-peak softening characteristic will allow for commensurate comparison between situations, for example, various levels of confinement or loading system stiffness. Therefore, the following work in this thesis is carried out using the DSM.

CHAPTER 4

INDICATORS OF UNSTABLE COMPRESSIVE FAILURE IN DEM COAL STRENGTH TESTS

This chapter is concerned with characterizing the expression of unstable compressive failure in the displacement softening model (DSM). Various measurements of DEM behaviors can be used to indicate whether failure is unstable or stable and give a measure of the degree of failure instability. These calculated values are called stability indicators. Nine stability indicators are explained and employed here. They are damping work, maximum instantaneous kinetic energy, cumulative kinetic energy, maximum instantaneous mean unbalanced force, cumulative mean unbalanced force, maximum instantaneous maximum unbalanced force, cumulative maximum unbalanced force, contact softening, and the number of broken contacts.

The nine indicators are first applied to a simulation of a laboratory test, the elastic platen strength (EPC) test from the previous chapter. Since both stable and unstable failure occurred within the series of EPC tests, the behavior of each indicator during unstable and stable failure is observed. The indicators are then compared to one another to determine suitability for tracking unstable failure.

It is useful to apply the stability indicators to DSM models of various sizes so that in-situ geometries can be investigated. Therefore, the nine stability indicators are applied to a series of slender pillar compressive strength (SPCS) tests. During these tests, pillars of various sizes are failed by loading systems with different stiffness to encourage stable and unstable failures. Failure stability is determined using a comparison between loading system stiffness and post-peak behavior similar to that used on the EPC tests. The effect of model size on stability indicator performance is observed and the indicators are once again compared for suitability in tracking unstable failure.

Due to the change of model size it is also beneficial to observe the spatial distribution of damage and damage intensity in the pillar. Additional analysis is performed on the SPCS tests to observe the spatial distribution of contact softening and the damping work due to failure. A grid based measurement technique used to track the two indicators is explained and then the correlations between model damage and failure stability are discussed.

4.1 Description and Calculation of Stability Indicators in DEM Compressive Failure

Each of the stability indicators are calculated using PFC2D particle and contact state information. This section provides details on how each indicator is calculated and references custom FISH functions that facilitate the calculations.

4.1.1 Damping Work

The PFC2D model uses a damping mechanism to dissipate kinetic energy, so that a steady state solution may be arrived at within a reasonable number of calculation steps. The damping mechanism applies force to particles undergoing acceleration in the direction opposite that of the particle's motion. Equation 4.1 shows the damping force applied to each particle:

$$\overrightarrow{F}_d = \alpha \left| \overrightarrow{F}_{unbal} \right| \cdot -(sign\ \overrightarrow{v}) \cdot \hat{v} \tag{4.1}$$

where $\overrightarrow{F}_d$ is the damping force, α is an dimensionless coefficient, $\overrightarrow{F}_{unbal}$ is the unbalanced force on the particle, and $\overrightarrow{v}$ is the particle velocity. The coefficient, α, is used to define the level of damping. A value of 0.7 is used in all of the simulations in this thesis. This is the value recommended by the authors of PFC2D for quasi-static conditions.

During failure, the damping mechanism applies larger forces to the model in order to stabilize the failure process. Over a calculation timestep, *dt*, the damping forces perform a quantifiable amount of work that can be summed over the entire model. Damping work is summed over each degree of freedom, i, over all particles, N, from timestep t_i to t_f. The work is summed over the interval of failure. Equation 4.2 is the work done for translational

motion where $d\overrightarrow{x}_i$ is the incremental translational displacement and Equation 4.3 is work done for rotational motion where $\overrightarrow{M}_d$ is the damping moment and $d\overrightarrow{r}$ is the incremental rotation. Translational damping work and rotational damping work are summed to obtain the total damping work. The functions responsible for calculating the total damping work are given Listing C.15. The function called *param_loop_bp* loops through all of the particles in the assembly and *pfc_wd* calculates the damping work on each particle.

$$W_{d_{trans}} = \sum_{t=t_i}^{t_f} \sum_{n_p=1}^{N} \sum_{i=1}^{2} \left(\left| \overrightarrow{F}_{d_i} \right| \cdot |d\overrightarrow{x}_i| \right)_{n_p,t} \tag{4.2}$$

$$W_{d_{rot}} = \sum_{t=t_i}^{t_f} \sum_{n_p=1}^{N} \left(\left| \overrightarrow{M}_d \right| \cdot |d\overrightarrow{r}| \right)_{n_p,t} \tag{4.3}$$

4.1.2 Maximum Instantaneous Kinetic Energy

During the simulation, the kinetic energy of the model is calculated by summing the rotational and translational kinetic energies of all the particles for a single timestep. Equation 4.4 and Equation 4.5 are the equations for rotational and translational kinetic energy respectively, and the total kinetic energy is given by Equation 4.6:

$$KE_{rot} = \frac{1}{2} I\omega^2 \tag{4.4}$$

$$KE_{trans} = \sum_{i=1}^{2} \frac{1}{2} m v_i^2 \tag{4.5}$$

$$KE = KE_{rot} + KE_{trans} \tag{4.6}$$

where, $I = 1/2\, mr^2$, and ω is the rotational velocity. KE is calculated every step as an instantaneous value. The failure stability and intensity of failure should be reflected in the velocity of particles. Therefore, the maximum value of instantaneous kinetic energy during failure is used as a stability indicator because it provides information on the velocity of particles.

4.1.3 Cumulative Kinetic Energy

The cumulative kinetic energy, KE_c, can be determined from the record of instantaneous kinetic energy by summing the instantaneous kinetic energy over the time interval of failure, from timestep t_i to t_f as in the case of damping work, Equation 4.7. The kinetic energy during the entire duration of failure reflects the stability and intensity of the failure in its entirety in terms of particle velocity.

$$KE_c = \sum_{t=t_i}^{t_f} KE_t \tag{4.7}$$

4.1.4 Maximum Instantaneous Mean Unbalanced Force

The instantaneous mean unbalanced force, F_μ, is the average of the absolute values of the out of balance force components for each particle and is calculated using Equation 4.8. The maximum instantaneous mean unbalanced force is the largest value of mean unbalanced force of all the timesteps during the failure interval. The mean unbalanced force provides a measure of the level of instability because unbalanced forces are lowest when the model is near static equilibrium. By taking the mean of all unbalanced forces the effect of outlying values is minimized.

$$F_\mu = \frac{\mathbb{F}}{N} \tag{4.8}$$

$$\mathbb{F} = \sum_{n_p=1}^{N} \sum_{i=1}^{3} \left(|F_{unbal_i}|\right)_{n_p}$$

4.1.5 Cumulative Mean Unbalanced Force

The cumulative mean unbalanced force is calculated in the same way as the cumulative unbalanced force. Equation 4.9 is used to calculate the cumulative mean unbalanced force.

$$F_{\mu_c} = \sum_{t=t_i}^{t_f} F_{\mu_t} \tag{4.9}$$

4.1.6 Maximum Instantaneous Maximum Unbalanced Force

The maximum unbalanced force is the unbalanced force of greatest magnitude during a timestep. This value is determined by a PFC2D intrinsic FISH function instantaneously and during each step. The maximum instantaneous maximum unbalanced force gives a measure of the intensity of failure using the element furthest from static equilibrium.

$$F_{max} = max\left\{\left(|F_{unbal_i}|\right)_{n_p} : i = 1, 2, 3 \;\&\; n_p = 1, \ldots, N_p\right\} \tag{4.10}$$

4.1.7 Cumulative Maximum Unbalanced Force

The cumulative maximum unbalanced force is determined similarly to the cumulative mean unbalanced force. This indicator provides a measure of failure intensity by finding the degree of freedom with the largest amount of applied force each step. The maximum unbalanced force should be larger the more unstable the failure is.

$$F_{max_c} = \sum_{t=t_i}^{t_f} F_{max_t} \tag{4.11}$$

4.1.8 Contact Softening

The DSM is a softening contact model, as explained in detail in the previous chapter. The contact begins to soften once the initial strength of the contact is reached (Figure 3.3). The contact bond is inactive once the softening limit is reached. Before the plastic displacement limit is reached the amount of softening, U_p, can be observed using an intrinsic FISH command to access a contact state variable called the contact softening ratio, U_{rat} . The contact softening ratio is the amount of contact softening divided by the plastic displacement limit, Equation 4.12.

$$U_{rat} = U_p / U_{pmax} \tag{4.12}$$

The value of U_{rat} becomes unity at maximum softening. By summing U_{rat} over all of the contacts in the model, a measure is made of the contact softening due to compressive failure. The sum of softening ratios is calculated incrementally. The functions responsible for calculating the sum of softening ratios are located in Listing C.15, where *param_loop_cp* loops through all of the contacts in the PFC2D assembly and *pfc_sof* retrieves contact state information. The amount of contact softening, the indicator used in the following analysis, is determined by multiplying the softening ratio sum by the plastic displacement limit. This yields a value for contact softening in units of meters. Equation 4.13 is the amount of contact softening, where C is the total number of contacts.

$$U = \left(\sum_{n_c=1}^{C} U_{rat} \right) \cdot U_{pmax} \tag{4.13}$$

4.1.9 Number of Broken Contacts

In a DSM contact, the contact is deemed broken once the plastic displacement limit, U_{pmax}, is achieved. One way of assessing damage in the DEM assembly is by tracking the number of contacts that have broken. The number of broken contacts is determined using the variable sof_numbroke shown in Listing C.15.

4.2 Stability Indicator Results in EPC Tests

Each of the indicators explained above are used here to describe the failure in elastic platen strength (EPC) tests presented in the previous chapter. The trends of indicators are shown by means of scatter plots of the indicator values versus time step. Values of indicators are determined from line plots of the indicator, so each point on the scatter plots represent indicator magnitude for an individual test.

Figure 4.1 shows the instantaneous and cumulative kinetic energy during the EPC test with 5 GPa platens. During the loading phase of the test, the cumulative kinetic energy

increases as a slow rate due to a consistent, low level of kinetic energy in the model. Kinetic energy in the model increases when failure occurs, resulting in a sharp increase in the cumulative value of kinetic energy. After the majority of stress in the sample has been dissipated, the kinetic energy in the model reduces and the rate of change of cumulative kinetic energy decreases. The black vertical lines in Figure 4.1 indicate the failure interval over which comparison is made to other tests. The failure interval is different for each test but the same for each indicator for a specific test. Below, analysis is conducted using scatter plots showing values extracted from the instantaneous and cumulative values of each indicator. The complete set of indicator plots for each EPC test is shown in Appendix D.

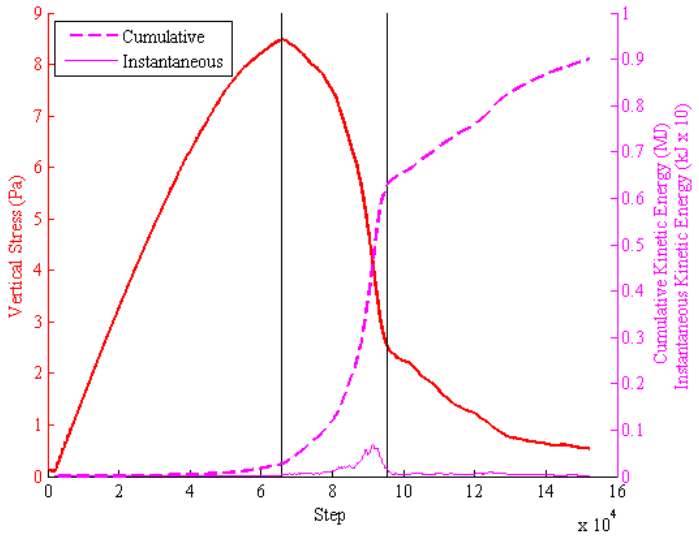

Figure 4.1: Kinetic energy indicator results for EPC test with 5 GPa platens

Figure 4.2 shows the damping work accumulated over the failure interval for each of the eight EPC tests. The damping work is normalized with respect to the drop in stress during the failure interval. As platen elastic modulus decreases from 50 GPa, the damping work remains near 5 kJ/MPa. According to the comparison of measured post-peak stiffness to loading system stiffness in the previous chapter, (Table 3.6) all tests with elastic modulus below 5 GPa are unstable with the 5 GPa test behaving in a quasi-stable manner. Figure 4.2 shows that the damping work increases beyond 5 kJ/MPa with 5 GPa platens and after a

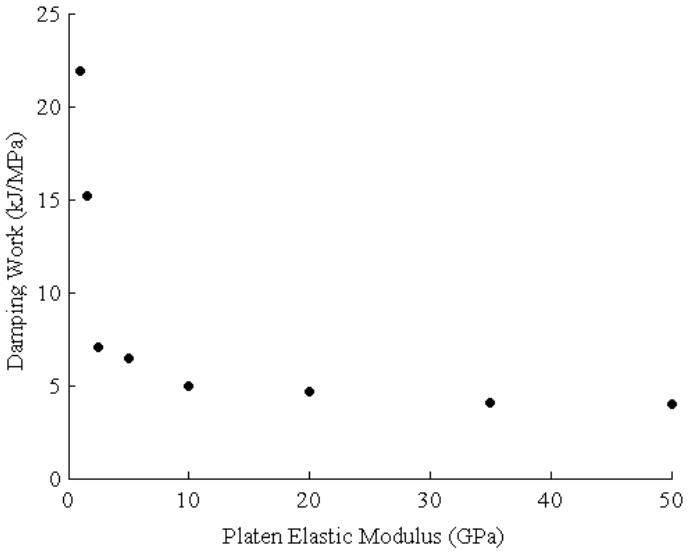

Figure 4.2: Accumulated damping work during the failure interval in EPC tests

small increase with 2.5 GPa platens the damping work begins a sharp increase for the two softest platens.

Figure 4.3 shows the maximum instantaneous kinetic energy during failure on a semi-log plot. While the trend seen in damping work of increasing indicator with decreasing stability of failure is present, the kinetic energy shows an even more drastic increase for the most unstable cases. The three highest platen moduli exhibit consistent maximum instantaneous kinetic energy, suggesting that this indicator may be particularly useful in identifying stable failure.

The maximum instantaneous mean unbalanced force is shown in Figure 4.4 on a semi-log plot. The results for this indicator are similar to the maximum instantaneous kinetic energy in that the most unstable failure has a significantly higher value than the next softest test, and the values for the most stable tests are very consistent. The maximum instantaneous maximum unbalanced force is shown in Figure 4.5. The trend in maximum instantaneous maximum unbalanced force is similar to kinetic energy and mean unbalanced force although there exists some irregularity in the value for the stable failures.

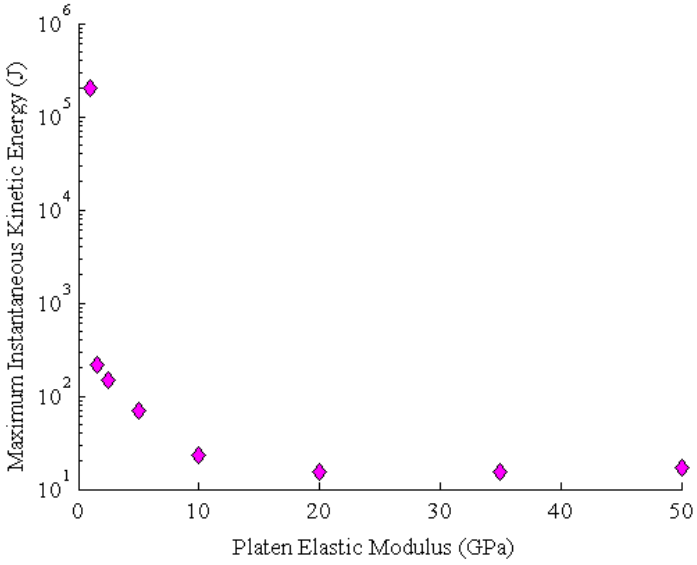

Figure 4.3: Maximum instantaneous kinetic energy in EPC tests

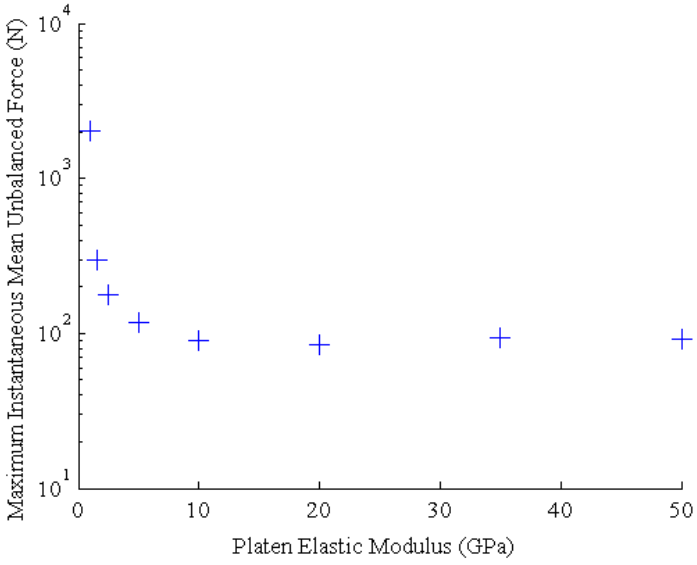

Figure 4.4: Maximum instantaneous mean unbalanced force in EPC tests

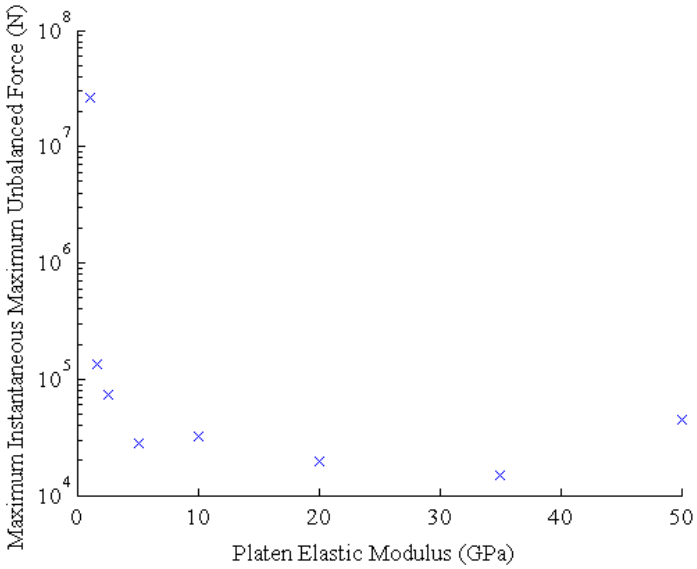

Figure 4.5: Maximum instantaneous maximum unbalanced force in EPC tests

Like damping work, cumulative values for kinetic energy, mean unbalanced force, and maximum unbalanced force were normalized with respect to the stress drop during failure. Figure 4.6 shows the cumulative kinetic energy. The cumulative kinetic energy is consistent for stable failures and increases as failure stability decreases.

In Figure 4.7, the cumulative mean unbalanced force generally shows the expected trends for stable versus unstable failure. Although, outlying results for the unstable failures using 2.5 and 5 GPa platens indicate that variability in mean unbalanced force in unstable failures can occur and caution should be exercised when using this indicator.

Figure 4.8 shows the cumulative maximum unbalanced force. The cumulative maximum unbalanced force is fairly consistent for all tests with the exception of the most unstable failure. Therefore, it does not reliably distinguish between stable and unstable failures.

Contact softening during the failure interval for each EPC test is shown in Figure 4.9. The amount of softening is normalized with respect to the stress drop during the failure interval for each test respectively. The amount of contact softening remains consistent for the most stable failures. For unstable failures the amount of contact softening exhibits no particular trend as the two most unstable failure result in the most extreme cases of softening.

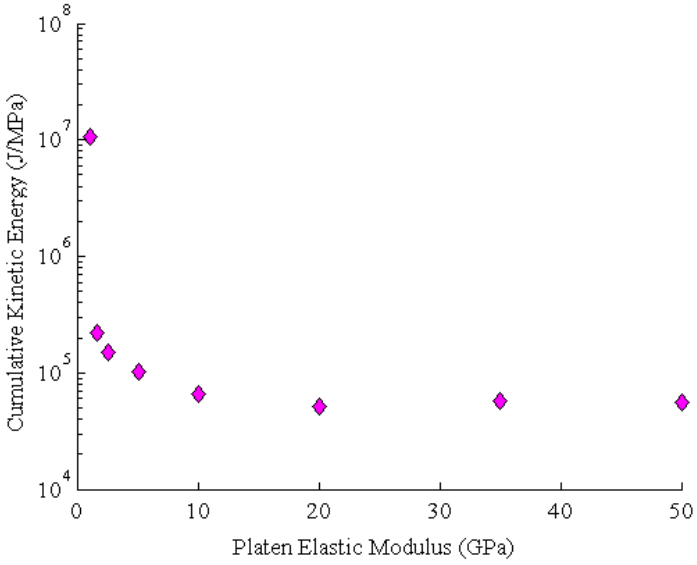

Figure 4.6: Cumulative kinetic energy during failure in EPC tests

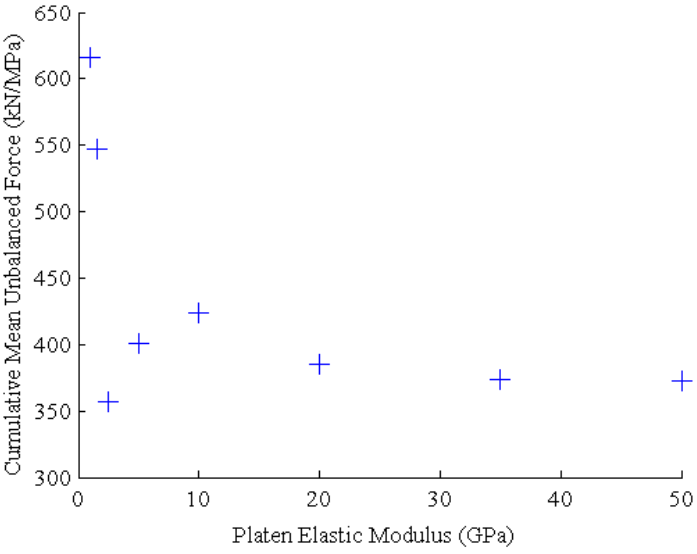

Figure 4.7: Cumulative mean unbalanced force in EPC tests

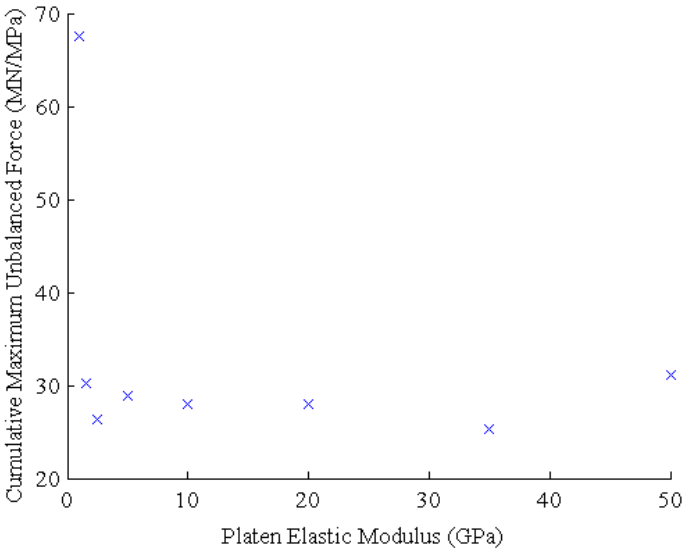

Figure 4.8: Cumulative maximum unbalanced force in EPC tests

The number of broken contacts for each tests is shown in Figure 4.10. The number of broken contacts is also normalized against the stress drop in each test. The number of broken contacts also suggests that stable failures have lower, consistent values while the as the failure becomes more unstable the value increases. Although, the number of broken contacts increases slightly as the elastic modulus increases.

4.2.1 EPC Indicator Results Discussion

With the exception of contact softening, each of the indicators utilized for the analysis of failure stability in EPC tests exhibit similar trends for the EPC tests. Each of the indicators shows high values for unstable failures and decrease as stability of failure increases. Although, the number of broken contacts exhibits an increase with increasing platen elastic modulus. The damping work, maximum instantaneous mean unbalanced force, maximum instantaneous kinetic energy and cumulative kinetic energy appear to be suitable indicators for tracking unstable failures. For each of these indicators, consistent values are measured for stable failures and as failure stability decreased, the indicator likewise increased to provide a qualitative measure of failure stability.

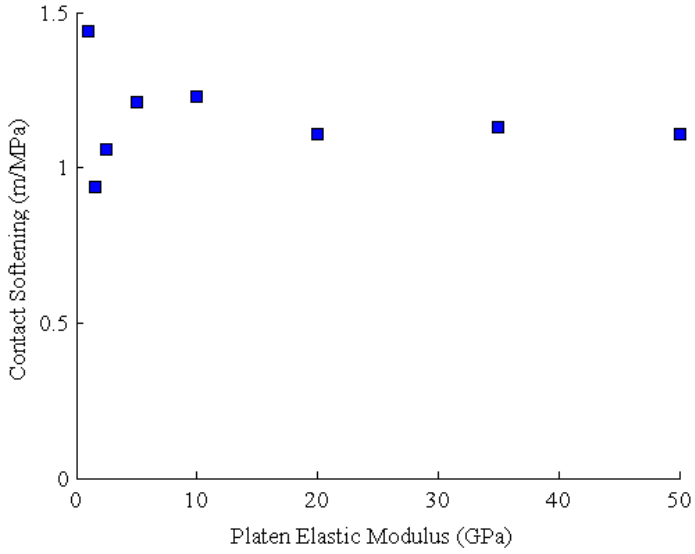

Figure 4.9: Contact softening in EPC tests

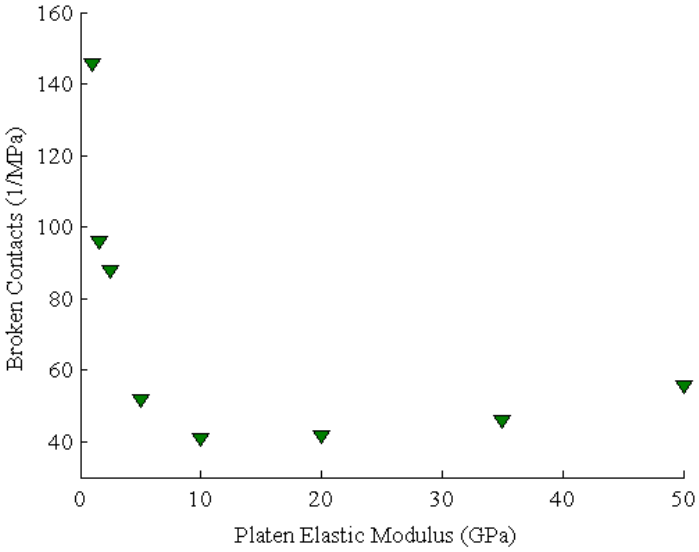

Figure 4.10: Number of broken contacts in EPC tests

Trends in cumulative values for kinetic energy, mean unbalanced force and maximum unbalanced force are helpful in describing failures in that the cumulative value contains information for the duration of the failure rather than a single calculation step. Each of these cumulative values performed with various levels of success in distinguishing between stable and unstable failures. The cumulative kinetic energy performs well in distinguishing between stable and unstable failure while the cumulative maximum unbalanced force looses the expression of instability for all unstable failures except for the 1 GPa test. The mean unbalanced force should be used with caution as there is some variability in the values of unstable failures. Although, additional work into methods of normalization may reveal the expected trend.

Contact softening does not increase with decreasing failure stability but the variability in the value increases. Additional analysis could possibly reveal a trend similar to the other indicators, but is not pursued further in this study. Rather, since contact softening is a result of failure in contact bonds, it can be used to identify the locations and extent of damage in the model. This application will be applied in the following pillar tests.

4.3 Slender Pillar Compressive Strength (SPCS) Test Description

In underground mining, both the material properties and the dimensions of the mine affect the loading system stiffness and consequently the failure mode. In this section, a series of slender coal pillars are failed under an elastic loading system. The stiffness of the loading system is varied by changing the modulus of elasticity of the loading system and also the size of the pillar. A total of nine tests are conducted, failing three pillar sizes under three separate loading systems of various elastic moduli. The pillar height is kept constant and the width is changed to produce three different sized pillars. The pillars are described by the ratio of pillar width to pillar height. Pillars are constructed of width to height ratios one, two, and three. Each pillar size is failed with a 5 GPa, 20 GPa, and 35 GPa loading system. Failure stability is determined by comparing the loading system stiffness to the pillar post-peak stiffness. Then, the performance of the nine stability indicators is assessed

for stable and unstable pillar failures.

4.3.1 SPCS Geometry and Boundary Conditions

Figure 4.11 shows a schematic depicting the geometry and boundary conditions of the slender pillar tests. The FLAC2D grid is comprised of a fine inner grid and a coarse outer grid in order to capture the forces and stresses at the resolution of the PFC2D model and to save memory. The grid input file for the width to height ratio one pillar is shown in Listing C.16. The grid is expanded for the larger pillar tests in the horizontal direction by adding a proportional amount of elements. The same FISH functions are used to facilitate coupling as with the EPC tests, only the coupling boundary segment list as seen in cpf_EPC.fis must be changed.

The model has a symmetric boundary condition along the vertical edges, simulating an infinite series of identical pillars. The width of the excavation is kept constant for each pillar size, and the width of the model is changed in accordance only to the pillar width. The model is first equilibrated with the entire FLAC2D nulled region filled with PFC2D elements. Then the entries are 'excavated' by deleting the elements within three meters of the left and right boundaries of the model. After a subsequent equilibration stage, the coal pillar, modeled in PFC2D, is loaded under an increasing compressive load by a constant velocity boundary condition applied to the upper and lower most boundaries of the model.

4.3.2 Local Mine Stiffness Calculation

Each pillar failure is determined to be stable or unstable based on a comparison of the local mine stiffness during failure and the post-peak pillar stiffness. Following from the laboratory tests above, if the pillar post-peak stiffness is equal to the unloading local mine stiffness then the failure is considered unstable. The stiffness of the loading system is measured using only the tributary area above and below the pillar width. From these calculations, a local mine stiffness measurement is made for each test by assessing average pillar vertical reaction force on the surrounding mine and average pillar-mine boundary

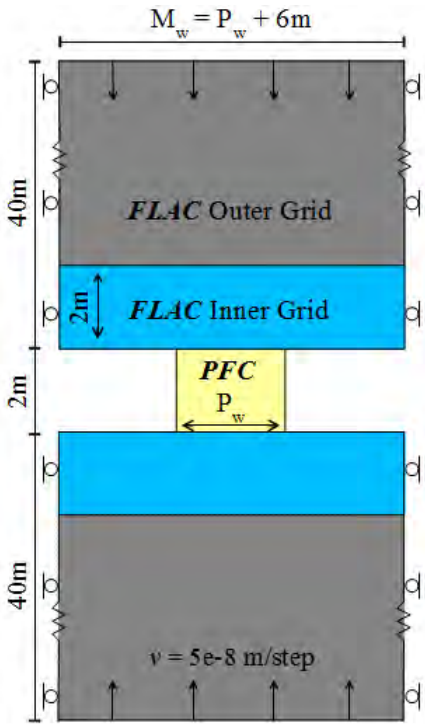

Figure 4.11: Slender pillar test geometry and boundary conditions

vertical displacement. The stiffness of the roof and floor can be determined individually using the the equation for force on a spring, Equation 4.14.

$$k = \Delta F_P / \Delta D \tag{4.14}$$

ΔF_P is the change in force exerted on the roof or floor by the pillar and ΔD is the change in displacement in the roof and floor respectively. ΔD is defined as the compression of the tributary area averaged along the width of the pillar. The pillar reaction force is calculated using average pillar stress and the cross sectional area of the pillar (P_W x 1m).

Figure 4.12 is a conceptual illustration of typical pillar behavior trends versus calculation step. The average pillar stress and the average loading system displacement exhibit similar trends, therefore they are both illustrated as the narrow width line. The bold line represents average pillar strain. The step interval, dT, denotes the time of failure and is defined as beginning at the onset of pillar softening through the occurrence of residual stress. The local stiffness is calculated using ΔF_P and ΔD during the interval dT. Then, by considering the

roof and floor as a series of springs, the local mine stiffness, LMS, is calculated by using the equation for stiffness of springs in series, Equation 4.15.

$$LMS = \frac{k_r k_f}{k_r + k_f} \tag{4.15}$$

where k_r and k_f are the roof and floor stiffness respectively. The pillar post-peak stiffness is calculated using Equation 4.16

$$K_{pp} = \frac{E_{pp} A}{L} = \frac{\Delta\sigma A}{\Delta\varepsilon L} \tag{4.16}$$

where E_{pp} is the post-peak modulus, A is the cross sectional area of the pillar, and L is the height of the pillar. E_{pp} is determined according to the definition of Young's modulus for $\Delta\sigma$ and $\Delta\varepsilon$ during the softening interval dT.

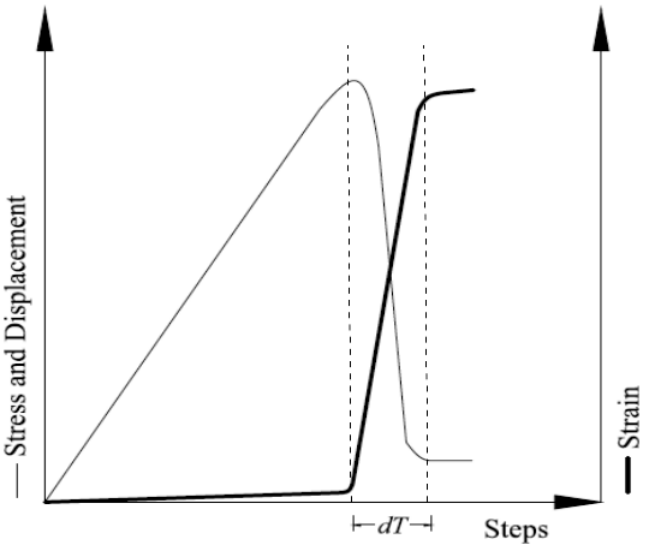

Figure 4.12: Illustration of typical pillar simulation behaviors

4.3.3 Grid Based Instability Indicator Measurements

The DEM exhibits micro-mechanical behavior that can be observed on a localized basis. Typically, in DEM models it is useful to visualize damage in the model by displaying contacts. The absence of contacts indicates the locations of cracks in the material. In the DSM model, because damage accumulates in the contacts before they are deleted an additional technique

for observing damage is necessary. Also, observing damping work on a localized basis could indicate whether the damage is due to a stable or unstable failure and give a measure of the intensity of failure. A grid based measurement technique is implemented to observe the behavior of the contact softening and damping work on a local level.

To track contact softening and damping work spatially in the model, a fictitious grid that is comprised of square pixels is superimposed onto the PFC2D assembly. The square pixels are 0.1 m on a side and grid resolution is kept constant in each model as model size changes. Each particle and contact is permanently assigned to a pixel at the beginning of the simulation, thereby ignoring effects of pixel-to-pixel movement. Irregular values at the model's boundaries, due to empty space in the pixels, have been found to be irrelevant to model behavior and can also been ignored.

Listing C.15 shows the FISH code used to execute the grid based measurement technique. The functions included in this algorithm compute both grid based values and totals for damping work and contact softening. Figure 4.13 is a flow chart depicting the process of calculation. The algorithm can be described as having two parts, the initialization and the calculation cycle. The initialization defines the necessary functions, grid, and memory arrays for data processing and histories. The grid based calculation is executed at the beginning of every PFC2D calculation step. During the grid based calculation, the function loops through each particle and then each contact in the DEM in order to calculate values of desired parameters. Then the data array is updated and the data histories are recorded. Although values of the indicators are accumulating every step, histories are only recorded once every 5000 calculation steps in order to reduce memory usage.

4.4 SPCS Test Results

The results of SPCS test results are presented in the following section using line plots to show the stress versus strain behavior of each pillar and the loading system displacement during each test. Stability indicator results are presented and then analyzed in the context of whether failure of the pillar is stable or unstable. Then the grid based indicator measurements

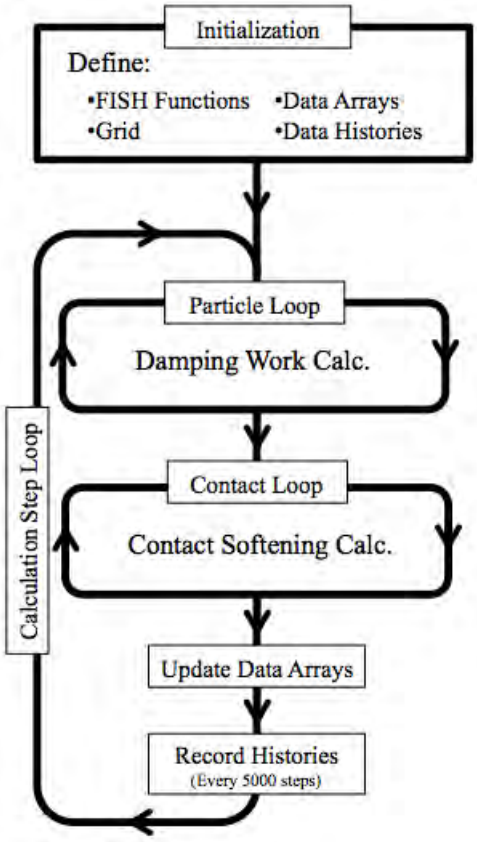

Figure 4.13: Grid based measurement algorithm flow chart

are presented and discussed.

4.4.1 Pillar Stress-Strain Behavior and Loading System Displacement

The stress-strain results from the nine pillar tests are organized into three plots. Each plot contains three tests, showing stress-strain behavior of one width to height ratio tested with 5, 20 and 35 GPa elastic modulus loading systems. Figure 4.14 shows stress-strain behavior for the width to height ratio one pillar, Figure 4.15 shows stress-strain behavior for the width to height ratio two pillar, and Figure 4.16 shows stress-strain behavior for the width to height ratio three pillar.

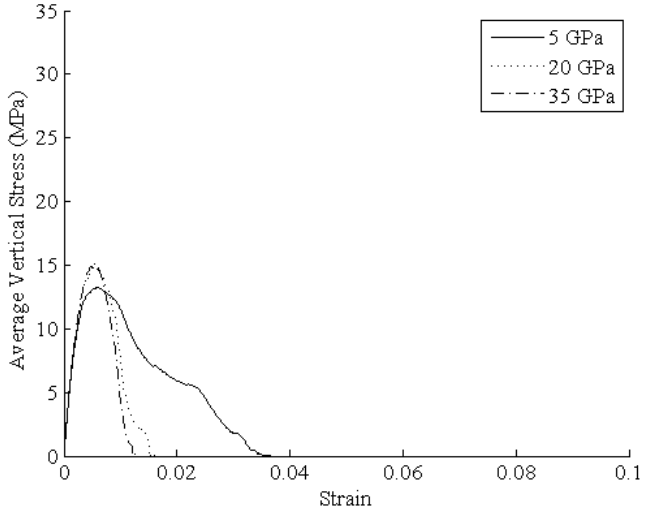

Figure 4.14: Stress-strain curves for width to height ratio one pillar tests

Each curve shows how pillar stress increases during the loading phase of the tests and then as the pillar fails, stress is dissipated. Pillar strength is dependent upon the pillar size and the loading system stiffness. As pillar size increases the strength of the pillar increases, and as loading system stiffness decreases the pillar strength decreases. In the post-peak region, the post-peak modulus is dependent upon both the pillar size and loading system stiffness. As pillar size increases, the post-peak modulus decreases and as loading system stiffness increases the post-peak modulus increases. A significant change in post-peak behavior is

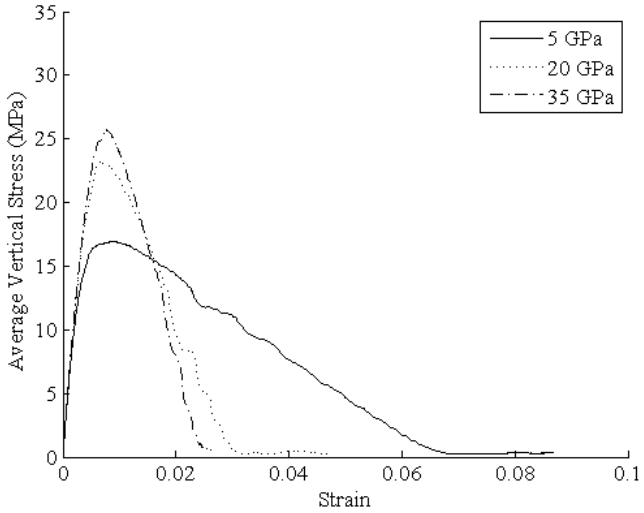

Figure 4.15: Stress-strain curves for width to height ratio two pillar tests

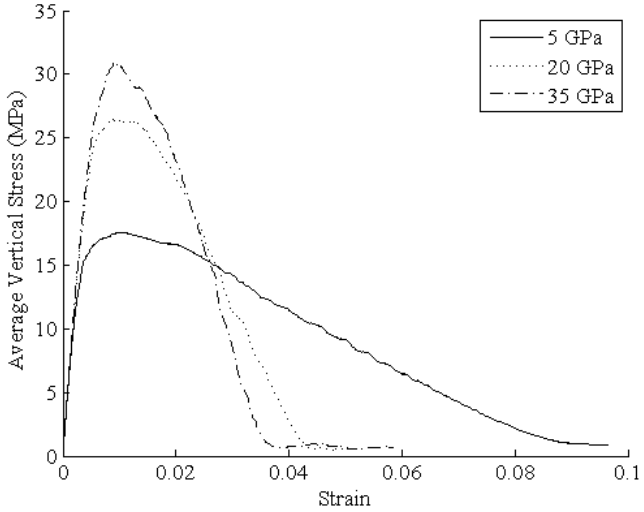

Figure 4.16: Stress-strain curves for width to height ratio three pillar tests

apparent in each of the 5 GPa tests where the change in post-peak modulus is more gradual from 35 GPa to 20 GPa loading system elastic modulus.

The elastic displacement of the loading system in each of the nine tests are shown in plots organized in the same way as the stress-strain plots. Figure 4.17 shows average loading system displacement for the width to height ratio one pillar tests, Figure 4.18 shows average loading system displacement for the width to height ratio two pillar tests, and Figure 4.19 shows average loading system displacement for the width to height ratio three pillar tests. Loading system displacement increases during the loading phase of the tests and then decreases as the pillar fails. Displacement at the point of failure is higher when elastic modulus of the loading system is low and increases as the pillar size increases. In the post peak region, the 5 GPa tests show a fast decrease in loading system displacement, while tests with 20 and 35 GPa loading system exhibit a more gradual decrease in loading system displacement.

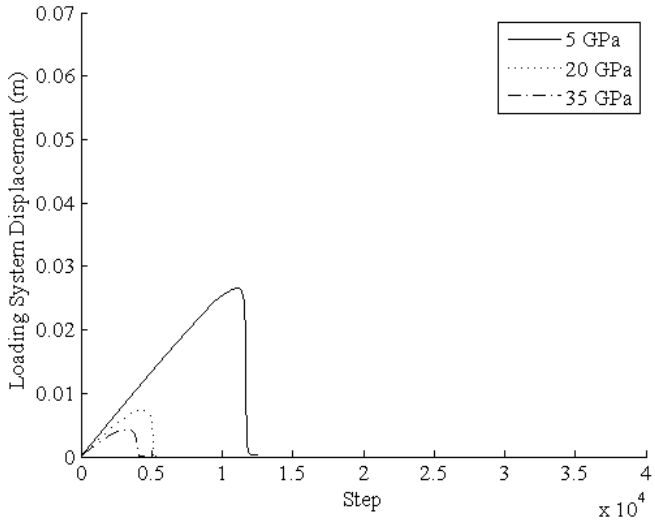

Figure 4.17: Loading system displacements for width to height ratio one pillar tests

Using data from the stress-strain and displacement plots, stability of the pillar failure can be assessed. Similar to the EPC tests, sudden rebound of the loading system indicates unstable failure. A sudden rebound of the loading system can be detected by comparing the measured post-peak stiffness of the pillar to the loading system stiffness during failure. If

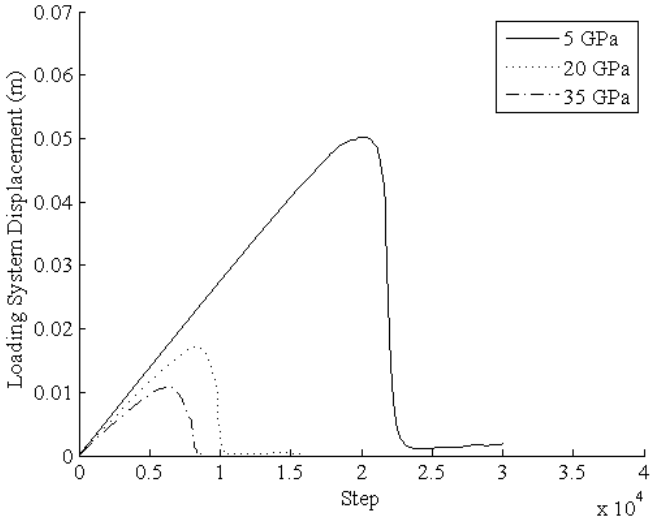

Figure 4.18: Loading system displacements for width to height ratio two pillar tests

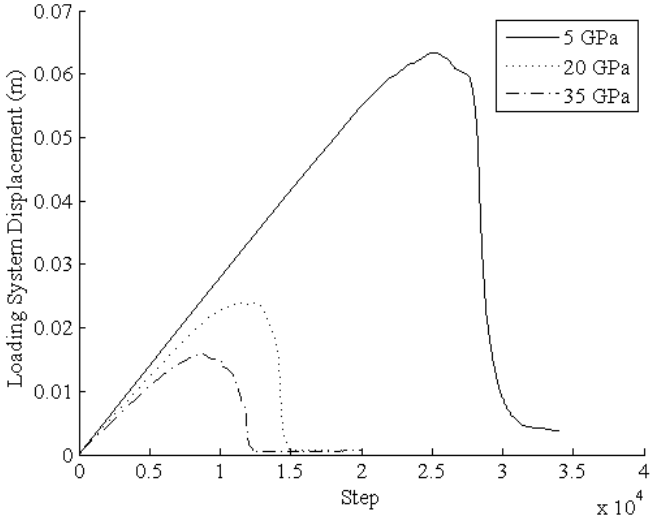

Figure 4.19: Loading system displacements for width to height ratio three pillar tests

these two values are similar, unstable failure is assumed to have occurred.

Figure 4.20 shows measurements of loading system stiffness and pillar post-peak stiffness during the failure interval for each test. The data are color coded according to loading system elastic modulus. Calculated loading system stiffness is represented by exes and pillar post-peak stiffness is represented by triangles. Generally, as loading system elastic modulus increases the pillar post-peak stiffness and loading system stiffness increases. Stability of the failure is determined by comparing the loading stiffness and post-peak stiffness for each test. The 20 GPa and 35 GPa tests show consistent difference between pillar behavior and loading system stiffness measurements indicating stable pillar failure for all six tests. The 5 GPa tests show coincident values, indicating unstable failure for all three pillar sizes. Based on these results, further analysis of indicators will assume stable failure for the 20 and 35 GPa tests and unstable failure for the 5 GPa tests.

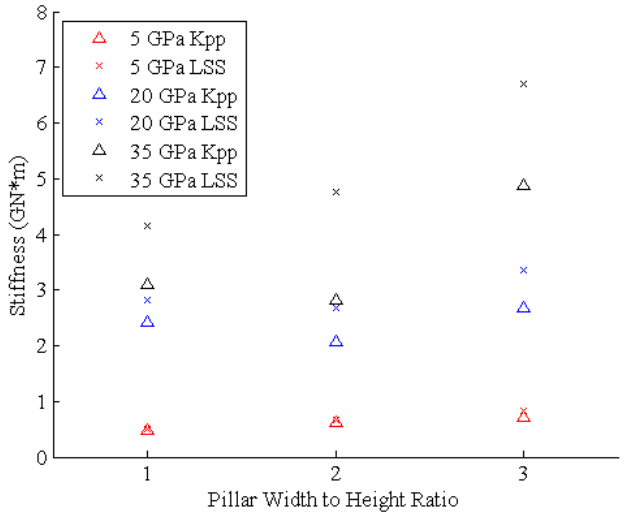

Figure 4.20: Pillar post-peak stiffness and loading system stiffness measurements

4.4.2 SPCS Test Indicator Results

Results are presented here for each of the nine indicators during the nine SPCS tests. Figure 4.21 shows cumulative and instantaneous mean unbalanced force versus calculation

step for the width to height ratio two pillar with 20 GPa loading system. The average vertical stress versus calculation step plot is added for reference to failure. The black vertical lines indicate the bounds of the interval of failure. The cumulative counterpart to the instantaneous kinetic energy, mean unbalanced force and maximum unbalanced force are given in the same plots. Six plots for each SPCS test are presented n this format in Appendix E. An analysis is conducted below by comparing the maximum instantaneous values or the change in cumulative value for each instantaneous or cumulative indicator respectively.

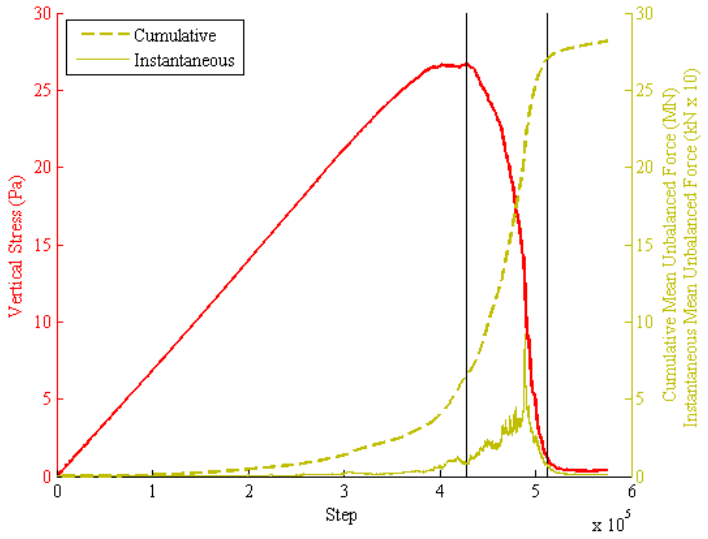

Figure 4.21: Mean unbalanced force, width to height ratio two pillar 20 GPa loading system

Figure 4.22 through Figure 4.30 show the results for stability indicator analysis. Each plot contains results for one indicator for each of the nine pillar tests. The 5 GPa test results are given a grey colored marker and the 20 and 35 GPa tests are given as black markers. This is done to show that the 5 GPa tests resulted in unstable failures while the 20 and 35 GPa tests resulted in stable failures. The cumulative values are each normalized by the stress drop during failure and the cross sectional area of each pillar, where a pillar width to height ratio of one equals 4 meters squared, pillar width to height ratio of two equals 8 meters squared, and pillar width to height ratio of three equals 12 meters squared.

Figure 4.22 shows damping work for the pillar strength tests. When unstable failure occurs the damping work is markedly increased, while for both the stable failures of each width to height ratio, the damping work is similar. Despite the normalization with respect to both stress drop and pillar size, the damping work is higher for larger pillars. As with the EPC tests, a larger amount of damping work suggests that the failures are more unstable or in other words, more violent.

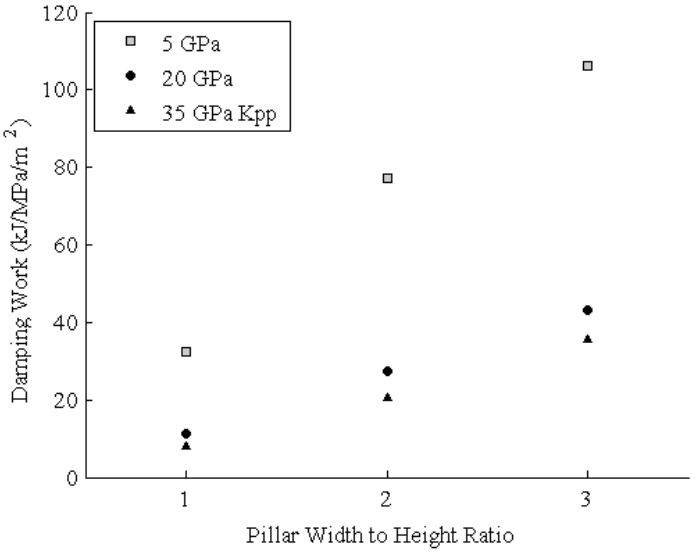

Figure 4.22: Damping work in pillar strength tests

Figure 4.23 shows the maximum instantaneous kinetic energy model during failure. Figure 4.24 and Figure 4.25 show the maximum instantaneous mean and maximum unbalanced forces in the pillar strength tests, respectively. For each of these indicators the unstable failures generally have higher values. Although the difference between stable and unstable cases is not as pronounced as with the damping work. The maximum instantaneous maximum unbalanced force for the 20 GPa width to height ratio two tests is an outlier in this trend. The maximum mean unbalanced force decreases for larger pillars. This likely is the result of averaging over a larger number of particles. Each of these indicators only contains model information for one calculation step, and therefore should be used with caution and in conjunction with other indicators.

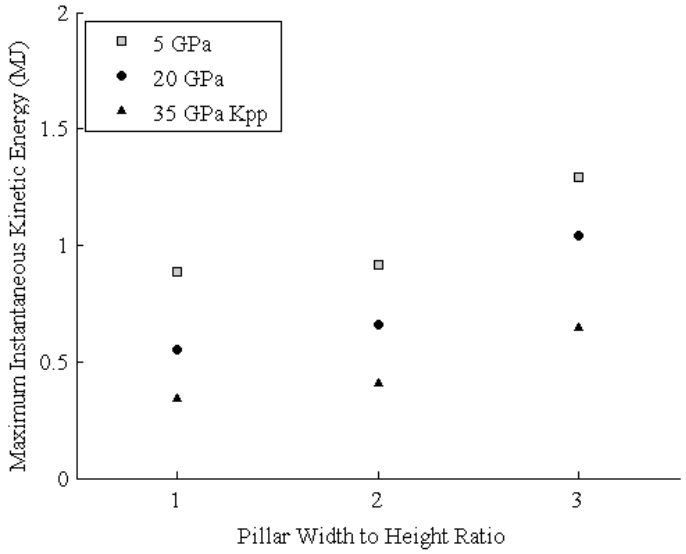

Figure 4.23: Maximum instantaneous kinetic energy in SPCS tests

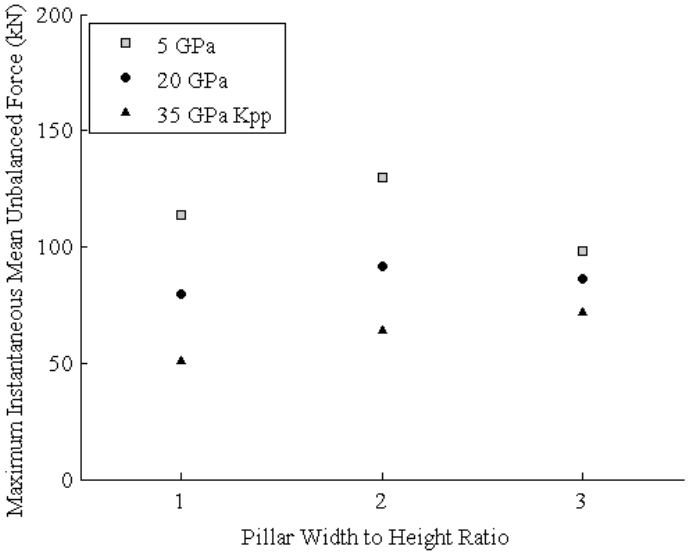

Figure 4.24: Maximum instantaneous mean unbalanced force in SPCS tests

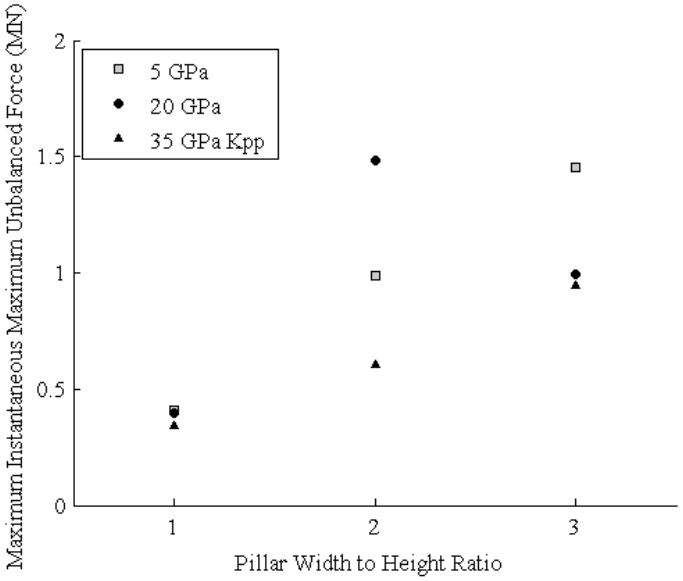

Figure 4.25: Maximum instantaneous maximum unbalanced force in SPCS tests

Cumulative values for kinetic energy, mean unbalanced force and maximum unbalanced force are presented in Figure 4.26 through Figure 4.28. Cumulative values may express the failure stability of the model better because information is contained from the entire duration of failure. The cumulative kinetic energy describes the total amount of energy translated into motion that was initially stored in the specimen and loading system as strain energy. Figure 4.26 shows that the kinetic energy increases drastically for unstable failures while values for stable failures are grouped at a noticeably lower magnitude. The cumulative mean unbalanced force in Figure 4.27 shows a similar behavior only the stable values are grouped more closely. However, as model size increases the number of elements over which the unbalanced force is averaged increases. Since unbalanced force is higher in the areas of damage many elements have low unbalanced force, therefore the mean unbalanced force decreases as model size increases. The values for stable failures also decrease slightly as the model size increases. The cumulative maximum unbalanced force in Figure 4.28 exhibits similar behavior, but values for stable cases increase for larger pillars. This trend suggests that for larger assemblies the maximum unbalanced force may not be able to clearly distinguish stable and unstable failure, but additional testing of larger pillars would need to be performed to verify

this.

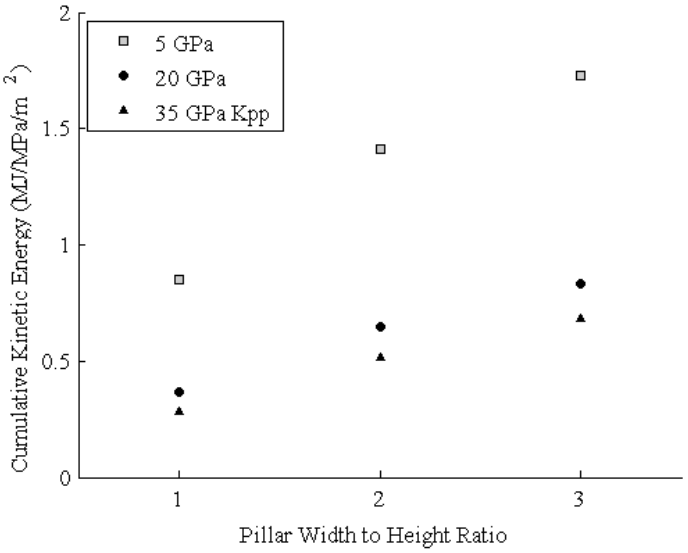

Figure 4.26: Cumulative kinetic energy in SPCS tests

Contact softening is shown in Figure 4.29. The cumulative amount of contact softening describes the plastic displacement of the model on the contact level. Contact softening distinguishes between stable and unstable failures in that stable failures for similar geometries exhibit similar amounts of contact softening while the unstable failures display a larger amount of contact softening. Although, as pillar size increases for unstable failures the amount of contact softening ceases to increase. Once again, additional tests on larger pillars may reveal additional features to the trend.

The number of broken contacts normalized with respect to stress drop and pillar size is shown in Figure 4.30. The number of broken contacts is the number of contacts that have reached the softening limit. Broken contacts are typically thought of as cracks in DEM models, but due to the softening component this definition is debatable. Regardless of the definition of crack location, the location of a broken contact identifies a location of significant damage in the model. The normalized number of broken contacts is consistently higher for unstable failures and there exists a large gap between closely grouped stable failures and the unstable failures. As with mean unbalanced force and softening indicators, the number of

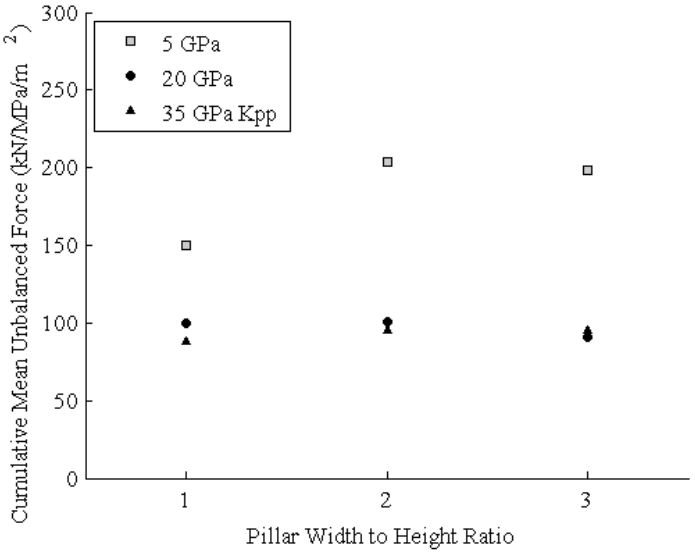

Figure 4.27: Cumulative mean unbalanced force in SPCS tests

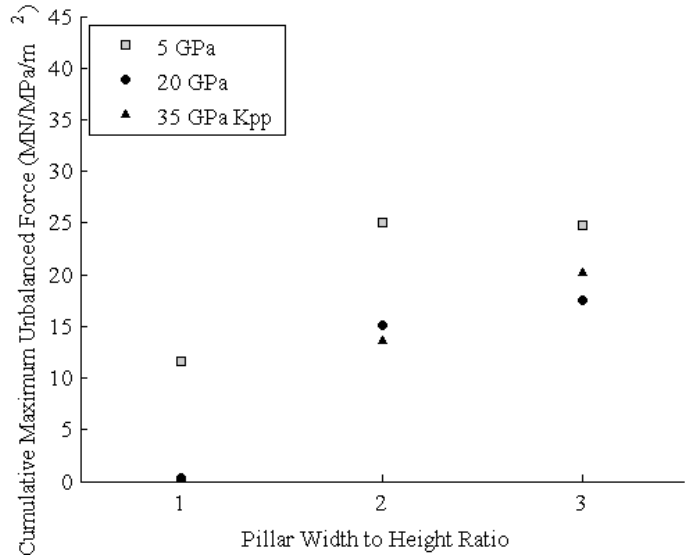

Figure 4.28: Cumulative maximum unbalanced force in SPCS tests

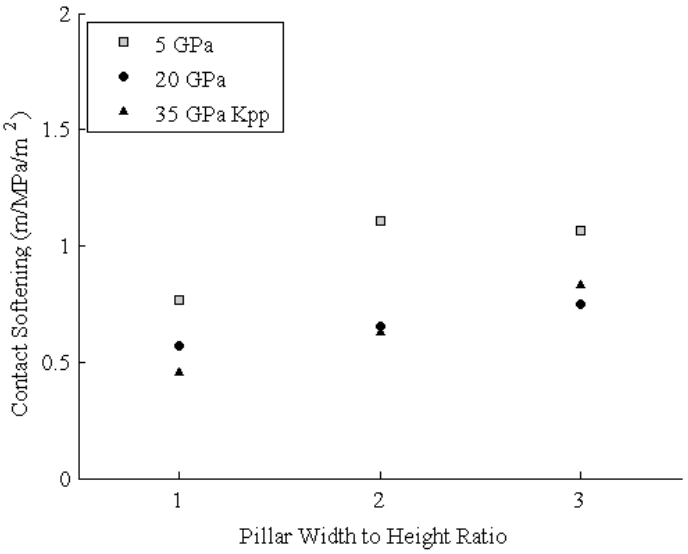

Figure 4.29: Contact softening in pillar strength tests

broken contacts levels off as pillar size increases for unstable failures.

4.4.3 Grid Based Instability Indicator Results

The damping work and contact softening were measured using the grid based measurement technique shown in Figure 4.13. Figure 4.31 through Figure 4.34 show contact softening and damping work for each of the pillar strength tests. Each image is produced from the data at the last step of the failure interval used for the previous indicator analysis. A shaded bar is provided with each image to indicate the range of values present. The image value range is determined by setting the maximum value to the maximum value detected in the grid. This way a comparison between tests can be made using both the local maximum magnitude of the indicator and the pattern of the indicator.

Figure 4.31, Figure 4.32, and Figure 4.33 each show that the maximum value of contact softening increases as the elastic modulus of the loading system decreases. Also, maximum contact softening increases as pillar size increases. A maximum of 1.4 meters in the unstable width to height ratio three pillar is measured. While cumulative values of contact softening show a distinguishing difference in magnitude between stable and unstable failures, the local

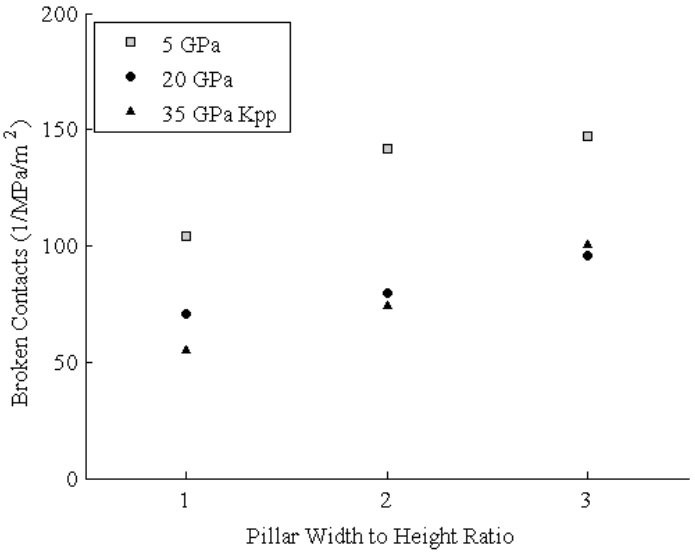

Figure 4.30: Broken contacts in pillar strength tests

measurements do not express the same trend. Rather, local maximum contact softening is higher in unstable failures than stable failures but not by a large enough degree to use with confidence to distinguish stable and unstable failures.

The contact softening in each tests shows that damage in the model occurs in planes that resemble shear planes. Both stable failures and unstable failures damage similarly in so far as planes of damage form in similar locations for similarly sized pillars. Although, concentrations of contact softening are noticeable in the damaged areas of the unstable failures. This can better be seen by comparing the 35 GPa tests, which are the most stable, to the 5 GPa tests, which is an unstable failure. Localization of failure along a plane would contribute to higher values for individual grid pixels and could explain the trend of higher local contact softening for unstable failures.

The maximum local damping work follows the trend previously demonstrated by cumulative damping work in Figure 4.22. The maximum local damping work for the unstable failures is noticeably higher compared to the stable failures. As the loading system elastic modulus increases and the failures become more stable, the damping work decreases further. Also, for stable failures the damping work is more distributed throughout the model. The

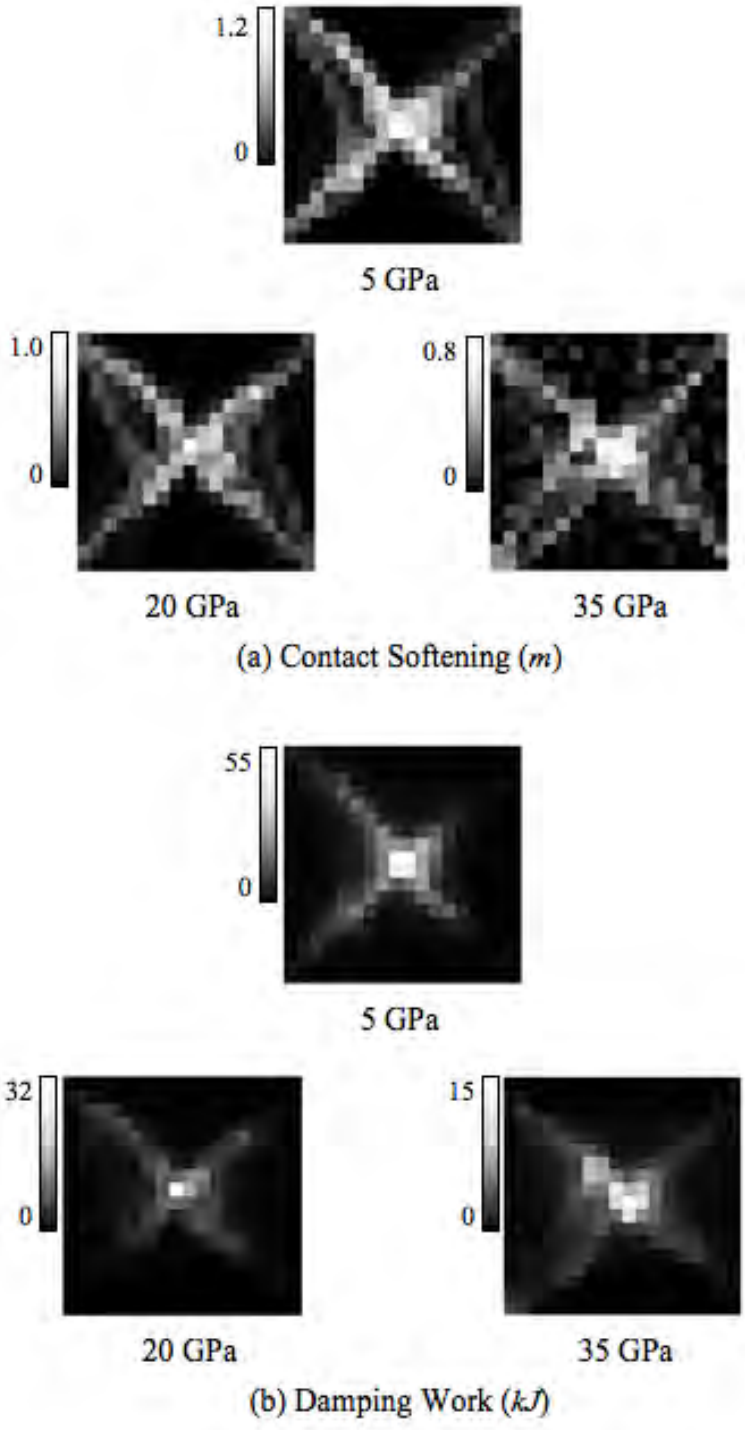

Figure 4.31: Grid based measurements for width to height ratio one pillars

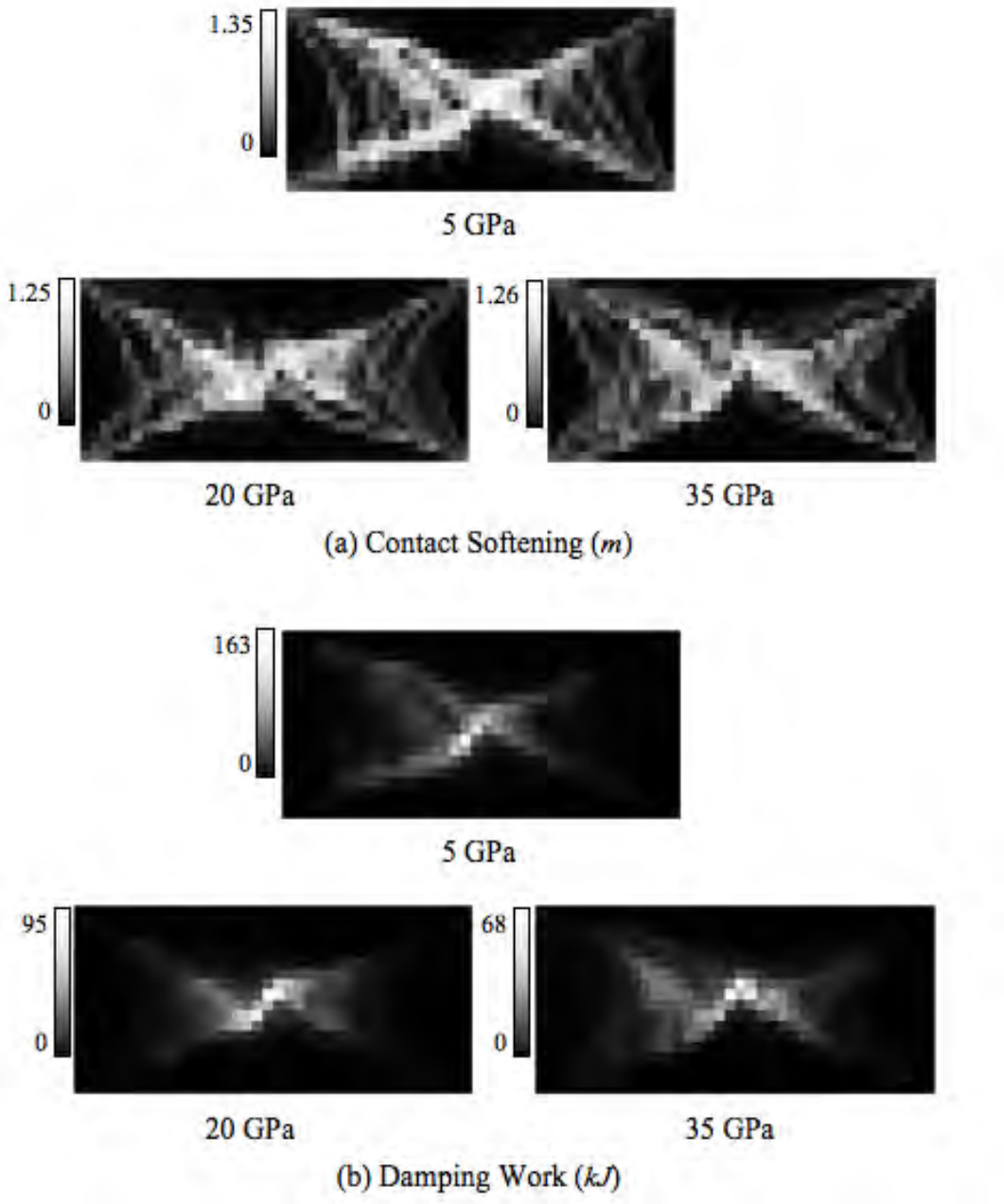

Figure 4.32: Grid based measurements for width to height ratio two pillars

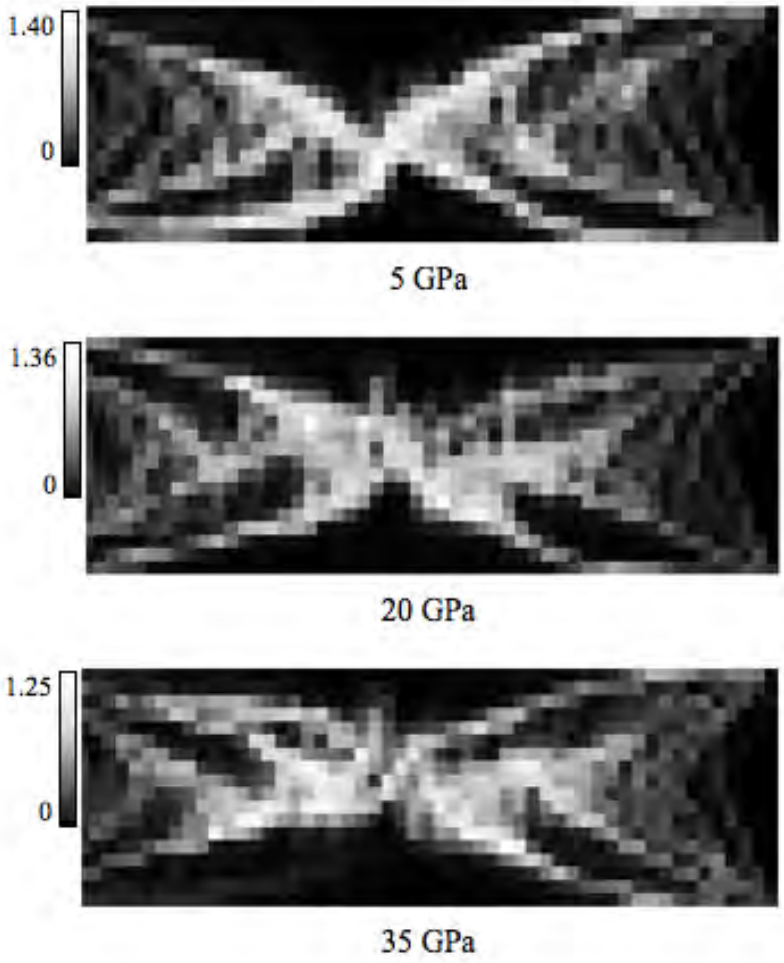

Figure 4.33: Grid based contact softening measurements for width to height ratio three pillars (m)

difference in localization of damping work can be seen more clearly by changing the range on the 5 GPa image to equal that of the 35 GPa image (Figure 4.35). The damping work pattern in the unstable failure suggests localization of damage along planes of failure. Similar to the local contact softening, damage localization can explain higher values of local damping work and could be used as a supporting indication of unstable failure.

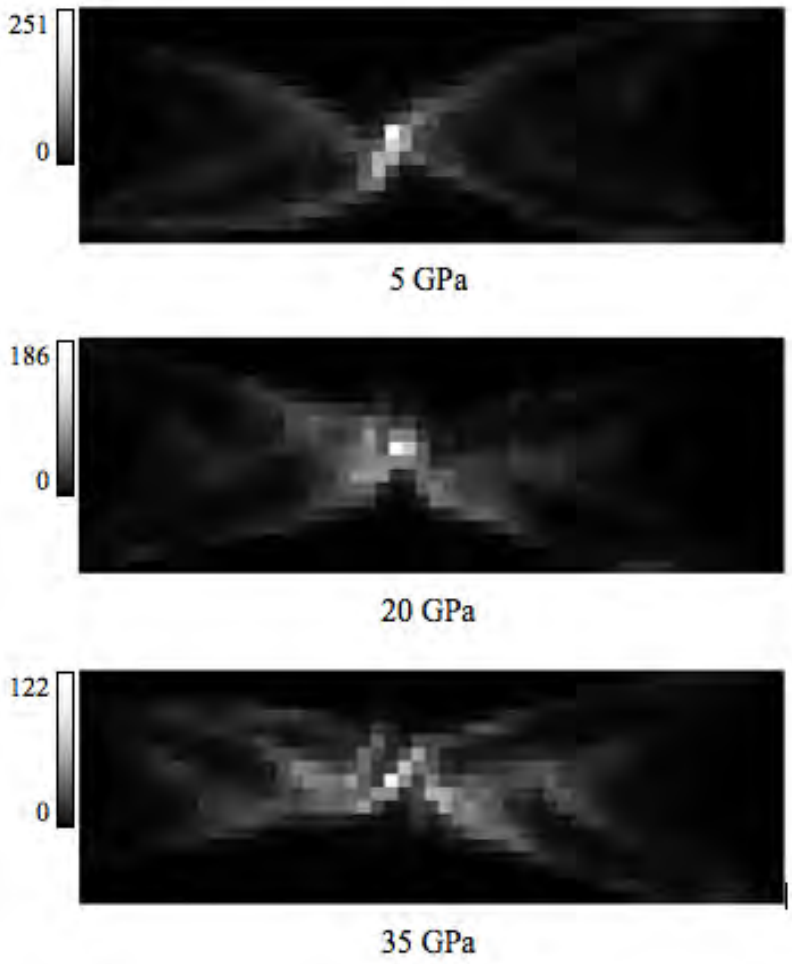

Figure 4.34: Grid based damping work measurements for width to height ratio three pillars (kJ)

4.5 Discussion and Conclusions

Each of the indicators presented in this chapter is able to distinguish stable and unstable failures, but to varying degrees of success. In general, a stability indicator exhibits similar

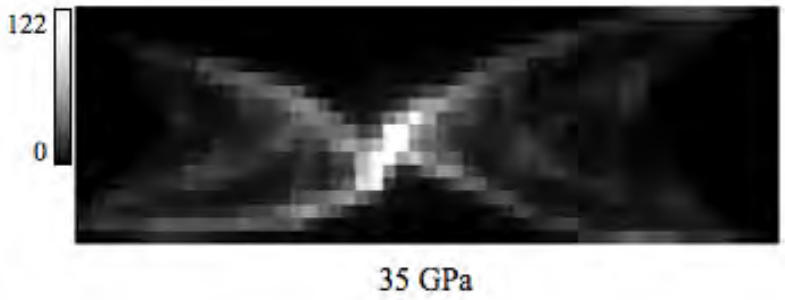

Figure 4.35: Damping work during unstable failure of width to height ratio three pillar with decreased value range (kJ)

values for stable failures and then increases with the degree of instability. The ideal indicator can perform both functions, to identify instability and to quantify the degree of instability. According to the results in this chapter, cumulative values more completely describe the failure and are more reliable than the maximum instantaneous values because of less variability in trends. The cumulative damping work and cumulative kinetic energy are superior indicators because they identify unstable failure when compared to stable failures and give a qualitative measure of the intensity of failure.

Other indicators are affected by the size of the model such as cumulative mean unbalanced force and contact softening. These indicators might be useful in conjunction with damping work and kinetic energy to confirm instabilities. The performance of contact softening as a viable stability indicator in the pillar tests was a surprising result given the highly variable nature of contact softening in the EPC tests. Continued caution should be exercised when using this indicator for anything but a damage indicator.

Grid based measurements showed that damping work and contact softening can not just provide a picture of damage in the model but also support identification of instability by cumulative indicators. The magnitude of local damping work, as tracked using the grid based technique, can indicate instability when compared to stable failure. The localization of damage, as shown with contact softening and damping work, further supports the determination of failure stability. During unstable failure, damage appears to localize along a

failure plain more so than during stable failures. The localization of damage is an interesting result that requires further study. A similar study, using the bonded particle model rather than the displacement softening model yielded a similar distinction in failure mode between stable and unstable failures, [48]. A study of unstable compressive failure using the program RFPA2D concluded a that the location of microseismicity in stable failures is more dispersed than with unstable failures [82]. Laboratory tests conducted by Bieniawski using stiff and soft loading machines to study the fracture of rock in stable and unstable failure modes indicated that small, dispersed cracks were less prevalent in specimens that failed unstably [9]. The results in this thesis along with works cited suggest that failure localization during unstable failure may be physical characteristic that is arising as an emergent behavior in the discrete element method. Additional work is required to thoroughly evaluate this claim.

CHAPTER 5

UNSTABLE FAILURE IN AN IN SITU PILLAR MODEL

In underground coal mining, as areas are mined out, failure occurs on the edges of the pillars, or ribs. As the excavated area increases and the pillar size decreases, the failed area proceeds into the pillar. Stable or unstable failure of the rib material can occur while the pillar as a whole retains load bearing capacity. In order for unstable failures to occur on the rib of the pillar two conditions must be met. First, the material must fail, and second, the loading system stiffness must be less than the material's post-peak stiffness.

In this chapter, an in situ pillar (ISP) model is used to investigate failure of pillar ribs. The model is first described in detail. Then the model is verified by comparing analytical solutions to an elastic FLAC2D model and then to the ISP model. The coal material, modeled using PFC2D, is mined in using a realistic mining sequence and failure of the pillar near the rib is observed. Stability indicators are used to distinguish between stable and unstable failure, namely, damping work, kinetic energy and mean unbalanced force. Spatial measurements of damping work and contact softening are then used to support the stability indicator results.

5.1 Model Description

A two-dimensional mechanically coupled DEM/FDM model similar to that of the previous chapters is utilized. The geometry and load application scheme is modified in order to simulate an in situ pillar panel under development and then further mining. The failing material is modeled using the displacement softening model (DSM) and the surrounding mine and pillar core is modeled in FLAC2D. In situ stresses are installed to simulate a deep coal mining scenario and the DSM material is slowly removed in order to simulate the mining process. As the DSM material is mined, installed stresses redistribute and cause failure

to occur. The failure is characterized by tracking stress measurements and damping work, kinetic energy, and mean unbalanced force.

5.1.1 ISP Geometry, Boundary Conditions, and Material Properties

Figure 5.1 shows the geometry and boundary conditions for the in situ pillar model. The grey and blue areas indicate FLAC2D zones of different grid types and the yellow region is the PFC2D assembly. The blue area, labeled *FLAC2D Inner Grid,* is a fine grid comprised of square zones one-fifteenth of a meter on each side. This fine grid is intended to achieve a high resolution of stress measurement near the PFC2D assembly and to comply with the recommended coupling boundary ratio of four to five PFC2D elements to one FLAC2D zone. The grey area labeled FLAC2D Outer Grid is graded outward to increase computational efficiency and adhere to memory constraints. Directly above and below the inner grid, the grid is graded only vertically, retaining constant zone width. To the right of the inner grid, the grid is graded only horizontally, retaining constant zone height. In the remaining areas the grid is graded in both directions. Listing F.17 shows the FLAC2D grid generation file.

The dimensions of the model are symmetric about the vertical center of the PFC2D part. The top, left and right boundaries are fixed with a roller boundary while the bottom boundary is pinned. The red arrow indicates the direction of excavation and the black dashed lines show the locations of two FLAC2D interfaces. The placement of the dashed lines is exaggerated to indicate that the interfaces are located one zone width within the FLAC2D grid. The PFC2D part is composed of twenty square pbricks stacked two high and ten wide.

The material properties and element size of the PFC2D material are the same as the DSM used in the previous chapters and shown in Table 3.2. The only difference is the number of pbricks in the horizontal direction. The FLAC2D material is divided in two sections. They are the surrounding rock and coal regions, both are elastic. The FLAC2D coal spans the same height of the PFC2D coal and extends from the right edge of the PFC2D part to the right boundary of the model. The zones in the FLAC2D coal region are assigned a shear modulus, bulk modulus and Poisson's ratio corresponding to the DSM elastic modulus and

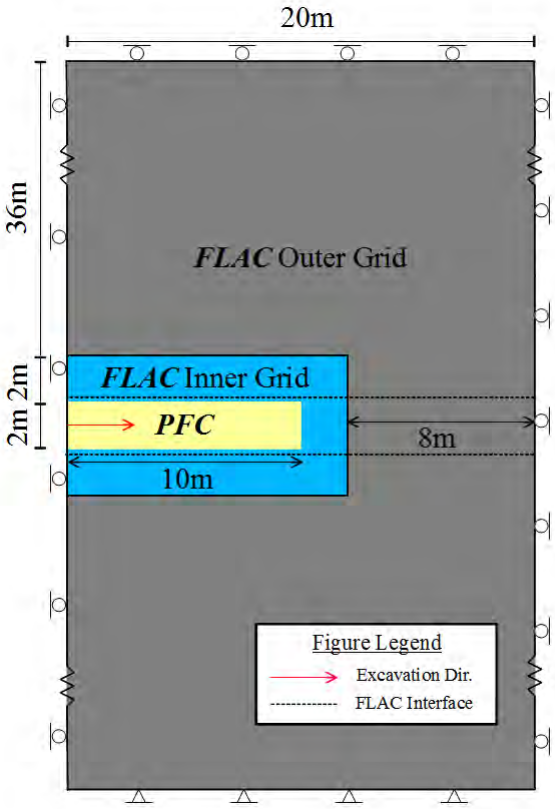

Figure 5.1: In situ pillar geometry and boundary conditions

Poisson's ratio shown in Table 3.4. The surrounding rock material is assigned bulk and shear moduli corresponding to an elastic modulus of 35 GPa and a Poisson's ratio of 0.25. The constitutive model used for the interfaces is a Mohr-Coulomb elastic perfectly plastic model. The assigned properties are given in Table 5.1. A zero degree friction angle and low cohesion are assigned to simulate a slick interface with low strength.

Table 5.1: FLAC2D interface properties

ϕ	(deg)	0
c	(MPa)	1
k_n	(GN/m)	50
k_s	(GN/m)	50

5.2 ISP Model Execution

The use of the discrete element method for modeling rock requires initial steps to generate the material and install in situ stresses. For coupled applications, where a continuum model performs the function of a surrounding rock, additional steps are needed to insert the PFC2D material into its assigned region and bring the coupled system into equilibrium. During any part of the initialization procedure, if unbalanced forces in the system are high, contact bonds can be broken. Any damage inflicted upon the system at this stage is unrealistic and should be minimized. Careful initialization of the model ensures that the expected DEM material properties are retained.

Unlike the slender pillar model of the previous chapter, the in situ pillar model utilizes in situ stresses for load application. During initialization, the free mining face creates an opportunity for high unbalanced forces to destabilize the DEM system. In order to prevent unnecessary damage to the system, the stresses are installed in the PFC2D part separately, then the mechanical coupling is initialized and the coupled model is equilibrated with installed stresses. Then the left boundary of the PFC2D part is slowly released to create a free mining face with minimal initial damage. Following model initialization, the PFC2D material is deleted in thin slices to simulate the mining process. The following sections provide a

detailed description of this process.

5.2.1 Stress Installation

In FLAC2D stress can be assigned explicitly prior to cycling. Stress installation in PFC2D requires a procedure that adjusts the positions of elements then measures the internal stresses, iterating until the target stress is achieved. Stress installation in PFC2D is performed using built in functions supplied in the FISH tank. The procedure is described in detail in the PFC2D manual. The file `acdc-si.dvr` initiates the process.

For the purpose of this study, two different stresses are applied to simulate a deep western coal mine with a lateral earth pressure coefficient of 0.3. Sixteen MPa vertical stress is installed to simulate a depth of 630 m. Figure 5.2 shows a screen shot of PFC2D at the termination of stress installation. The blue area is the location of PFC2D elements and the yellow circles show the locations of measurement circles used for the stress calculation. The black and red line plots are average horizontal and vertical stress respectively. The red line shows that 16 MPa vertical stress is achieved while the black line shows that the horizontal stress is 4.5 MPa. For FLAC2D stress installation, all zones are assigned the target stress values for vertical and horizontal stress just prior to cycling in the coupled model equilibration step.

5.2.2 ISP Model Initialization

The coupled model is initialized by defining the coupling boundary and then cycling with three damage preventing measures. First, the damping coefficient in PFC2D, α, is increased to 0.95. Second, the *cycle calm* command is utilized. This command causes velocities of the elements to be set to zero after every 25 steps. The third measure is to make the PFC2D material elastic by increasing normal and shear strength of each of the contacts so as to make the contacts unbreakable. At the left boundary of the PFC2D part, a pressure boundary is used to fix the elements in the horizontal direction. Appendix F shows the custom FISH codes and input files for the ISP model. Listing F.18 and Listing F.19 are the files used to

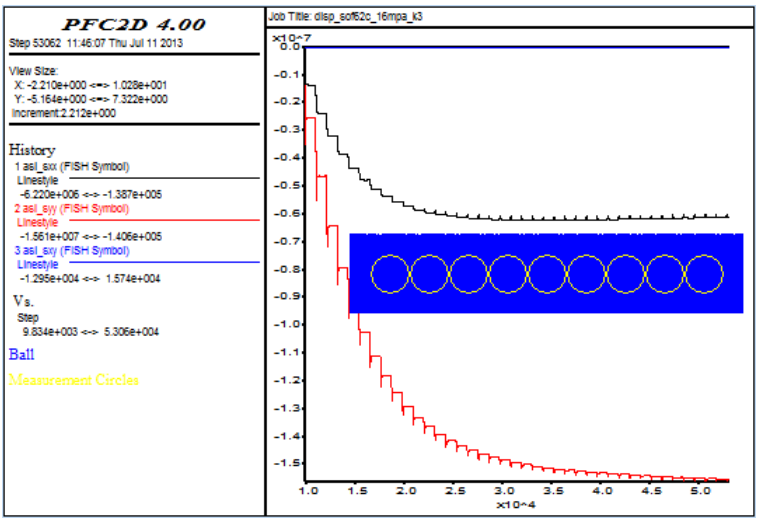

Figure 5.2: PFC2D stress installation screen shot, 16 MPa vertical stress target

execute the equilibration process in FLAC2D and Listing F.20 and Listing F.21 are used for PFC2D. Additional custom files necessary for the in situ pillar (ISP) model runs in this chapter are shown in Listing F.22 through Listing F.26

The final step in initializing the coupled model is to remove the pressure boundary on the PFC2D part and bring the model to equilibrium. Listing F.27 shows the sequence of commands to initiate this process in FLAC2D and Listing F.28 shows the commands for PFC2D. The functions needed to excavate material and bring the model to equilibrium automatically are shown in Listing F.25 and Listing F.26 for FLAC2D and PFC2D respectively. The pressure must be removed gradually so that minimal damage is imposed due to sudden deconfinement. A pressure reducing function performs this task. Calling the function *bdry_loop* in both FLAC2D and PFC2D starts a pressure reduction process in which the pressure is reduced incrementally and brought to equilibrium after each reduction step until the pressure is reduced to zero. Then, finite strength is restored to the PFC2D element contacts.

5.2.3 Excavation

Excavation then begins by calling the function *slice_loop* in both FLAC2D and PFC2D. Excavation proceeds by deleting elements to the left of an advancing mining face position. Once a selection of elements is deleted, the model is cycled until equilibrium is achieved. Then the face position moves forward one mining increment. The mining increment used in this study is equal to the average element diameter. The single layer of FLAC2D zones adjacent to the PFC2D model and under the interface are deleted as the mining face passes by. The model is saved at 0.5 m mining face advance increments until the mining distance limit is reached. In this study, eight of the ten meters of PFC2D material is mined.

5.3 Model Verification

To verify the performance of the coupled in situ pillar model, first, analytical solutions for closure of a tabular excavation and associated abutment vertical stress are compared to a FLAC2D model. Then closure and abutment stress is compared between elastic versions of the coupled in situ pillar model and FLAC2D. Closure of the excavation and abutment vertical stresses are compared for a tabular excavation span of 6 m at 630 m depth with a lateral earth pressure coefficient of $K_E = 0.3$ and a surrounding rock elastic modulus of 35 GPa.

5.3.1 FLAC2D Measurements

The stresses and displacements are captured in each model using FLAC2D zones and grid points respectively. Figure 5.3 shows the FLAC2D grid for the ISP model at the final excavation stage. This figure includes an inset of the FLAC2D grid adjacent to the PFC2D part of the model. The inset shows the locations of zones used for stress measurement and grid points used for displacement measurement in the roof. In order to plot vertical stress as a function of position, stress is averaged among the two zones adjacent a grid point at a given position x. While only mine roof measurement locations are shown, a mirrored scheme is used for the mine floor. The vertical stress presented for comparison is the average of the

roof and the floor stress for each x position. Closure is the sum of roof and floor grid point displacement for a given position, x, where displacements toward the excavation are positive.

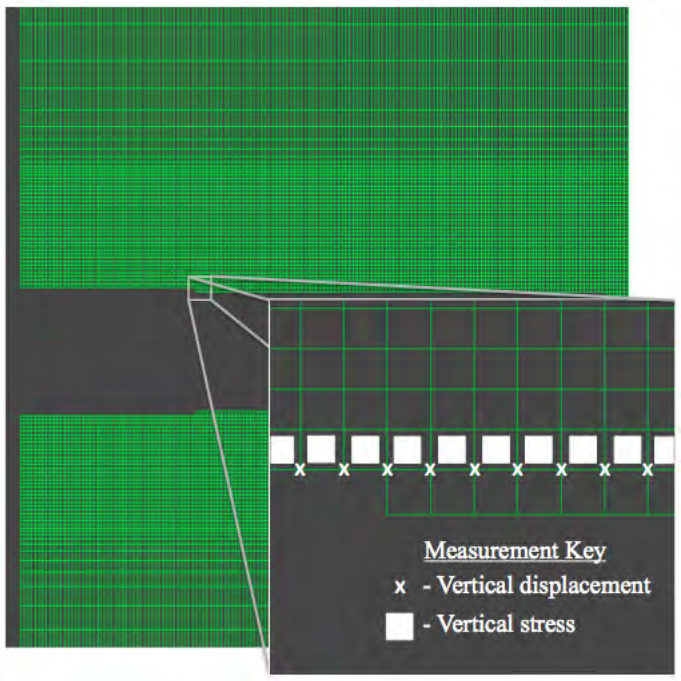

Figure 5.3: ISP model FLAC2D grid measurement locations

5.3.2 Closure and Vertical Stress in FLAC2D

Equation 5.1 is the closure of a tabular excavation at a distance x_e from the center of the width of the excavation where the span is $2l_e$, the in situ vertical stress is σ_v, and the surrounding rock has shear modulus G, and Poisson's ratio ν. Figure 5.4 shows a rectangular excavation in which the dimensions are labeled and the closure is demonstrated. This solution assumes plane strain conditions, that the closure at the edge of the excavation is zero, and the extent of the rock in the vertical and horizontal directions is infinite. Abutment vertical stress (σ_z) into the abutment a distance x_a is given by Equation 5.2 Ozbay [62].

$$s = \frac{2\sigma_v (1-\nu)}{G} \sqrt{l_e^2 - x_e^2} \tag{5.1}$$

$$\sigma_z = \frac{\sigma_v x_a}{\sqrt{x_a^2 - l_e^2}} \tag{5.2}$$

The tabular excavation is modeled in FLAC2D using a vertical line of symmetry about the center of the excavation. Roller boundary conditions are applied to the grid edges and the rib is fixed. A vertical stress of 16 MPa is used and lateral earth pressure coefficient of $K_E = 0.3$ is used to generate the corresponding horizontal stress.

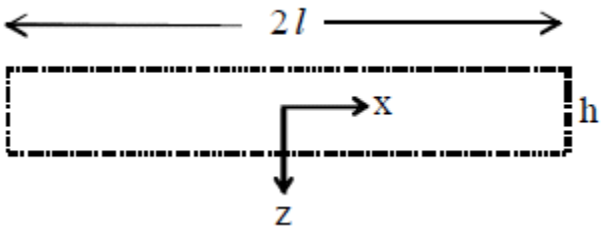

(a) Excavation dimensions

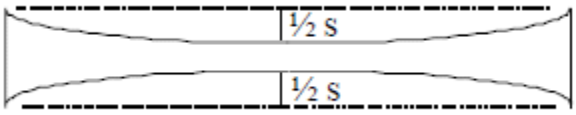

(b) Excavation closure

Figure 5.4: Static deformation of a tabular excavation in elastic medium

Figure 5.5 shows the comparison of closure for the analytical and FLAC2D solutions. The difference between the FLAC2D and analytical closure at the center of a 6 meter wide excavation is approximately 0.01% of the excavation height (2m). Figure 5.6 and Figure 5.7 show the vertical stress comparison for the FLAC2D and analytical solutions near the rib and for the full width of the coal respectively. Figure 5.6 shows that the FLAC2D model experiences a sharp increase in stress at the rib similar to the analytical solution, but not as high in magnitude. Figure 5.7 includes two horizontal lines indicating the virgin stress magnitude at 16 MPa. As the distance from the rib increases, the vertical stress decreases to meet the virgin stress value.

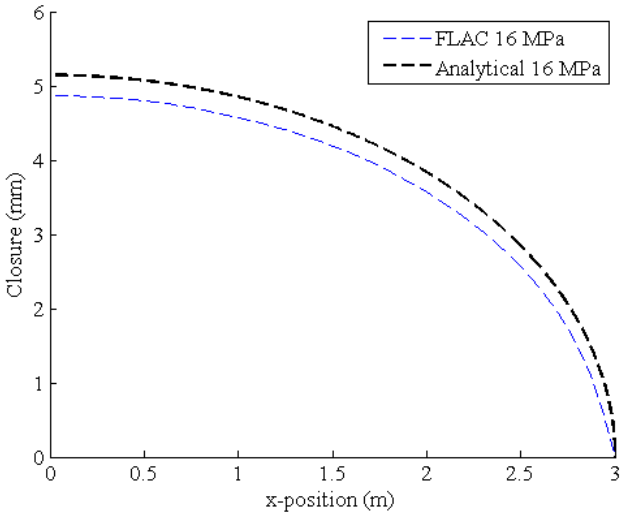

Figure 5.5: Closure comparison between FLAC2D and analytical solutions

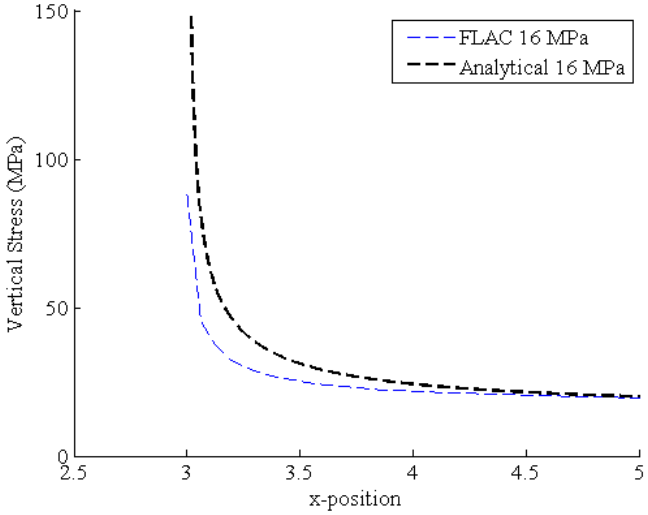

Figure 5.6: Vertical stress comparison between FLAC2D and analytical solutions

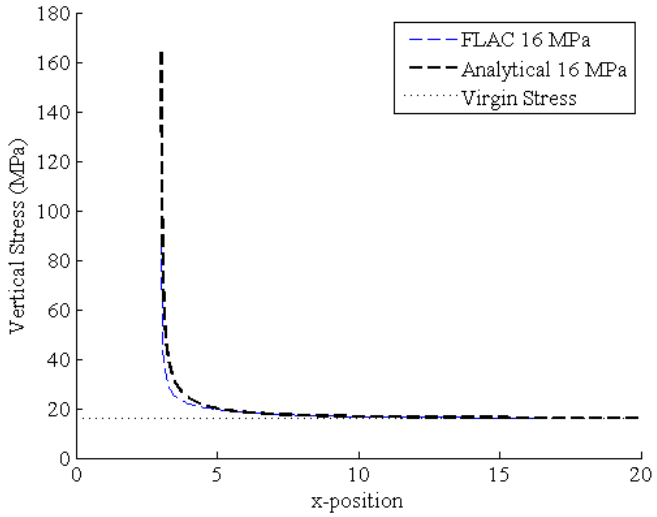

Figure 5.7: Vertical stress comparison between FLAC2D and analytical solution, full model span

Figure 5.8 shows closure for the FLAC2D and coupled ISP models for a 6 m by 2 m tabular excavation. In these models, the rib displacement is not fixed, so the value of closure at the rib is non zero. The closure values for each model are in close agreement indicating that the DSM material satisfactorily simulates elastic displacement due to a given stress field.

Figure 5.9 and Figure 5.10 show vertical stress in the FLAC2D and coupled ISP models near the rib and for the full span of the coal respectively. Near the rib, vertical stress values are similar for each model for respective depths. Each result exhibits an stress increase at the coal rib. The coupled ISP model shows an unexpected decrease in stress at the rib, where the FLAC2D model does not show this decrease. This inward movement of the stress concentration in the coupled model is due to larger horizontal displacement of the rib in the coupled ISP model resulting in slight rib destressing and therefore, inward movement of the stress concentration.

Figure 5.10 shows the full span of the coal material. The plot terminates just after 16 meters because stress is the average of two adjacent zones. Because of zone gradation, the

zone adjacent to the the grid point near x equal 16 meters is nearly 4 meter in width. The dotted lines in Figure 5.10 show the installed virgin stress state. As distance from the rib increases, vertical stress approaches these values for each depth. The irregular stress pattern, as measured in the FLAC2D zones, is due to roughness of the PFC2D assembly. This stress pattern is periodic as a result of using identical pbricks to create the PFC2D assembly.

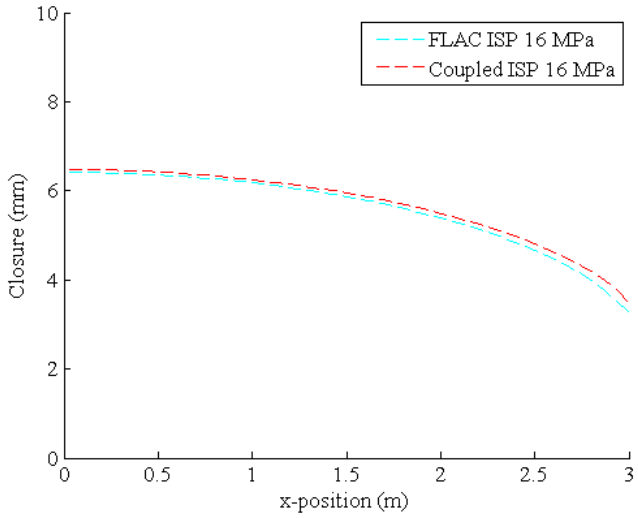

Figure 5.8: Closure comparison between FLAC2D and coupled ISP model solutions

5.3.3 Effect of the Coupling Boundary on Vertical Stress

Figure 5.10 shows a stress increase in the coupled ISP model near the right coupling boundary. The stress increase is due to the mismatch of material behavior at the coupling boundary and can influence results and interpretation of results if the area of interest is near this boundary. In order to examine this effect in greater detail, elastic simulations for various entry widths are performed. The model is initialized, then the PFC2D material to the left of the appropriate excavation boundary is deleted, then the model is cycled until equilibrium was achieved. Roof stress is then analyzed, as opposed to average roof and floor stress, so detail in stress changes could be seen.

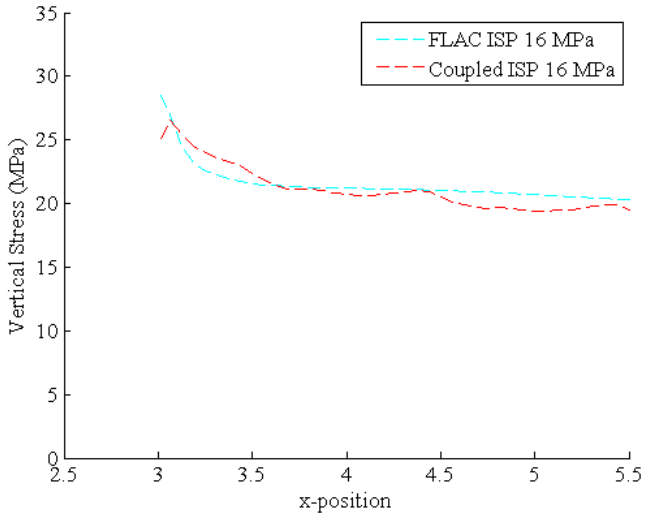

Figure 5.9: Vertical stress comparison between FLAC2D and coupled ISP model solutions

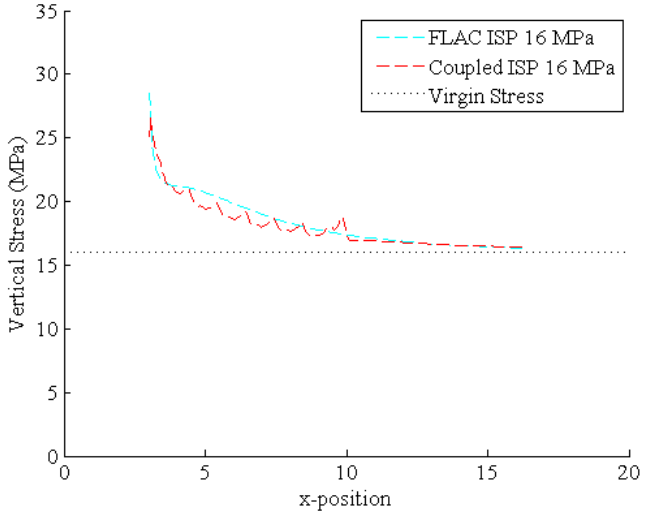

Figure 5.10: Vertical stress comparison between FLAC2D and coupled ISP model solutions, full model width

Figure 5.11 shows vertical stress in the roof for various entry widths. The right coupling boundary is located at 10 meters. Comparing the rib stress for different entry widths shows an incremental increase at all locations. At a entry width of 16 meters, the mismatch in material behavior results in a lower than expected rib stress and higher than expected abutment stress . Therefore, if the area of interest is within two to three meters of the coupling boundary, analysis of model output should consider the effect of the coupling boundary.

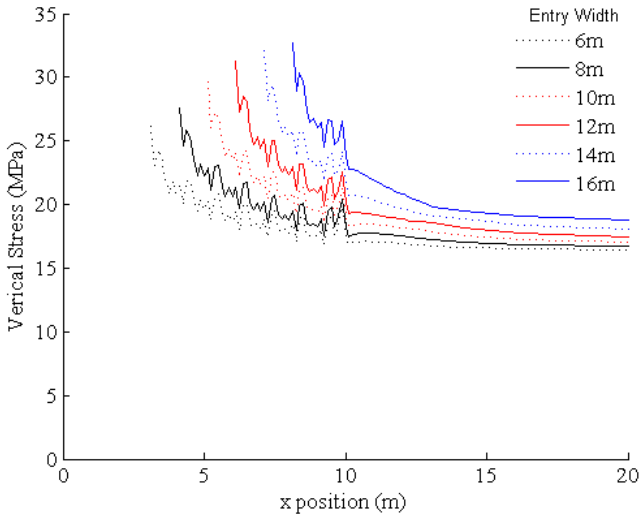

Figure 5.11: Vertical roof stress for various entry widths

5.4 Results

Results are presented here for the ISP model with inelastic DSM material. As the excavation proceeds material fails at the rib due to the redistribution of stress. Stress profiles reveal the extent of failure by denoting the location of maximum stress for a given entry width. Damping work, kinetic energy, and mean unbalanced force are utilized to detect occurrences of unstable failure. Then, grid based, spatial measurements of contact softening and damping work are used to support identifier and stress results.

5.4.1 Zone Stress Measurements

Roof stress profiles identical to Figure 5.11 are shown in Figure 5.12. As the excavation widens, high stresses on the edge of the material cause failure and redistribution of vertical stress inward, towards the unfailed portions of the pillar. As the entry widens, more stress must be carried by the pillar so at the point of maximum stress the magnitude increases for successive excavation steps.

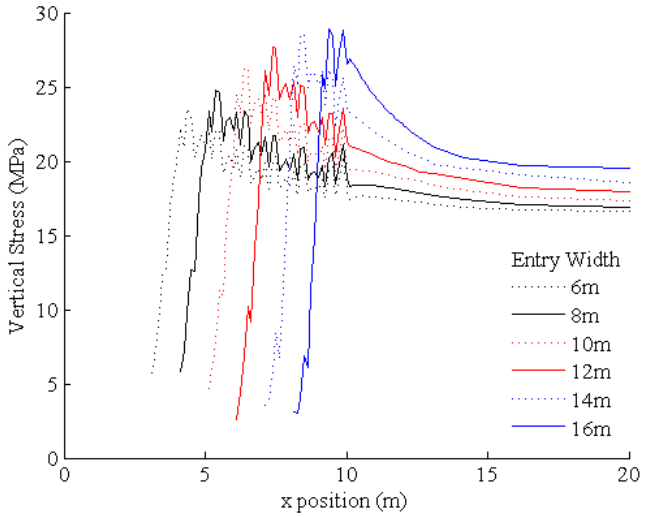

Figure 5.12: Deep depth roof stress profiles for various entry widths

The degree of failure at specific instances during the excavation process can be determined from the stress profile in Figure 5.12. The degree of failure is indicated by comparing the difference in vertical stress to the location of maximum stress. A low value of residual stress on the pillar rib compared to the maximum stress indicates extensive failure. Whereas if the pillar rib exhibited a greater amount residual stress, it would indicate that the material is still capable of bearing load and therefore has been damaged to a lesser degree.

The degree of failure can be quantified by calculating the gradient of vertical stress from the pillar rib to the point of maximum stress. The vertical stress gradient is calculated by dividing the change in stress from the rib to the point of maximum stress by the distance between the rib and the x position of maximum stress. Figure 5.13 shows the rib stress

gradient at one meter excavation intervals.

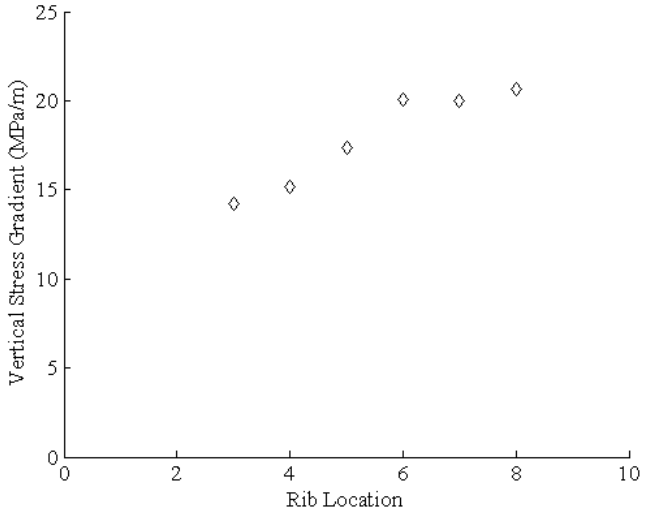

Figure 5.13: Rib stress gradient versus rib position for ISP model

The trend of the vertical stress gradient shows how the degree of failure changes as the entry widens and stress on the pillar edges increases. There is an increasing trend as pillar size decreases but also a significant jump in the degree of failure while mining from four meters to six meters. The inconsistent jump in vertical stress gradient could indicate an unstable failure event or series of unstable failures that warrants further investigation using stability indicators.

5.4.2 Stability Indicators

As seen in the previous chapter, stability of failure can be measured using stability indicators. The most useful indicators from the previous chapter are chosen to analyze the failure of the in situ pillar of this chapter. They are damping work, instantaneous kinetic energy, and instantaneous mean unbalanced force. Figure 5.14 shows the damping work, Figure 5.15 shows the instantaneous kinetic energy, and Figure 5.16 shows the instantaneous mean unbalanced force. For reference, plots for contact softening, maximum unbalanced force, and number of broken contacts are included for reference in Appendix G. In each of

these plots, the vertical lines are the excavation steps, when a layer of elements is deleted. Since these plots are showing results from the same model, these mining steps are identical in each plot. The spaces in between the excavation steps is are the number of steps required to bring the simulation to equilibrium. There are 158 excavation steps in the simulation as the mining face advances from x equals 4 to 6 meters. The lines showing the time step of mining each have the same width. The appearance of thicker lines is an indication of several mining steps occurring closely to one another.

It can be seen in Figure 5.14 that two particular mining steps result in significant increases in the cumulative damping work performed. The first is at approximately 6.8×10^6 steps and the other is near 8.4×10^6 steps. In Figure 5.15, significant increases in the instantaneous kinetic energy are present during these steps and also in Figure 5.16, large amounts of unbalance force are present. As compared to other mining steps, the number of steps required for equilibration and the increase in identifier value signifies that unstable failures of the rib occurred at these locations.

Despite the fact that the mining increments are very small in distance, it is rational to assume that there be some instability resulting from removal of elements. By comparing a typical stable mining step and the first unstable mining step, a significant difference in identifier behavior emerges. The stable step chosen is when the mining face is at x equals 4.709 meters, at timestep 6.678×10^6. The unstable mining step is when the mining face is at x equals 4.772 meters, at timestep 6.784×10^6. Figure 5.17 shows the damping work in the stable and unstable mining steps. The damping work accumulates during both mining steps, although the increase in damping work in the unstable case is an order of magnitude higher than the stable case. As seen in the SPCS tests, a large relative increase in damping work can indicate unstable failure.

By plotting the incremental increase of damping work versus the mining extent in meters, the magnitude of damping work performed during each mining step can be clearly compared. Figure 5.18 shows the amount of damping work performed between excavation steps. Typ-

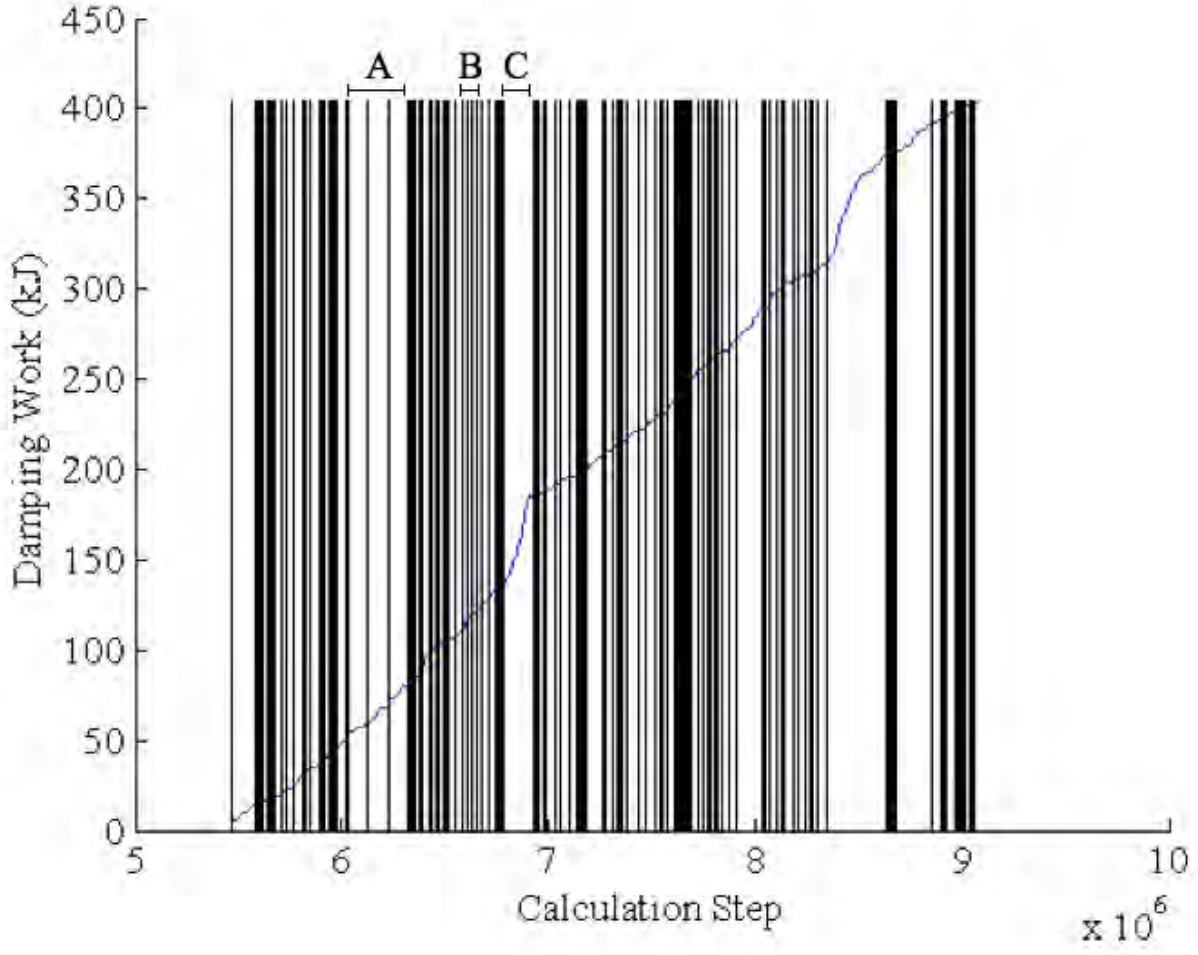

Figure 5.14: Damping work in the ISP simulation

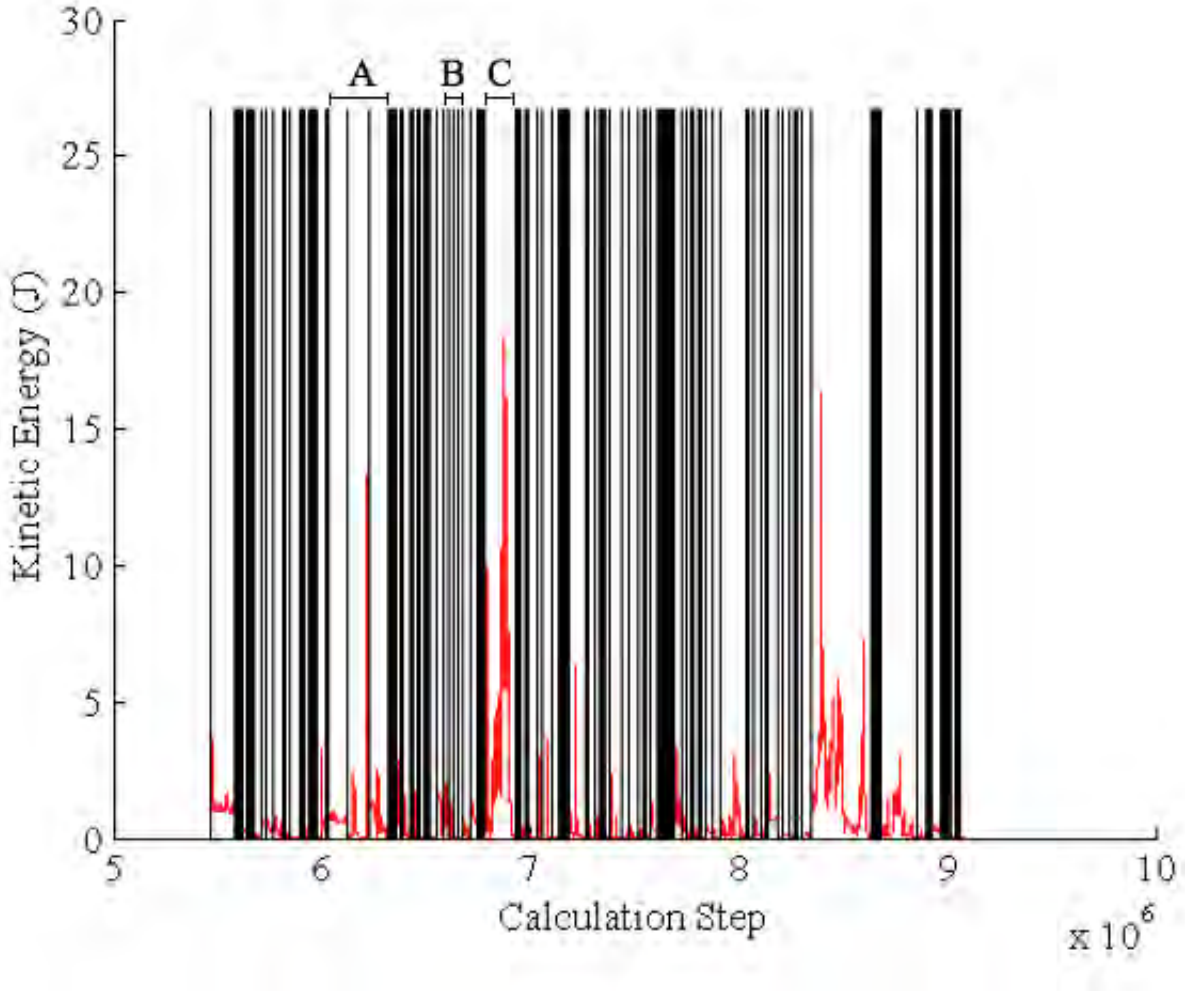

Figure 5.15: Kinetic energy in the ISP simulation

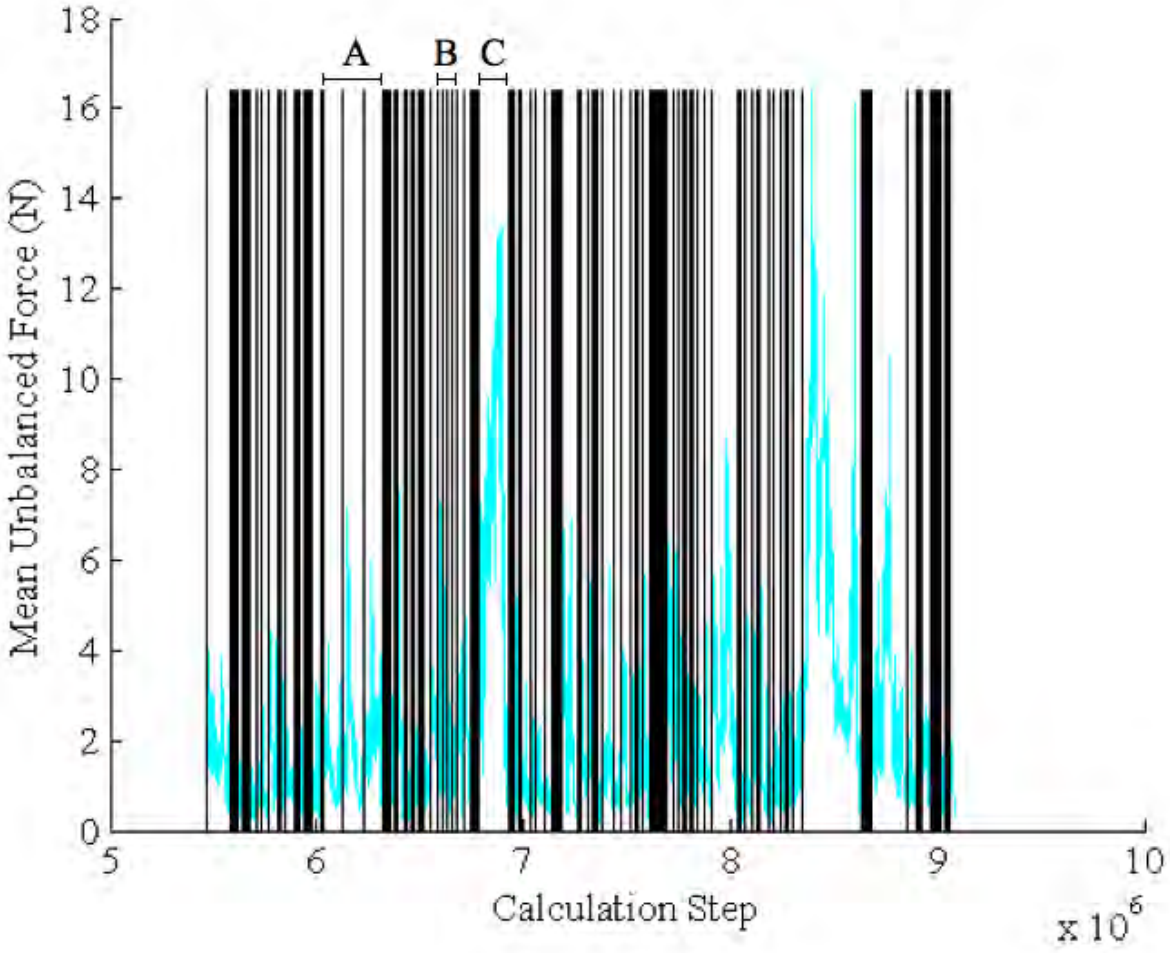

Figure 5.16: Mean unbalanced force in the ISP simulation

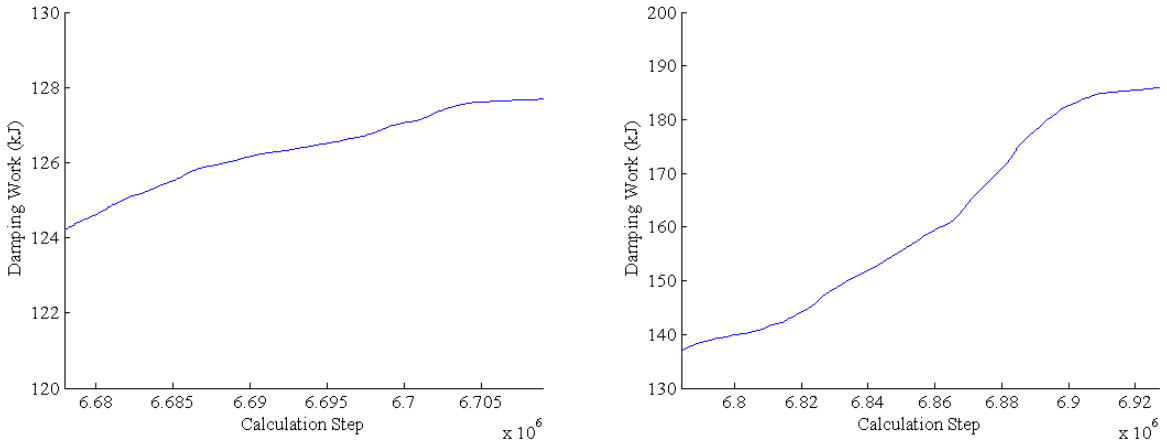

(a) Stable (b) Unstable

Figure 5.17: Damping work during a stable and unstable mining steps

ically, the amount of damping work performed during a mining step is below 5 kJ, but the damping work at the two unstable mining steps at 6.8 and 8.4 million calculation steps correspond to the high values near 4.8 meters and 5.65 meters. Figure 5.18 also reveals that there is a second tier of instability with intensities between 5 and 20 kJ. It should be noted that this value of energy is of a numerical nature and should not be considered as the amount of energy associated with a real unstable failure. Additional work must be undertaken to assess the accuracy of energy calculation using the ISP model.

The kinetic energy and mean unbalanced force also exhibit a difference in magnitude between stable and unstable cases. However, aside from a change in magnitude, another revealing difference between the stable and unstable cases is shown in kinetic energy and mean unbalanced force. Figure 5.19 shows instantaneous kinetic energy in the unstable and stable mining steps and Figure 5.20 shows the instantaneous mean unbalanced force. For both cases, kinetic energy and mean unbalanced force increase immediately after the elements are deleted. In the stable step, the model equilibrates steadily as shown by steadily decreasing identifier value. In the unstable step, there is a secondary increase in indicator value unrelated to the initial deconfinement due to mining. This failure results from the mechanism for instability in which excess energy stored in the loading system is unable to

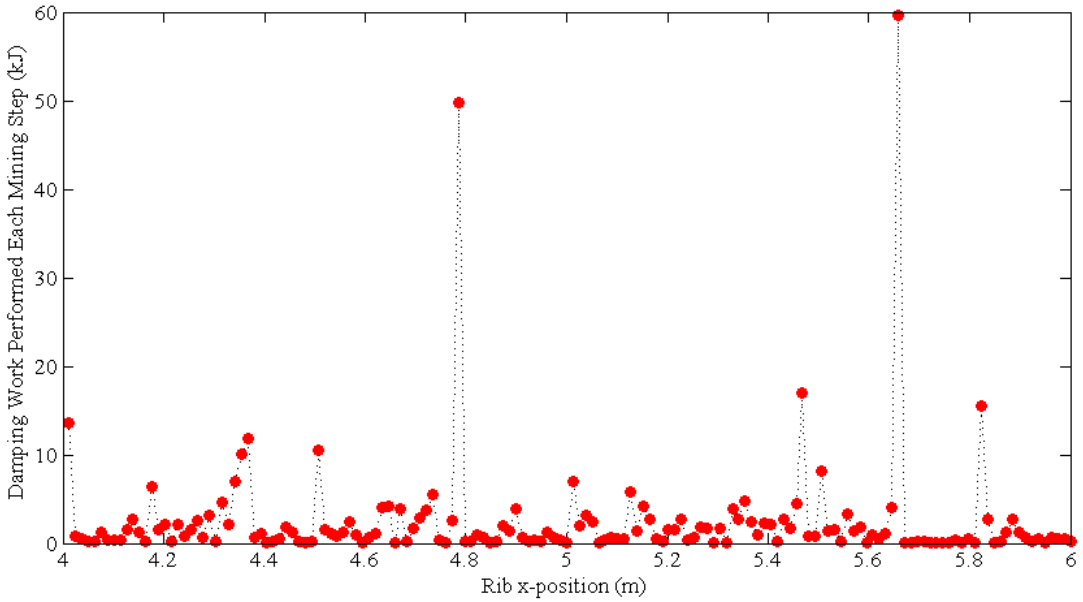

Figure 5.18: Damping work between excavation steps in the deep simulation

be absorbed by the failing material.

5.4.3 Indicator Results Discussion

In Figure 5.14, Figure 5.15, and Figure 5.16 three regions of time step are labeled A, B, and C. These serve to signify different types of mining activity as depicted using stability indicators. Region A includes three mining steps that each required a larger than average number of steps in order to equilibrate and indicate significant amounts of damping work performed, kinetic energy in the model, and increases in mean unbalanced force. Region B includes mining step with lesser number of time steps required for equilibration. The lines are close together and less indicator activity occurs during these steps. Region C includes only one mining step that requires a large amount of steps to achieve equilibration and an extreme amount of indicator activity occurs during this step.

The results of EPC tests in Chapter 4 showed consistent values of indicator magnitude for stable failures and increasing indicator magnitude as failure stability decreases. The three regions defined by A, B, and C can be seen as indicating various points along this exponential

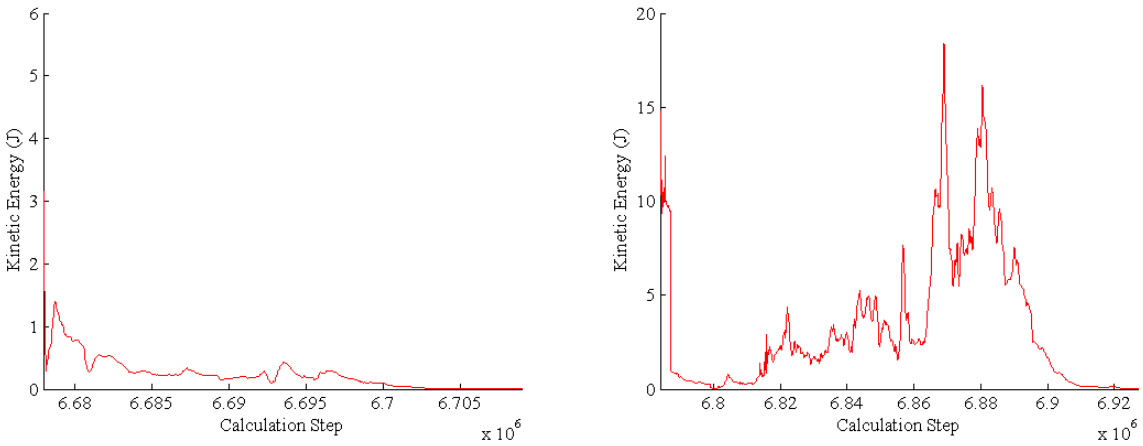

(a) Stable (b) Unstable

Figure 5.19: Kinetic energy during stable and unstable mining steps

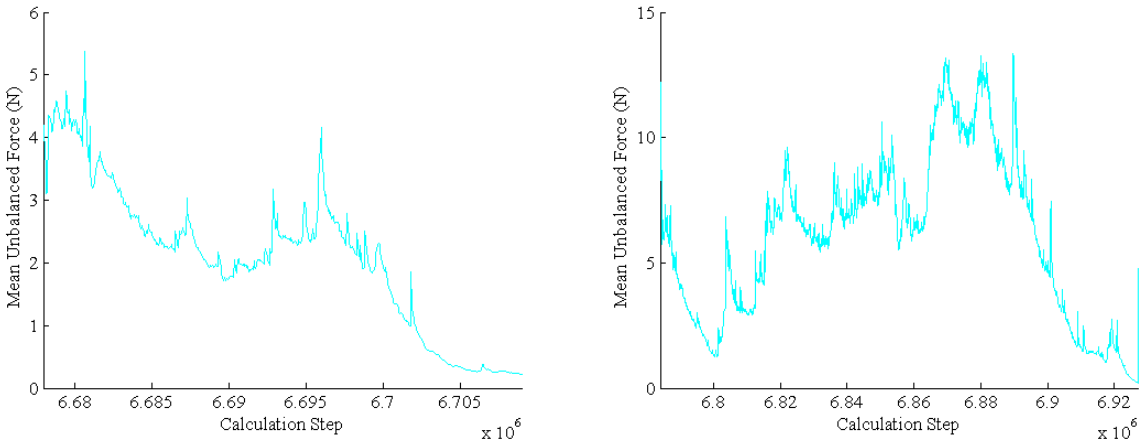

(a) Stable (b) Unstable

Figure 5.20: Mean unbalanced force during stable and unstable mining steps

indicator trend. Region B indicates stable mining, Regions A indicates quasi stable mining, and Region C indicates and unstable failure. Figure 5.18 shows that the damping work magnitudes performed during the stable, quasi-stable, and unstable steps are in agreement with failure stability interpretation from Figure 5.14, Figure 5.15, and Figure 5.16.

5.4.4 Grid Based Measurements

The previous section showed that stability indicators could detect the mechanism for unstable failure and revealed a distinct difference between an example of a stable mining step and an unstable failure resulting from a single mining step. By tracking the damping work and contact softening using the grid based measurement technique, the damage and instability in the model during each of these steps can be observed spatially.

Figure 5.21 shows the damping work before and after the stable and unstable mining steps. Each of the images shows the rib region of the model, from x equals 4.8 to 7 meters. For comparability, each of the images is shaded according to the same scale. The scale used, from 0 to 160 J, is shown next to the image of the state before the stable mining step. Each of the images shows a parabolic shaped area of failure. There are subtle increases in the magnitude of damping work as mining progresses from the beginning of the stable mining step to the beginning of the unstable mining step. The image showing the state after the unstable mining step indicates that a large amount of instability occurs along the outer edge of the parabolic damage region. Figure 5.22 shows the damping work after the unstable mining step with the scale reset to resolve the larger pixel values. This image reveals a possible new failure surface further into the pillar than the most inner failure surface seen before the unstable mining step. Also, the magnitude of the damping work performed along the new failure surface far exceeds the values seen in the unstable mining step in Figure 5.21.

Figure 5.23 shows the contact softening for the stable and unstable mining steps. The shading scale is common to each image and is given next to the image depicting the model state before the stable mining step. The maximum value is set to 0.5 m of contact softening to highlight the pattern of damage. As mining progresses the softening of the rib exceeds

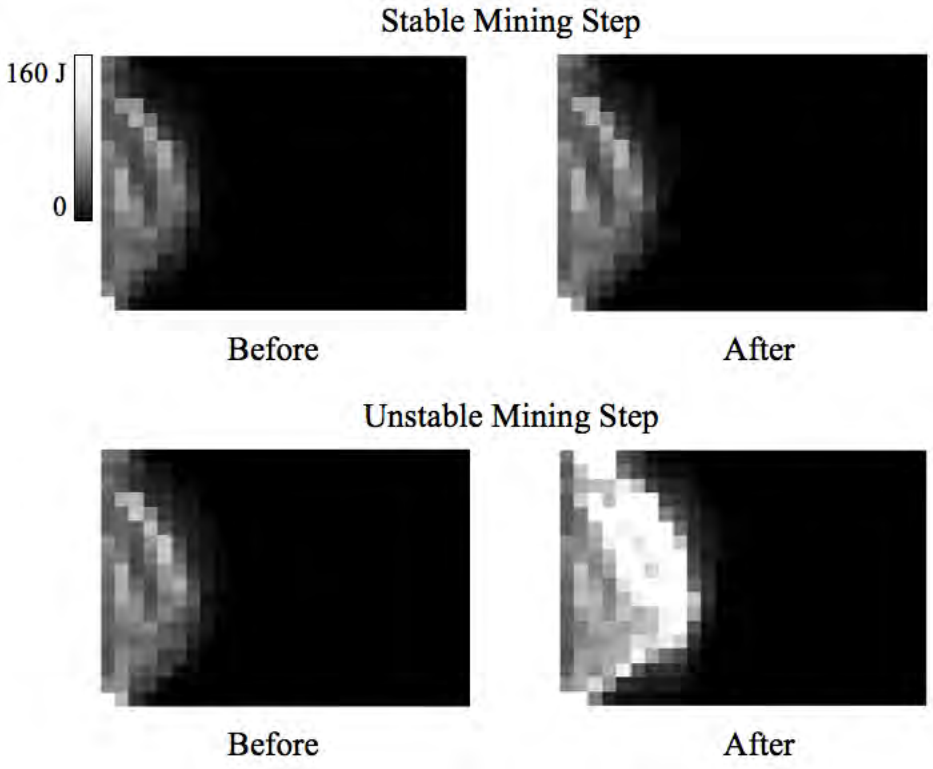

Figure 5.21: Damping work in the rib during the ISP test

Figure 5.22: Damping work in the rib during the ISP test

the maximum value on the scale and therefore the outer most pixels are white. The dashed line adjacent each image denotes the edge of the measurement grid at x equals 4.8 meters.

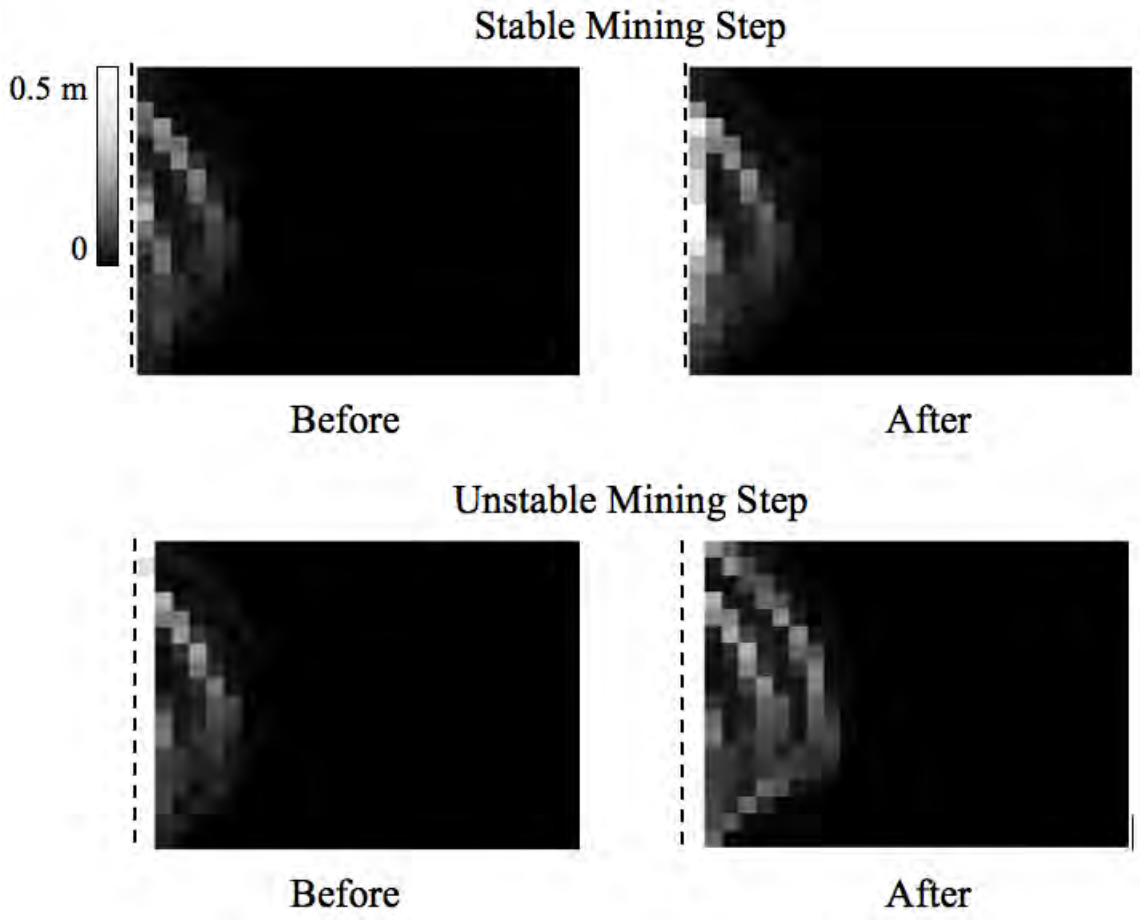

Figure 5.23: Contact softening in the rib during the ISP test

Figure 5.23 shows that damage has accumulated near the rib in the form of planes of failure which extend from the rib corners inwards, toward the vertical centerline of the pillar. Before the stable mining step, one such failure plane is depicted along with a region of damaged material near central part of the rib. After the excavation of the stable mining step, damage accumulates in these two areas. In subsequent mining steps, the material at the rib softens but there is no significant accumulation of damage along the failure plane, as seen in the state of the model before the unstable mining step. After the unstable mining step, the contact softening shows the formation of a new failure plane.

5.5 Conclusions

The damping work stability indicator successfully detected two unstable failures in the ISP model, as shown in Figure 5.18. By inspecting the kinetic energy and mean unbalanced force versus timestep, it could be seen that a different trend is present during unstable failures than during stable failures. The failure triggered by the unstable failure mechanism resulted in an additional spike in indicator value unrelated to the initial removal of material. Together, Figure 5.21 and Figure 5.23 reveal a direct correlation between a single unstable failure event and appearance of a failure plane. By inspecting indicator trends versus time step, the number of steps required for equilibrium helps to reaveal the failure stability of each mining step. When stable mining is occuring, the number of time steps required to achieve equilibrium is less. The number of time steps and indicator activity during the step allows one to classify failure stability, with a high amount of indicator activity representing increased failure stability.

CHAPTER 6
CONCLUSIONS AND FUTURE WORK

To summarize the work in this thesis briefly, first, an appropriate DEM model for studying compressive failure stability was chosen. Then a series of model behaviors were defined to use as indicators of failure stability. These were evaluated during a series of pillar strength tests and the most appropriate indicators were identified. Then the failure of an excavation loaded under in situ, mining conditions was investigated using the indicators on a global and also localized basis. In general, the numerical models behaved acceptably for the purpose of studying unstable compressive failure in western U.S. coal and the methods used to distinguish between stable and unstable failure were successful. The following is a concise list of conclusions on a chapter by chapter basis. Then a list of suggested future work is given followed by some additional research questions inspired by this work.

Chapter Conclusions

Ch 2. Background Information on Unstable Failure in Underground Coal Mining

- A need exists to ensure failure stability in deep underground western U.S. coal mines due to the high probability and potential risks associated with unstable failure in western U.S. coal mines.
- A theoretical background for the mechanism of unstable compressive failure in brittle rocks exists, but additional work is needed to include stable and unstable failure modes in mechanistic numerical studies.
- The DEM code PFC offers features such as emergent rock like behaviors and an implicit time steping solution scheme that allows for multi-stage simulation of unstable failure.

- To the best of the author's knowledge no previous work successfully simulates unstable compressive failure using a discrete element model.

Ch 3. Evaluation of Two DEM Models for Simulating Unstable Failure in Compression

- The BPM and DSM described in Chapter 3 are two discrete element models that are capable of simulating a western United States coal with post-peak softening behavior for the purpose of studying compressive failure stability.

- Currently, the BPM requires a 'black-box' type of computer algorithm to determine microparameters, because the combination of parameters necessary to define characteristic post-peak behavior is not known.

- The DSM requires an iterative calibration that can be conducted manually. The key microparameter influencing the post-peak softening behavior is the contact plastic softening limit, U_{pmax}.

- Triaxial tests results revealed lower than desired friction angle for the BPM, an expected result. The DSM triaxial tests showed a higher than desired friction angle.

- The DSM model showed more consistent behavior during the failure stability (EPC) tests in that post peak behavior remained consistent for stable failures than did the BPM model. Furthermore, the transition from stable to unstable failure mode with various loading system stiffnesses was more defined with the DSM, while the BPM exhibited a fairly large quasi-stable region.

- The BPM exhibits a clear dependency of post-peak softening on loading rate. For lower loading rates, the BPM post-peak stiffness increases in magnitude.

- The DSM exhibits an effect on post-peak behavior for different loadings rate, however the general softening characteristic of the material is retained.

- The DSM is a more appropriate DEM to use in studying failure stability than the BPM based on consistency of behavior in stable and unstable failure mode and the independence of DSM post-peak softening by loading rate.

Chapter 4. Indicators of Unstable Compressive Failure in DEM Coal Strength Tests

- Cumulative indicators better represent the failure of the model because they embody information from the entire failure rather than from one calculation step as was the case with maximum instantaneous values. Although, trends of instantaneous values also indicate the behavior in the model.

- In both the EPC tests and the SPCS tests the damping work and kinetic energy differentiated between stable and unstable failure and provided a qualitative indication of the magnitude of failure.

- Some indicators are affected by the size of the model as shown in SPCS tests. The mean unbalanced force, for example appears to decrease as model size increases. So, this indicator should be used in conjunction with damping work and kinetic energy.

- The contact softening indicator does not clearly distinguish between stable and unstable failure when analyzed globally. However, this indicator could be used to provide information on location and extent of damage in the model.

- Grid based measurements for damping work and contact softening showed higher local values for unstable failures and similar values for stable failures and depicted the failure patterns in the models.

Chapter 5. Indicators of Unstable Compressive Failure in DEM Coal Strength Tests

- The stress gradient after arbitrarily chosen mining steps suggested increased possibility of unstable failures as the excavation is expanded to exceed four times the excavation height.

- When instabilities occur, an increase in indicator value will occur that is independent of the initial removal of elements. The mean unbalanced force, damping work, and kinetic energy indicate two significant unstable failures with increased magnitude of values after increasing the excavation width beyond four times the seam height..

- Plots of damping work, kinetic energy, and mean unbalanced force versus step show that fewer steps are required to equilibrate the model during stable mining. A larger number of steps are needed to equilibrate the model when unstable failure occurs.

- As revealed by the grid based measurements, single mining steps can result in the initiation of significant unstable failures.

Future Work

The DEM models and stability indicators in this thesis are applicable to investigating specific mechanisms of unstable failure and conditions that influence them. By changing existing model parameters the identifiers can be used to potentially study the effect mine conditions have on the intensity and frequency of unstable failures. In this context, additional numerical analysis should be conducted on the following topics:

- The effect of the coal/mine contact condition

  The FLAC2D part of the model in Chapter 5 contains an interface with Mohr-Coulomb strength properties with perfectly plasticity. This interface is intended to simulate the contact condition between the coal and a competent adjacent rock. While it is difficult to determine the actual material properties of discontinuities in mines the effect of different idealized discontinuity behaviors on unstable compressive failure can be evaluated. For example, using the Mohr-Coulomb with perfect plasticity interface, the strength of the discontinuity could be changed to simulate various levels of horizontal confinement on the coal due to contact conditions. By improving the constitutive law

of the effect of unstable slip along the interface could considered. Unstable failure researcher Gu demonstrated that a discontinuity with a softening post-peak behavior can simulate stable and unstable slip, analogous to compressive failure stability criteria. By modifying the discontinuity plasticity law in FLAC2D by means of user defined FISH function to include a softening post-peak behavior the effect of unstable slip on compressive unstable failure could be studied [28].

- Depth of the mine

  It is widely agreed upon that unstable failure is more probable as depth of the mining activity increases. By initializing a series of ISP models at different depths. The effect of depth on frequency and intensity of unstable failure can be evaluated.

- Various types of coal

  The post-peak behavior of coal is kept constant throughout this study. Using the DSM, coal materials with different levels of brittleness can be calibrated and tested under similar conditions. Both EPC and ISP tests on these coals could serve to confirm Cook's stiffness stability criteria concept on a theoretical basis.

- Mining rate

  In this thesis, the criteria for model equilibrium is set to simulate the onset of static equilibrium. The mining rate in actual coal mines is known to effect mine stability [90].

- Pillar design schemes

  Various combinations of pillar sizes are used to offer support in gateroad entries in longwall coal mining. The ISP model provides an opportunity to study the effects of pillar design and pillar loads on stability in these entries.

Additional Research Questions

- Failure localization

  An interesting result that arose from this study is that of the failure localization due to unstable failure. In chapters four and five the grid based measurements of damping work and contact softening showed a more dispersed type of failure resembling crushing for stable failures and localized failure along planes, resembling shear bands, for unstable failures. This behavior is more prevalent in BPM models as compared to DSM models [49]. This result suggests that a different failure mechanism is in effect when failure is unstable. DEM models hold promise in studying the failure mechanism due to their micromechanical nature. Effects of model properties on failure pattern such as particle assembly, particle size, and contact and bonding models should be systematically tested to determine the nature of failure localization in DEM. If not already sufficiently performed, laboratory testing could reveal if there is a physical analogue.

- Alternatives to the DSM for studying unstable failure

  The BPM has been used widely to simulate the failure of rock because it exhibits physical properties, such as increased strength with confinement and the Poisson effect, of rock with out the explicit assignment of such properties [68][5]. The difficulty in calibrating a velocity dependent post-peak behavior in the BPM, in part, lead to the selection of the DSM for the work in this thesis. The DSM exhibits undesirable properties, such as an unrealistically high friction angle and high Poisson's ratio. However, the ease at which post-peak softening is calibrated is key to simulating unstable behavior in in situ loading conditions. Improvements should be made on these existing models to cope with their respective drawbacks by closely examining the effect of contact laws on post-peak behavior. A simple comparison between BPM and DSM suggests that some form of softening behavior must be in action on the contact level. Alternatives to the these contact models should be thoroughly reviewed and possible usage of other numerical methods should be considered.

REFERENCES CITED

[1] Agapito, J. F. T. 1997 (Jan.). Dealing With Coal Bursts At Deer Creek. *In: Mining Engineering July - Dec. Vol. 49.*

[2] ANSYS Inc. 2013. ANSYS - A Finite Element Program. Canonsburg, PA.

[3] Babcock, C.O., & Bickel, D.L. 1984. Constraint - The Missing Variable In The Coal Burst Problem. *In: The 25th U.S. Symposium on Rock Mechanics (USRMS).* Evanston, IL: American Rock Mechanics Association.

[4] Badr, S. 2004. *Numerical Analysis of Coal Yield Pillars at Deep Longwall Mines.* Ph.D. Thesis, Colorado School of Mines.

[5] Bahrani, N., Valle, B., & Kaiser, P. 2011. Discrete element modeling of drilling-induced core damage and its influence on laboratory properties of Lac du Bonnet granite. *In: Proc. of the 45th U.S. Rock Mechanics/Geomechanics Symposium.* San Francisco, CA: Curran Associates, Inc.

[6] Bardet, J. P. 1989. Finite element analysis of rockburst as surface instability. *Computers and Geotechnics*, **8**(3), 177–193.

[7] Barron, Lance R. 1990. Longwall Stability Analysis Of A Deep, Bump-Prone Western Coal Mine-Case Study - Document Summary. *Page 8 of: Ninth Conference on Ground Control Mining Proceedings (ICGCM) 9th.* Morgantown, WV: ICGCM.

[8] Barton, N. 1995. The influence of joint properties in modelling jointed rock masses. Keynote Lecture. vol. 3. Tokyo: Balkema, Rotterdam.

[9] Bieniawski, Z. 1967. Mechanism of brittle fracture of rock Part II—experimental studies. *International Journal of Rock Mechanics and Mining Sciences & Geomechanics Abstracts*, **4**(4), 407–423.

[10] Bryan, A., Bryan, J. G., & Fouche, J. 1966. Some Problems of Strata Control and Support in Pillar Workings. *The Mining Engineer*, **123**, 238–254.

[11] Cai, M, Kaiser, P, Morioka, H, Minami, M, Maejima, T, Tasaka, Y, & Kurose, H. 2007. FLAC/PFC coupled numerical simulation of AE in large-scale underground excavations. *International Journal of Rock Mechanics and Mining Sciences*, **44**(4), 550–564.

[12] Campoli, A.A., Kertis, C.A., & Goode, C.A. 1987. *Coal Mine Bumps: Five Case Studies in the Eastern United States*. Information Circular 9149. U.S. Department of the Interior, Bureau of Mines.

[13] Chase, F.E., Zipf, R.K., & Mark, C. 1995. The massive collapse of coal pillars-case histories from the United States. *International Journal of Rock Mechanics and Mining Sciences and Geomechanics Abstracts*, **32**(8), 396A–396A(1).

[14] Chen, Z. 1997. A double rock sample model for rockbursts. *International Journal of Rock Mechanics and Mining Sciences*, **34**(6), 991–1000.

[15] Cho, N, Martin, C, & Sego, D. 2007. A clumped particle model for rock. *International Journal of Rock Mechanics and Mining Sciences*, **44**(7), 997–1010.

[16] Cook, N. G. W. 1963. The seismic location of rockbursts. *In: Proc. of the 5th Rock Mechanics Symposium*. Minneapolis, MN: Pergamon Press.

[17] Cook, N. G. W. 1965. The failure of rock. *International Journal of Rock Mechanics and Mining Science & Geomechanics Abstracts*, **2**(4), 389–403.

[18] Cundall, P. A., & Strack, O. D. L. 1979. A discrete numerical model for granular assemblies. *Géotechnique*, **29**(1), 47–65.

[19] Dalian Mechsoft Co. 2013. RFPA - Realistic Failure Process Analysis Software. Dalian, CN.

[20] Deisman, Nathan, Mas Ivars, Diego, Darcel, Caroline, & Chalaturnyk, Richard J. 2010. Empirical and numerical approaches for geomechanical characterization of coal seam reservoirs. *International Journal of Coal Geology*, **82**(3-4), 204–212.

[21] Diederichs, M. S. 2000. *Instability of hard rock masses: the role of tensile damage and relaxation*. Ph.D. Thesis, University of Waterloo.

[22] Esmaieli, Kamran, Hadjigeorgiou, John, & Grenon, Martin. 2010. Estimating geometrical and mechanical REV based on synthetic rock mass models at Brunswick Mine. *International Journal of Rock Mechanics and Mining Sciences*, **47**(6), 915–926.

[23] Esterhuizen, E., Mark, C., & Murphy, M. 2010. The ground response curve, pillar loading and pillar failure in coal mines. *Pages 19–27 of: 29th International Conference on Ground Control in Mining*. Morgantown, WV: ICGCM.

[24] Fakhimi, A. 2004. Application of slightly overlapped circular particles assembly in numerical simulation of rocks with high friction angles. *Engineering Geology*, **74**(1-2), 129–138.

[25] Fakhimi, A., & Villegas, T. 2006. Application of Dimensional Analysis in Calibration of a Discrete Element Model for Rock Deformation and Fracture. *Rock Mechanics and Rock Engineering*, **40**(2), 193–211.

[26] Garvey, R. 2013. *Study of Unstable Failures Using Finite Difference and Discrete Element Methods*. Ph.D. Thesis, Colorado School of Mines.

[27] Garvey, R., & Ozbay, U. 2011. Computer aided calibration of PFC3D coal samples using a genetic algorithm. *Pages 493–499 of: 2nd International FLAC/DEM Symposium*. Melbourne, Australia: Itasca C.G.

[28] Gu, Ruixiang. 2013. *Distinct Element Model Analysis of Unstable Failures in Underground Coal Mines*. Ph.D. Thesis, Colorado School of Mines.

[29] Haramy, K. Y., Kneisley, R. O., & McDonnell, J. P. 1987. Longwall Face Bursts and Inadequate Caving: A Case Study. *In: Proceedings 6th International Conference on Ground Control in Mining*. Morgantown, WV: ICGCM.

[30] Haramy, K. Y., Kneisley, R. O., & Brady, B. T. 1988. Analysis Of Major Failure Through Integration Of Static And Dynamic Rock Mechanics Investigation - Document Summary. *Page 10 of: Proceedings 7th International Conference on Ground Control in Mining*. Morgantown, WV: ICGCM.

[31] Hazzard, James F., Young, R. Paul, & Maxwell, S. C. 2000. Micromechanical modeling of cracking and failure in brittle rocks. *Journal of Geophysical Research*, **105**(B7), 16683–16697.

[32] Heasley, K. A. 1998. *Numerical modeling of coal mines with a laminated displacement-discontinuity code*. Ph.D., Colorado School of Mines, Golden, CO.

[33] Holland, C.T. 1955. Rock Burst or Bumps in Coal Mines. *The Colliery Engineer*, Apr., 145–153.

[34] Hsieh, Y, Li, H, Huang, T, & Jeng, F. 2008. Interpretations on how the macroscopic mechanical behavior of sandstone affected by microscopic properties—Revealed by bonded-particle model. *Engineering Geology*, **99**(1-2), 1–10.

[35] Hudson, J, Crouch, S, & Fairhurst, C. 1972. Soft, stiff and servo-controlled testing machines: a review with reference to rock failure. *Engineering Geology*, **6**(3), 155–189.

[36] Hudson, J. A., Brown, E. T., & Fairhurst, C. 1971. Optimizing the control of rock failure in servo-controlled laboratory tests. *Rock Mechanics Felsmechanik Mecanique des Roches*, **3**(4), 217–224.

[37] Iannacchione, A. 1990. The effects of roof and floor interface slip on coal pillar behavior. *In: Rock Mechanics Contributions and Challenges*. A. A. Balkema, Rotterdam. Editors: Hustrulid and Johnson.

[38] Iannacchione, A., & DeMarco, M. J. 1992. Optimum mine designs to minimize coal bumps: A review of past and present U.S. practices. *Pages 235–247 of: New Technology in Mining Health and Safety*. Soc. Min. Eng.

[39] Iannacchione, A. T., & Tadolini, S. 2008. Coal mine burst prevention controls. *Pages 20–28 of: Proc. of the 27th International Conference on Ground Control in Mining*.

[40] Iannacchione, A. T., & Zelanko, J. C. 1995. Occurrence and remediation of coal mine bumps: A historical review. *Pages 27–67 of: Mechanics and Mitigation of Violent Failure in Coal and Hard-Rock Mines USBM Spec. Pub. 01-95*.

[41] Itasca Inc. 2008. FLAC2D - Fast Lagrangian Analysis of Continua in Two Dimensions. Version 6.0. Minneapolis, MN.

[42] Itasca Inc. 2009. FLAC3D - Fast Lagrangian Analysis of Continua in Three Dimensions. Version 4.0. Minneapolis, MN.

[43] Itasca Inc. 2010a. PFC2D - Particle Flow Code in Two Dimensions. Version 4.0. Minneapolis, MN.

[44] Itasca Inc. 2010b. PFC3D - Particle Flow Code in Three Dimensions. Version 4.0. Minneapolis, MN.

[45] Itasca Inc. 2013. UDEC - Universal Distinct Element Code. Minneapolis, MN.

[46] Jiang, Q., Feng, X., Xiang, T., & Su, G. 2010. Rockburst characteristics and numerical simulation based on a new energy index: a case study of a tunnel at 2,500 meters depth. *Bulletin of Engineering Geology and the Environment*, **69**(3), 381–388.

[47] Khair, A. Wahab. 1985. An analysis of coal bump liability in a bump prone mine. *International Journal of Mining Engineering*, **3**(4), 243–259.

[48] Kias, E. M. C., & Ozbay, U. 2013. Modeling unstable failure of coal pillars in underground mining using the discrete element method. *In: Proc. of the 45th U.S. Rock Mechanics/Geomechanics Symposium*. San Francisco, CA: Curran Associates, Inc.

[49] Kias, E. M. C., Gu, R., Garvey, R., & Ozbay, U. 2011. Modeling unstable rock failure during an uniaxial compressive strength test. *In: The 45th U.S. Rock Mechanics/Geomechanics Symposium*. SanFrancisco, CA: Curran Associates, Inc.

[50] Koehler, J. R., DeMarco, M. J., & Wuest, W. J. 1996. Critical pillar concept in yield-pillar-based longwall gate-road design. *Mining Engineering*, Aug., 73.

[51] Koyama, T, & Jing, L. 2007. Effects of model scale and particle size on micro-mechanical properties and failure processes of rocks—A particle mechanics approach. *Engineering Analysis with Boundary Elements*, **31**(5), 458–472.

[52] Kulatilake, P. 2001. Physical and particle flow modeling of jointed rock block behavior under uniaxial loading. *International Journal of Rock Mechanics and Mining Sciences*, **38**(5), 641–657.

[53] Larson, M. K., & Whyatt, J. K. 2009. Deep coal longwall panel design for strong strata: The influence of software choice on results. *Pages 75–87 of: Proceedings of the International Workshop of Numerical Modeling for Underground Mine Excavation Design*, vol. IC 9512. Pittsburg, PA: National Institute for Occupational Safety and Health.

[54] Linkov, A. 1996. Rockbursts and the instability of rock masses. *International Journal of Rock Mechanics and Mining Science & Geomechanics Abstracts*, **33**(7), 727–732.

[55] Mark, C. 1987. *Analysis of longwall pillar stability.* Ph.D., Pennsylvania State University, State College, PA.

[56] Mark, C., & Chase, F.E. Analysis of retreat mining pillar stability (ARMPS). *Pages 17–34 of: New Technology for Ground Control in Retreat Mining*, vol. 97-122, IC 9446. Pittsburg, PA: U.S. Department of Health and Human Services, Public Health Service, Centers for Disease Control and Prevention, National Institute for Occupantional Safety and Health, DHHS (NIOSH).

[57] Mark, Chris. 2009 (Jan.). Deep Cover Pillar Recovery in the US. *In: 28th International Conference on Ground Control in Mining (ICGCM).*

[58] Mas Ivars, Diego, Pierce, Matthew E., Darcel, Caroline, Reyes-Montes, Juan, Potyondy, David O., Paul Young, R., & Cundall, Peter A. 2011. The synthetic rock mass approach for jointed rock mass modelling. *International Journal of Rock Mechanics and Mining Sciences*, **48**(2), 219–244.

[59] Müller, W. 1991. Numerical simulation of rock bursts. *Mining Science and Technology*, **12**(1), 27–42.

[60] Oelfke, S. M., Mustoe, G. G. W., & Kripakov, N. P. 1996. Yielding gate pillar design with and elasto-plastic discrete element code. *In: 2nd North American Rock Mechanics Symposium.* Montreal, Quebec, Candada: A. A. Balkema.

[61] Ortlepp, W, & Stacey, T. 1994. Rockburst mechanisms in tunnels and shafts. *Tunnelling and Underground Space Technology*, **9**(1), 59–65.

[62] Ozbay, U. 2011. *Abutment Stress and Closure Around Tabular Excavations*. Advanced Rock Mechanics Lecture. Colorado School of Mines: Golden, CO.

[63] Peng, S. 1973. Time-dependent aspects of rock behavior as measured by a servocontrolled hydraulic testing machine. *International Journal of Rock Mechanics and Mining Sciences & Geomechanics Abstracts*, **10**(3), 235–246.

[64] Peng, Syd S. 1978. Bumps and Gas Outbursts. *Pages 343–364 of: Coal mine ground control*. New York: Wiley.

[65] Pierce, Matt, Cundall, Peter A., Potyondy, D., & Mas Ivars, D. 2007. A synthetic rock mass model for jointed rock. *Pages 341–349 of: Rock Mechanics: Meeting Society's Chanllenges and Demands*. Vancouver, Canada: Eberhardt, E., et al. (Ed.).

[66] Potyondy, D. 2007. Simulating stress corrosion with a bonded-particle model for rock. *International Journal of Rock Mechanics and Mining Sciences*, **44**(5), 677–691.

[67] Potyondy, D. 2011. Parallel-bond refinements to match macroproperties of hard rock. *In: Continuum and Distinct Element Numerical Modeling in Geomechanics*.

[68] Potyondy, D, & Cundall, P. 2004. A bonded-particle model for rock. *International Journal of Rock Mechanics and Mining Sciences*, **41**(8), 1329–1364.

[69] Potyondy, D. O. 2010. A grain based model for rock: approching the true microstructure. *In: Proceedings of Rock Mechanics in Nordic Countries*. Konigsberg, Norway: Norwegian Group for Rock Mechanics.

[70] Rice, G. S. 1935. *Bumps in coal mines of the cumberland field, Kentucky and Virginia - Causes and Remedy*. Tech. rept. USBM RI 3267.

[71] Rocscience Inc. 2013a. Examine2D - A Boundary Element Program. Toronto, Canada.

[72] Rocscience Inc. 2013b. Examine3D - A Boundary Element Program. Toronto, Canada.

[73] Rocscience Inc. 2013c. Phase2 - A Finite Element Program. Toronto, Canada.

[74] Rudajev, V., Teisseyre, R., Kozák, J., & Šílený, J. 1986. Possible mechanism of rockbursts in coal mines. *Pure and Applied Geophysics PAGEOPH*, **124**(4-5), 841–855.

[75] Saiang, David. 2009. Stability analysis of the blast-induced damage zone by continuum and coupled continuum–discontinuum methods. *Engineering Geology*, July.

[76] Salamon, M. 1970. Stability, instability and design of pillar workings. *International Journal of Rock Mechanics and Mining Science & Geomechanics Abstracts*, **7**(6), 613–631.

[77] Salamon, M. D. G. 1974. Rock mechanics of underground excavations. *Pages 951–1099 of: Proceedings of 3rd International Congress on Rock Mechanics*, vol. 1-B. Denver, CO: American Geophysical Union.

[78] Schopfer, M, Abe, S, Childs, C, & Walsh, J. 2009. The impact of porosity and crack density on the elasticity, strength and friction of cohesive granular materials: Insights from DEM modelling. *International Journal of Rock Mechanics and Mining Sciences*, **46**(2), 250–261.

[79] Starfield, A, & Cundall, P. 1988. Towards a methodology for rock mechanics modelling. *International Journal of Rock Mechanics and Mining Sciences & Geomechanics Abstracts*, **25**(3), 99–106.

[80] Stricklin, K. 2007. *Crandall Canyon Mine - Fatal Underground Burst Accident Report*. Tech. rept. CAI-2007-15-17, 19-24. U.S. Dept. of Labor Mine Safety and Health Administration.

[81] Tan, Yun-liang, Sun, Chun-jiang, & Zhang, Zhen-yu. 2009. 2D-ball simulations on stiffness influences for coal bump. *Journal of Coal Science and Engineering (China)*, **15**(2), 161–165.

[82] Tang, C. 1997. Numerical simulation of progressive rock failure and associated seismicity. *International Journal of Rock Mechanics and Mining Sciences*, **34**(2), 249–261.

[83] Tarasov, B.G. 2008. Intersonic shear rupture mechanism. *International Journal of Rock Mechanics and Mining Sciences*, **45**(6), 914–928.

[84] Van Heerden, W. L. 1975. In situ complete stress strain characteristics of lage coal specimens. *Journal of the South African Institute of Mining and Metalurgy*, **75**(8), 207–217.

[85] Wagner, H. 1974. Determination of the complete load-deformation characteristics of coal pillars. *Pages 1076–1080 of: Proceedings of 3rd International Congress on Rock Mechanics*. Denver, CO: American Geophysical Union.

[86] Wang, S. Y., Lam, K. C., Au, S. K., Tang, C. A., Zhu, W. C., & Yang, T. H. 2005. Analytical and Numerical Study on the Pillar Rockbursts Mechanism. *Rock Mechanics and Rock Engineering*, **39**(5), 445–467.

[87] Wang, Y., & Tonon, F. 2010. Calibration of a discrete element model for intact rock up to its peak strength. *International Journal for Numerical and Analytical Methods in Geomechanics*, **34**(5), 447–469.

[88] Wawersik, W, & Fairhurst, C. 1970. A study of brittle rock fracture in laboratory compression experiments. *International Journal of Rock Mechanics and Mining Sciences & Geomechanics Abstracts*, **7**(5), 561–575.

[89] Wawersik, W. R., & Brace, W. F. 1971. Post-failure behavior of a granite and diabase. *Rock Mechanics Felsmechanik Mecanique des Roches*, **3**(2), 61–85.

[90] Whyatt, J. K., Blake, W., Williams, T., & White, B. 2002. Sixty Years Of Rock Bursting In The Coeur d'Alene District Of Northern Idaho: Lessons Learned And Remaining Issues. *In: SME Transactions*, vol. 312.

[91] Yoon, J. 2007. Application of experimental design and optimization to PFC model calibration in uniaxial compression simulation. *International Journal of Rock Mechanics and Mining Sciences*, **44**(6), 871–889.

[92] Zipf, R.K. 1992. *MULSIM/NL: application and practitioner's manual.* Tech. rept. IC 9322. U.S. Dept. of the Interior, U.S. Bureau of Mines, Pittsburg, PA. NTIS No. PB93-131993.

[93] Zipf, R.K. 1996. Analysis and design methods to control cascading pillar failure in room and pillar mines. *Pages 225–264 of: Milesones In Rock Engineering.* Balkema. Ed. Bieniawski, Z.T.

[94] Zipf, R.K., & Heasley, K. A. 1990. Decreasing coal bump risk through optimal cut sequencing with a non-linear boundary element program. *In: U.S. Symposium on Rock Mechanics.* Golden, CO: A. A. Balkema, Rotterdam - ARMA.

[95] Zubelewicz, A., & Mroz, Z. 1983. Numerical simulation of rock burst processes treated as problems of dynamic instability. *Rock Mechanics and Rock Engineering*, **16**(4), 253–274.

APPENDIX A - EPC FISH CODES

Listing A.1: Custom spanning chain functions

```
; filename: ch_p.fis  author: E.Kias
;
; These functions facilitate spanning chain logic for biaxial
; tests on a pfc2d specimen generated using pbricks
;
; ==========================================================================
def def_arrs
        array b_vec(2)
end
def_arrs

def find_s0
  first_ball = ball_near2(fbpx,fbpy)
  last_ball = ball_near2(0.0,0.0)   ; dummy, algorithm will not find
     this
end

def fill_b1
        plot_item
        bp = ball_near2(fbpx,fbpy)
        b_vec(1) = b_x(bp)
        b_vec(2) = b_y(bp)
        stat = fill_circle(b_vec,0.7*b_rad(bp))
end
; --------------------------------------------------------------------------
def cs_getc0_p
;
; ------ Return the starting contact for traversal.
;
; INPUT: cs_s0
;
;
; OUTPUT: cs_getc0_biax - contact of [cs_s0] that has {y-coord above,
;                       cs_s0 centroid and smallest x-coord}
;                       and does not have c_extra(cp,1)=100
;
  c_xmin = 1000
  cp = b_clist( ch_s0 )
  loop while cp # null
```

```
    if c_y(cp) > b_y(ch_s0) then
                if c_x(cp) < c_xmin then
                        c_xmin = c_x(cp)
                        cs_getc0_p = cp
                        cx_c0 = c_x(cp)
                        cy_c0 = c_y(cp)
                endif
        endif
        if c_ball1(cp) = ch_s0 then
                cp = c_b1clist(cp)
        else
                cp = c_b2clist(cp)
        endif
  end_loop
  dd = out(string(cx_c0))
  dd = out(string(cy_c0))
end
; ------------------------------------------------------------------
def cs_spanchain_p
;
; ----- Form the requested spanning chain.  Return value indicates
   success.
;       Clear all marked contacts upon exit.
;
; INPUT: ch_num, ch_s0, ch_s1, ch_cw, cs_sort
;
   cs_clear
   ch_c0 = cs_getc0_p
   if ch_c0 = null then
     cs_clearmarks
     cs_spanchain = 0
     exit
   end_if
  loop while ch_walk = 0
    ;command
;               pause
        ;end_command
    c_extra(ch_c0,1) = 100
    ch_c0 = cs_getc0_p
    if ch_c0 = null then
      cs_clearmarks
      cs_spanchain = 0
      exit
    end_if
    cs_clear
  end_loop
  cs_clearmarks
```

```
   cs_spanchain = 1
   cs_pressapply   ; {i: ch_num}
end
; ============================================================================
;EOF ch_p.fis
RETURN
```

Listing A.2: Driver file for TCS tests

```
; fname: sW_mL_tA-tw_ch.dvr  original fname:sW_mL_tA-tw.dvr
; edited by: EKias
; taken from: %fist%\templates\gen-2d, PFC2D
;
;Editor Notes: This file performs confined compression tests using the
;              spanning chain functions in
;              - %fist%\2d\ch.fis
;              - %fistp%\2d\ch_p.fis ~ A custom Fishtank
;
```

```
SET logfile sW_mL_tA-tw_ch.log
SET log on
; ******************************************
restore filepath\filename-bv.sav ;BPM or DSM assembly
CALL %fist%\2d\ch.fis
CALL %fist_p%\2d\ch_p.fis
;
ch_init
;
SET fbpx = -0.7  ;Coordinates of first ball in spanning chain, vary if
SET fbpy = 0.13  ;unsuccessful in completing chain.
find_s0
;
; DEFINE the pressure in Pascals below, ex. 2e6
SET ch_press= !!DEFINE!! ch_num=1 ch_s0=first_ball ch_s1=last_ball
   ch_cw=1
;
cs_spanchain_p
;
; Comment out the following 10 lines for BPM
MODEL udm_softening
PROPERTY sof_broken=0 &
          sof_fric=1.75 &
          sof_fsmax=0.65e4 &
          sof_ftmax=0.65e4 &
          sof_knc=6e9 &
          sof_knt=6e9 &
          sof_ks=2.0e9  &  ;k_rat = 1.75
          sof_rfric=0.5 &
          sof_uplim=0.007  ;md_ravg ~ .006
;
 SET dt dscale
;SET safe_conversion on
 SET md_run_name='sW_mL_tAtt_ch'
```

```
 title 'sW_mL_tAtt_ch'
 CALL tAtt-param.dat
 CALL %fist%\2d\_tt1.dvr
  SET avi_Ns=50 avi_S=40e-3
 CALL %fist%\2d\_tt2_avi.dvr
;
    ================================================================================

SET log off
return
;EOF: sW_mL_tA-tw_ch.dvr
```

Listing A.3: Front end file for FLAC2D EPC tests

```
; filename: cm_flac_CMUCS.dvr    author: EKias
;
;  This file specifies elastic modulus and calls
;  the general driver for EPC tests.
;
; ------------------------------------------------------------------
def flac_model_init_UCS
 ; ***************************************
 ;  Specify FLAC Geometry:
 ;
 flac_geom = 1 ; UCS grid
 ; ---------------------------------------
 ; ***************************************
 ;  Specify FLAC Elastic Modulus
 ;
 ; flac_emod = 1 ; - 5 GPa Elastic Modulus
 ; flac_emod = 2 ; - 35 GPa Elastic Modulus
 ; flac_emod = 3 ; - 50 GPa Elastic Modulus
 ; flac_emod = 4 ; - 150 GPa Elastic Modulus
 ; flac_emod = 5 ; - 250 GPa Elastic Modulus
 ; flac_emod = 6 ; - 500 GPa Elastic Modulus
 ; flac_emod = 7 ; - 750 GPa Elastic Modulus
 ; flac_emod = 8 ; - 1000 GPa Elastic Modulus
 ; flac_emod = 9 ; - 1 GPa Elastic Modulus
 flac_emod = 10 ; - 1.5 GPa Elastic Modulus
 ; ***************************************
 ;  Specify pillar geometry
 ;
 pillar_geom = 0 ; w/h = 1/2 pillar
 ; ***************************************
 end
 flac_model_init_UCS
 ;
 call FLAC_CMUCS_general.dvr
 ; ------------------------------------------------------------------
 ; eof. cm_flac_CMUCS.dvr
```

Listing A.4: General driver file for FLAC2D EPC tests

```
; fname: FLAC_EPC_general.dvr  author: EKias
;
; General EPC test driver file
;
;
   ==========================================================================

 CONFIG extra 1  ; for gp-mass multipliers
;
 SET echo off
 CALL CallMe_FLAC_EPC.dat
 SET echo on
; ------------------------------------------------------
SET_mdfrunname
        title 'mdf_run name'
SET log on
; ***********************************************
; Initialize Coupling, Generate Grid, set BCs
        cpf_init_p
SET load_vel = 5.85e-8
        cpf_fixbdry
; ------------------------------------------------------
; Define material properties
        cpf_matprops
; ***********************************************
; Cycle/Equilibrate to initialize the model
   cpf_cyc
; Stray element deletion in PFC, here.
   cpf_cyc
;
; Apply Loading Velocity
        cpf_apply_vels
;
; Zero displacments
INI xdis 0.0 ydis 0.0
;
; Save initialized state
SET mdf_tag_name = '-pre'
        mdf_save_state
;
; ------------------------------------------------------
; Call functions to calculate coal layer strain, roof/floor disps/
   stress, etc.
SET echo off
CALL filepath\FLAC_mfuncs_EPC.dat
```

```
SET echo on
;
; Cycle the model to completion
        cpf_cyc
;
; Save the final model state
SET mdf_tag_name = '-post'
        mdf_save_state
;
```

```
SET log off
RETURN
;EOF: FLAC_EPC_general.dvr
```

Listing A.5: Function definition call file

```
;fname: CallMe_FLAC_CMUCS.dat   author: EKias
;
;  This file loads the functions necessary for the EPC test
;
;
   ================================================================================

CALL filepath\app.fin
CALL filepath\cplib.fis
CALL filepath\cpflib_CMUCS.fis
CALL cpf_FLAC_CMUCS.fis
;
   ================================================================================

RETURN
;EOF: CallMe_FLAC_CMUCS.dat
```

Listing A.6: Custom Fishtank file for FLAC2D EPC

```
;fname: cpflib_CMUCS.fis  author: EKias
;
; Private functions for coupled PFC2D-FLAC analysis, FLAC file.
;
;
   ==========================================================================

def cpf_init_p
;
; ----- Initialize the coupling scheme (for FLAC) which involves:
;         (1) establishing socket-based connection between FLAC & PFC2D
   ;
;         (2) creating the FLAC grid, and establishing a coupling bdry
   in
;             the form of a segment list in which each segment is the
   edge
;             of a FLAC zone (these zones are in group 'cplBdry');
;         (3) transfer segment geometry to PFC2D, and
;         (4) install coupling FISHCALLs.
;
; INPUT: cpf_gpmm       - gp-mass multiplier for GPs along cpl-bdry
;       <cpf_makegrid> - create FLAC grid
;       <_slf_putlist> - send segment-list info. to PFC2D
;
; EFFECT: Create group 'cplBdry' (boundary zones, some may be null)
;
  if cpf_gpmm = 0 then
    cpf_gpmm = 2.0
  end_if
  ;
  oo=out('*** Initializing the coupling scheme.')
  cpf_open
  ;
    cp_bufn = 2        ; dimensions of right-rectangular PFC2D inclusion
   cp_read
   cpf_ix = cp_buf(1)
   cpf_iy = cp_buf(2)

   caseof flac_geom
        case 1
                seam_height = 2
                command
                        call CM_UCS_grid.dat
                end_command
   endcase
```

```
    cp_bufn = 3
    cp_buf(1) = cpf_nseg
    cp_buf(2) = cpf_yoff
    cp_buf(3) = cpf_rad
   cp_write
   ;
 command
    SET nexgpm 1 ; hidden functionality: multiply gp-masses by ex_1(i,j
        ).
                 ;   If ex_1(i,j) <= 0, then multiply by one.
                 ;   We will set ex_1(i,j)=cpf_gpmm along FLAC-PFC2D
                     bdry.
  end_command
  ;
  _slf_init
   _slf_putwhat = 4  ; identify boundary zones
  _slf_putlist
   _slf_putwhat = 0  ; coords.
  _slf_putlist
   _slf_putwhat = 2  ; create apply list
  _slf_putlist
   _slf_putwhat = 3  ; increase gp-masses along FLAC-PFC2D boundary
  _slf_putlist
  ;
 command
   SET fishcall 15 cpf_putvel_getfor
;   SET large  ; If running in large-strain mode, then also remap
               ; the segment list --- see [cpf_remap, cpp_remap]
  end_command
  oo=out('*** Coupling scheme successfully initialized.')
end
;
```

```
RETURN
;EOF: cpflib_CMUCS.fis
```

Listing A.7: FLAC EPC custom functons file

```
; fname: cpf_CMUCS.fis   author: EKIAS
;
; Coupled PFC2D-FLAC analysis, FLAC file. Model-specific functions,
   thus, not in cpflib.fis.
; The functions <cpf_makegrid> and <_slf_putlist> must be replaced
; when creating a new grid-inclusion system.
;
;
   ================================================================

def set_mdfrunname
                tag1 = string(flac_geom)
                tag2 = string(pillar_geom)
                tag3 = '.log'
                rname = 'FLAC_CM_geom' + tag1 + '_' +tag2 + 'x1'
                logname = 'FLAC_CM_geom' + tag1 + '_' +tag2 + 'x1' +
                   tag3
                command
                        SET mdf_run_name = rname
                        SET log @logname
                end_command
end
;
   ----------------------------------------------------------------

def _slf_putlist
;
; ------ Send segment list information to PFC2D, traverse in ccw order.
;       TODO: Improve efficiency by using buffered I/O.
;
; INPUT:   _sbf_{i,j}{2,3}
;          _slf_putwhat - {0,1,2,3} = {coords,
;                                      velocities,
;                                      create apply list,
;                                      increase gp-masses along bdry}
; OUTPUT: _slf_apf{0,1} - iff _slf_putwhat = 2
;
  _nseg = 0
       _i0 = 17
       _i1 = 16
       _j0 = 1
       _j1 = 1
      _slf_putseg  ;{i: _{i,j}{0,1}}
           _i0 = 16
       _i1 = 15
```

```
 _j0 = 1
 _j1 = 1
_slf_putseg  ;{i: _{i,j}{0,1}}
     _i0 = 15
 _i1 = 14
 _j0 = 1
 _j1 = 1
_slf_putseg  ;{i: _{i,j}{0,1}}
     _i0 = 14
 _i1 = 13
 _j0 = 1
 _j1 = 1
_slf_putseg  ;{i: _{i,j}{0,1}}
     _i0 = 13
 _i1 = 12
 _j0 = 1
 _j1 = 1
_slf_putseg  ;{i: _{i,j}{0,1}}
     _i0 = 12
 _i1 = 11
 _j0 = 1
 _j1 = 1
_slf_putseg  ;{i: _{i,j}{0,1}}
     _i0 = 11
 _i1 = 10
 _j0 = 1
 _j1 = 1
_slf_putseg  ;{i: _{i,j}{0,1}}
     _i0 = 10
 _i1 = 9
 _j0 = 1
 _j1 = 1
_slf_putseg  ;{i: _{i,j}{0,1}}
     _i0 = 9
 _i1 = 8
 _j0 = 1
 _j1 = 1
_slf_putseg  ;{i: _{i,j}{0,1}}
     _i0 = 8
 _i1 = 7
 _j0 = 1
 _j1 = 1
_slf_putseg  ;{i: _{i,j}{0,1}}
     _i0 = 7
 _i1 = 6
 _j0 = 1
 _j1 = 1
```

```
_slf_putseg  ;{i: _{i,j}{0,1}}
     _i0 = 6
 _i1 = 5
 _j0 = 1
 _j1 = 1
_slf_putseg  ;{i: _{i,j}{0,1}}
     _i0 = 5
 _i1 = 4
 _j0 = 1
 _j1 = 1
_slf_putseg  ;{i: _{i,j}{0,1}}
     _i0 = 4
 _i1 = 3
 _j0 = 1
 _j1 = 1
_slf_putseg  ;{i: _{i,j}{0,1}}
     _i0 = 3
 _i1 = 2
 _j0 = 1
 _j1 = 1
_slf_putseg  ;{i: _{i,j}{0,1}}
     _i0 = 2
 _i1 = 1
 _j0 = 1
 _j1 = 1
_slf_putseg  ;{i: _{i,j}{0,1}}
     _i0 = 1
 _i1 = 2
 _j0 = 34
 _j1 = 34
_slf_putseg  ;{i: _{i,j}{0,1}}
     _i0 = 2
 _i1 = 3
 _j0 = 34
 _j1 = 34
_slf_putseg  ;{i: _{i,j}{0,1}}
     _i0 = 3
 _i1 = 4
 _j0 = 34
 _j1 = 34
_slf_putseg  ;{i: _{i,j}{0,1}}
     _i0 = 4
 _i1 = 5
 _j0 = 34
 _j1 = 34
_slf_putseg  ;{i: _{i,j}{0,1}}
     _i0 = 5
```

```
 _i1 = 6
 _j0 = 34
 _j1 = 34
_slf_putseg  ;{i: _{i,j}{0,1}}
     _i0 = 6
 _i1 = 7
 _j0 = 34
 _j1 = 34
_slf_putseg  ;{i: _{i,j}{0,1}}
     _i0 = 7
 _i1 = 8
 _j0 = 34
 _j1 = 34
_slf_putseg  ;{i: _{i,j}{0,1}}
     _i0 = 8
 _i1 = 9
 _j0 = 34
 _j1 = 34
_slf_putseg  ;{i: _{i,j}{0,1}}
     _i0 = 9
 _i1 = 10
 _j0 = 34
 _j1 = 34
_slf_putseg  ;{i: _{i,j}{0,1}}
     _i0 = 10
 _i1 = 11
 _j0 = 34
 _j1 = 34
_slf_putseg  ;{i: _{i,j}{0,1}}
     _i0 = 11
 _i1 = 12
 _j0 = 34
 _j1 = 34
_slf_putseg  ;{i: _{i,j}{0,1}}
     _i0 = 12
 _i1 = 13
 _j0 = 34
 _j1 = 34
_slf_putseg  ;{i: _{i,j}{0,1}}
     _i0 = 13
 _i1 = 14
 _j0 = 34
 _j1 = 34
_slf_putseg  ;{i: _{i,j}{0,1}}
     _i0 = 14
 _i1 = 15
 _j0 = 34
```

```
        _j1 = 34
       _slf_putseg  ;{i: _{i,j}{0,1}}
            _i0 = 15
        _i1 = 16
        _j0 = 34
        _j1 = 34
       _slf_putseg  ;{i: _{i,j}{0,1}}
            _i0 = 16
        _i1 = 17
        _j0 = 34
        _j1 = 34
       _slf_putseg  ;{i: _{i,j}{0,1}}
end
; ------------------------------------------
def cpf_fixbdry
;
        load_vel_down = load_vel*(-1)
        command
                ;left boundary
                FIX x i=1
                ;right boundary
                FIX x i=17
                ;bottom boundary
                FIX y j 18
                FIX x j 18
                ;top boundary
                FIX y j 17
        end_command
end
; ------------------------------------------
def cpf_apply_vels
        command
                ; apply bottom gp velocities
                APPLY yvel load_vel j 18
                ;
                ; apply top gp velocities
                APPLY yvel load_vel_down j 17
        end_command
end
; ------------------------------------------
def cpf_matprops
;
; INPUT: cpf_emod, cpf_nu - modulus and Poisson's ratio of FLAC grid
;        cpf_dens         - density of FLAC grid
;
;  Elastic model property calcs and property definition
   cpf_dens = 2600 ; cpf_dens
```

```
    caseof flac_emod
    ;cpf_emod / (3.0*(1.0-2.0*cpf_nu))
    ;cpf_emod / (2.0*(1.0+cpf_nu))
          case 1
                _fbulk = 3.333e9    ;|5 GPa .25 nu
                _fshear = 2.0e9     ;|
          case 2
                _fbulk = 23.33e9    ;|35 GPa .25 nu
                _fshear = 14.00e9   ;|
          case 3
                _fbulk  = 33.33e9    ;|50 GPa .25 nu
                _fshear = 20.00e9    ;|
          case 4
                _fbulk = 100.00e9    ;|150 GPa .25 nu
                _fshear = 60.00e9    ;|
          case 5
                _fbulk = 166.66e9    ;|250 GPa .25 nu
                _fshear = 100.00e9   ;|
          case 6
                _fbulk = 333.33e9    ;|500 GPa .25 nu
                _fshear = 200.00e9   ;|
          case 7
                _fbulk = 500.00e9    ;|750 GPa .25 nu
                _fshear = 300.00e9   ;|
          case 8
                _fbulk = 666.66e9    ;|1000 GPa .25 nu
                _fshear = 400.00e9   ;|
          case 9
                _fbulk = 0.666e9     ;|1.0 GPa .25 nu
                _fshear = 0.4e9   ;|
          case 10
                _fbulk = 1.0e9     ;|1.5 GPa .25 nu
                _fshear = 0.6e9   ;|
    endcase
    ;
  command
        PROP dens=cpf_dens bulk=_fbulk shear=_fshear notnull
  end_command
end
;
```

```
return
;EOF: cpf_CMUCS.fis
```

Listing A.8: FLAC2D EPC grid generation file

```
; filename: CMUCS_grid.dat  author: EKias
;
; Create FLAC2D grid for EPC test
;
; ------------------------------------------------------------
SET cpf_nseg = 32 ; number of segments
GRID 16 33
;
MOD elas i 1 16 j 1 17
MOD null j 17
MOD elas i 1 16 j 18 33
;
; Top and bottom fine grids
GEN 4.5,2.0 4.5,3.0 5.5,3.0 5.5,2.0 i=1,17 j=1,17
;
GEN 4.5,-1.0 4.5,0.0 5.5,0.0 5.5,-1.0 i=1,17 j=18,34
; ------------------------------------------------------------
; eof CMUCS_grid.dat
RETURN
```

Listing A.9: fLAC EPC measurement functions and histories

```
; filename FLAC_functions_CMUCS.dat  author: EKias
;
; Measurement functions for the EPC test
;
; ------------------------------------------------------------------
def get_Los
        array r_Yo(17,1)
        array f_Yo(17,1)
        array Lo_coal(17,1)
        array L_coal(17,1)
        array e_coal(17,1)
        loop iz(1,17)
                r_Yo(iz,1) = y(iz,1) + ydisp(iz,1)
                f_Yo(iz,1) = y(iz,34) + ydisp(iz,34)
                Lo_coal(iz,1) = r_Yo(iz,1) - f_Yo(iz,1)
        end_loop
end
get_Los

def flac_hist_function
        ; Roof and Floor dL accounting for loading velocity
                ;
                        Top_yd = ydisp(1,17)
                        Bottom_yd = ydisp(1,18)
                ;
        rdL_1 = ydisp(1,1) - Top_yd ; compression is positive
        rdL_2 = ydisp(2,1) - Top_yd
        rdL_3 = ydisp(3,1) - Top_yd
        rdL_4 = ydisp(4,1) - Top_yd
        rdL_5 = ydisp(5,1) - Top_yd
        rdL_6 = ydisp(6,1) - Top_yd
        rdL_7 = ydisp(7,1) - Top_yd
        rdL_8 = ydisp(8,1) - Top_yd
        rdL_9 = ydisp(9,1) - Top_yd
        rdL_10 = ydisp(10,1) - Top_yd
        rdL_11 = ydisp(11,1) - Top_yd
        rdL_12 = ydisp(12,1) - Top_yd
        rdL_13 = ydisp(13,1) - Top_yd
        rdL_14 = ydisp(14,1) - Top_yd
        rdL_15 = ydisp(15,1) - Top_yd
        rdL_16 = ydisp(16,1) - Top_yd
        rdL_17 = ydisp(17,1) - Top_yd
        ;
        fdL_1 = Bottom_yd - ydisp(1,34)
        fdL_2 = Bottom_yd - ydisp(2,34)
```

```
fdL_3 = Bottom_yd - ydisp(3,34)
fdL_4 = Bottom_yd - ydisp(4,34)
fdL_5 = Bottom_yd - ydisp(5,34)
fdL_6 = Bottom_yd - ydisp(6,34)
fdL_7 = Bottom_yd - ydisp(7,34)
fdL_8 = Bottom_yd - ydisp(8,34)
fdL_9 = Bottom_yd - ydisp(9,34)
fdL_10 = Bottom_yd - ydisp(10,34)
fdL_11 = Bottom_yd - ydisp(11,34)
fdL_12 = Bottom_yd - ydisp(12,34)
fdL_13 = Bottom_yd - ydisp(13,34)
fdL_14 = Bottom_yd - ydisp(14,34)
fdL_15 = Bottom_yd - ydisp(15,34)
fdL_16 = Bottom_yd - ydisp(16,34)
fdL_17 = Bottom_yd - ydisp(17,34)
;
; Height of the coal layer including single zone interface
   layer
sum_c = 0.0
loop iz(1,17)
        L_coal(iz,1) = Lo_coal(iz,1) - ydisp(iz,34) + ydisp(iz
           ,1)
        sum_L_coal = sum_c + L_coal(iz,1)
end_loop
        avg_L_coal = sum_L_coal/17
;
;  Coal layer strain
loop iz(1,17)
        e_coal(iz,1) = (Lo_coal(iz,1)-L_coal(iz,1))/Lo_coal(iz
           ,1)
end_loop
;
e_1 = e_coal(1,1)
e_2 = e_coal(2,1)
e_3 = e_coal(3,1)
e_4 = e_coal(4,1)
e_5 = e_coal(5,1)
e_6 = e_coal(6,1)
e_7 = e_coal(7,1)
e_8 = e_coal(8,1)
e_9 = e_coal(9,1)
e_10 = e_coal(10,1)
e_11 = e_coal(11,1)
e_12 = e_coal(12,1)
e_13 = e_coal(13,1)
e_14 = e_coal(14,1)
e_15 = e_coal(15,1)
```

```
        e_16 = e_coal(16,1)
        e_17 = e_coal(17,1)
        ;
end

HISTORY 100 nstep = 50 flac_hist_function
HISTORY 301 syy i=1 j=2
HISTORY 302 syy i=2 j=2
HISTORY 303 syy i=3 j=2
HISTORY 304 syy i=4 j=2
HISTORY 305 syy i=5 j=2
HISTORY 306 syy i=6 j=2
HISTORY 307 syy i=7 j=2
HISTORY 308 syy i=8 j=2
HISTORY 309 syy i=9 j=2
HISTORY 310 syy i=10 j=2
HISTORY 311 syy i=11 j=2
HISTORY 312 syy i=12 j=2
HISTORY 313 syy i=13 j=2
HISTORY 314 syy i=14 j=2
HISTORY 315 syy i=15 j=2
HISTORY 316 syy i=16 j=2
;
HISTORY 501 syy i=1 j=32
HISTORY 502 syy i=2 j=32
HISTORY 503 syy i=3 j=32
HISTORY 504 syy i=4 j=32
HISTORY 505 syy i=5 j=32
HISTORY 506 syy i=6 j=32
HISTORY 507 syy i=7 j=32
HISTORY 508 syy i=8 j=32
HISTORY 509 syy i=9 j=32
HISTORY 510 syy i=10 j=32
HISTORY 511 syy i=11 j=32
HISTORY 512 syy i=12 j=32
HISTORY 513 syy i=13 j=32
HISTORY 514 syy i=14 j=32
HISTORY 515 syy i=15 j=32
HISTORY 516 syy i=16 j=32
;
HISTORY 701 rdL_1
HISTORY 702 rdL_2
HISTORY 703 rdL_3
HISTORY 704 rdL_4
HISTORY 705 rdL_5
HISTORY 706 rdL_6
HISTORY 707 rdL_7
```

```
HISTORY 708 rdL_8
HISTORY 709 rdL_9
HISTORY 710 rdL_10
HISTORY 711 rdL_11
HISTORY 712 rdL_12
HISTORY 713 rdL_13
HISTORY 714 rdL_14
HISTORY 715 rdL_15
HISTORY 716 rdL_16
HISTORY 717 rdL_17
;
HISTORY 901 fdL_1
HISTORY 902 fdL_2
HISTORY 903 fdL_3
HISTORY 904 fdL_4
HISTORY 905 fdL_5
HISTORY 906 fdL_6
HISTORY 907 fdL_7
HISTORY 908 fdL_8
HISTORY 909 fdL_9
HISTORY 910 fdL_10
HISTORY 911 fdL_11
HISTORY 912 fdL_12
HISTORY 913 fdL_13
HISTORY 914 fdL_14
HISTORY 915 fdL_15
HISTORY 916 fdL_16
HISTORY 917 fdL_17
;
HISTORY 1101 e_1
HISTORY 1102 e_2
HISTORY 1103 e_3
HISTORY 1104 e_4
HISTORY 1105 e_5
HISTORY 1106 e_6
HISTORY 1107 e_7
HISTORY 1108 e_8
HISTORY 1109 e_9
HISTORY 1110 e_10
HISTORY 1111 e_11
HISTORY 1112 e_12
HISTORY 1113 e_13
HISTORY 1114 e_14
HISTORY 1115 e_15
HISTORY 1116 e_16
HISTORY 1117 e_17
;
```

```
HISTORY 2001 avg_L_coal
;
def get_cb_vels
        vy_1t = yvel(4,1)
        vy_2t = yvel(8,1)
        vy_3t = yvel(12,1)
        ;
        vy_1b = yvel(4,34)
        vy_2b = yvel(8,34)
        vy_3b = yvel(12,34)
        ;
        vy_avgt = (vy_1t+vy_2t+vy_3t)/3
        vy_avgb = (vy_1b+vy_2b+vy_3b)/3
end

HISTORY get_cb_vels nstep = 50
HISTORY vy_avgt nstep = 50
HISTORY vy_avgb nstep = 50
; ------------------------------------------------------------------------
; eof FLAC_mfuncs_CMUCS.dat
```

Listing A.10: Front end file for PFC2D EPC

```
; cm_pfc_EPC.dvr    author: EKias
;
;  This file specifies elastic modulus and calls
;  the general PFC2D driver for EPC tests.
;
; ------------------------------------------------------------------
; Restore PFC2D specimen
;
RESTORE filepath\filename-bv.sav
;
; Uncomment the following 10 lines for DSM
;MODEL udm_softening
;PROPERTY sof_broken=0 &
;         sof_fric=1.75 &
;         sof_fsmax=0.65e4 &
;         sof_ftmax=0.65e4 &
;         sof_knc=6e9 &
;         sof_knt=6e9 &
;         sof_ks=2.0e9  &  ;k_rat = 1.75
;         sof_rfric=0.5 &
;         sof_uplim=0.007  ;md_ravg ~ .006
; ------------------------------------------------------------------
def pfc_model_init
 ; ***************************************
 ;  Specify pillar geometry
 ;
       pillar_geom = 0 ; w/h = 1/2 pillar
 ; ***************************************
 ; Specify number of steps
 numsteps = ???? ; try 150000 steps
 end
 pfc_model_init
 ;
 CALL PFC_EPC_general.dvr
 ; ------------------------------------------------------------------
 ; eof. cm_pfc_EPC.dvr
 RETURN
```

Listing A.11: General driver file for PFC2D EPC

```
;fname: PFC_EPC_general.dvr  author: EKias
;
; General EPC test driver file
;
;
   ==========================================================================

def set_mdrunname
        tag1 = '.log'
        rname = 'PFC_EPC'
        logname = rname + tag1
        command
                SET md_run_name = rname
                SET logfile logname
        end_command
end
        set_mdrunname
TITLE 'md_run name'
SET log on
; ********************************************
;
SET echo off
 CALL %fist%\2d\cpl\cplib.fis
 CALL %fist_emck%\2D\CM\cpplib_EPC.fis
 CALL %fist%\2d_3d\crk.fis
SET echo on
CALL %fist_emck%\2D\CM\CM_functions_PFC_EPC.fis
;
SET cp_chan=0 ; make non-zero for each simultaneous coupled run
        cpp_init_CMUCS
SET md_tag_name = '-ini0'
        md_save_state
; ********************************************
;
DAMP local 0.95
SET cpp_cycnum= 1000
        cpp_cyc
SET cpp_cycend= 1
        cpp_cyc
;
; Delete stray balls that may have escaped during si process.
SET mv_W = 1.0
SET mv_H = 2.0
        del_strays
;
```

```
DAMP local 0.7
SET cpp_cycnum= 1000
        cpp_cyc
SET cpp_cycend= 1
        cpp_cyc
; ------------------------------------------------------------------
;
SET md_tag_name = '-pre'
md_save_state
;
CALL %fist_emck%\2d\pfc_mfuncs_EPC.fis
;
; Start crack tracking, uncomment next line for BPM
;  crk_init
;
cpp_cyc
SET cpp_cycend= 1
cpp_cyc
;
SET md_tag_name = '-post'
md_save_state
;
   ==================================================================

set log off
return
;EOF: PFC_EPC_general.dvr
```

Listing A.12: Custom Fishtank file for PFC2D EPC

```
; fname: cpplib_EPC.fis  author: EKias
;
; Private functions for coupled PFC2D-FLAC analysis, FLAC file.
; Naming convention: [cpp_] = CouPled Pfc LIBrary
;
;
;=============================================================================

def cpp_init_EPC
;
; ----- Initialize the coupling scheme (for PFC2D) which involves:
;         (1) establishing socket-based connection between FLAC & PFC2D
   ;
;         (2) sending PFC2D inclusion dimensions to FLAC;
;         (3) establish PFC2D-side data structures for the segment list
   ,
;             the geometry of which is received from FLAC (See [
   cpf_init]
;             for description of the segment list and associated data
;             structures.);
;         (4) create controlled-ball list; and
;         (5) install coupling FISHCALLs.
;
; INPUT: cpp_putfor_approx - boolean, if =1, use simpler approximate
   scheme
;                                          to interpolate ball forces
    to
;                                          segment forces
;
; The if statement below is commented because 'set dt dscale' is issued
    below, no changes to the
; coupling algorithm have been made.
  ; if tdel # 1.0 then
    ; error = 'PFC2D timestep must be unity, but it is '+string(tdel)
       +'.'
  ; end_if
  ;
  oo=out('*** Initializing the coupling scheme.')
  cpp_open
  ;
  ; --- Compute and send null-zone region dimensions to FLAC.
  ;     This region is offset inwards by average ball radius from the
  ;     walls of the material vessel.
    md_radii ; {o: md_ravg}
   cp_buf(1) = mv_W - 2.0*md_ravg  ; rectangle width
```

```
    cp_buf(2) = mv_H - 2.0*md_ravg   ; rectangle height
    cp_bufn = 2
  cp_write
  ;
    cp_bufn = 3
  cp_read
  cpp_nseg = cp_buf(1)
  cpp_yoff = cp_buf(2)
  cpp_rad  = cp_buf(3)
  cpp_nseg0 = cpp_nseg
  ;
 ; _cpp_excavate
  _slp_init_EPC
    _slp_getwhat = 0   ; coords
  _slp_getlist
  cbi_init
  ;
  command
    SET dt dscale   ; Assumes that FLAC is running in static-mode (
       default).
                    ; By making PFC2D also run in static-mode, we insure
                    ; that the displacements during one step in each
                       code
                    ; will be the same.  Static-mode means timestep of
                       unity,
                    ; so velocities have units of [meters/step].
    SET fishcall             0 cpp_getvel
    SET fishcall             3 cpp_putfor
    SET fishcall #FC_BALL_DEL cpp_delball
    SET fishcall #FC_NEW_QUIT cpp_delballremove
  end_command
  ;
  cpp_coupled_view
  oo=out('*** Coupling scheme successfully initialized.')
end
; ---------------------------------------
def cpp_cyc_calm
;
; ----- Controls synchronous cycling between PFC2D and FLAC.  PFC2D is
    the
;       controlling process such that when FLAC is in slave-mode, calls
     to
;       [cpp_cyc] from PFC2D will force both codes to take one step.
;       The coupling scheme assumes that cycling occurs only by calling
;       [cpp_cyc] from PFC2D.  DO NOT ISSUE CYCLE COMMANDS DIRECTLY AND
;       DO NOT TYPE ESCAPE WHILE CYCLING IN EITHER CODE!
;
```

```
;       FLAC enters slave mode by calling [cpf_cyc] from FLAC, and FLAC
;       exits slave mode by calling [cpp_cyc, with cpp_cycend=1] from
   PFC2D.
;
;       Both the FLAC and PFC2D states can be saved and restored for
;       later analysis.  If communication has not yet been established
;       between FLAC and PFC2D (e.g., if both codes have just been
;       started and saved states restored), then first [cpf_open] must
   be
;       called from FLAC and next [cpp_open] must be called from PFC2D.
;
;       To perform synchronous cycling:
;          (1) call [cpf_cyc] from FLAC,
;          (2) perform cycling by calling [cpp_cyc, with cpp_cycnum
   given]
;              from PFC2D, and
;          (3) end synchronous control by calling [cpp_cyc, w/
   cpp_cycend=1]
;              from PFC2D.  After a restore operation, synchronous
   cycling
;              must be initiated by performing step 1.
;
; INPUT: cpp_cycnum - number of cycles to execute
;   I/O: cpp_cycend - boolean: if =1, end FLAC slave mode
;
  if cpp_cycnum < 0 then
    error = '[cpp_cyc]: requested negative number of cycles.'
  end_if
  ;
  if cpp_cycend = 0 then
    oo=out('*** Synchronous cycling, taking '+string(cpp_cycnum)+'
       steps.')
     cp_buf(1) = cpp_cycnum
     cp_bufn = 1
    cp_write
    command
      cycle @cpp_cycnum calm 25
    end_command
  else  ; end FLAC slave mode
    oo=out('*** Ending synchronous cycling.')
     cp_buf(1) = -1
     cp_bufn = 1
    cp_write
    cpp_cycend = 0
  end_if
end
```

```
;
   ================================================================

def _slp_init_EPC
;
; INPUT: cpp_nseg  - number of segments
;        cpp_nseg0 - previous number of segments (used if reentrant)
;
  if _slp_reentrant = 1 then  ; will be zero upon first entrance
    kk = lose_mem(cpp_nseg0, _slp_null); null segment indicator
    kk = lose_mem(cpp_nseg0, _slp_x0)  ; coords
    kk = lose_mem(cpp_nseg0, _slp_x1)
    kk = lose_mem(cpp_nseg0, _slp_y0)
    kk = lose_mem(cpp_nseg0, _slp_y1)
    kk = lose_mem(cpp_nseg0, _slp_xv0) ; velocities
    kk = lose_mem(cpp_nseg0, _slp_xv1)
    kk = lose_mem(cpp_nseg0, _slp_yv0)
    kk = lose_mem(cpp_nseg0, _slp_yv1)
    kk = lose_mem(cpp_nseg0, _slp_xf0) ; forces
    kk = lose_mem(cpp_nseg0, _slp_xf1)
    kk = lose_mem(cpp_nseg0, _slp_yf0)
    kk = lose_mem(cpp_nseg0, _slp_yf1)
  else
    _slp_reentrant = 1
  end_if
  ;
  _slp_null = get_mem( cpp_nseg ) ; null segment indicator
  _slp_x0   = get_mem( cpp_nseg ) ; coords
  _slp_x1   = get_mem( cpp_nseg )
  _slp_y0   = get_mem( cpp_nseg )
  _slp_y1   = get_mem( cpp_nseg )
  _slp_xv0  = get_mem( cpp_nseg ) ; velocities
  _slp_xv1  = get_mem( cpp_nseg )
  _slp_yv0  = get_mem( cpp_nseg )
  _slp_yv1  = get_mem( cpp_nseg )
  _slp_xf0  = get_mem( cpp_nseg ) ; forces
  _slp_xf1  = get_mem( cpp_nseg )
  _slp_yf0  = get_mem( cpp_nseg )
  _slp_yf1  = get_mem( cpp_nseg )
  ;
  ; --- Initialize cbi-block information.
  cbi_head = null
  cbi_NEXT = 0
  cbi_BALL = 1
  cbi_SEG  = 2
  cbi_XI   = 3
  cbi_NUMB = 4  ; # entries in block
```

```
  ;
  command
    SET extra ball 2 ;Usually 1, but one more for damping_work.dat
  end_command
end
;
```

```
;EOF: cpplib_EPC.fis
RETURN
```

Listing A.13: Custom FISH functions for PFC2D EPC

```
; filename EPC_functions_PFC.fis   author: EKias
;
; Various support functions
;
; ------------------------------------------------------------------
def del_strays
        bp = ball_head
        Lim_yh = mv_H + 2*md_ravg
        Lim_yl = -2*md_ravg
        Lim_xh = mv_W + 4.5 + 2*md_ravg
        Lim_xl = Lim_yl + 4.5
        loop while bp # null
                bnext = b_next(bp)
                if b_y(bp) > Lim_yh then
                        ii = b_delete(bp)
                endif
                if b_y(bp) < Lim_yl then
                        ii = b_delete(bp)
                endif
                ; if b_x(bp) > Lim_xh then
                        ; ii = b_delete(bp)
                ; endif
                ; if b_x(bp) < Lim_xl then
                        ; ii = b_delete(bp)
                ; endif
                bp = bnext
        end_loop
 end
; ------------------------------------------------------------------
; eof. EPC_functions_PFC.fis
```

Listing A.14: PFC2D EPC measurement functions and histories

```
; filename: pfc_mfuncs.fis   author: EKias
;
; Model state measurement functions for EPC test in PFC
; Must be called after tt1.dvr because histories are cleared there.
;
; ------------------------------------------------------------------------
def id_gage_bs
        gb1t = ball_near2(4.75,2.0)
        gb2t = ball_near2(5.00,2.0)
        gb3t = ball_near2(5.25,2.0)
        ;
        gb1b = ball_near2(4.75,0.0)
        gb2b = ball_near2(5.00,0.0)
        gb3b = ball_near2(5.25,0.0)
end
id_gage_bs

def gage_bs_Lo
        Top_o = (b_y(gb1t)+b_y(gb2t)+b_y(gb3t))/3
        Bot_o = (b_y(gb1b)+b_y(gb2b)+b_y(gb3b))/3
        gb_Lo = Top_o - Bot_0
end
gage_bs_Lo

def gage_bs_eyy
        Top_t = (b_y(gb1t)+b_y(gb2t)+b_y(gb3t))/3
        Bot_t = (b_y(gb1b)+b_y(gb2b)+b_y(gb3b))/3
        gb_Lt = Top_t - Bot_t
        ;
        gb_eyy = (gb_Lo - gb_Lt)/gb_Lo
end

history gage_bs_eyy nstep 50
history gb_eyy nstep 50


def EPC_big_mcs
 command
        measure id 1 x 5.0 y .5131 rad 0.4869
        measure id 2 x 5.0 y 1.0  rad 0.4869
        measure id 3 x 5.0 y 1.487 rad 0.4869
        history measure s22 id 1
        history measure s22 id 2
        history measure s22 id 3
 end_command
```

```
end
EPC_big_mcs

def get_big_mcs
        bmc1 = find_meas(1)
        bmc2 = find_meas(2)
        bmc3 = find_meas(3)
end
get_big_mcs

def big_mcs_et2
        syy1 = m_s22(bmc1)
        syy2 = m_s22(bmc2)
        syy3 = m_s22(bmc3)
        bmc_et2_syy = (syy1 + syy2 + syy3)/3
end

history big_mcs_et2 nstep 50
history bmc_et2_syy nstep 50
; ------------------------------------------------------------------------
;EOF pfc_mfuncs.fis
RETURN
```

APPENDIX B - INVESTIGATING THE EFFECT OF INTERNAL STRAIN ENERGY ON POST-PEAK BEHAVIOR OF THE BPM AND DSM

In response to the results of the LRC tests, an additional study was conducted in order to test a possible explanation for the velocity dependent post-peak behavior. The interaction between internal strain energy and strength increase due to confinement could possibly lead to the observation of different levels of characteristic softening under different loading rates. Stored strain energy accrued during elastic deformation might lead to instability in the post-peak region of the DEM material if the post-peak characteristic is such that the strain energy cannot be absorbed during failure. At the moment of failure, this loading condition would lead to sudden failure with no post-peak softening. Although, if the loading rate is high, the amount of work added to the system each step may exceed the amount of energy released. If so, a higher material strength in the post-peak region could be observed due to increased confinement. In other words, a post-peak softening characteristic would be observed that is not a characteristic property of the material, but dependent upon the loading condition.

Three specimens are subjected to a modified UCS test to investigate the effect of elastic strain energy on DEM stability in the post-peak region. Here, a UCS test is conducted as in Chapter 3.4, but here, the specimen is loaded just beyond failure and loading is halted when the vertical stress on the specimen is ninety five percent of the strength. At this point the model is cycled in order to determine stability of the specimen. If no change in stress occurs then the specimen is stable, if the stress continues to drop then the specimen is unstable. The three specimens tested are the two DEM specimens from Chapter 3 and a recalibrated DSM to with a steeper post-peak softening curve. First, the results of the tests on the DEMs from Chapter 3 are discussed then the results for the two DSM tests are discussed.

Figure B.1 shows the stress versus step curves for the modified UCS test on the two DEMs from Chapter 3. The black dot on each line designates the point where loading is halted.

The DSM model shows a slight decrease in stress indicating a brief period of instability. The BPM model shows shows a greater decrease in stress. The small amount of instability in the DSM model reflects the material's ability to regain stability after some energy release, whereas the instability of the BPM specimen shows that stability is not regained.

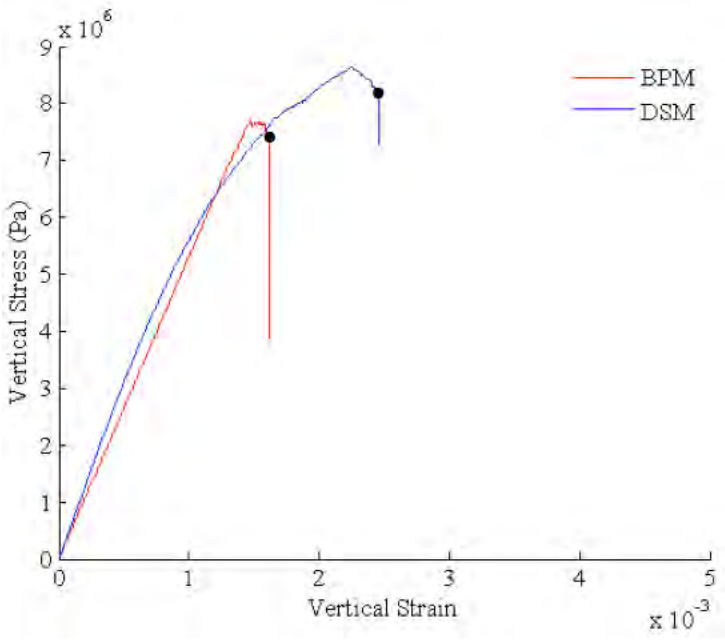

Figure B.1: Stability test stress-strain curves for Chapter 3 DEM models

The stability concept tested in Chapter 3 using the EPC tests states that if the energy stored within the loading system at the point of failure cannot be absorbed by the specimen then the failure will be unstable. During unstable failure, the characteristic post-peak behavior of the material is hidden, and the strain measurement taken at the platen-specimen boundary reflects the rebound of the platens. In the case of the BPM tested here, when loading is halted, work is no longer done on the system by the loading mechanism. If the failure is unstable, another source of energy must be acting on the system. Elastic strain energy in the BPM specimen could cause unstable failure if the specimen is not able to dissipate all of the stored energy during the failure process.

DEM material is not perfectly linear in the elastic region or in the post-post peak. Although a simplification of the behavior is useful in illustrating a possible mechanism for

failure stability of DEM specimens under rigid loading conditions. Figure B.2 shows a schematic of a stress strain curve where the elastic region and post-peak region are made linear for simplification. The hatched area U_E is stored elastic strain energy up to the point of failure. The unhatched region, U_C, can be thought of as the capacity of energy storage in the specimen during failure. In order for failure to be stable, $U_E < |U_C|$. If $U_E > |U_C|$, then the available energy is greater than the material's capacity to store the energy and failure will be unstable.

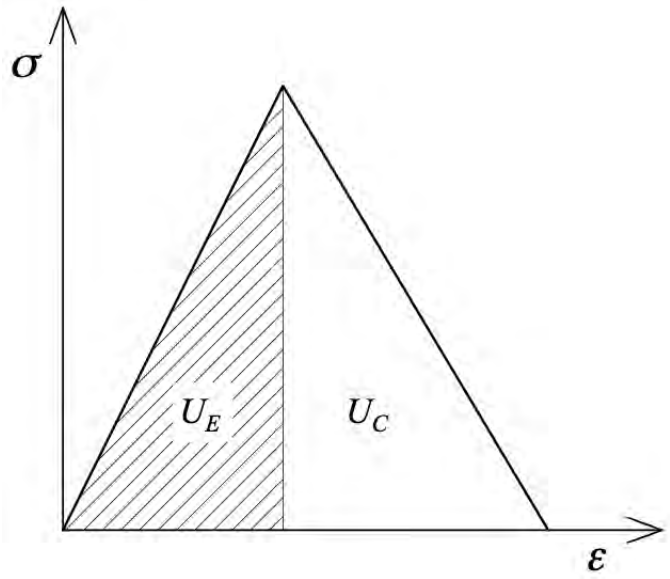

Figure B.2: Strain energy regions for linear elastic material with linear softening

Figure B.3 shows two stress-strain curves, one for the DSM from Chapter 3 and one for the recalibrated DSM, labeled DSMr. The DSMr curve is calibrated to have similar elastic modulus and strength, but with a steeper post-peak curve. The steeper post-peak curve reflects a post-peak behavior in which less energy can be absorbed during failure than by the DSM specimen. The curves in Figure B.3 are both non-linear in both elastic and post-peak regions. So, making an exact determination of available strain energy versus energy storage capacity would require a determination of elastic unloading behavior at any given point in the post-peak curve. Although, an estimation on the likelihood of failure stability can be

made based on the energy criteria above. DEM materials with shallow post-peak softening compared to the elastic modulus will most likely be stable under rigid loading, materials with steep post-peak softening will likely be unstable and material with post-peak softening approximately equal in magnitude to the elastic modulus are questionable and should be closely examined. By approximating the post-peak behavior versus the pre-peak behavior in Figure B.3, it is likely that DSMr will be unstable under rigid loading conditions.

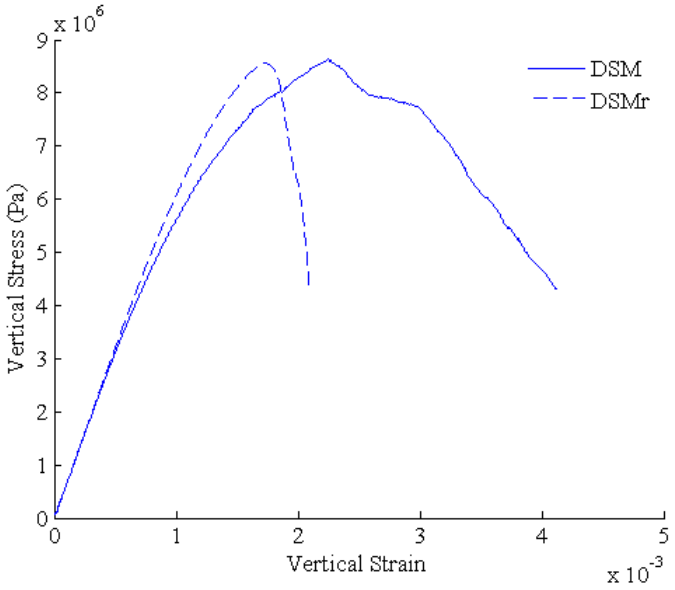

Figure B.3: DSM characteristic stress-strain curves

Figure B.4 shows two stress-strain curves, one for the DSM and one for the DSMr. The black dots show the point at which loading is halted and the model is cycled to test stability. Figure B.4 shows that the DSM has a partial instability and the DSMr material fails completely after loading is halted and the model is cycled. Total failure of the material indicates that the DSMr is unstable under rigid loading. The instability of the DSMr specimen supports the claim that internal strain energy magnitude in reference to the post-peak softening characteristic plays a significant role in modeling rock behavior with DEM.

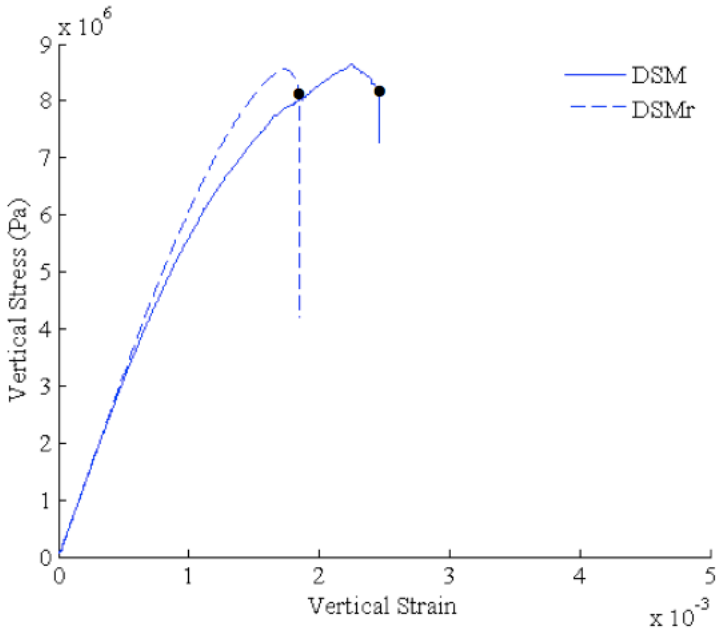

Figure B.4: Stability test stress-strain curves for two DSM specimens with different post-peak behavior

Listing C.15: Grid based measurement algorithm FISH codes

```
; Filename: PFC_grid_based_meas.dat  Author: EKias
;
; This file computes values of defined parameters within a grid
;
;
```

```
; Allocate a memory slot to bin each ball and contact
set extra ball 4
set extra contact 2

def define_grid_CBM
        grid_res = 5
        hist_step = 5000
        pillar_H = 2.0
        caseof pillar_geom
                case 1
                pillar_W = 2.0
                case 2
                pillar_W = 4.0
                case 3
                pillar_W = 6.0
                case 4
                pillar_W = 8.0
                case 5
                pillar_W = 1.0
        end_case
        ncells_x = int(grid_res*pillar_W*2) ; [W: ncells_x = 2:20, 4:40,
            6:60, 8:80, 1:10]
        ncells_y = int(grid_res*pillar_H*2) ; [ncells_y = 20]
end
define_grid_CBM

def init_PFC_grid_params
        ; Define arrays
        array gridcell_ke(ncells_y, ncells_x)  ; (row,col) = (y,x)
        array gridcell_ball_count(ncells_y, ncells_x)
        array avg_gridcell_ke(ncells_y, ncells_x)
        ;
```

```
array gridcell_se(ncells_y, ncells_x)
array gridcell_cont_count(ncells_y, ncells_x)
array avg_gridcell_se(ncells_y, ncells_x)
;
array gridcell_prod(ncells_y, ncells_x)
array gridcell_syy(ncells_y, ncells_x)
;
array gridcell_sof(ncells_y, ncells_x)
array avg_gridcell_sof(ncells_y, ncells_x)
array gridcell_sofnuminit(ncells_y, ncells_x)
array gridcell_cont_nbcount(ncells_y, ncells_x)
array gridcell_sofnumbroke(ncells_y, ncells_x)
;
array gridcell_wd(ncells_y, ncells_x)
;
; Initiallize arrays to zero
loop r (1,ncells_y)
        loop c (1,ncells_x)
                gridcell_ke(r,c) = 0.0
                gridcell_ball_count(r,c) = 0.0
                avg_gridcell_ke(r,c) = 0.0
                gridcell_se(r,c) = 0.0
                gridcell_cont_count(r,c) = 0.0
                avg_gridcell_se(r,c) = 0.0
                gridcell_prod(r,c) = 0.0
                gridcell_syy(r,c) = 0.0
                gridcell_sof(r,c) = 0.0
                avg_gridcell_sof(r,c) = 0.0
                gridcell_wd(r,c) = 0.0
        end_loop
end_loop
;
grid_Lx = pillar_W+0.05*pillar_W
grid_Ly = pillar_H+0.05*pillar_H
grid_origin_x = 3.0 - 0.025*pillar_W ; Bottom left corner (x-
   coord) of the grid, used for binning
y_offset = 0.025*mv_H  ; need to offsett grid because of
   loading scheme and
;                      ; resulting movement of specimen
cell_dx = grid_Lx/ncells_x
cell_dy = grid_Ly/ncells_y
cell_A = cell_dx*cell_dy
;
nb = 0
bp = ball_head
loop while bp # null
        outgrid = 0
```

```
        ;first, bin each ball
        ball_x = b_x(bp)
        ball_y = b_y(bp)
        cell_indexX = int((ball_x-grid_origin_x)/cell_dx)+1
        cell_indexY = int((ball_y+y_offset)/cell_dy)+1
        ;second, determine if inside the grid
        if cell_indexX < 0
                b_extra(bp,3) = -1
                outgrid = 1
        endif
        if cell_indexX > ncells_x
                b_extra(bp,3) = -1
                outgrid = 1
        endif
        if cell_indexY < 0
                b_extra(bp,4) = -1
                outgrid = 1
        endif
        if cell_indexY > ncells_y
                b_extra(bp,4) = -1
                outgrid = 1
        endif
        ;Third, assign extra variable that assigns gridcell
        if outgrid # 1
                b_extra(bp,3) = cell_indexX
                b_extra(bp,4) = cell_indexY
        endif
        nb = nb+1
        bp = b_next(bp)
endloop
;
sof_numinit = 0
cp = contact_head
loop while cp # null
        outgrid = 0
        ;first, bin each contact
        cont_x = c_x(cp)
        cont_y = c_y(cp)
        cell_indexX = int((cont_x-grid_origin_x)/cell_dx)+1
        cell_indexY = int((cont_y+y_offset)/cell_dy)+1
        ;second, determine if inside the grid
        if cell_indexX < 0
                c_extra(bp,1) = -1
                outgrid = 1
        endif
        if cell_indexX > ncells_x
                c_extra(cp,1) = -1
```

```
                outgrid = 1
            endif
            if cell_indexY < 0
                c_extra(cp,2) = -1
                outgrid = 1
            endif
            if cell_indexY > ncells_y
                c_extra(cp,2) = -1
                outgrid = 1
            endif
            ;Third, assign extra variables that assign gridcell
            if outgrid # 1
                c_extra(cp,1) = cell_indexX
                c_extra(cp,2) = cell_indexY
            endif
            ;
            if c_model(cp) = 'udm_softening'
                if c_prop(cp,'sof_broken') = 0
                    sof_numinit = sof_numinit + 1
                else
                    sof_brokeinit = sof_brokeinit + 1
                endif
            endif
        cp = c_next(cp)
        endloop
        ;
        ;get initial contact count
        dumA = 0
        cp = contact_head
        loop while cp # null
            if c_prop(cp,'sof_broken') = 0
                ; get gridcell assignment
                cell_indexX = c_extra(cp,1)
                cell_indexY = c_extra(cp,2)
                dumA = gridcell_sofnuminit(cell_indexY,
                    cell_indexX)
                dumA = dumA + 1
                gridcell_sofnuminit(cell_indexY,cell_indexX) =
                    dumA
            endif
            cp = c_next(cp)
        endloop
end
init_PFC_grid_params

def Wdamp_array_init
        Wxd_sum = 0.0 ; Work done by local damping in x-dir
```

```
        Wyd_sum = 0.0 ; Work done by local damping in y-dir
        Wrd_sum = 0.0 ; Work done by local damping in r-dir
        Wd_tot = 0.0  ; Total work done by local damping
        ;
        array b_array(nb,6)
        arr_row = 1
        bp = ball_head
        alpha = b_damp(bp)
        loop while bp # null
                b_array(arr_row,1) = b_x(bp)
                b_array(arr_row,2) = b_y(bp)
                b_array(arr_row,3) = b_rot(bp)
                b_array(arr_row,4) = b_xfob(bp)
                b_array(arr_row,5) = b_yfob(bp)
                b_array(arr_row,6) = b_mom(bp)
                b_extra(bp,2) = arr_row
                arr_row = arr_row + 1
                bp = b_next(bp)
        endloop
        ; print_array
end

def print_array
        loop m (1,nb)
                hed = '    '
                msg = '  '+string(m)
                loop n (1,4)
                        hed = hed + '                    '+string(n)
                        msg = msg + '  '+string(b_array(m,n))
                end_loop
                if m = 1
                        dum = out(hed)
                end_if
                dum = out(msg)
        end_loop
end
Wdamp_array_init

def Wdamp_array
        bp = ball_head
        loop while bp # null
                arr_row = b_extra(bp,2)
                b_array(arr_row,1) = b_x(bp)
                b_array(arr_row,2) = b_y(bp)
                b_array(arr_row,3) = b_rot(bp)
                b_array(arr_row,4) = b_xfob(bp)
                b_array(arr_row,5) = b_yfob(bp)
```

```
            b_array(arr_row,6) = b_mom(bp)
            bp = b_next(bp)
        endloop
        ; print_array
end

set fishcall 0 Wdamp_array

call %fist_emck%\2d\CM\CBM_grid_hist_lists.fis   ;for wd, ke, syy, and
   sof variables and histories









def pfc_ke ; ball kinetic energy calculation
        mass = b_mass(bp)
        MOI = b_moi(bp)
        _xv = b_xvel(bp)
        _yv = b_yvel(bp)
        _rv = b_rvel(bp)
        bp_ke = 0.5*mass*(_xv^2+_yv^2) + 0.5*MOI*(_rv^2) ;
           translational + rotational
end

def pfc_se
; contact strain energy calculation
   ------------------------------------------------------

        _kn = c_kn(cp)
        _ks = c_ks(cp)
        _cFn = c_nforce(cp)
        _cFs = c_sforce(cp)
; due to a normal force
```

```
        if _kn = 0.0 then
                SE_cp_n = 0.0
        else
                SE_cp_n = 0.5*(_cFn^2/(_kn))
        endif
; due to a shear force
        if _ks = 0.0
                SE_cp_s = 0.0
        else
                SE_cp_s = 0.5*(_cFs^2/_ks) ;(_cFxs^2/(_ks) + _cFys^2/(
                   _ks) + _cFzs^2/(_ks))
        endif
; Total
        SE_cp = SE_cp_s + SE_cp_n
        ;
; parallel bond strain energy calculation
   ------------------------------------------------
        if c_pb(cp) # null then
        pbp = c_pb(cp)
        Rad = pb_rad(pbp)
        pb_A = 2*Rad
        pb_I = (2*Rad)^3/12 ; (1/12)bh^3, b=1
        _pb_kn = pb_kn(pbp)
        _pb_ks = pb_ks(pbp)
        _pbFn = pb_nforce(pbp)
        _pbFs = pb_sforce(pbp)
        _pbM = abs(pb_mom(pbp))
; due to a normal force
        if _pb_kn = 0.0 then
                SE_pbn = 0.0
        else
                SE_pbn = 0.5*_pbFn^2/(_pb_kn) ;from U = P^2*L/2AE where
                   , E = Lk/A
        endif
; due to a shear force
        if _pb_ks = 0.0 then
                SE_pbs = 0.0
        else
                SE_pbs = 0.5*_pbFs^2/(_pb_ks) ;axial strain in the
                   shear direction, see SE_pbn ?????????? CHECK!!!
        endif
; due to a bending moment
        if _pb_kn = 0.0
                SE_pbb = 0.0
        else
                SE_pbb = (pb_mom(pbp))^2*pb_A/(2*_pb_kn*pb_I) ; from U
                   = M^2*L/2EI where, E = Lk/A
```

```
        endif
; Total
        SE_pb = SE_pbn + SE_pbb + SE_pbs
        else
        SE_pb = 0.0
        endif
        ; Total Strain Energy at contact cp
          ------------------------------------------------
        cp_se = SE_cp + SE_pb
end

def pfc_sof
        if c_model(cp) = 'udm_softening' then
                if c_prop(cp,'sof_broken') = 0
                        cp_sof = c_prop(cp,'sof_softened')
                        ;ratio of amt. yielded to yield limit , 0 = no
                           yield
                        sof_nbcnt = sof_nbcnt + 1
                        dumA = gridcell_cont_nbcount(cell_indexY,
                           cell_indexX)
                        dumA = dumA + 1
                        gridcell_cont_nbcount(cell_indexY,cell_indexX)
                           = dumA
                endif
        else
                cp_sof = 0.0
        endif
        sof_tot = sof_tot + cp_sof
end

def pfc_wd
        bp_wd = 0.0 ;This is the amount of work done in one step on one
            ball
                                ;and it should be zeroed before pfc_wd
                                   calculates the work
                                ;in order to get a cummulative value
                                   for each grid cell.
                                ;
                                ;Incremental values can be computed by
                                   zeroing the grid array
                                ;after each step, but this is not wise
                                   because the histories for
                                ;each grid must be recorded every step
                                   for the values to be useful
                                ;quantitatively. Otherwise, they can be
                                    a qualitative indicator.
                                ;
```

```
arr_row = b_extra(bp,2)
; Get new coords
bx_new = b_x(bp)
by_new = b_y(bp)
br_new = b_rot(bp)
; Get coord change increments
xdif = bx_new - b_array(arr_row,1)
ydif = by_new - b_array(arr_row,2)
rdif = br_new - b_array(arr_row,3)
; Get forces
F_unbal_x = b_array(arr_row,4)
F_unbal_y = b_array(arr_row,5)
M_unbal = b_array(arr_row,6)
; Test directionality dependence
if xdif > 0 then
v_xdir = 1 ; Positive direction
else
v_xdir = 0 ; Negative direction
endif
;
if ydif > 0 then
v_ydir = 1
else
v_ydir = 0
endif
;
if rdif > 0 then
v_rdir = 1
else
v_rdir = 0
endif
;
if F_unbal_x > 0 then
F_xdir = 1
else
F_xdir = 0
endif
;
if F_unbal_y > 0 then
F_ydir = 1
else
F_ydir = 0
endif
;
if M_unbal > 0 then
M_dir = 1
else
```

```
        M_dir = 0
        endif
        ;
        ; Calculate damping forces
        ;
        ; These eqns assume that F_unbal = Ffob + Fdamp
        ; where Ffob is the sum of contact forces and
        ;                Fdamp = alpha*Ffob
        ; So,
        ;        F_unbal = 1/alpha*Fdamp + Fdamp
        ;
        if v_xdir = F_xdir then
        Fx_damp = (alpha/(1-alpha))*abs(F_unbal_x)
        else
        Fx_damp = (alpha/(1+alpha))*abs(F_unbal_x)
        endif
        ;
        if v_ydir = F_ydir then
        Fy_damp = (alpha/(1-alpha))*abs(F_unbal_y)
        else
        Fy_damp = (alpha/(1+alpha))*abs(F_unbal_y)
        endif
        ;
        if v_rdir = M_dir then
        M_damp = (alpha/(1-alpha))*abs(M_unbal)
        else
        M_damp = (alpha/(1+alpha))*abs(M_unbal)
        endif
        ;
        ; Calculate work done by damping mechanism
        Wx_damp = Fx_damp*abs(xdif)
        Wy_damp = Fy_damp*abs(ydif)
        Wr_damp = M_damp*abs(rdif)
        ;
        bp_wd = Wx_damp + Wy_damp + Wr_damp
        ;
        ; The following can be recorded to get totals for the entire
           model
        Wxd_sum = Wxd_sum + Wx_damp
        Wyd_sum = Wyd_sum + Wy_damp
        Wrd_sum = Wyd_sum + Wr_damp
        ;
        Wd_tot = Wd_tot + bp_wd
        ;
end

def param_loop_bp
```

```
        ;
        bp = ball_head
        loop while bp # null
                ;get gridcell assignment
                        cell_indexX = b_extra(bp,3)
                        cell_indexY = b_extra(bp,4)
                        if cell_indexX > 0
                        if cell_indexY > 0
                        ; call param functions
                        ; pfc_ke
                        ;gridcell_ke(cell_indexY,cell_indexX) =
                           gridcell_ke(cell_indexY,cell_indexX) + bp_ke
                        ;gridcell_ball_count(cell_indexY,cell_indexX) =
                            gridcell_ball_count(cell_indexY,cell_indexX
                           ) + 1
                        ;
                        pfc_wd
                        dumA = gridcell_wd(cell_indexY,cell_indexX)
                        dumA = dumA + bp_wd
                        gridcell_wd(cell_indexY,cell_indexX) = dumA
                        endif
                        endif
                bp = b_next(bp)
        end_loop

        ;divide gridcell energy by number of balls
        ;loop r (1,ncells_y)
        ;       loop c (1,ncells_x)
        ;               if gridcell_ball_count(r,c) # 0 then
        ;                 avg_gridcell_ke(r,c) = gridcell_ke(r,c)/
           gridcell_ball_count(r,c)
        ;               else
        ;                 avg_gridcell_ke(r,c) = 0.0
        ;               endif
        ;       end_loop
        ;end_loop
end

def get_phi
        b1 = c_ball1(cp)
        b2 = c_ball2(cp)
        y1 = b_y(b1)
        y2 = b_y(b2)
        x1 = b_x(b1)
        x2 = b_x(b2)
        dy = y2 - y1
        dx = x2 - x1
```

```
        if dx = 0.0 then
                phi = pi/2.0
        else
                phi = abs(atan(dy/dx))
        endif
end

def contact_product
        ; from contact force
        cp_yf = _cFn*sin(phi)
        ; from pbond force
        if c_pb(cp) # null
                pb_yf = _pbFn*sin(phi)
        else
                pb_yf = 0.0
        endif
        ;
        cont_yf = cp_yf + pb_yf
        ; y component of branch vector (vector connecting contact ball
           centroids)
        ball1 = c_ball1(cp)
        ball2 = c_ball2(cp)
        yball1 = b_y(ball1)
        yball2 = b_y(ball2)
        branch_y = abs(yball1 - yball2)
        ;
        cont_prod = cont_yf*branch_y
end

def zero_arrays
        loop r (1,ncells_y)
                loop c (1,ncells_x)
                        gridcell_prod(r,c) = 0.0
                        gridcell_sof(r,c) = 0.0
                        gridcell_cont_nbcount(r,c) = 0.0
                end_loop
        end_loop
end

def param_loop_cp
        zero_arrays
        sof_tot = 0.0
        sof_nbcnt = 0
        cp = contact_head
        loop while cp # null
                ; get gridcell assignment
                cell_indexX = c_extra(cp,1)
```

```
        cell_indexY = c_extra(cp,2)
        if cell_indexX > 0
        if cell_indexY > 0
                ; call param functions
                ;pfc_se
                pfc_sof
                ;gridcell_se(cell_indexY,cell_indexX) =
                   gridcell_se(cell_indexY,cell_indexX) + cp_se
                gridcell_sof(cell_indexY,cell_indexX) =
                   gridcell_sof(cell_indexY,cell_indexX) +
                   cp_sof
                ;gridcell_cont_count(cell_indexY,cell_indexX) =
                    gridcell_cont_count(cell_indexY,cell_indexX
                   ) + 1
                ;get_phi
                ;contact_product
                ;gridcell_prod(cell_indexY,cell_indexX) =
                   gridcell_prod(cell_indexY,cell_indexX) +
                   cont_prod
        endif
        endif
cp = c_next(cp)
end_loop

;for global measurement
sof_numbroke = sof_numinit - sof_nbcnt
sof_tot = sof_tot + sof_numbroke ;Add 1 for each deleted
   contact.
;
;for gridcell measurement
dumB = 0
loop r (1,ncells_y)
        loop c (1,ncells_x)
                dumA = gridcell_sofnuminit(r,c)
                dumB = gridcell_cont_nbcount(r,c)
                gridcell_sofnumbroke(r,c) = dumA - dumB
                ; Add to the softening of each cell
                gridcell_sof(r,c) = gridcell_sof(r,c) +
                   gridcell_sofnumbroke(r,c)
        end_loop
end_loop

;divide gridcell values by number of contacts
;loop r (1,ncells_y)
;       loop c (1,ncells_x)
;               if gridcell_cont_count(r,c) # 0 then
```

```
        ;                   avg_gridcell_se(r,c) = gridcell_se(r,c)/
           gridcell_cont_count(r,c)
        ;                   avg_gridcell_sof(r,c) = gridcell_sof(r,c)/
           gridcell_cont_count(r,c)
        ;                   gridcell_syy(r,c) = gridcell_prod(r,c)/cell_A
        ;                 else
        ;                   avg_gridcell_se(r,c) = 0.0
        ;                   gridcell_syy(r,c) = 0.0
        ;                 endif
        ;       end_loop
        ;end_loop
end

def cont_count
        cp = contact_head
        not_broken_dsm = 0
        broken_dsm = 0
        linear = 0
        loop while cp # null
                if c_model(cp) = 'linear'
                        linear = linear + 1
                endif
                if c_model(cp) = 'udm_softening'
                        if c_prop(cp,'sof_broken') = 0
                                not_broken_dsm = not_broken_dsm + 1
                        endif
                        if c_prop(cp,'sof_broken') = 1
                                broken_dsm = broken_dsm + 1
                        endif
                endif
        cp = c_next(cp)
        end_loop
        ;msg = 'num linear contacts = '
        ;oo = out(msg + string(linear))
        ;msg = 'num broken dsm contacts = '
        ;oo = out(msg + string(broken_dsm))
        ;msg = 'num unbroken dsm contacts = '
        ;oo = out(msg + string(not_broken_dsm))
end

set fishcall 3 param_loop_bp       ;Need fishcall 'cause work is
   cumulative
history nstep = 5000 param_loop_cp ;Ok, because no cumulative vals
   calculated
history nstep = 5000 wd_vars
;history nstep = 5000 Wxd_sum
;history nstep = 5000 Wyd_sum
```

```
;history nstep = 5000 Wrd_sum
history nstep = 5000 Wd_tot
history nstep = 5000 sof_vars
history nstep = 5000 sof_tot
history nstep = 5000 sof_numbroke
history nstep = 5000 cont_count
history nstep = 5000 not_broken_dsm
history nstep = 5000 broken_dsm
history nstep = 5000 linear

; Gridcell histories, defined in %fist_emck%\2d\CM\
   CBM_wd_syy_hist_lists.fis
sof_hists
wd_hists
; syy_hists
; ke_hists

; ------------------------------------------------------------------------
; eof. pfc_grid_based_meas.dat
return
```

Listing C.16: Width to height ratio one test grid

```
; filename: wtoh1_grid.dat
;
; Create Pillar-flac grid for w/h = 1 pillar
;
;
   ------------------------------------------------------------------------

set cpf_nseg = 256
grid 128 140
model elastic
generate  0 ,-38  0 ,-2   8,-2  8,-38  i=1,129    j=1,23     ratio
   =1,0.78
generate  0 ,-2   0 ,4    8,4   8,-2   i=1,129    j=23,119
generate  0 ,4    0 ,40   8,40  8,4    i=1,129    j=119,141  ratio=1,
   1.3
model null j=55,86

ini y add  0.0063  j=55  ; to create overlap with pfc part
ini y add -0.0063  j=87
------------------------------------------------------------------------

; eof. wtoh1_grid.dat
return
```

APPENDIX D - EPC TEST INDICATOR PLOTS

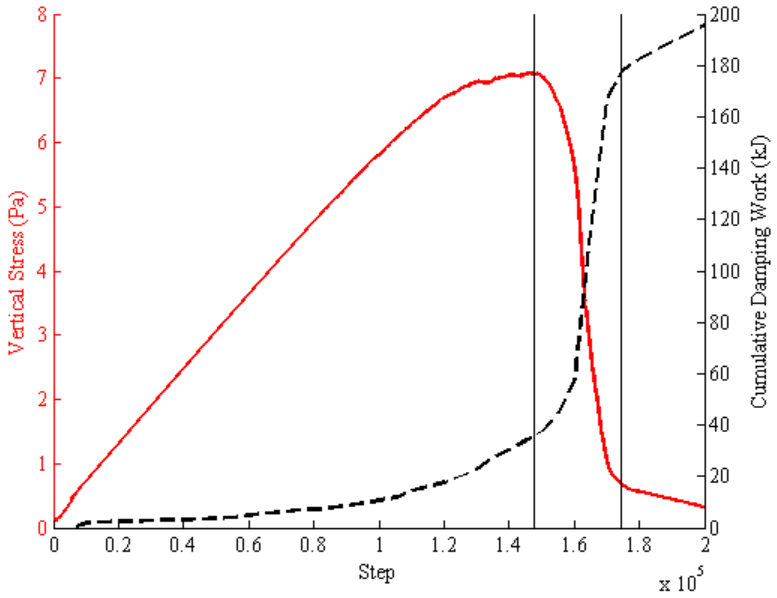

Figure D.1: Damping work, EPC Test with 1 GPa loading system

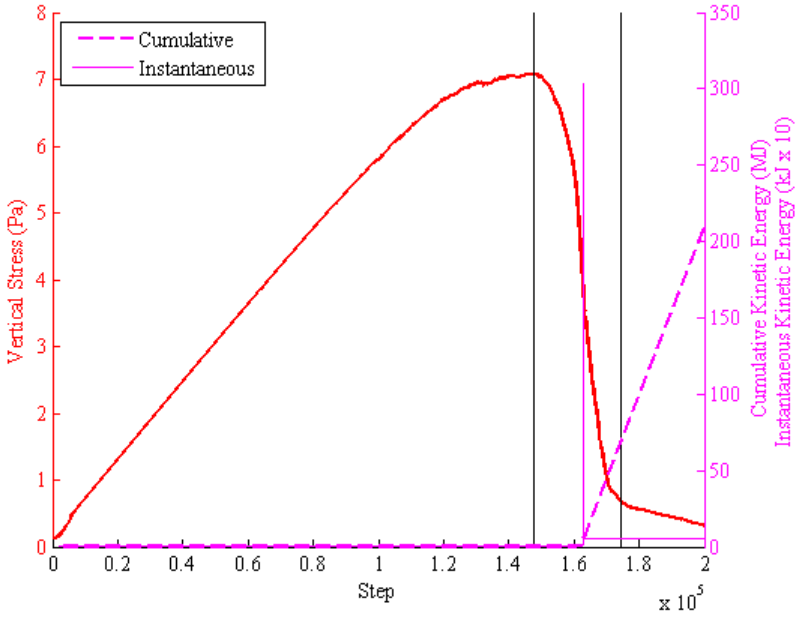

Figure D.2: Kinetic energy, EPC Test with 1 GPa loading system

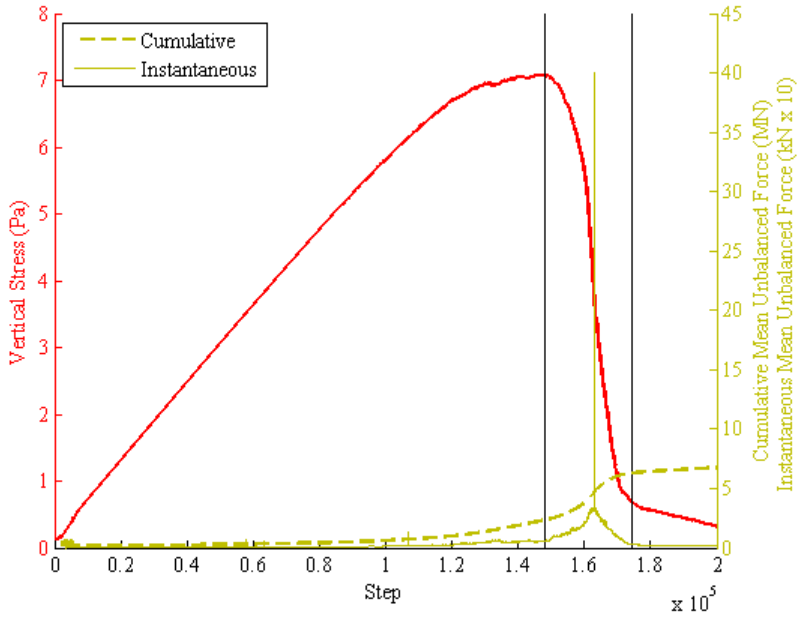

Figure D.3: Mean unbalanced force, EPC Test with 1 GPa loading system

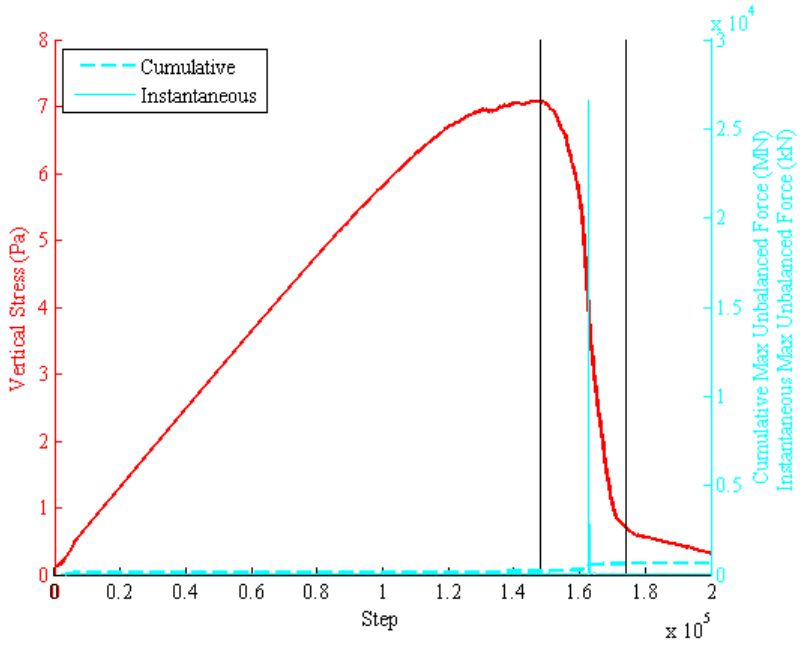

Figure D.4: Maximum unbalanced force, EPC Test with 1 GPa loading system

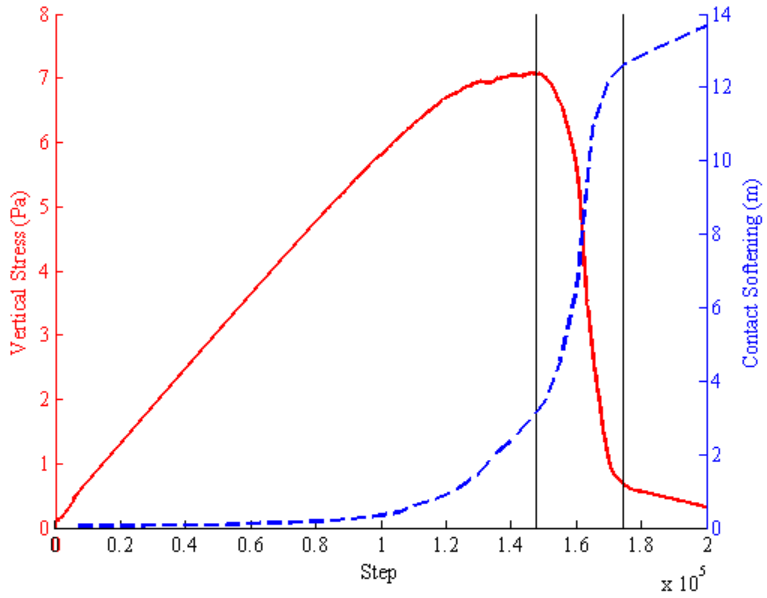

Figure D.5: Contact softening, EPC Test with 1 GPa loading system

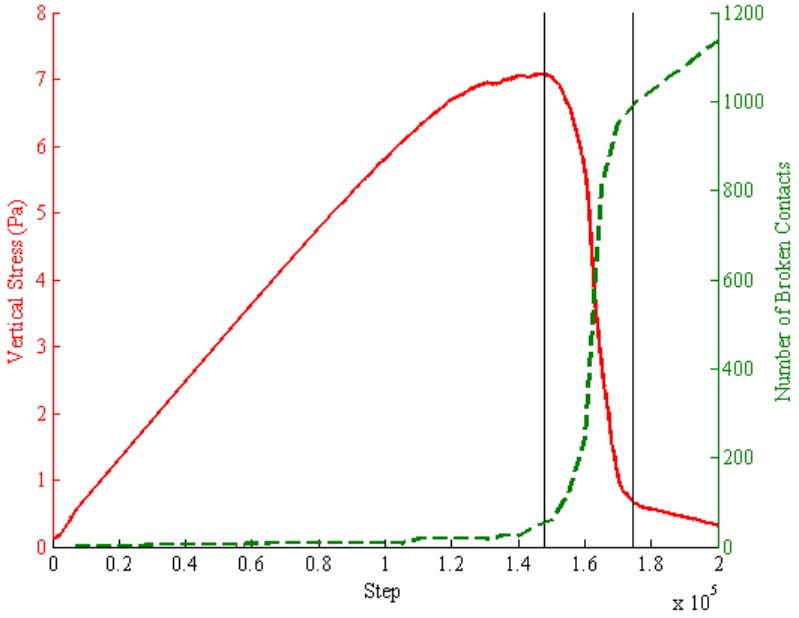

Figure D.6: Broken contacts, EPC Test with 1 GPa loading system

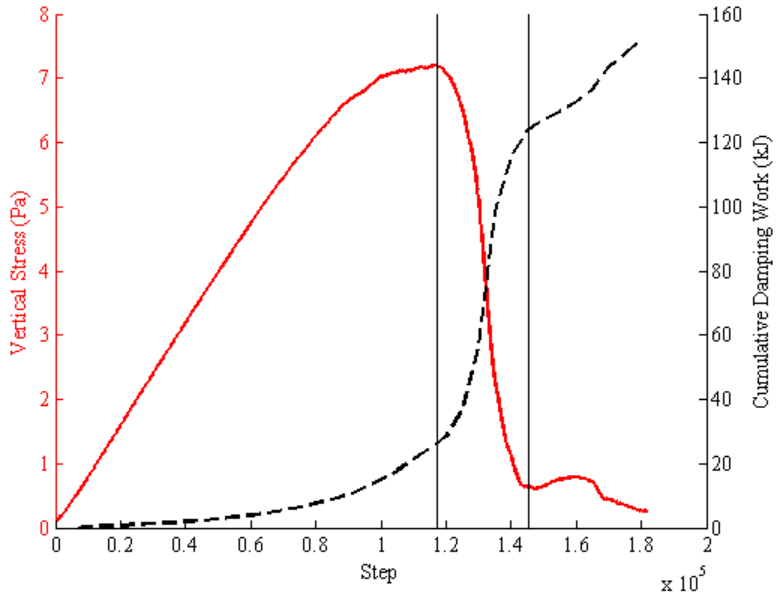

Figure D.7: Damping work, EPC Test with 1.5 GPa loading system

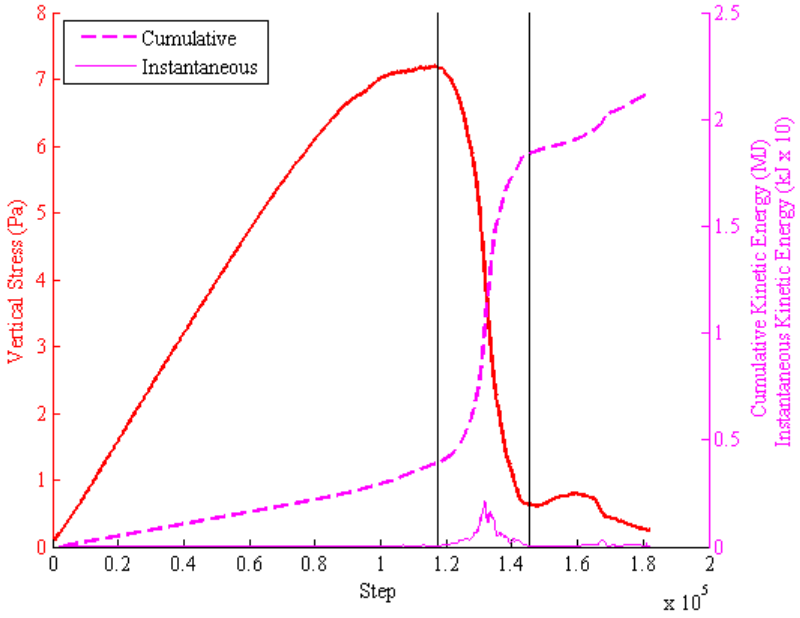

Figure D.8: Kinetic energy, EPC Test with 1.5 GPa loading system

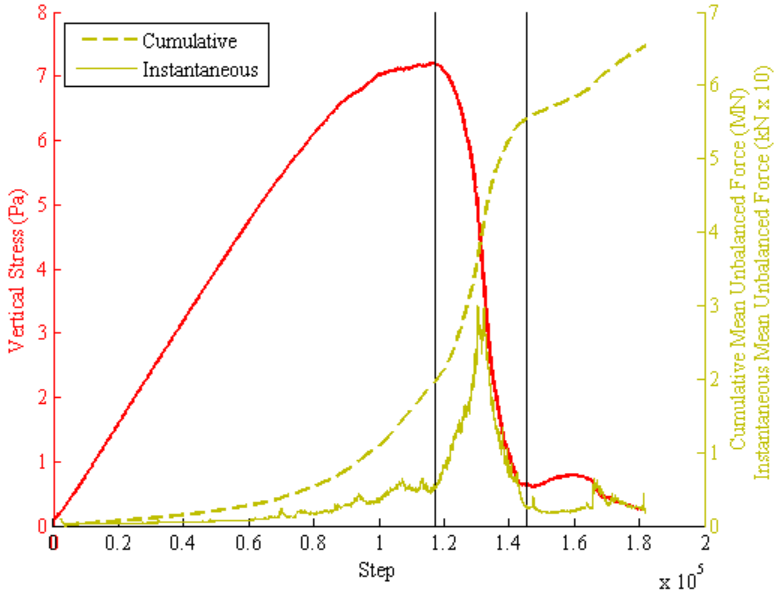

Figure D.9: Mean unbalanced force, EPC Test with 1.5 GPa loading system

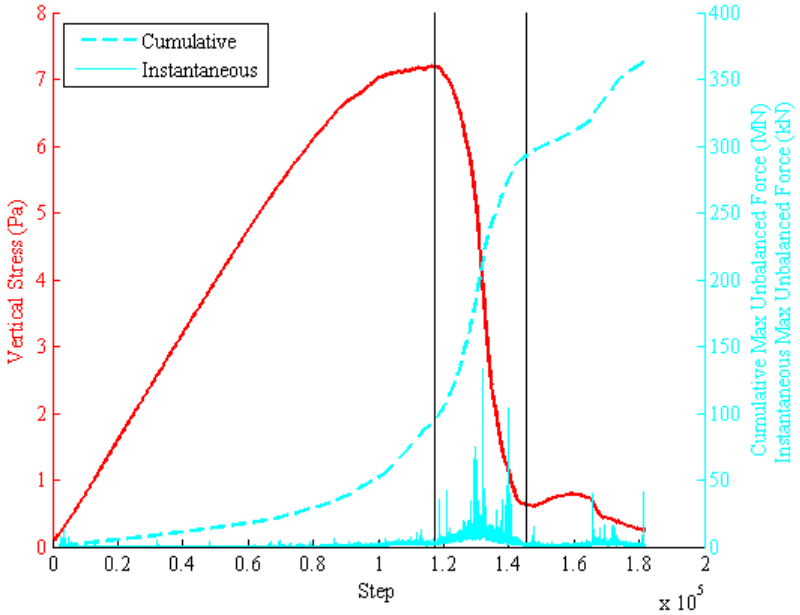

Figure D.10: Maximum unbalanced force, EPC Test with 1.5 GPa loading system

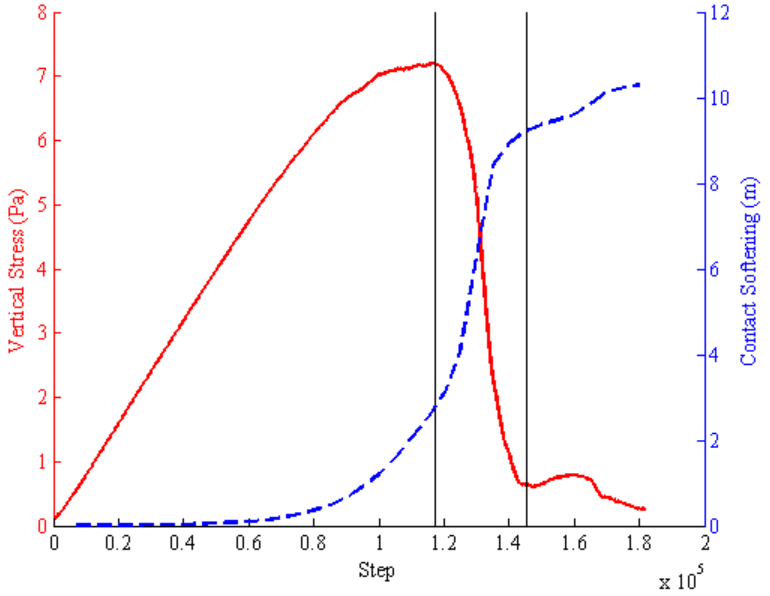

Figure D.11: Contact softening, EPC Test with 1.5 GPa loading system

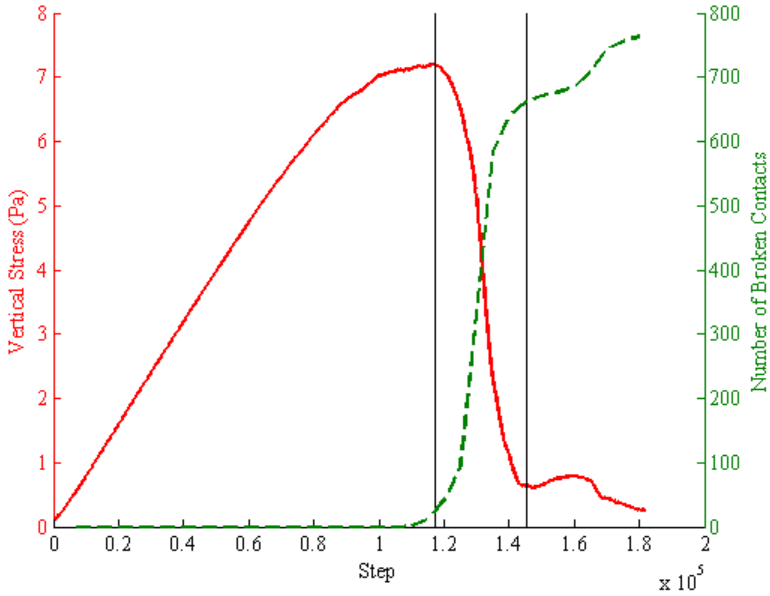

Figure D.12: Broken contacts, EPC Test with 1.5 GPa loading system

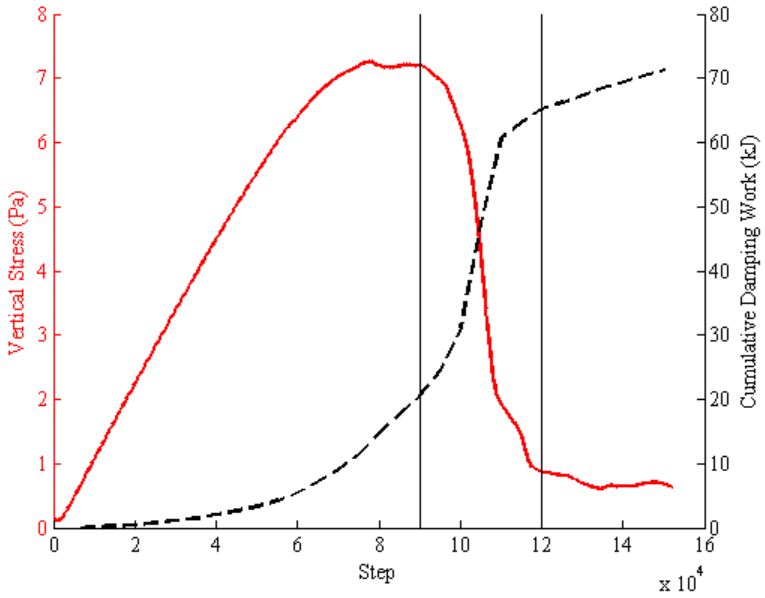

Figure D.13: Damping work, EPC Test with 2.5 GPa loading system

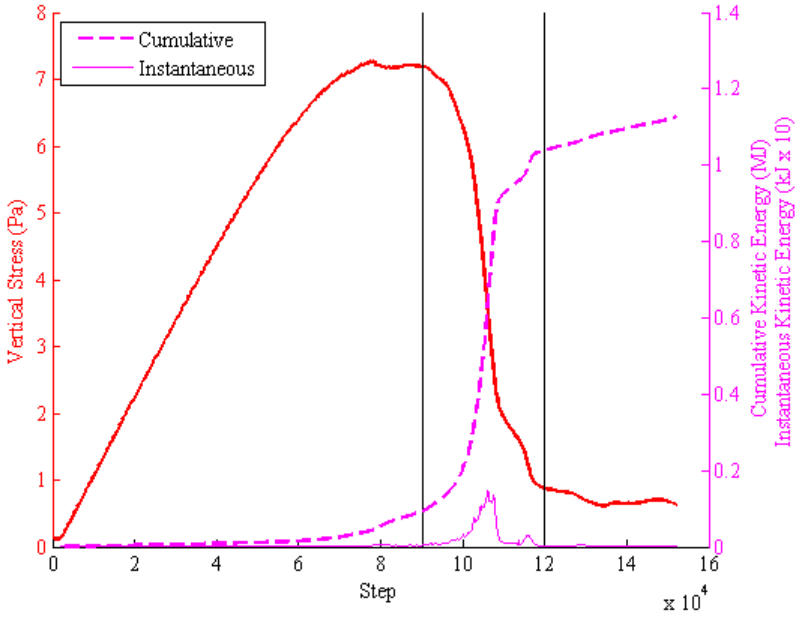

Figure D.14: Kinetic energy, EPC Test with 2.5 GPa loading system

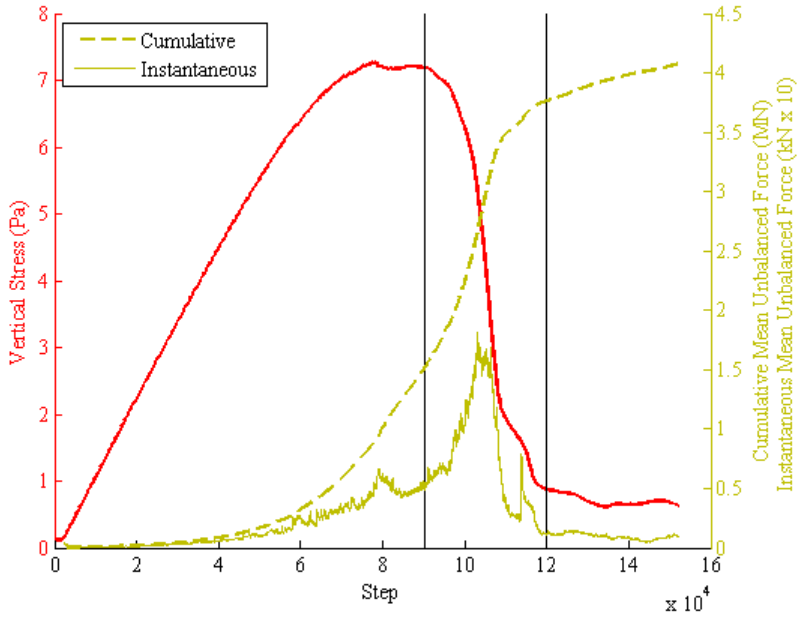

Figure D.15: Mean unbalanced force, EPC Test with 2.5 GPa loading system

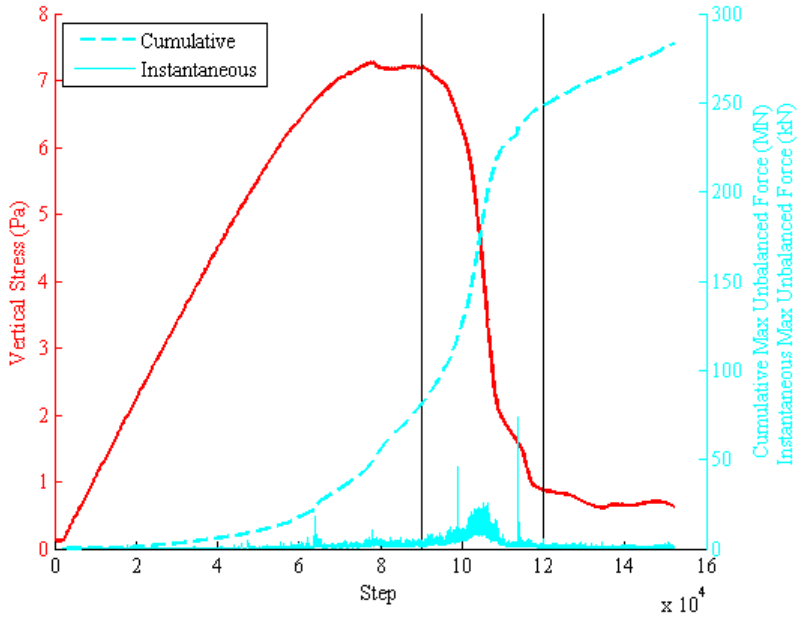

Figure D.16: Maximum unbalanced force, EPC Test with 2.5 GPa loading system

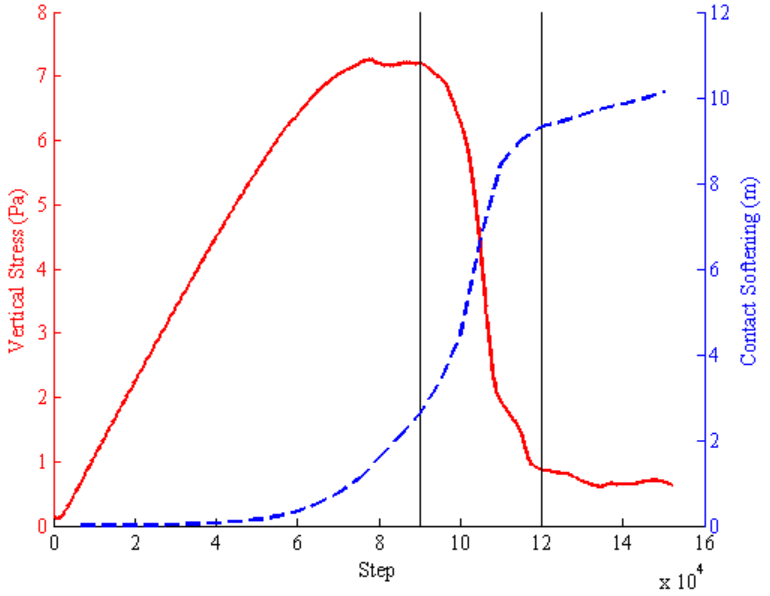

Figure D.17: Contact softening, EPC Test with 2.5 GPa loading system

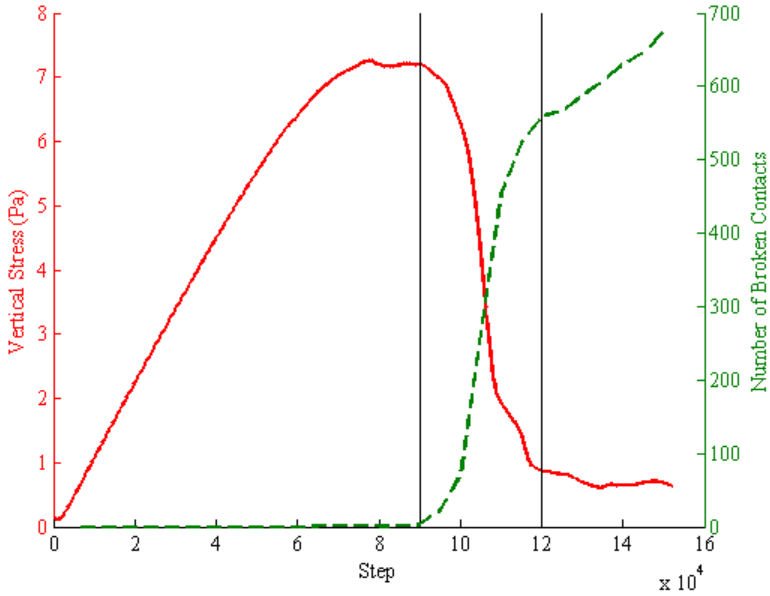

Figure D.18: Broken contacts, EPC Test with 2.5 GPa loading system

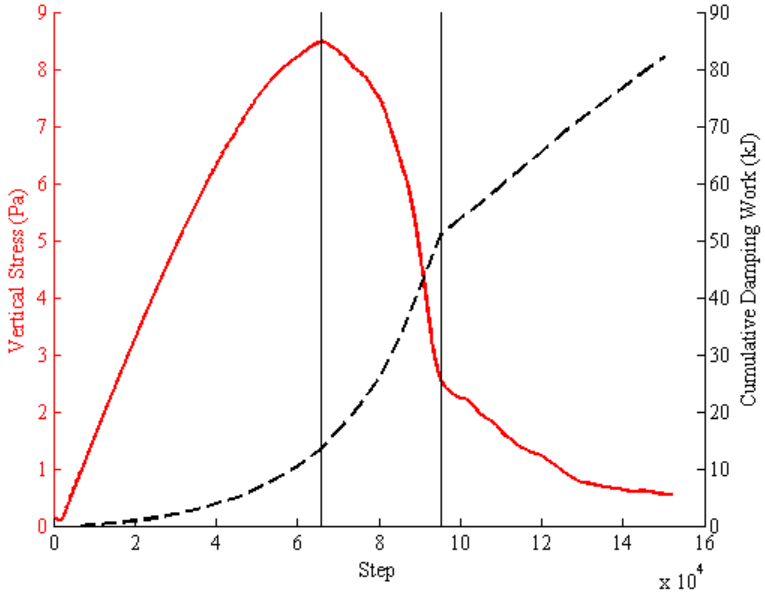

Figure D.19: Damping work, EPC Test with 5 GPa loading system

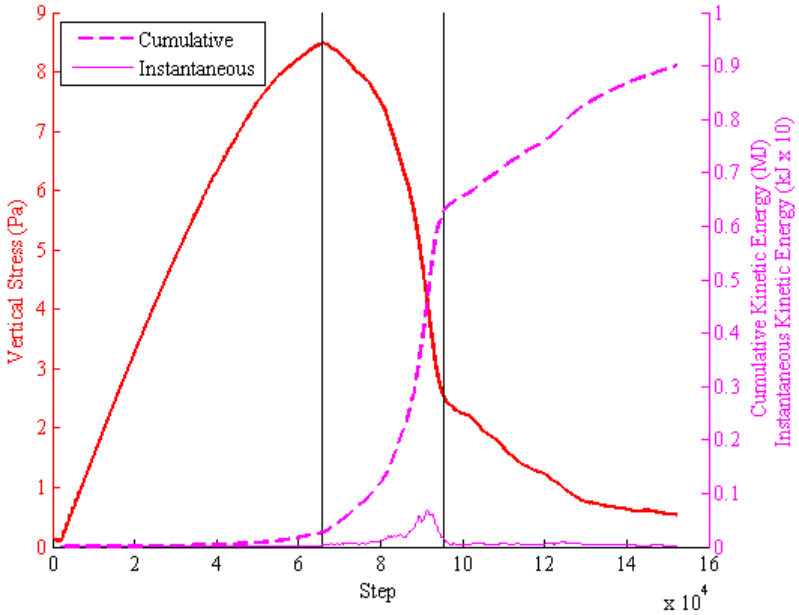

Figure D.20: Kinetic energy, EPC Test with 5 GPa loading system

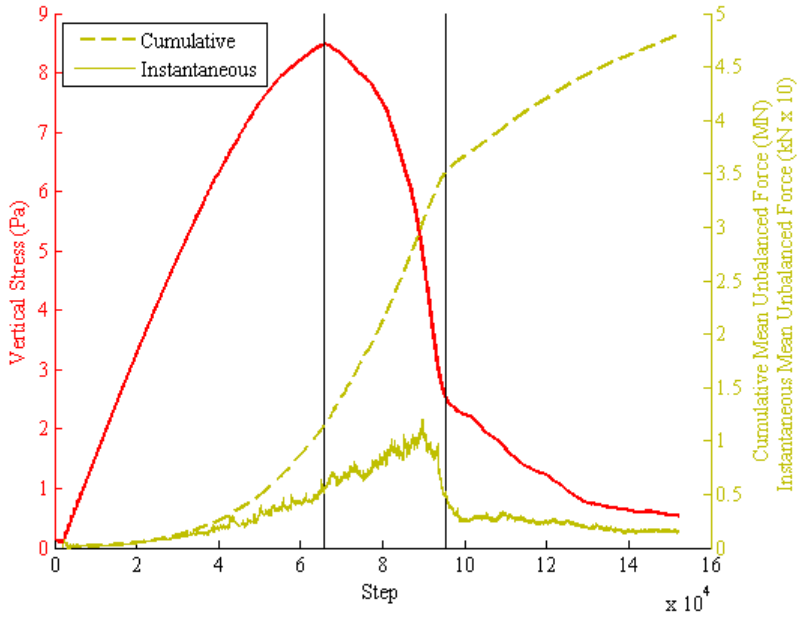

Figure D.21: Mean unbalanced force, EPC Test with 5 GPa loading system

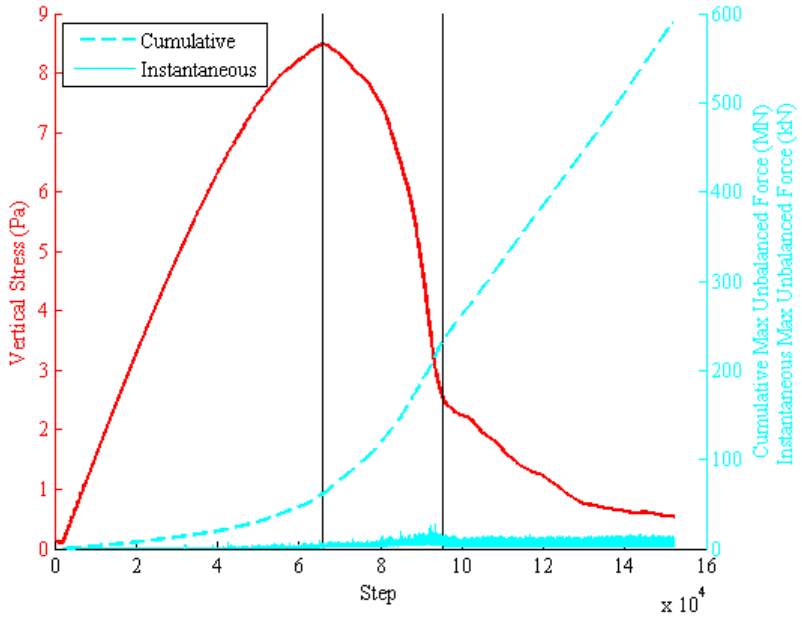

Figure D.22: Maximum unbalanced force, EPC Test with 5 GPa loading system

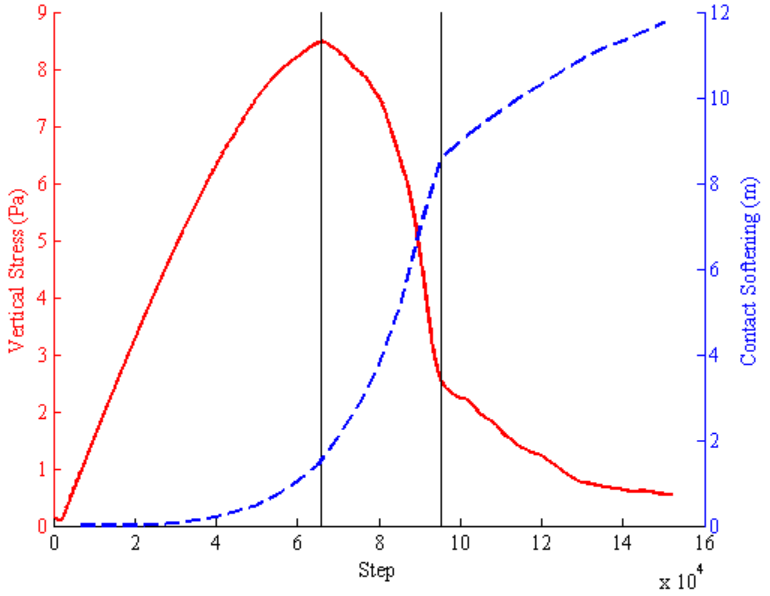

Figure D.23: Contact softening, EPC Test with 5 GPa loading system

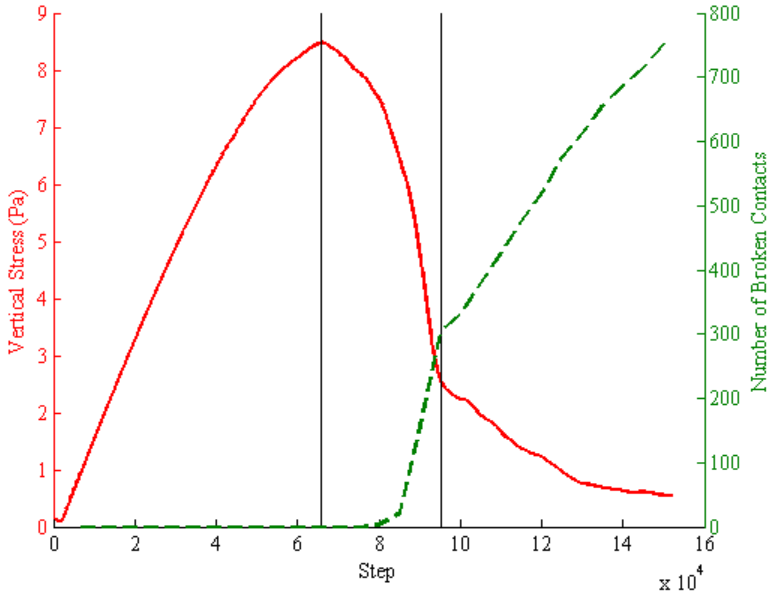

Figure D.24: Broken contacts, EPC Test with 5 GPa loading system

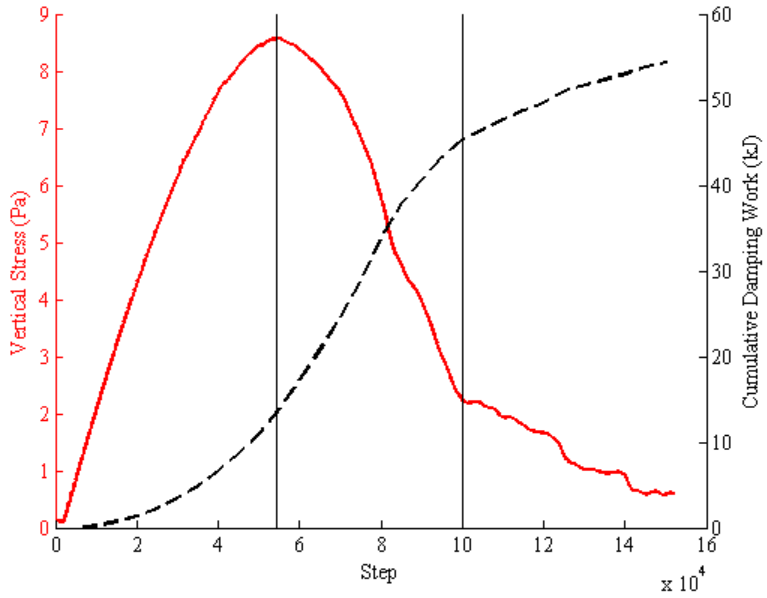

Figure D.25: Damping work, EPC Test with 10 GPa loading system

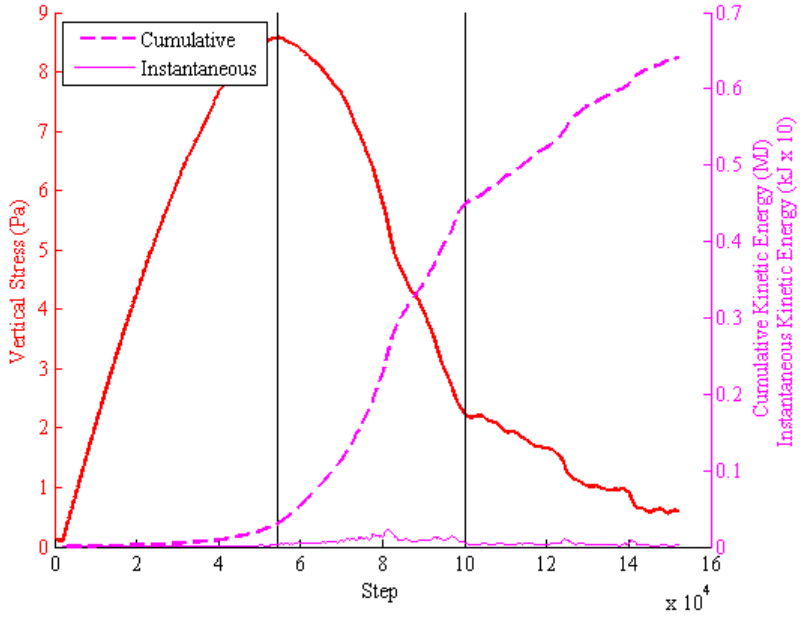

Figure D.26: Kinetic energy, EPC Test with 10 GPa loading system

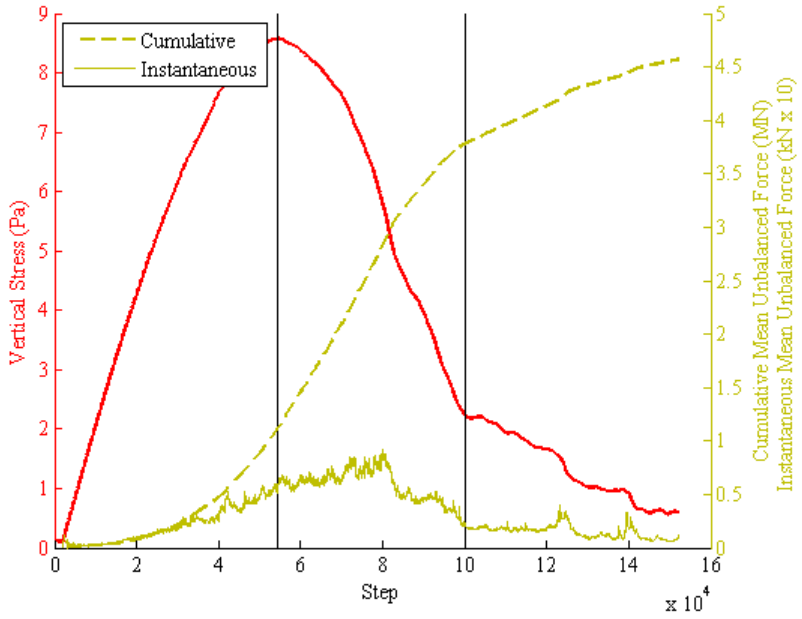

Figure D.27: Mean unbalanced force, EPC Test with 10 GPa loading system

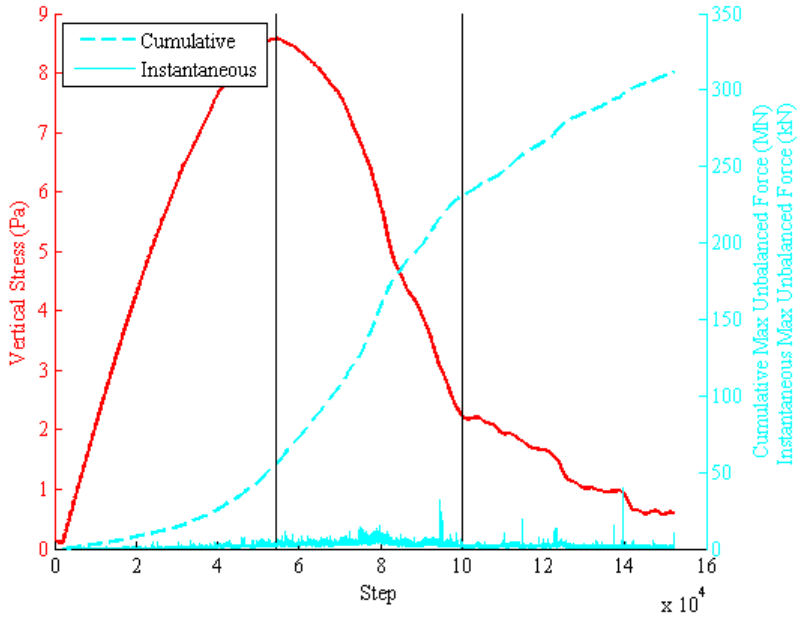

Figure D.28: Maximum unbalanced force, EPC Test with 10 GPa loading system

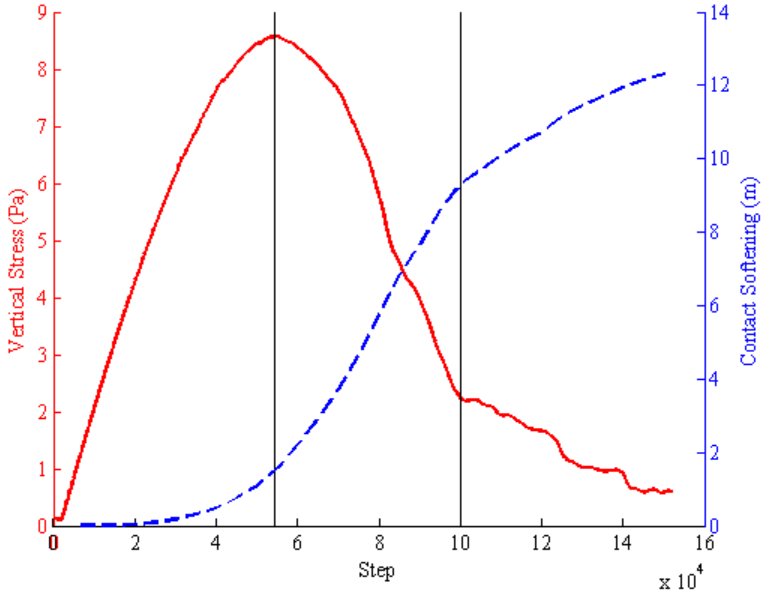

Figure D.29: Contact softening, EPC Test with 10 GPa loading system

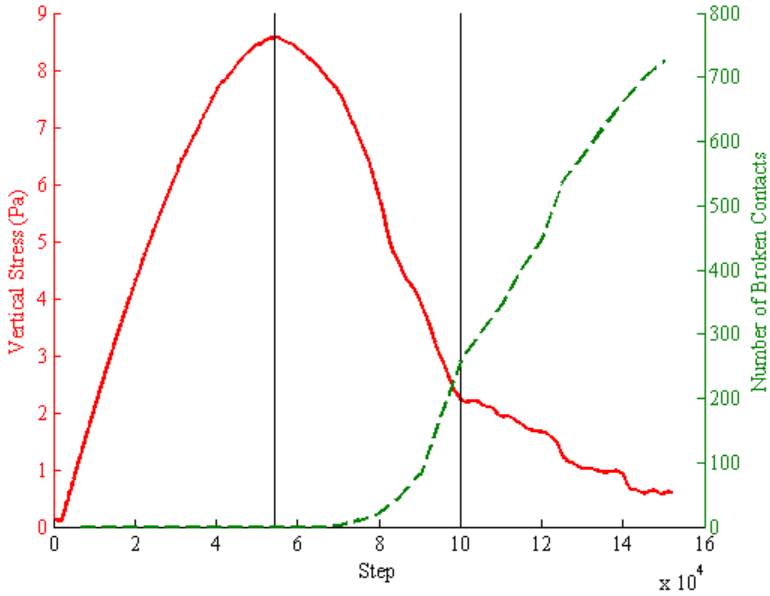

Figure D.30: Broken contacts, EPC Test with 10 GPa loading system

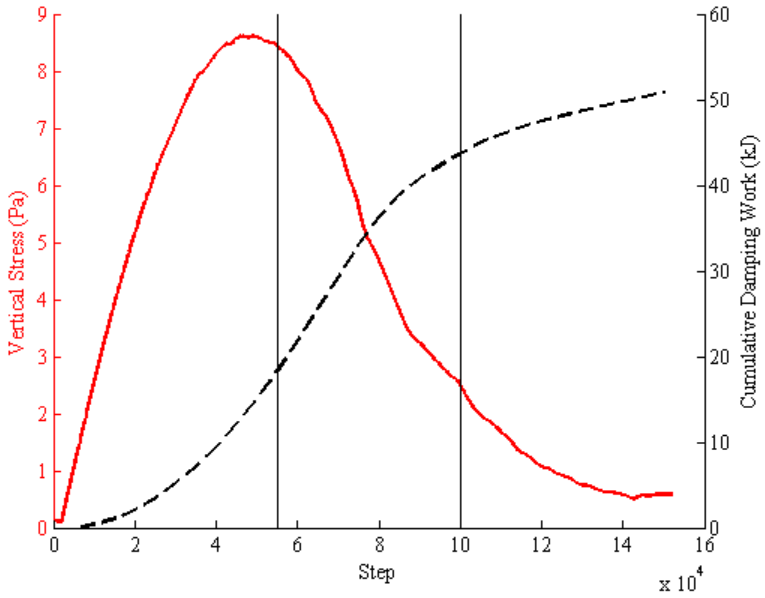

Figure D.31: Damping work, EPC Test with 20 GPa loading system

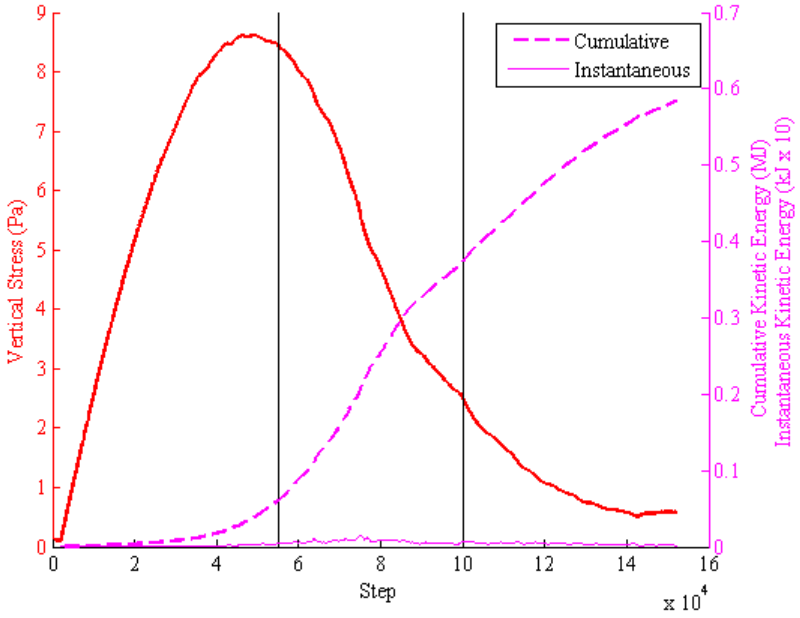

Figure D.32: Kinetic energy, EPC Test with 20 GPa loading system

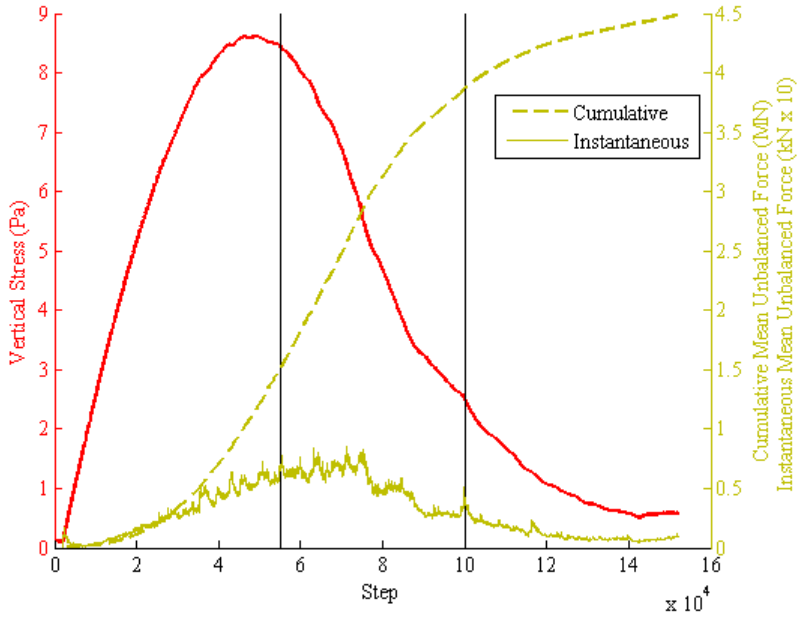

Figure D.33: Mean unbalanced force, EPC Test with 20 GPa loading system

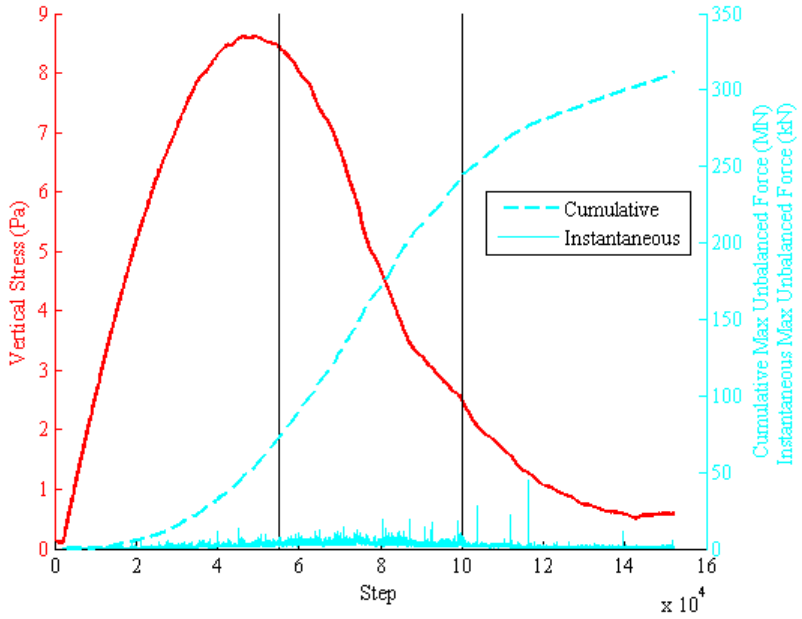

Figure D.34: Maximum unbalanced force, EPC Test with 20 GPa loading system

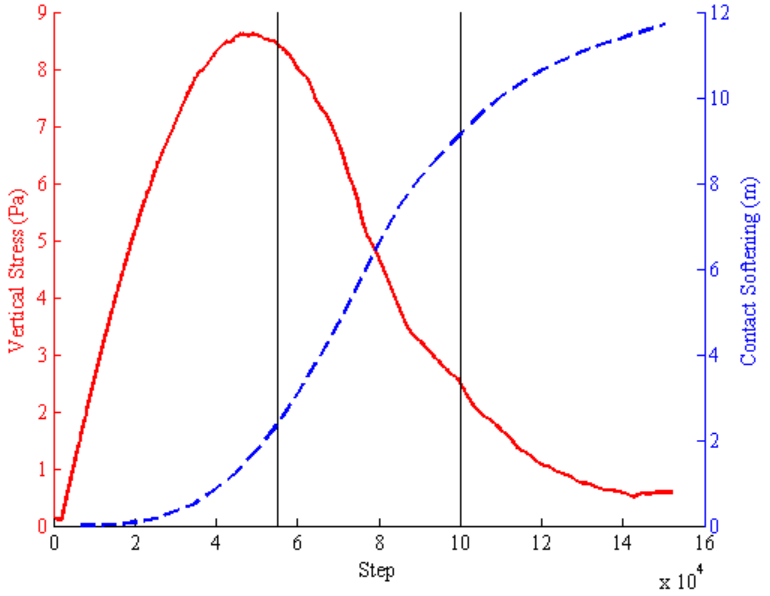

Figure D.35: Contact softening, EPC Test with 20 GPa loading system

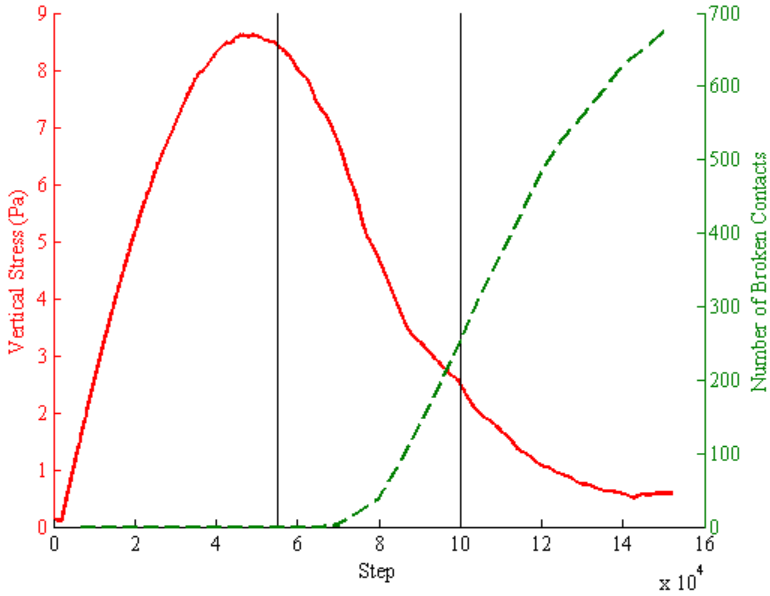

Figure D.36: Broken contacts, EPC Test with 20 GPa loading system

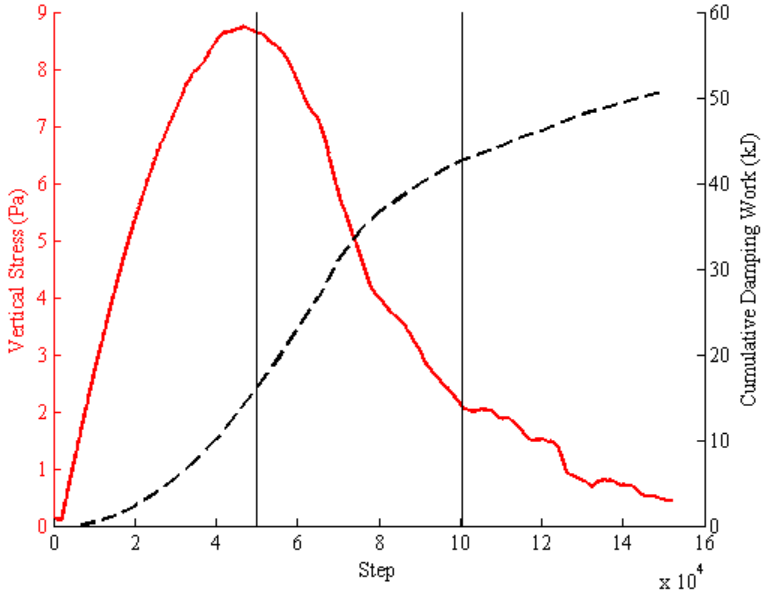

Figure D.37: Damping work, EPC Test with 35 GPa loading system

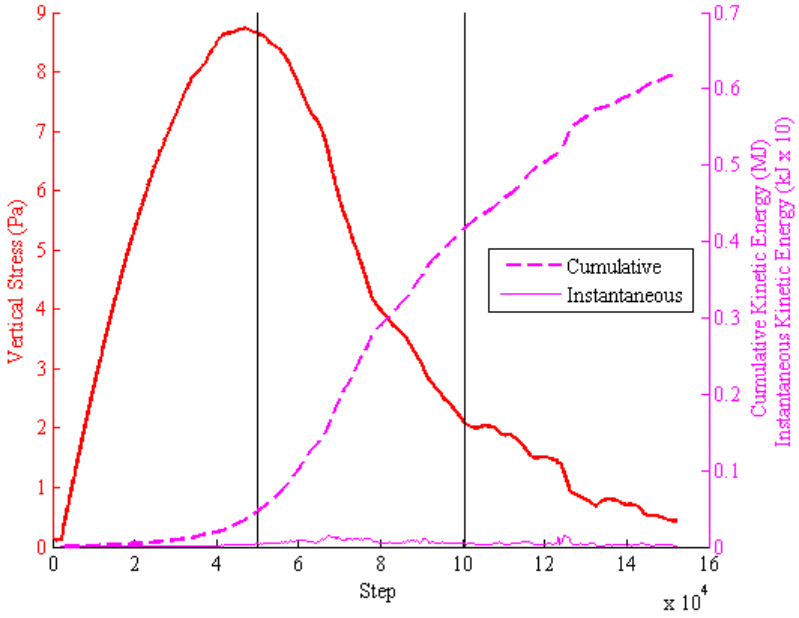

Figure D.38: Kinetic energy, EPC Test with 35 GPa loading system

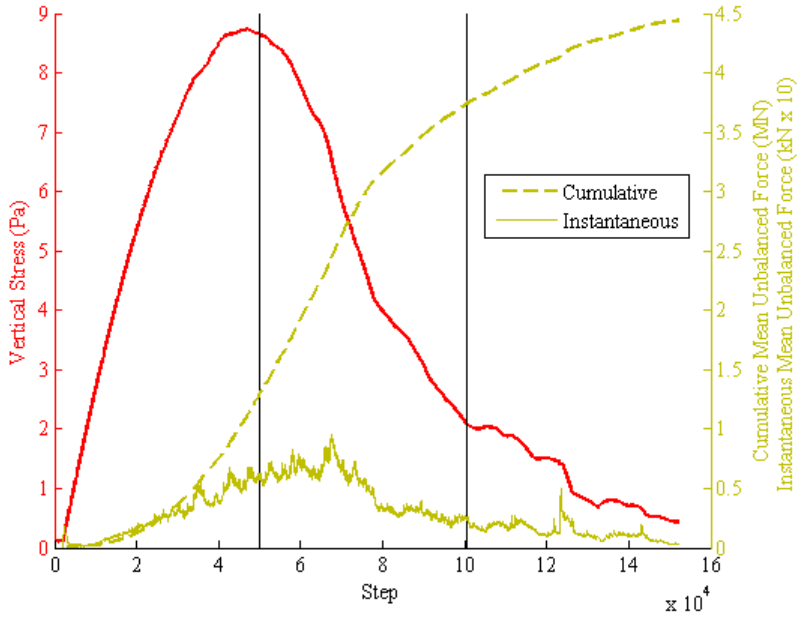

Figure D.39: Mean unbalanced force, EPC Test with 35 GPa loading system

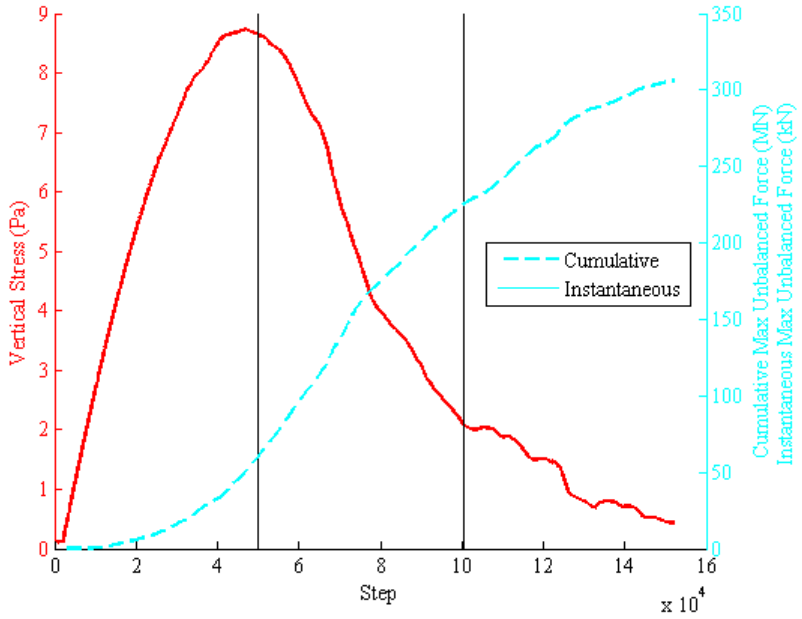

Figure D.40: Maximum unbalanced force, EPC Test with 35 GPa loading system

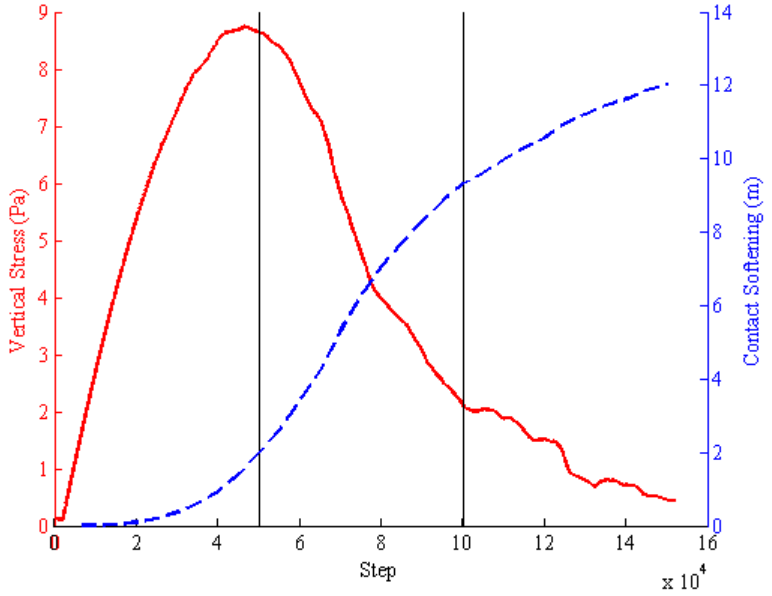

Figure D.41: Contact softening, EPC Test with 35 GPa loading system

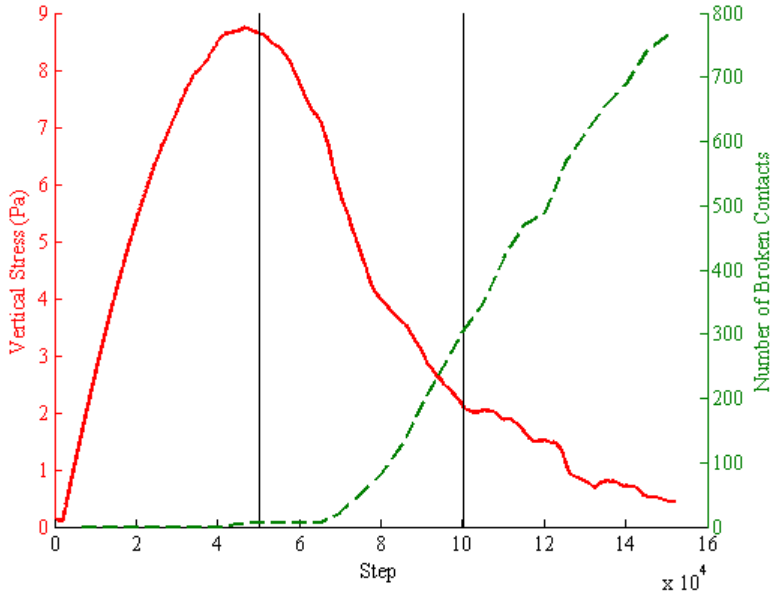

Figure D.42: Broken contacts, EPC Test with 35 GPa loading system

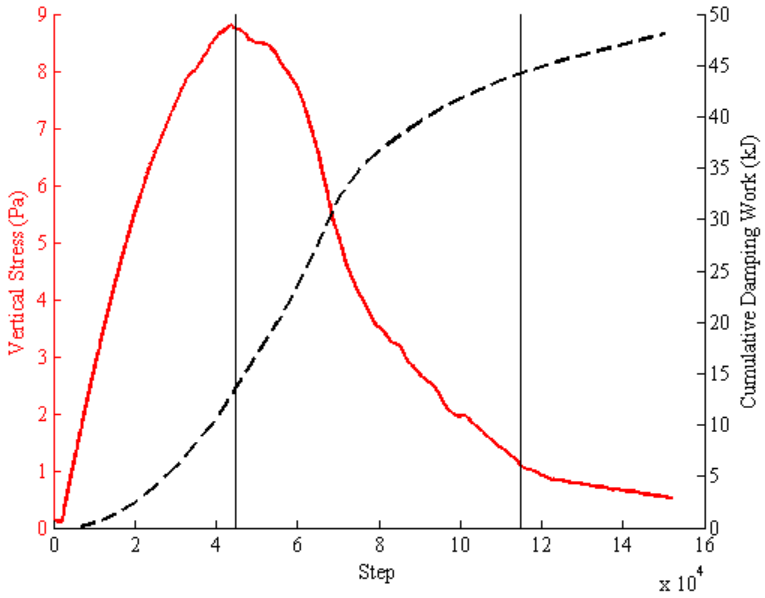

Figure D.43: Damping work, EPC Test with 50 GPa loading system

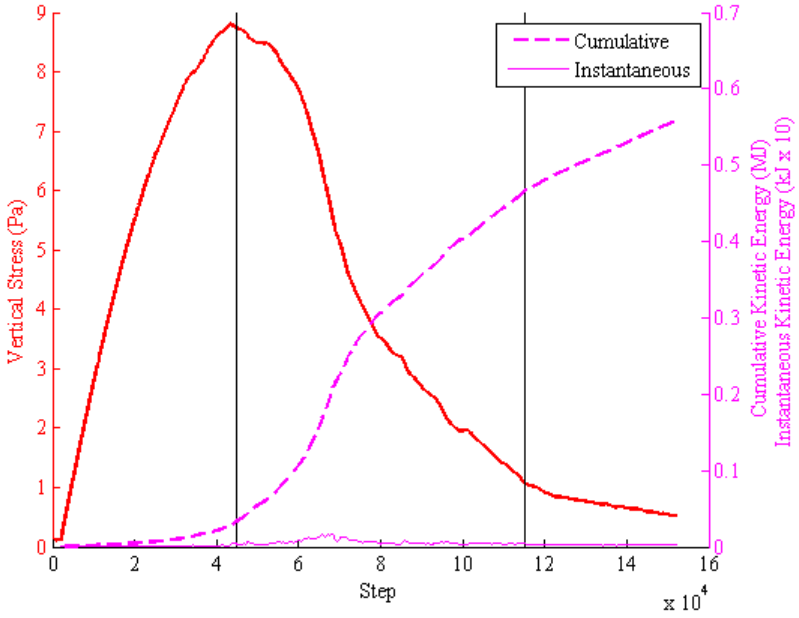

Figure D.44: Kinetic energy, EPC Test with 50 GPa loading system

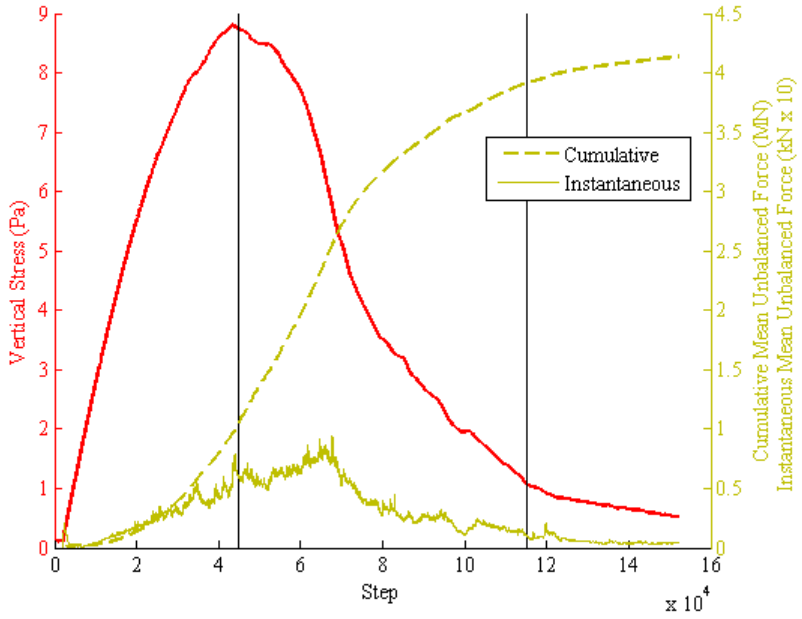

Figure D.45: Mean unbalanced force, EPC Test with 50 GPa loading system

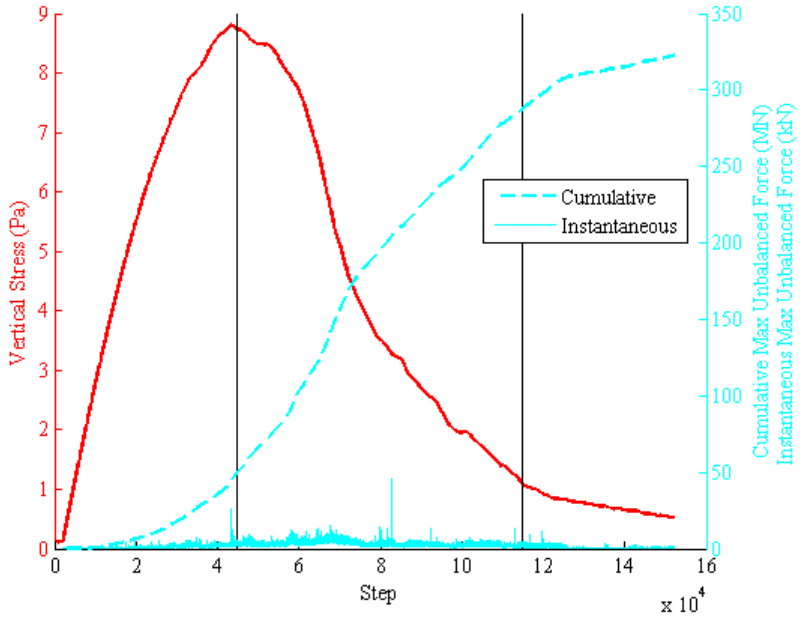

Figure D.46: Maximum unbalanced force, EPC Test with 50 GPa loading system

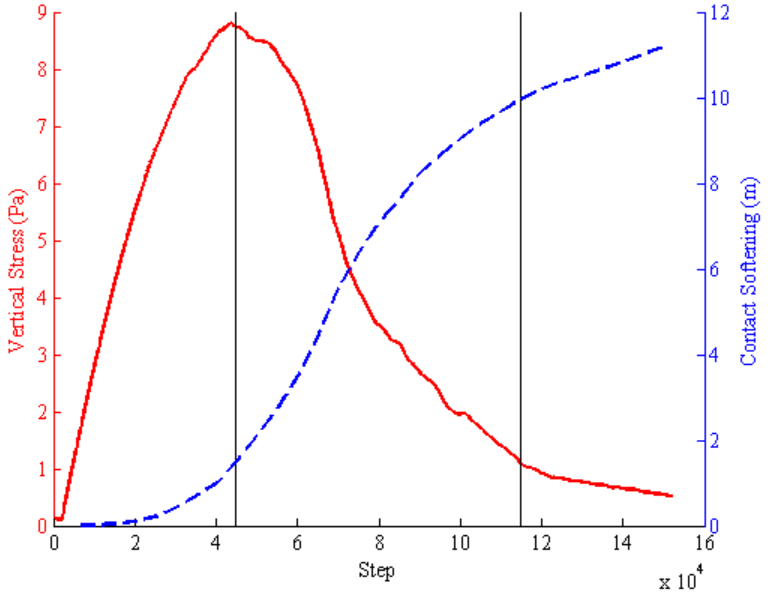

Figure D.47: Contact softening, EPC Test with 50 GPa loading system

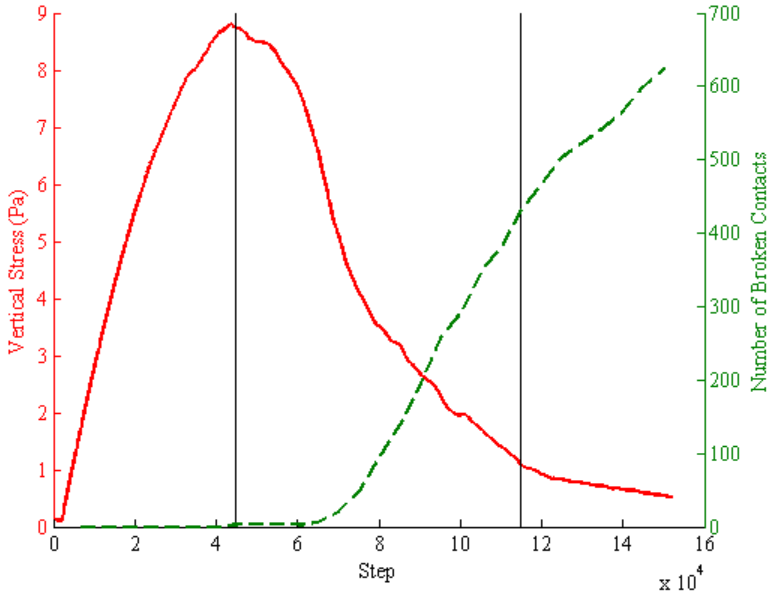

Figure D.48: Broken contacts, EPC Test with 50 GPa loading system

APPENDIX E - SPCS TEST INDICATOR PLOTS

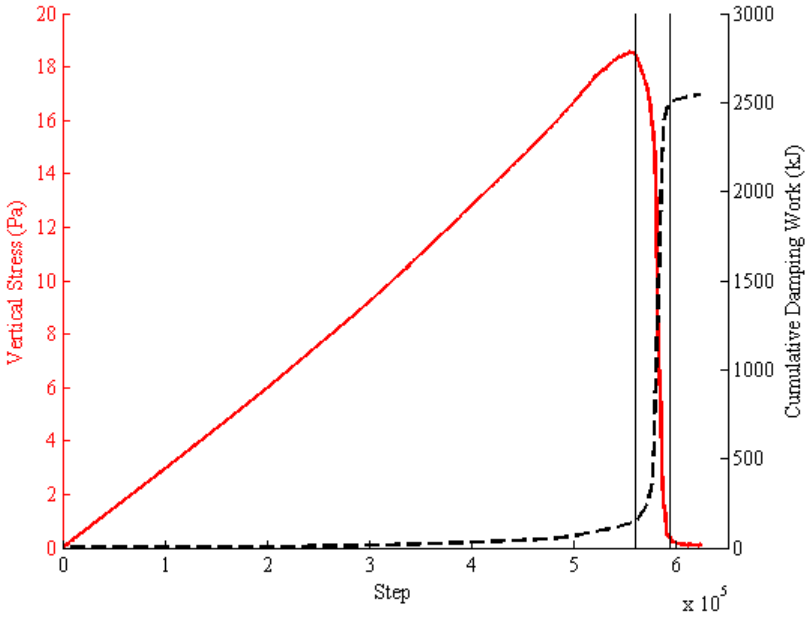

Figure E.1: Damping work, width to height one pillar 5 GPa loading system

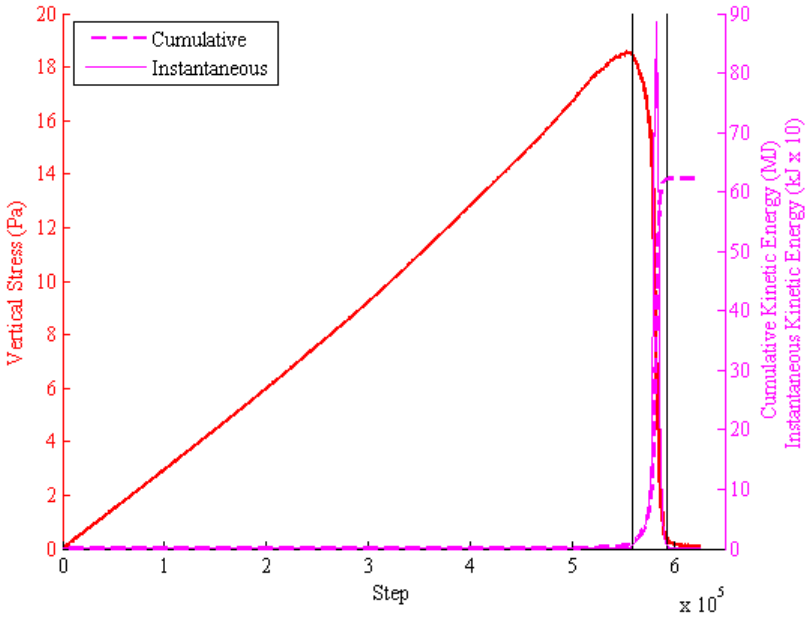

Figure E.2: Kinetic energy, width to height one pillar 5 GPa loading system

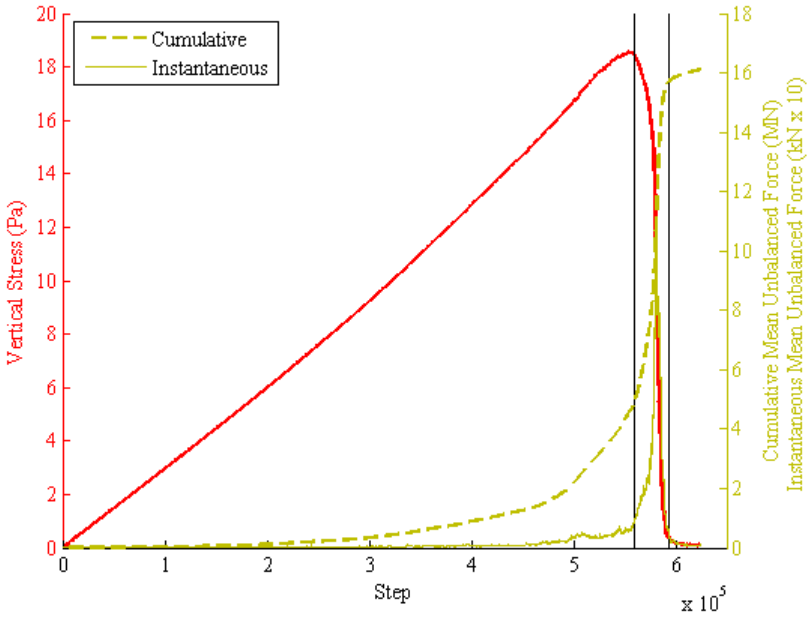

Figure E.3: Mean unbalanced force, width to height one pillar 5 GPa loading system

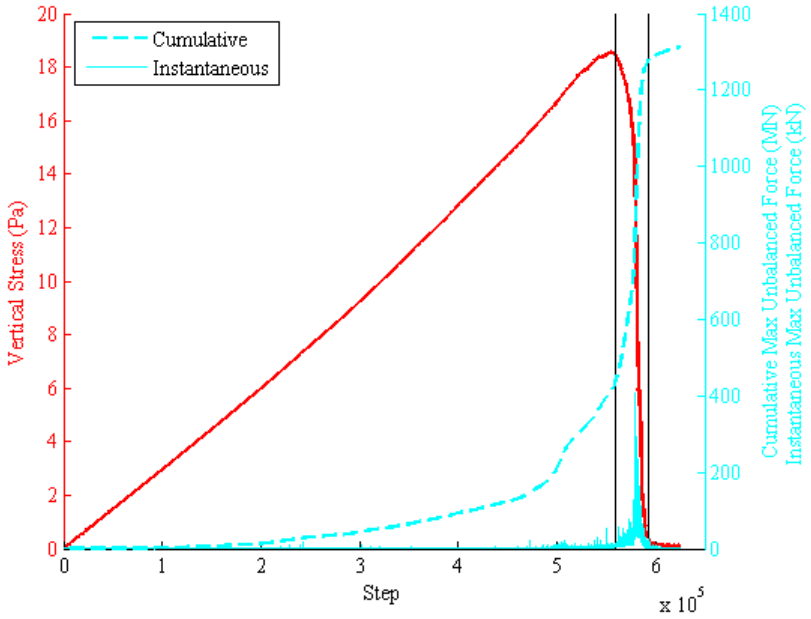

Figure E.4: Max unbalanced force, width to height one pillar 5 GPa loading system

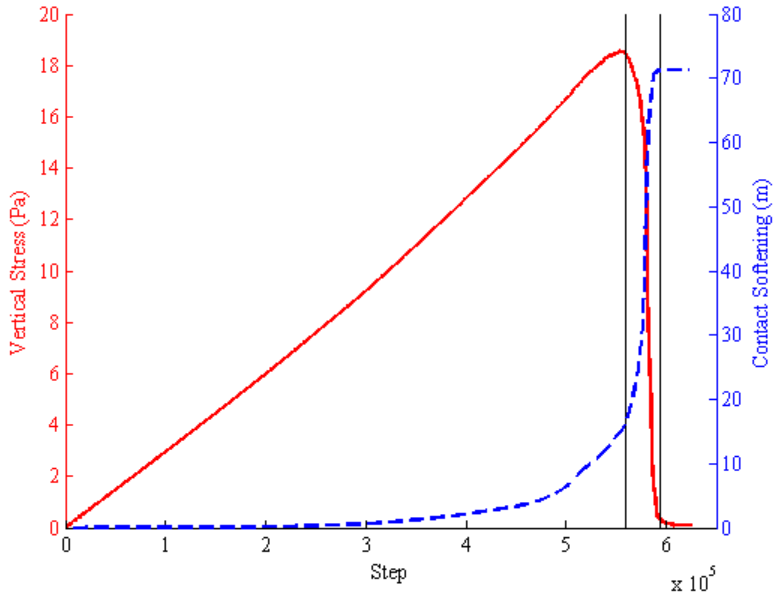

Figure E.5: Contact softening, width to height one pillar 5 GPa loading system

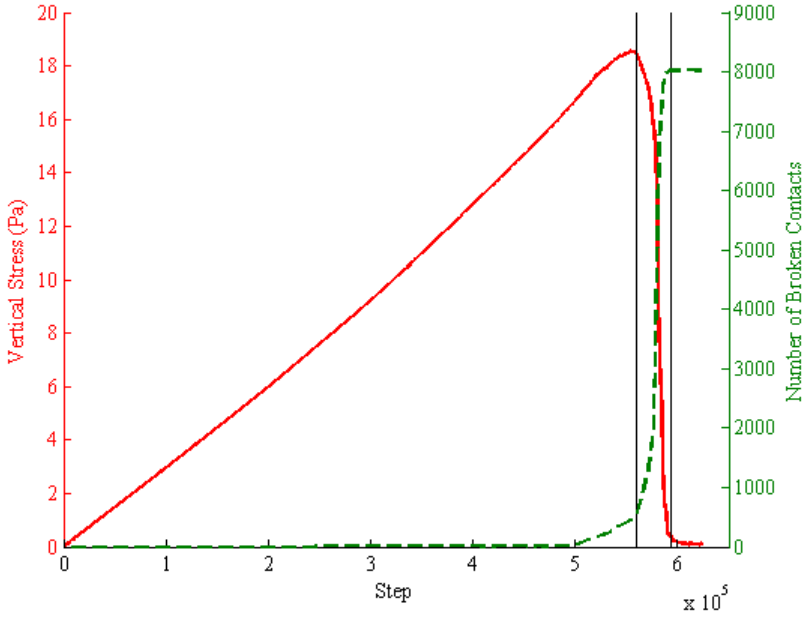

Figure E.6: Broken contacts, width to height one pillar 5 GPa loading system

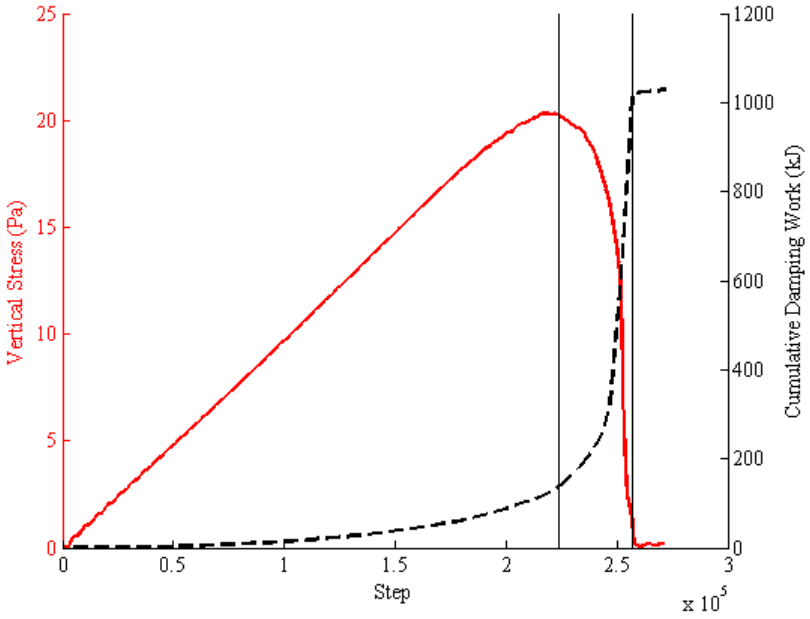

Figure E.7: Damping work, width to height one pillar 20 GPa loading system

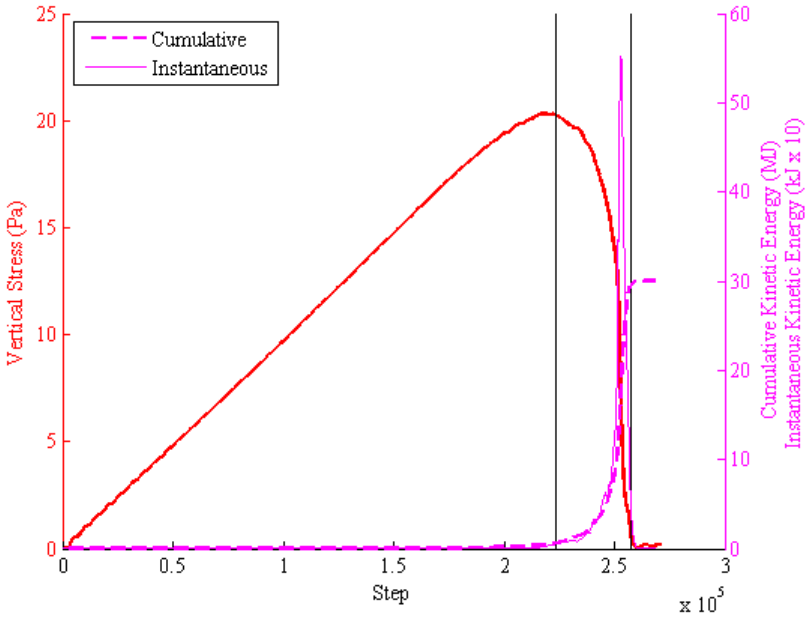

Figure E.8: Kinetic energy, width to height one pillar 20 GPa loading system

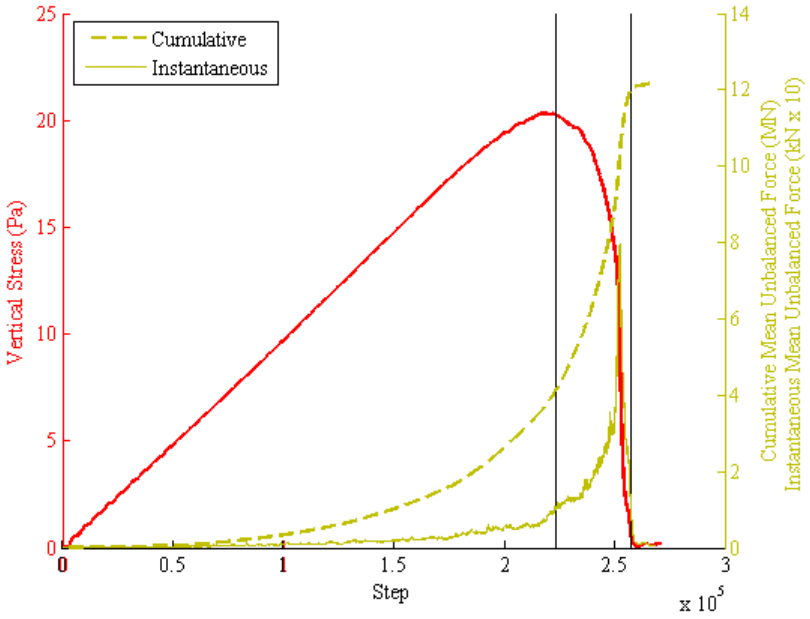

Figure E.9: Mean unbalanced force, width to height one pillar 20 GPa loading system

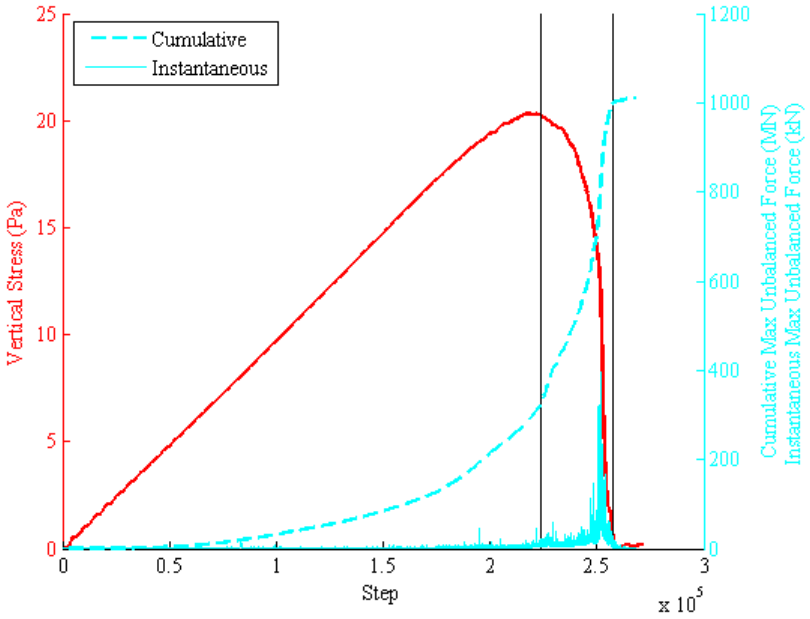

Figure E.10: Max unbalanced force, width to height one pillar 20 GPa loading system

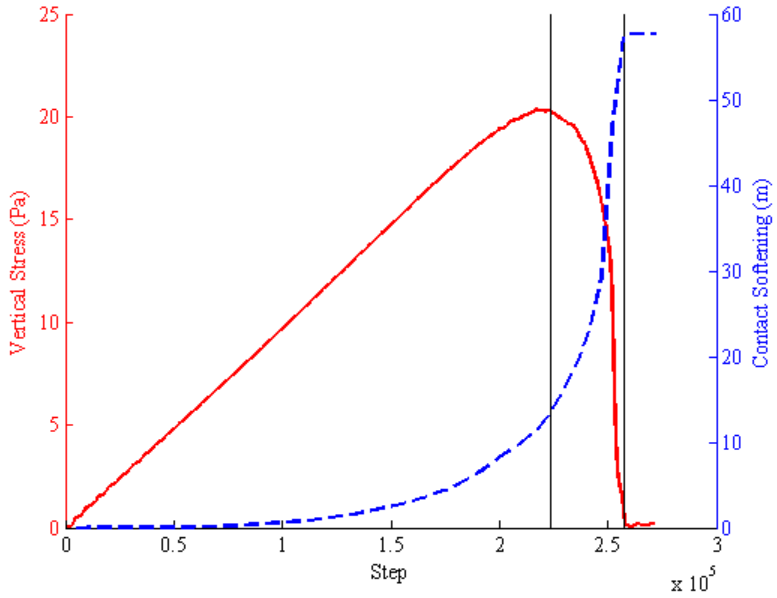

Figure E.11: Contact softening, width to height one pillar 20 GPa loading system

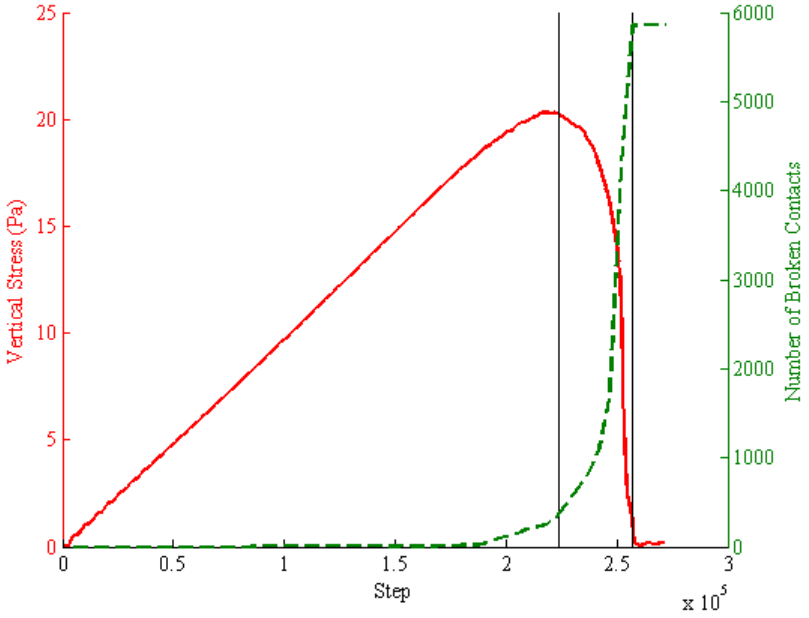

Figure E.12: Broken contacts, width to height one pillar 20 GPa loading system

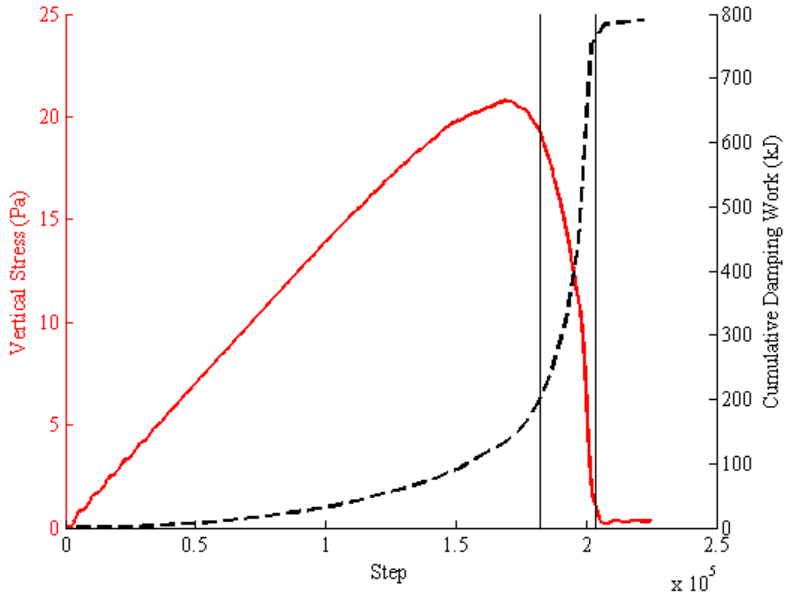

Figure E.13: Damping work, width to height one pillar 35 GPa loading system

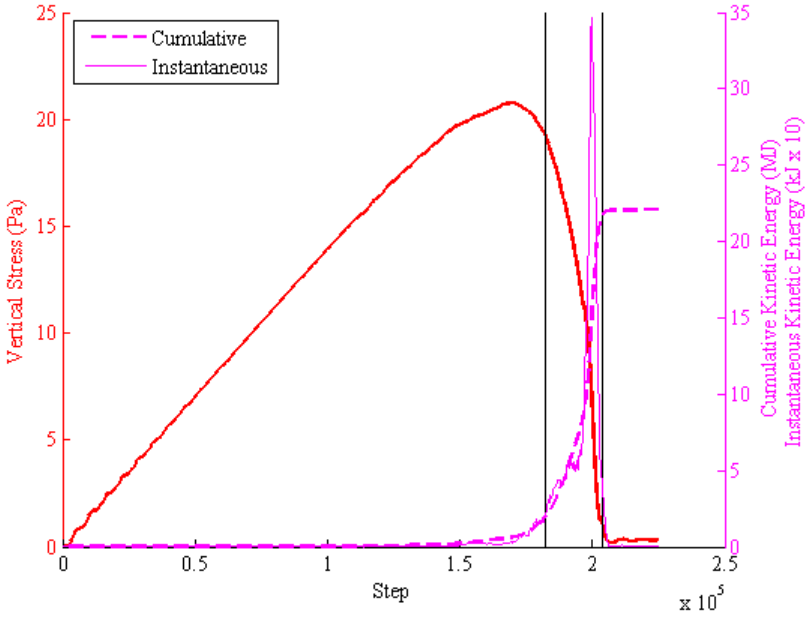

Figure E.14: Kinetic energy, width to height one pillar 35 GPa loading system

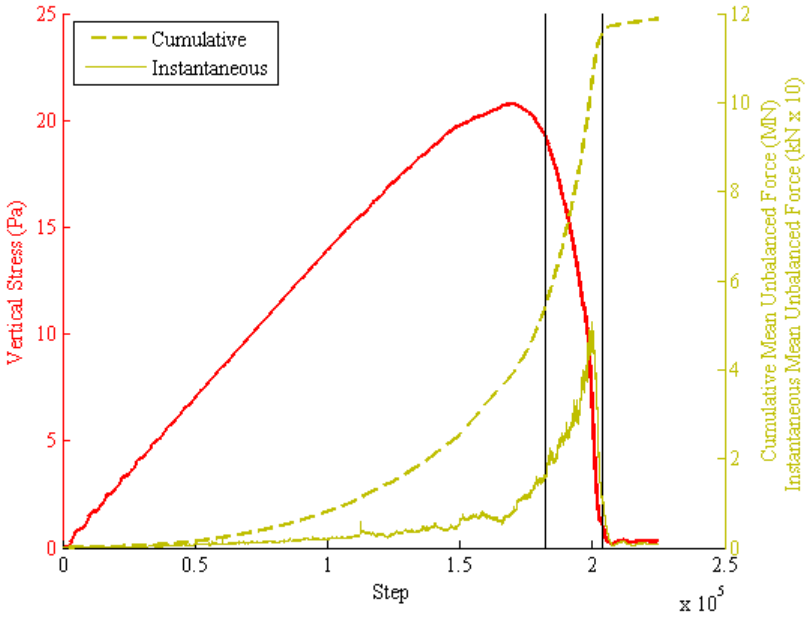

Figure E.15: Mean unbalanced force, width to height one pillar 35 GPa loading system

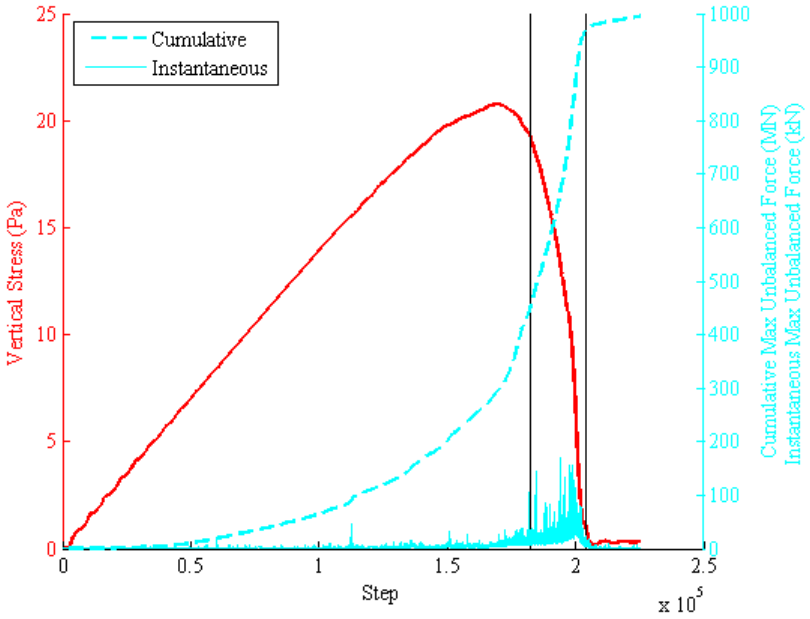

Figure E.16: Max unbalanced force, width to height one pillar 35 GPa loading system

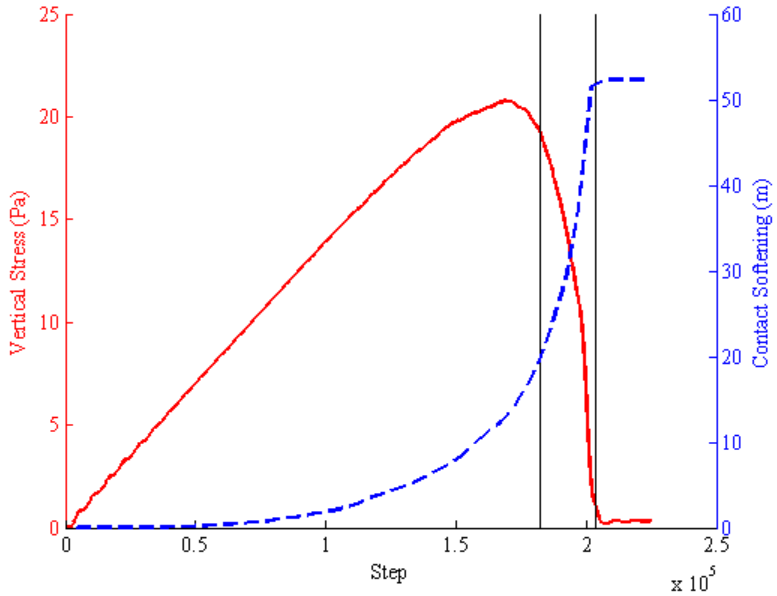

Figure E.17: Contact softening, width to height one pillar 35 GPa loading system

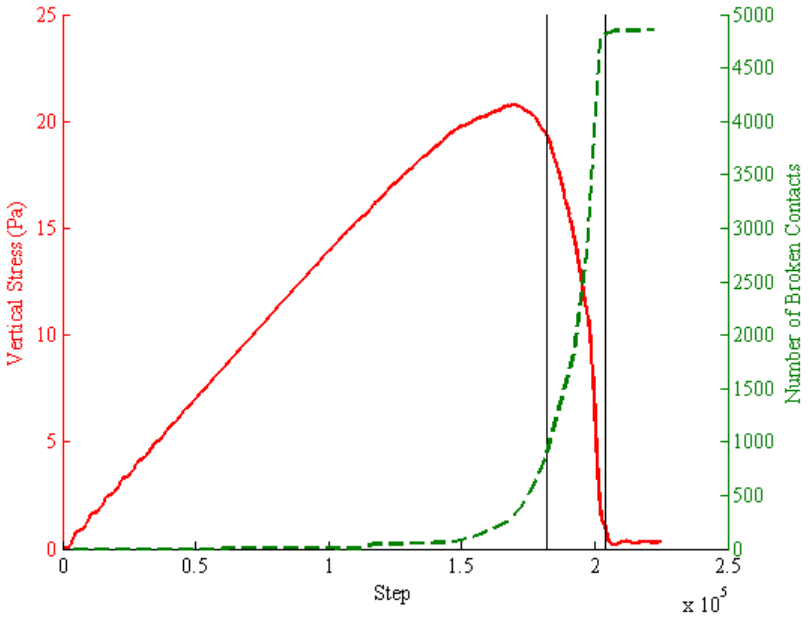

Figure E.18: Broken contacts, width to height one pillar 35 GPa loading system

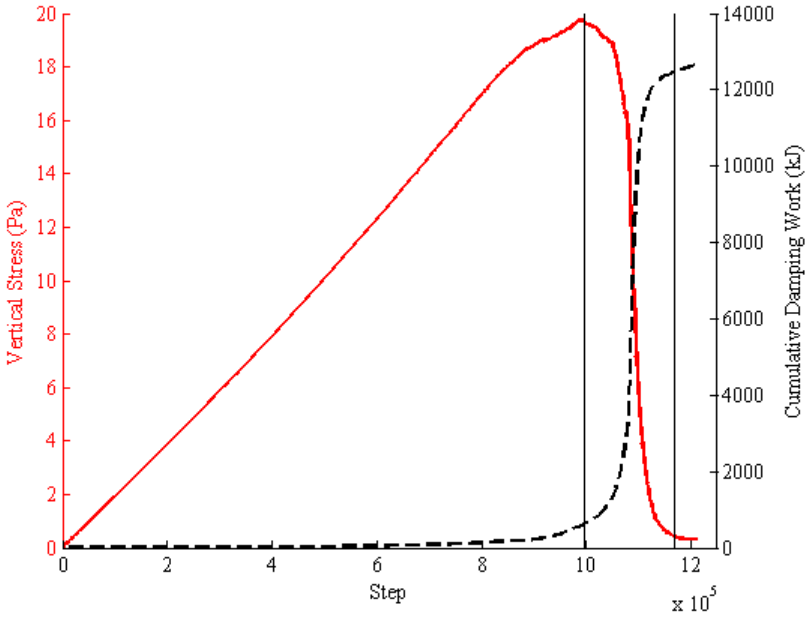

Figure E.19: Damping work, width to height two pillar 5 GPa loading system

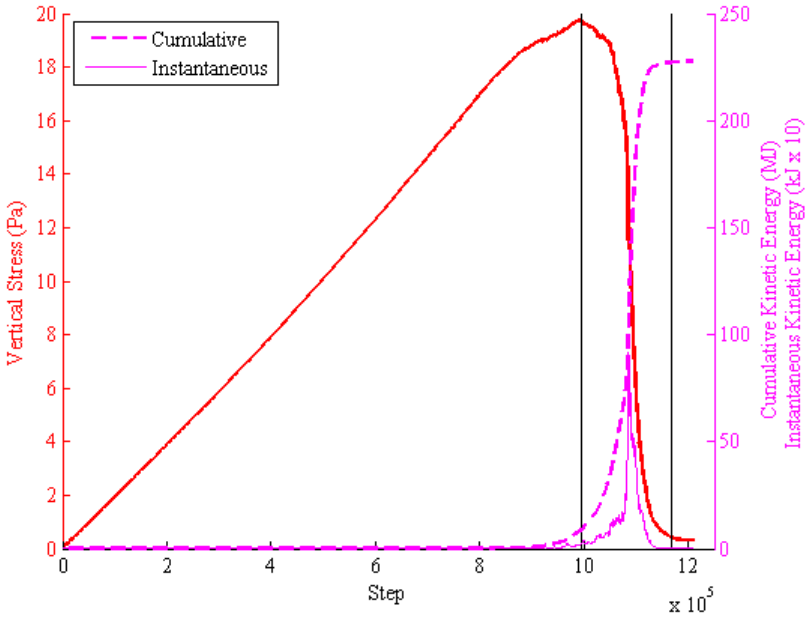

Figure E.20: Kinetic energy, width to height two pillar 5 GPa loading system

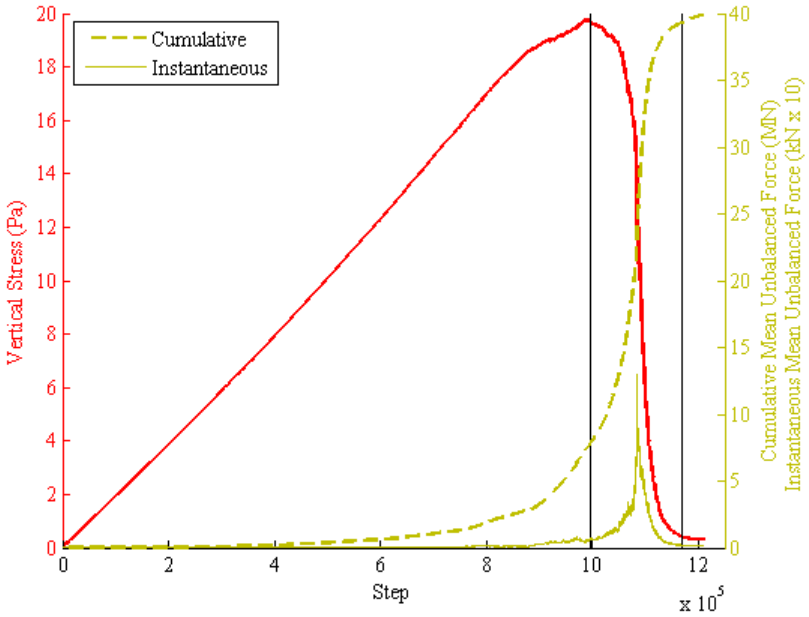

Figure E.21: Mean unbalanced force, width to height two pillar 5 GPa loading system

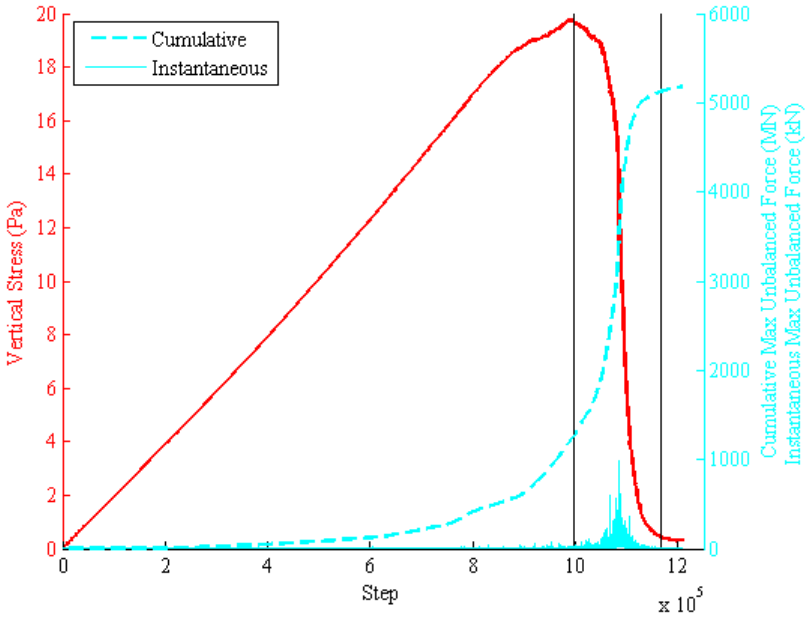

Figure E.22: Max unbalanced force, width to height two pillar 5 GPa loading system

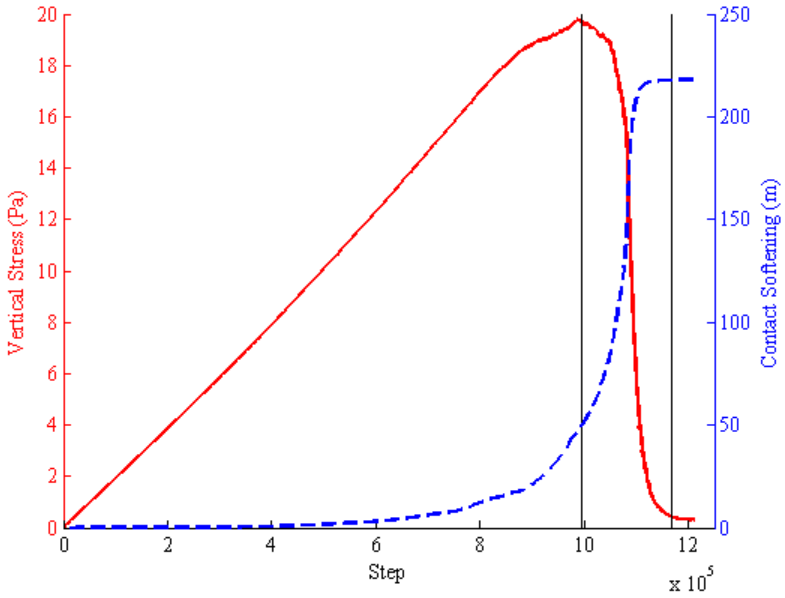

Figure E.23: Contact softening, width to height two pillar 5 GPa loading system

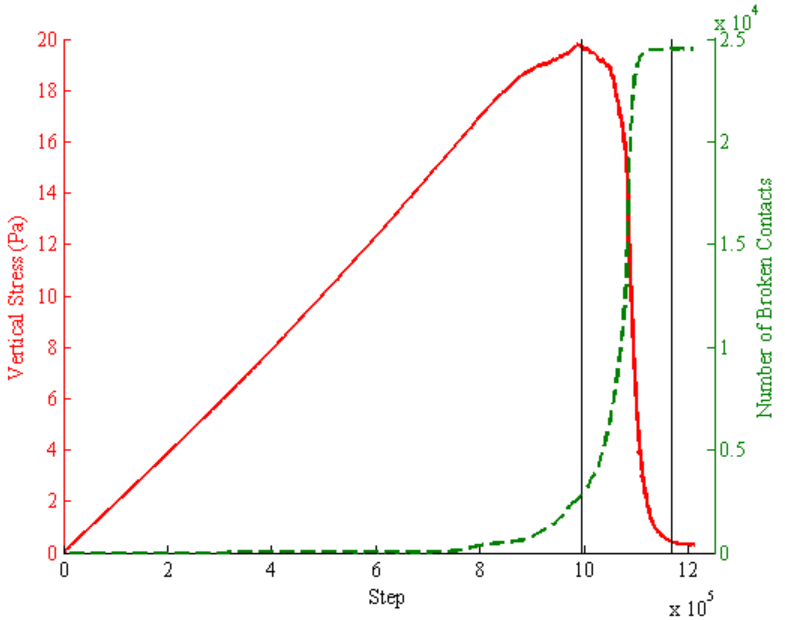

Figure E.24: Broken contacts, width to height two pillar 5 GPa loading system

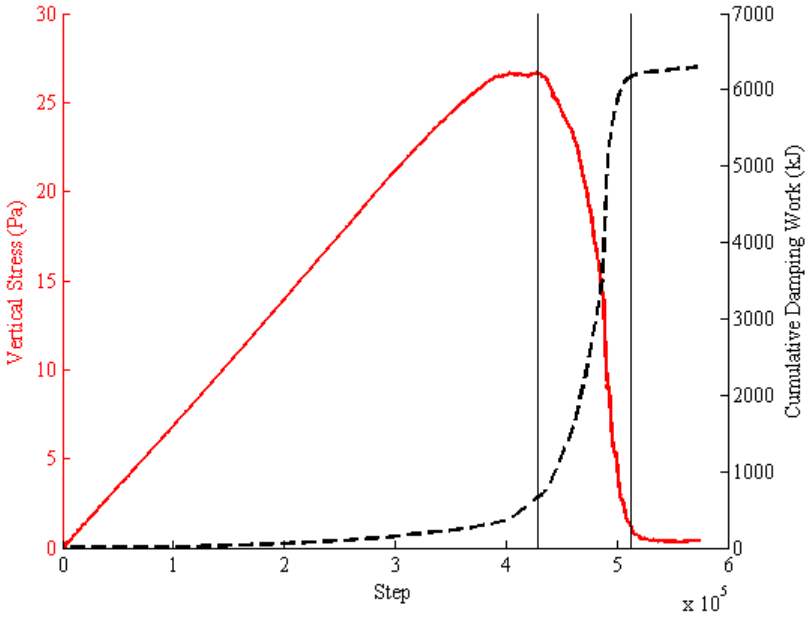

Figure E.25: Damping work, width to height two pillar 20 GPa loading system

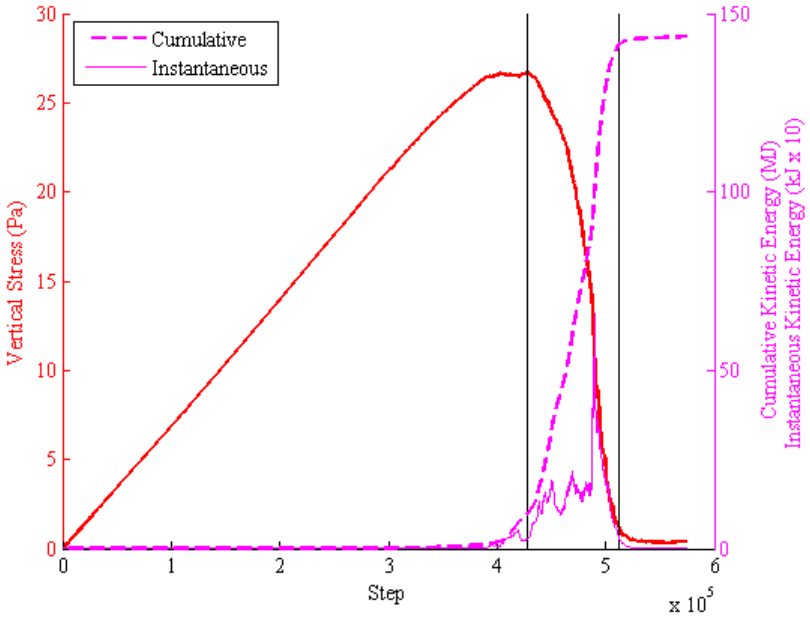

Figure E.26: Kinetic energy, width to height two pillar 20 GPa loading system

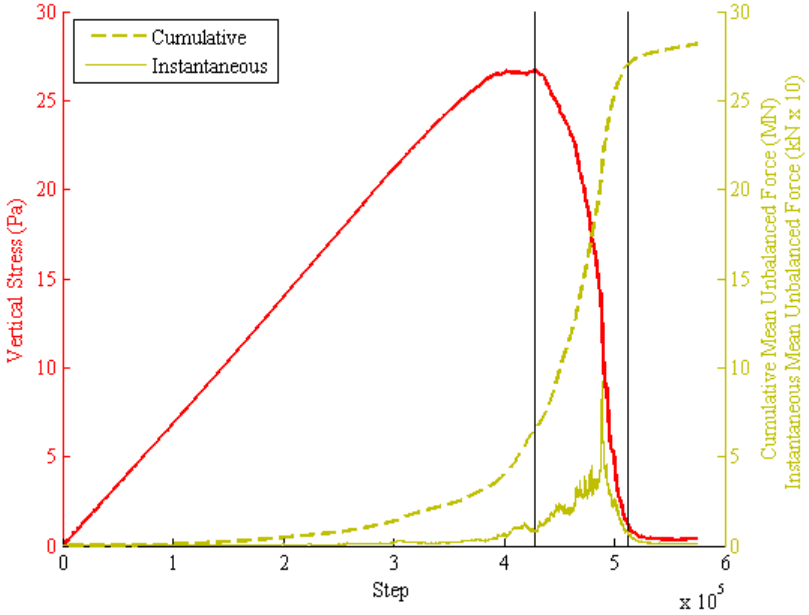

Figure E.27: Mean unbalanced force, width to height two pillar 20 GPa loading system

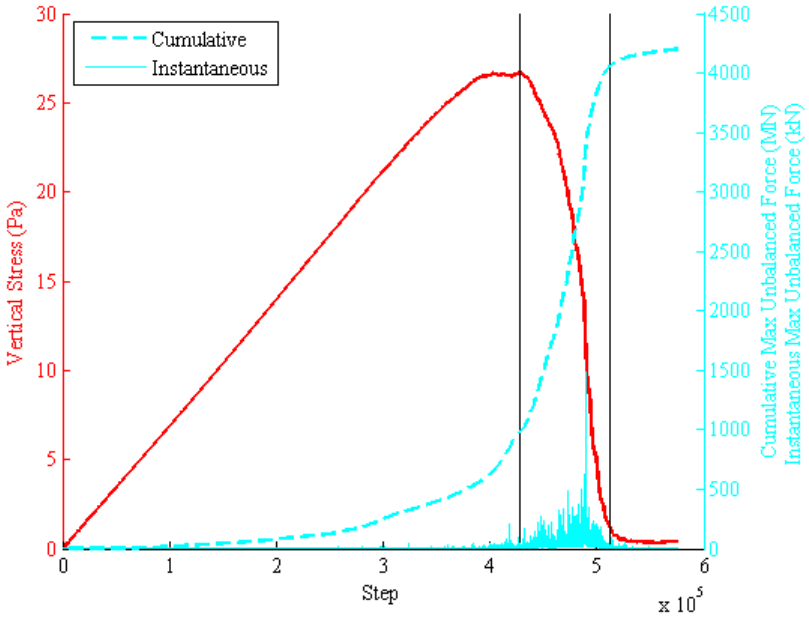

Figure E.28: Max unbalanced force, width to height two pillar 20 GPa loading system

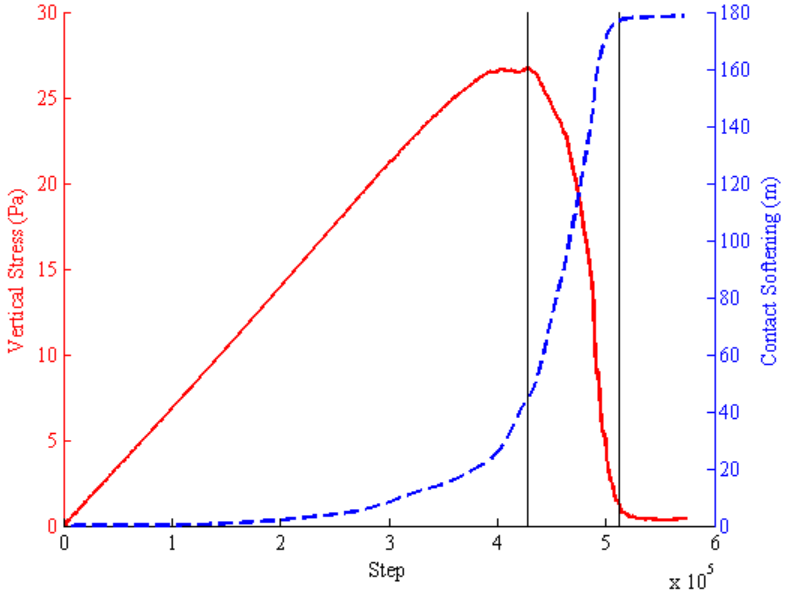

Figure E.29: Contact softening, width to height two pillar 20 GPa loading system

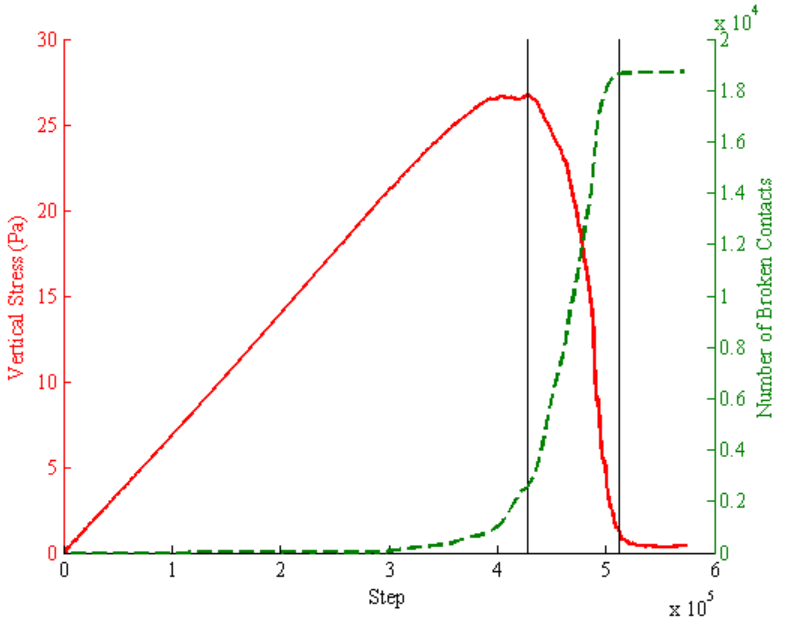

Figure E.30: Broken contacts, width to height two pillar 20 GPa loading system

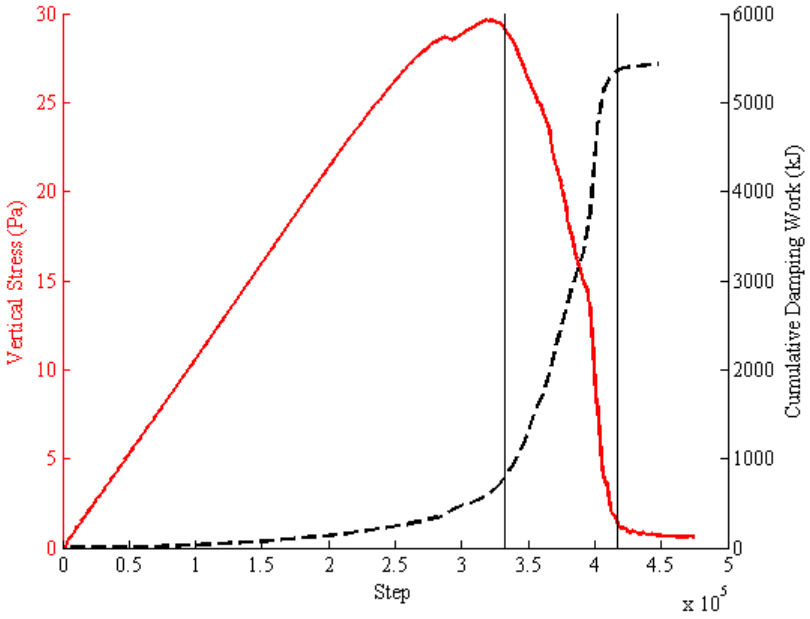

Figure E.31: Damping work, width to height two pillar 35 GPa loading system

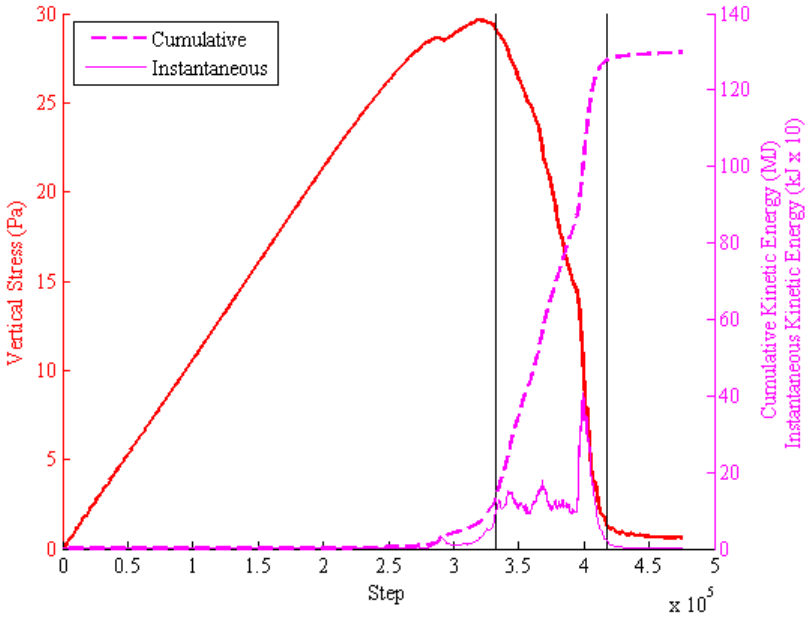

Figure E.32: Kinetic energy, width to height two pillar 35 GPa loading system

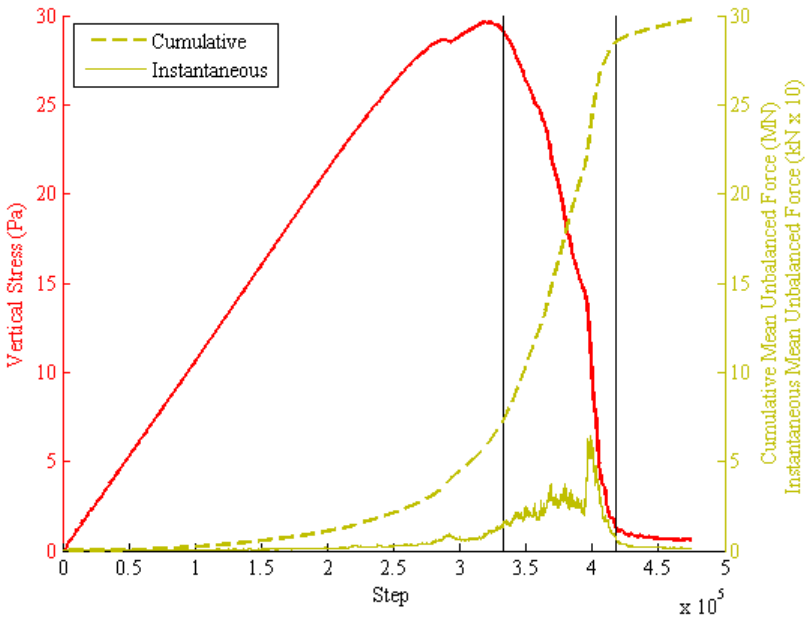

Figure E.33: Mean unbalanced force, width to height two pillar 35 GPa loading system

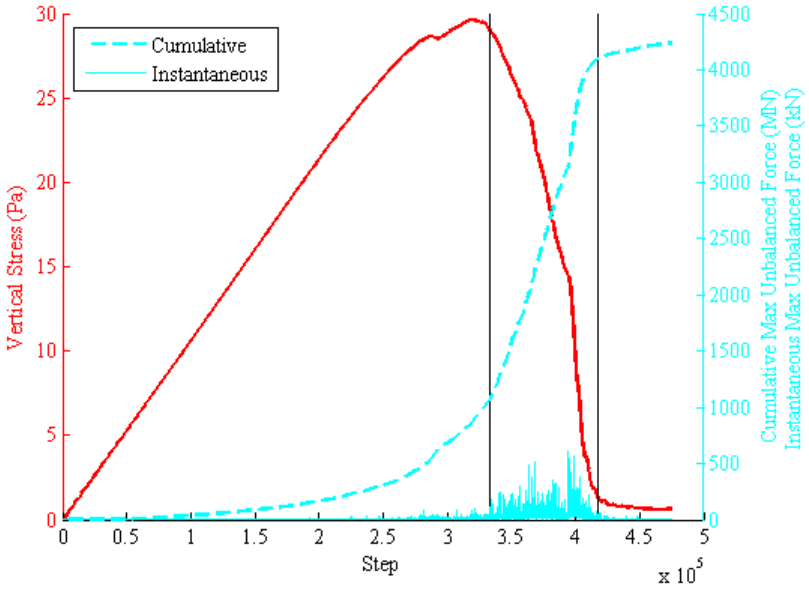

Figure E.34: Max unbalanced force, width to height two pillar 35 GPa loading system

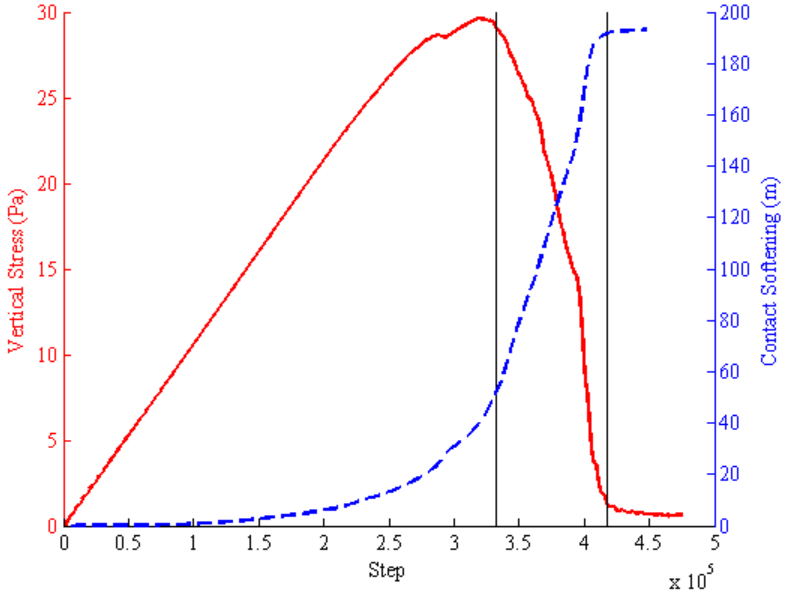

Figure E.35: Contact softening, width to height two pillar 35 GPa loading system

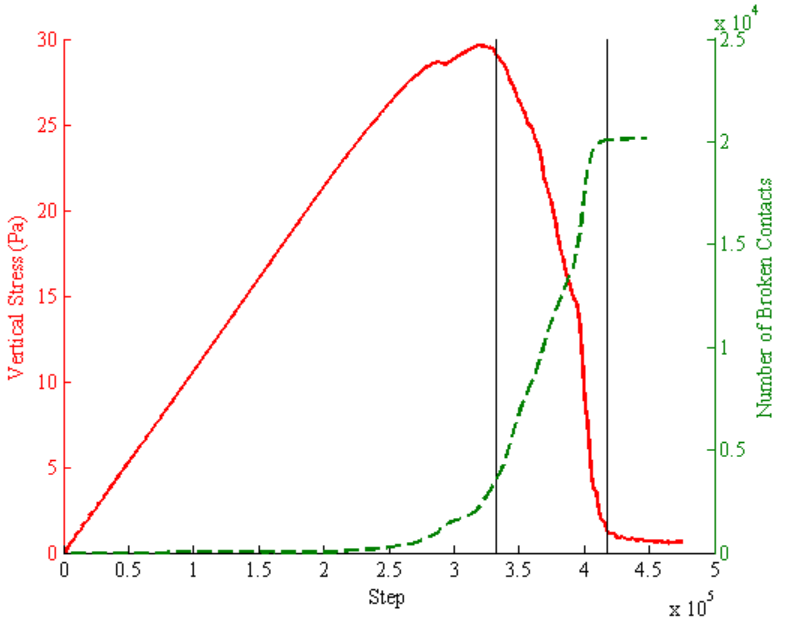

Figure E.36: Broken contacts, width to height two pillar 35 GPa loading system

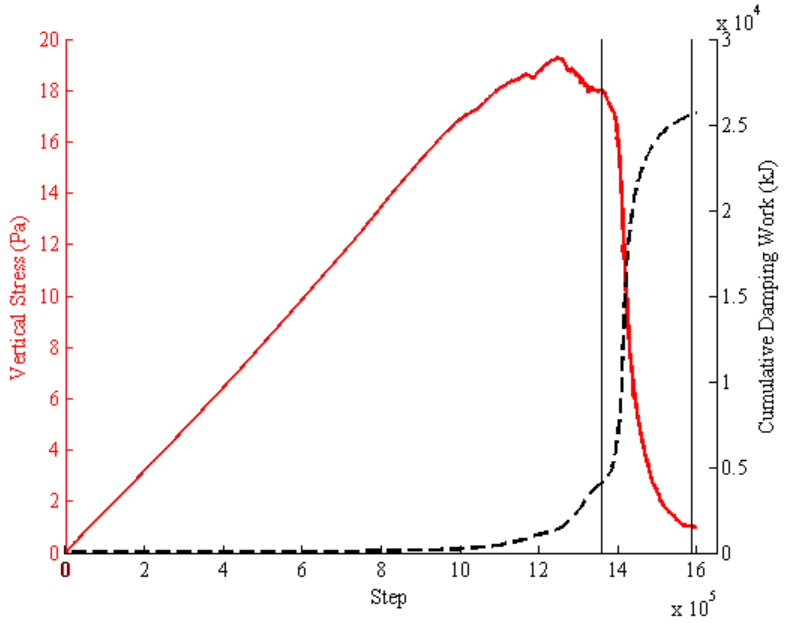

Figure E.37: Damping work, width to height three pillar 5 GPa loading system

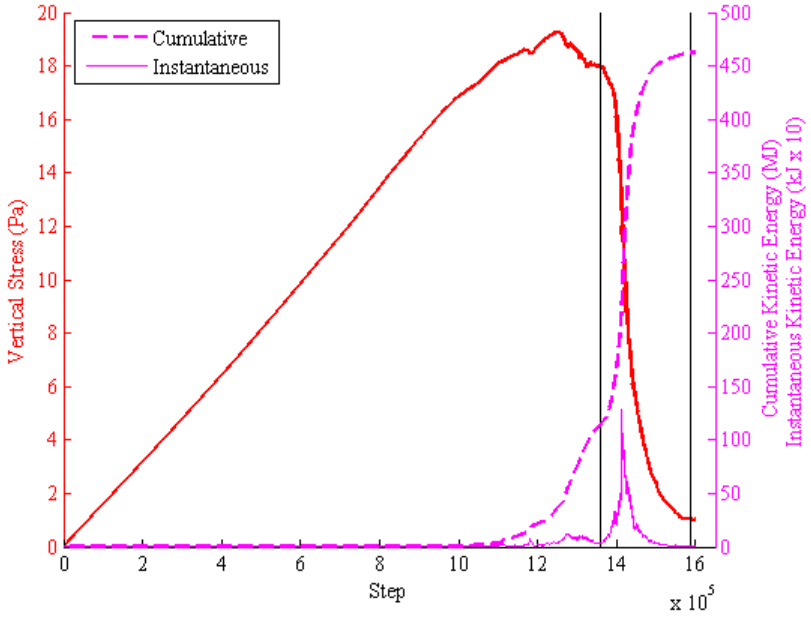

Figure E.38: Kinetic energy, width to height three pillar 5 GPa loading system

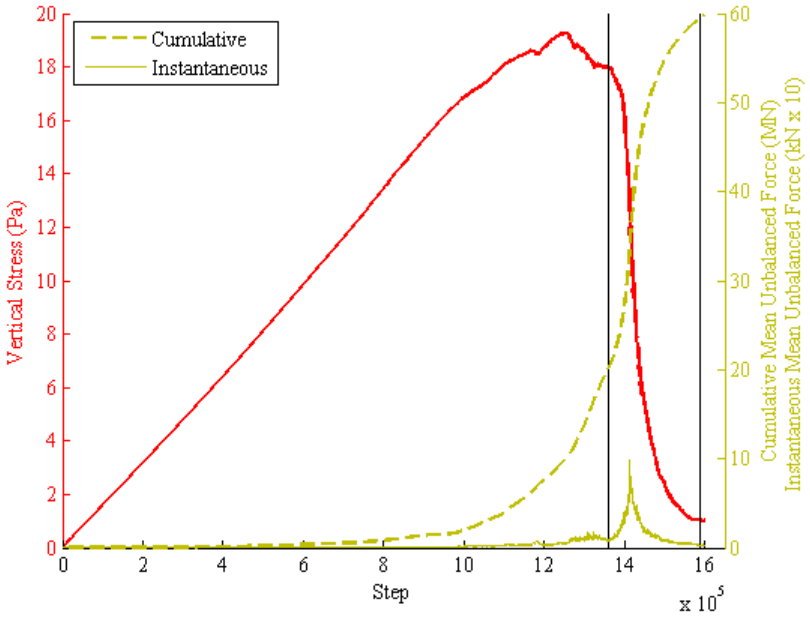

Figure E.39: Mean unbalanced force, width to height three pillar 5 GPa loading system

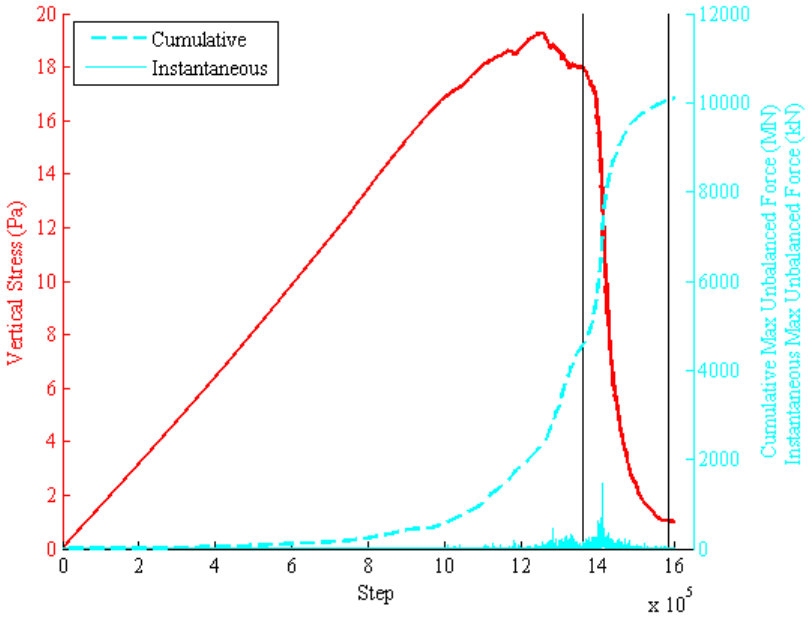

Figure E.40: Max unbalanced force, width to height three pillar 5 GPa loading system

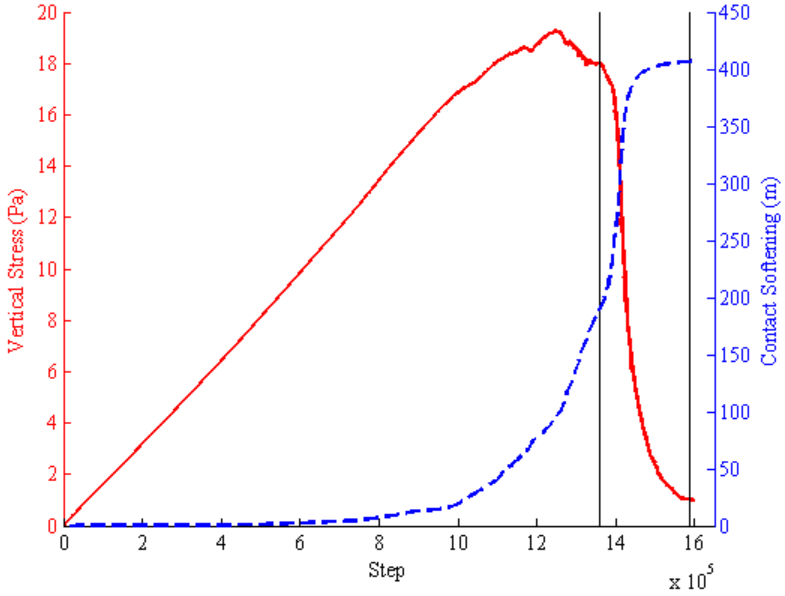

Figure E.41: Contact softening, width to height three pillar 5 GPa loading system

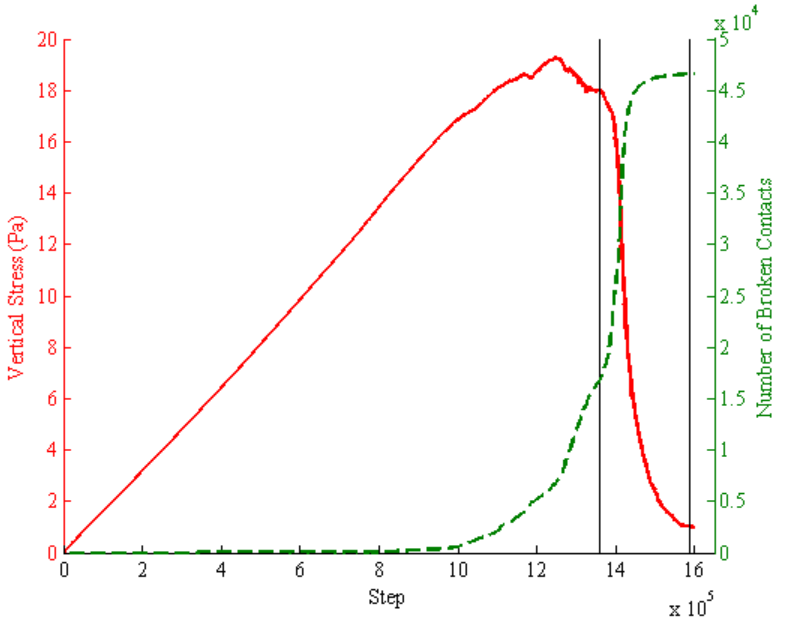

Figure E.42: Broken contacts, width to height three pillar 5 GPa loading system

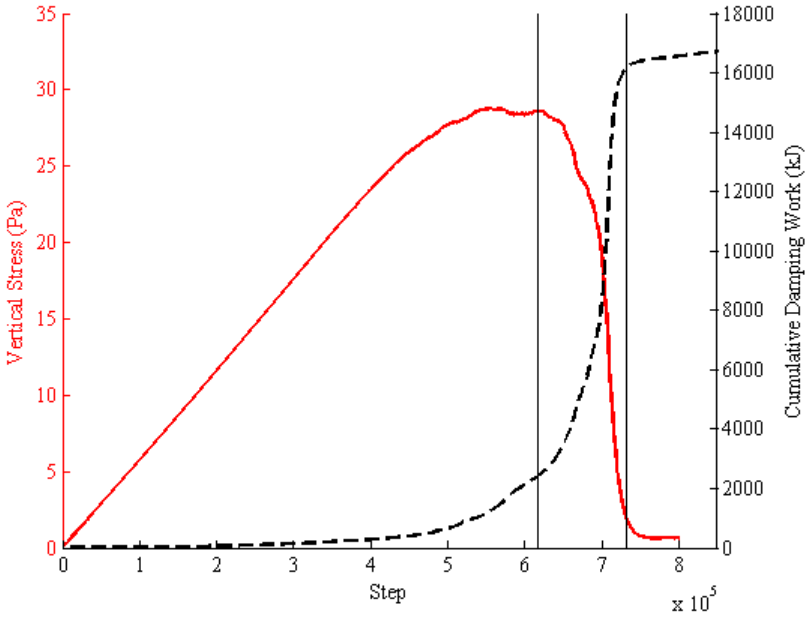

Figure E.43: Damping work, width to height three pillar 20 GPa loading system

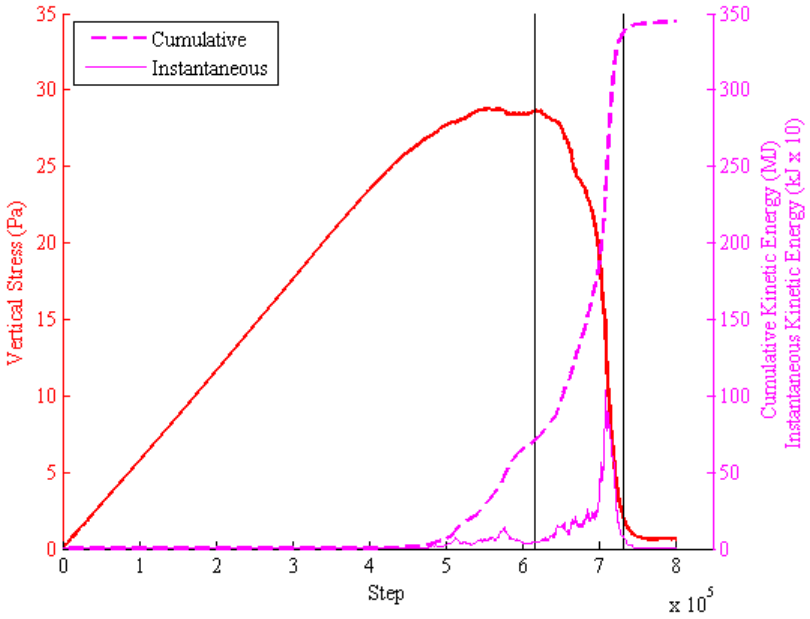

Figure E.44: Kinetic energy, width to height three pillar 20 GPa loading system

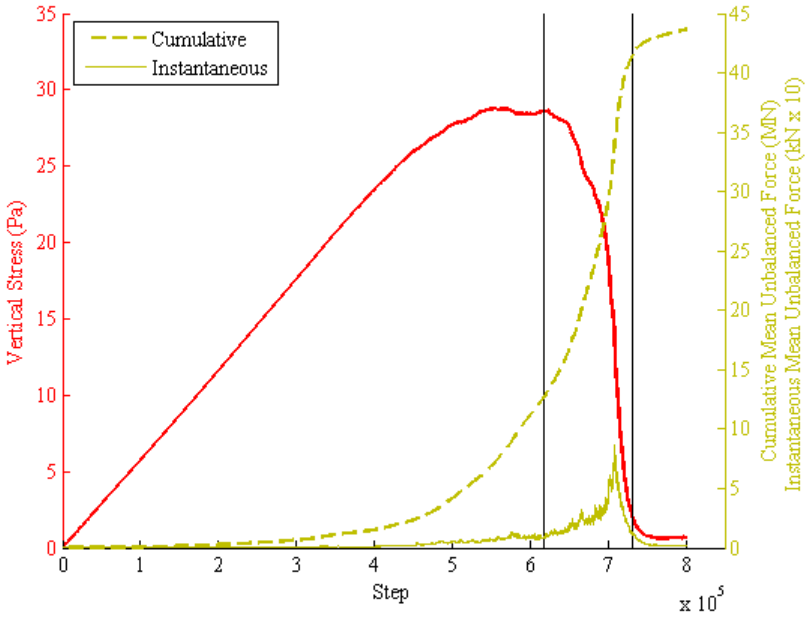

Figure E.45: Mean unbalanced force, width to height three pillar 20 GPa loading system

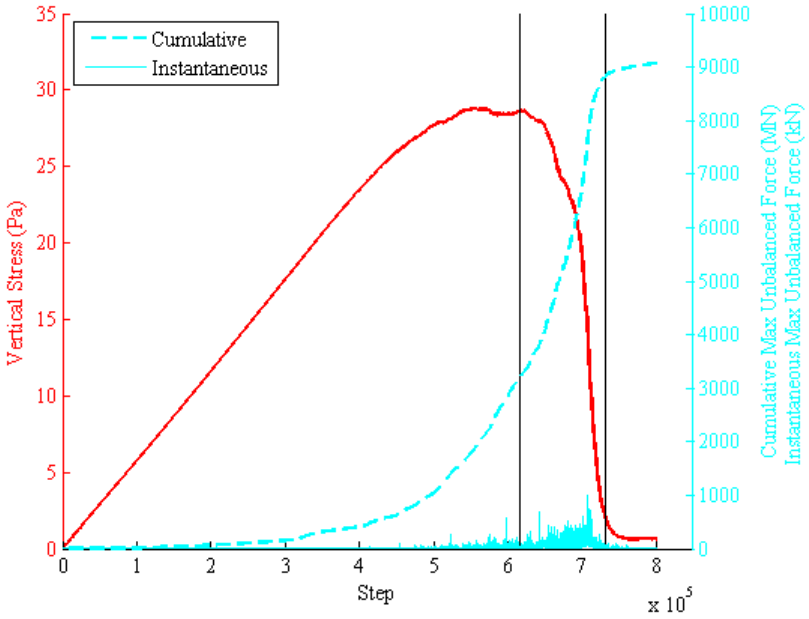

Figure E.46: Max unbalanced force, width to height three pillar 20 GPa loading system

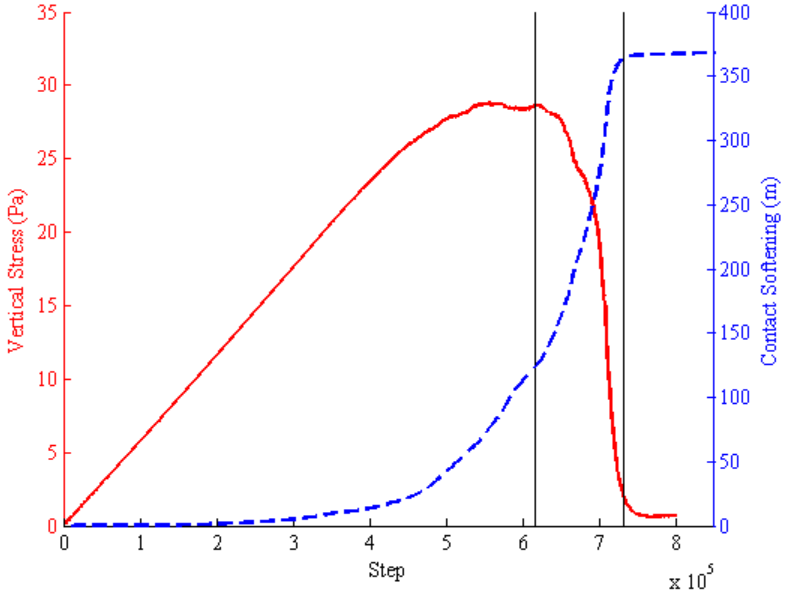

Figure E.47: Contact softening, width to height three pillar 20 GPa loading system

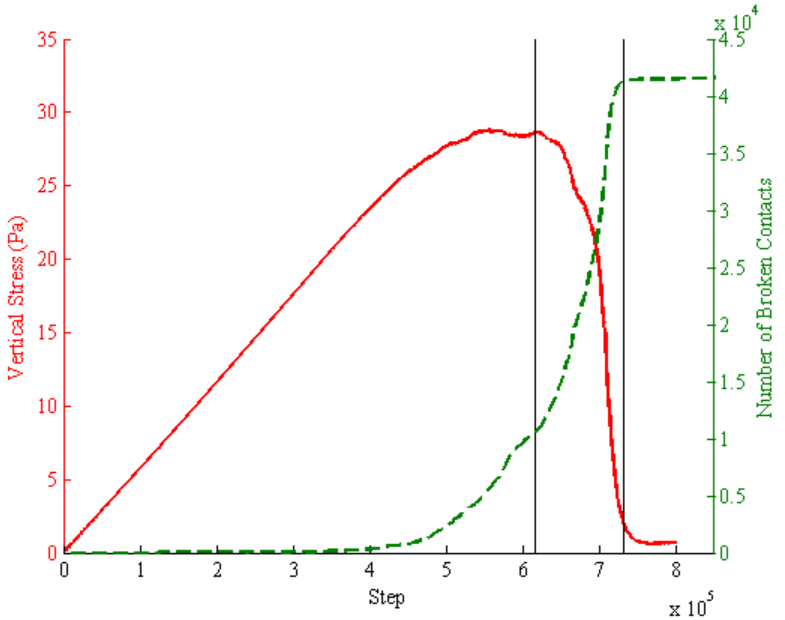

Figure E.48: Broken contacts, width to height three pillar 20 GPa loading system

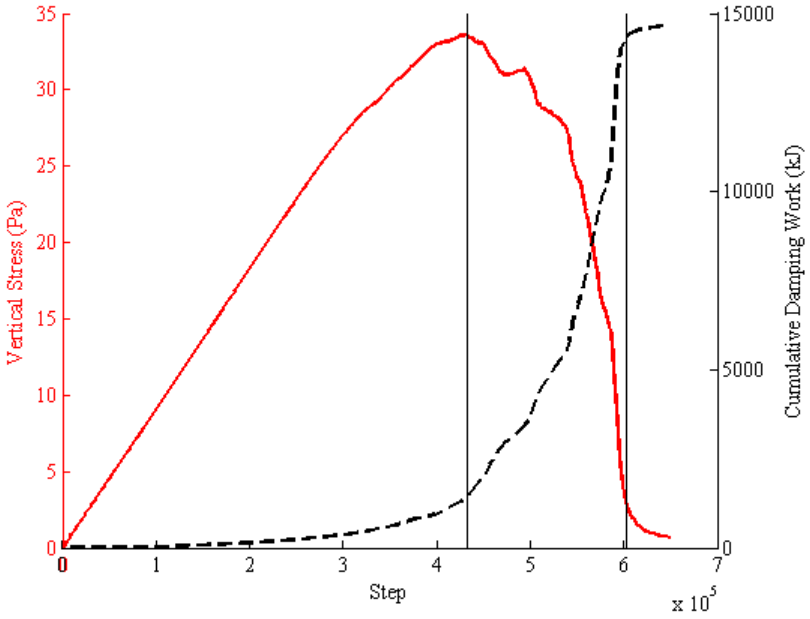

Figure E.49: Damping work, width to height three pillar 35 GPa loading system

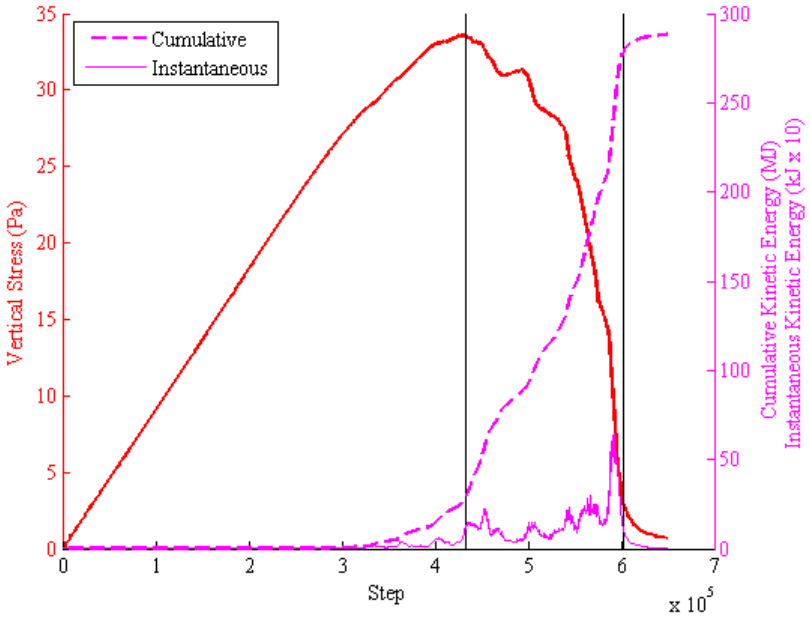

Figure E.50: Kinetic energy, width to height three pillar 35 GPa loading system

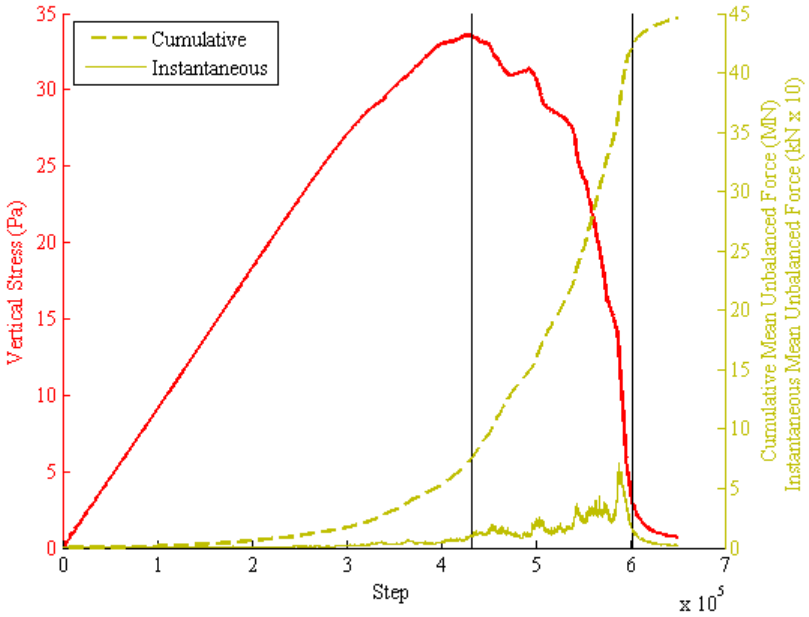

Figure E.51: Mean unbalanced force, width to height three pillar 35 GPa loading system

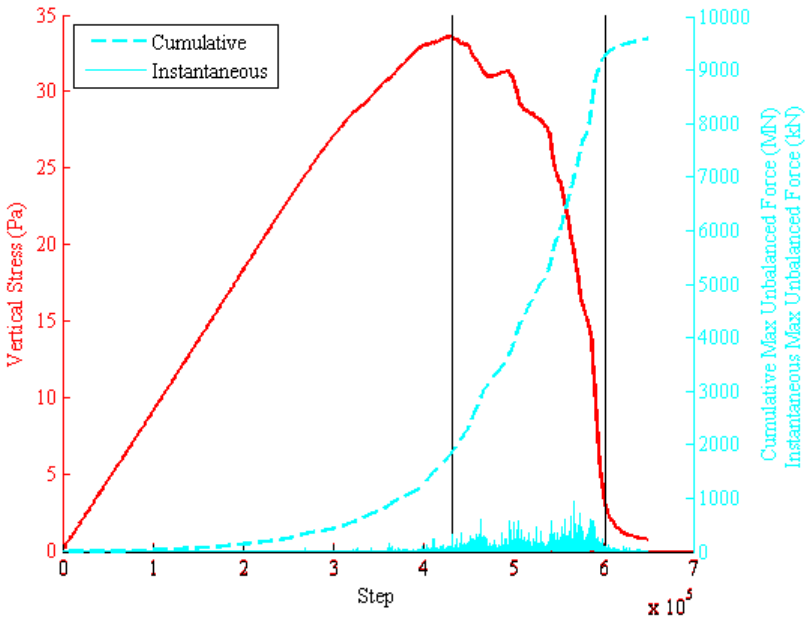

Figure E.52: Max unbalanced force, width to height three pillar 35 GPa loading system

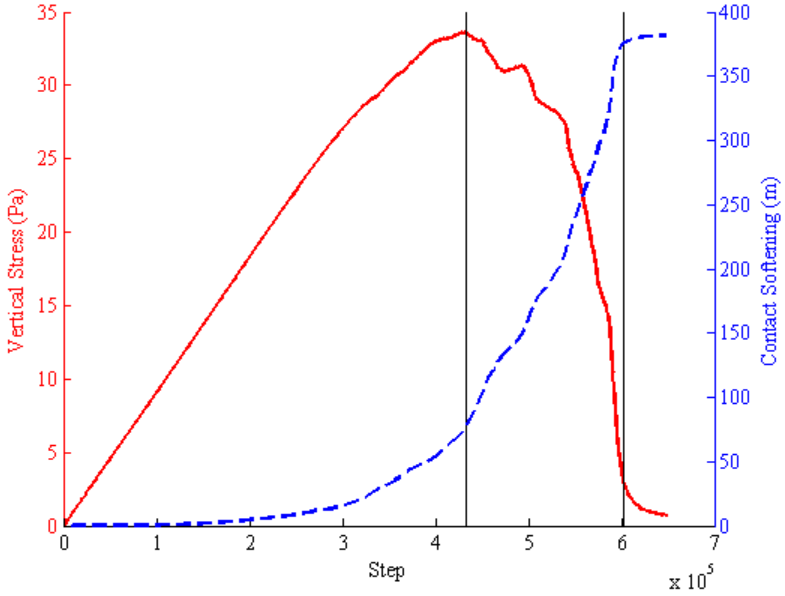

Figure E.53: Contact softening, width to height three pillar 35 GPa loading system

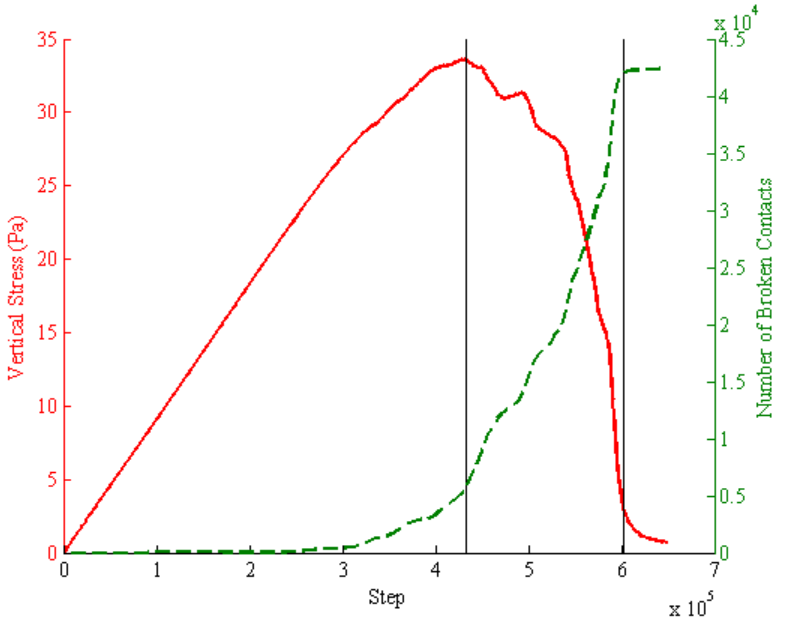

Figure E.54: Broken contacts, width to height three pillar 35 GPa loading system

APPENDIX F - ISP FISH CODES

Listing F.17: In situ pillar FLAC grid generation file

```
; filename: ISP_grid.dat  author: EKias
;
; Create Pillar-flac grid for in situ pillar model
;
;
   ------------------------------------------------------------------------

set cpf_nseg = 352
grid 200 140
model elastic
generate  0 ,-38  0 ,-2   12,-2  12,-38  i=1,193    j=1,23    ratio
   =1,0.78
generate  0 ,-2   0 ,4    12,4   12,-2   i=1,193    j=23,119
generate  0 ,4    0 ,40   12,40  12,4    i=1,193    j=119,141 ratio=1,
   1.3
generate  12,-38  12,-2   20,-2  20,-38  i=193,201  j=1,23    ratio
   =1.9,0.78
generate  12,-2   12,4    20,4   20,-2   i=193,201  j=23,119  ratio
   =1.9,1
generate  12,4    12,40   20,40  20,4    i=193,201  j=119,141 ratio
   =1.9,1.3
model null i=1,160 j=55,86

ini y add  0.0063  j=55
ini y add -0.0063  j=87
ini x add  0.0126  i=161

model null j=88
model null j=53

ini y add -0.0625 j=89,141
ini y add  0.0625 j=1, 53

interface 2 aside from 1,88 to 201,88 bside from 1,89 to 201,89
interface 3 aside from 1,53 to 201,53 bside from 1,54 to 201,54

interface 2 coh 1e6 kn 50e9 ks 50e9
interface 3 coh 1e6 kn 50e9 ks 50e9
```

```
;
    ------------------------------------------------------------------------------

;eof ISP_grid.dat
return
```

Listing F.18: Front end driver file for ISP FLAC runs

```
; cm_FLAC_ISP.dvr    Author: EKias
;
; This file specifies model parameters and calls the Flac .dvr
;
; ------------------------------------------------------------------
def flac_model_init
;
; Specify Grid Properties:
; ****************************************
flac_geom = 1 ; Call ISP grid file  1 = yes
; ****************************************
;
; Specify FLAC material property (Elastic Modulus)
; ****************************************
; flac_emod = 1 ; - 5 GPa Elastic Modulus
flac_emod = 2 ; - 35 GPa Elastic Modulus
; flac_emod = 3 ; - 50 GPa Elastic Modulus
; ****************************************
;
; Specify field stress parameters
; ****************************************
cpf_isxx = -2.667e6   ; for 315m
cpf_isyy = -8.0e6         ; for 315m
;
;cpf_isxx = -5.333e6   ; for 630m
;cpf_isyy = -16.0e6        ; for 630m
; ****************************************
;
end
flac_model_init
call FLAC_CM_general.dvr
; ------------------------------------------------------------------
; eof. cm_FLAC_ISP.dvr
return
```

Listing F.19: Generalized driver file for ISP FLAC runs

```
; fname: FLAC_ISP_general.dvr   author: EKias
;
; Generalized file for ISP FLAC runs
;
;
   ==========================================================================

 CONFIG extra 1   ; for gp-mass multipliers
;
 SET echo off
   call CallMe_FLAC_ISP.dat
 SET echo on
 ; ------------------------------------------------------
def set_mdfrunname
        tag1 = '.log'
        rname = 'FLAC_ISP'
        logname = rname + tag1
        command
                SET mdf_run_name = rname
                SET log @logname
        end_command
end
set_mdfrunname
title rname
set log on
; ***********************************************
cpf_init
cpf_fixbdry
cpf_definegroups_BM1
cpf_matprops
cpf_initstress
;
cpf_cyc
;
cpf_cyc
SET mdf_tag_name = '-ini'
mdf_save_state
;
   ==========================================================================

;EOF: FLAC_ISP_general.dvr
set log off
return
```

Listing F.20: Front end driver file for ISP PFC runs

```
; cm_PFC_ISP.dvr    Author: EKias
;
; This file specifies model parameters and calls the Flac .dvr
;
; ------------------------------------------------------------------
restore ..\..\Field_Stress\syy8_sxx3.sav
restore ..\..\Field_Stress\syy16_sxx5.sav
free x y

; ************************************************
; Specify PFC material property
; ************************************************
model udm_softening

def sof_vals
        sofbroken=1
        soffric=1.75
        soffsmax=1e20
        sofftmax=1e20
        sofknc=6e9
    sofknt=6e9
        sofks=2.0e9     ;k_rat = 1.75
        sofrfric=0.5
        sofuplim=0.007   ;md_ravg ~ .006
end
sof_vals

property sof_broken= 0 &
                sof_fric= soffric &
                sof_fsmax= soffsmax &
                sof_ftmax= sofftmax &
                sof_knc= sofknc &
        sof_knt= sofknt &
                sof_ks= sofks &  ;k_rat = 1.75
                sof_rfric= sofrfric &
                sof_uplim= sofuplim   ;md_ravg ~ .006
; ------------------------------------------------------------------
def pfc_model_init
 ; ****************************************************
 ; Set Boundary pressure value
 x_press = 2.667e6 ; for 8MPa vertical stress
 ;x_press = 5.33e6 ; for 16 MPa vertical stress
 ; ****************************************************
end
pfc_model_init
```

```
call PFC_ISP_general.dvr
; ------------------------------------------------------------------------
; eof. cm_pfc_ISP.dvr
return
```

Listing F.21: Generalized driver file for ISP PFC runs

```
;fname: PFC_ISP_general.dvr  author: EKias
;
; Generalized file for ISP PFC runs
;
;
   ================================================================================

def set_mdrunname
        tag1 = '.log'
        rname = 'PFC_ISP'
        logname = rname + tag1
        command
                SET md_run_name = rname
                SET logfile logname
        end_command
end
set_mdrunname
title rname
set log on
; ********************************************
;
SET echo off
 call %fist%\2d\cpl\cplib.fis
 call %fist_emck%\2D\CM\cpplib_emck.fis
 call %fist_emck%\2D\CM\CM_functions_PFC_2seams.fis
SET echo on
;
SET cp_chan=0 ; make non-zero for each simultaneous coupled run
cpp_init
;
def del_edge_bs
bcnt = 0
        bp = ball_head
        loop while bp # null
                bnext = b_next(bp)
                if b_x(bp) < 0.0 then
                        ii = b_delete(bp)
                        bcnt = bcnt + 1
                endif
                bp = bnext
        end_loop
end
del_edge_bs
; ------------------Apply Boundary Fixity---------------------------------
def xfap_layer
```

```
  lcnt = 0
  layer_thick = 0.0313
  bp = ball_head
  loop while bp # null
        if b_x(bp) < layer_thick then
          if b_extra(bp,1) # 1
            ;b_diam = 2*b_rad(bp)
            ;b_xfap(bp) = x_press*b_diam
            b_xfix(bp) = 1
            ;b_yfix(bp) = 1
                b_extra(bp,2) = 5
            lcnt = lcnt + 1
          endif
        endif
        bp = b_next(bp)
  end_loop
end
xfap_layer
; ---------------------------------------------------------------------------
; trace energy on
; history id=1126 nstep=50 energy kinetic
; history id=1127 nstep=50 KE_Total
; history id=2126 nstep=50 energy strain ; contacts
; history id=2127 nstep=50 energy bond   ; pbonds
; history id=2128 nstep=50 SE_Total
; history id=5000 nstep=50 diagnostic smr
; history id=5001 nstep=50 di muf
; history id=5002 nstep=50 max_unbal_force
; history id=5003 crk_num
;
;
damp local 0.95
SET cpp_cycnum= 5000
cpp_cyc
SET cpp_cycend= 1
cpp_cyc
;
; Delete stray balls that may have escaped during si process.
set mv_W = 10.0
set mv_H = 2.0
del_strays
;
property sof_uplim = sofuplim
damp local 0.7
SET cpp_cycnum= 5000
cpp_cyc
SET cpp_cycend= 1
```

```
cpp_cyc
SET md_tag_name = '-ini'
md_save_state
;
```

```
;EOF: PFC_ISP_general.dvr
set log off
return
```

Listing F.22: Suplementary FLAC coupling function call file

```
;fname: CallMe_FLAC_ISP.dat
;
call D:\Research_A\disp_sof\pfc2d_4.00.194\fist\2d\cpl\app.fin
call D:\Research_A\disp_sof\pfc2d_4.00.194\fist\2d\cpl\cplib.fis
call cpf_FLAC_ISP.fis
;
;EOF: CallMe_FLAC_ISP.dat
return
```

Listing F.23: FLAC ISP model specific coupling functions

```
;fname: cpf_FLAC_CM.fis
;                Coupled PFC2D-FLAC analysis, FLAC file.
;                Model-specific functions, thus, not in cpflib.fis.
;
; The functions <cpf_makegrid> and <_slf_putlist> must be replaced
; when creating a new grid-inclusion system.
;
;
   ==========================================================================

def cpf_makegrid
        command
                call ISP_grid.dat
        end_command
end
; ---------------------------------------
def _slf_putlist
;
; ----- Send segment list information to PFC2D, traverse in ccw order.
;       TODO: Improve efficiency by using buffered I/O.
;
; INPUT:  _sbf_{i,j}{2,3}
;         _slf_putwhat - {0,1,2,3} = {coords,
;                                     velocities,
;                                     create apply list,
;                                     increase gp-masses along bdry}
; OUTPUT: _slf_apf{0,1} - iff _slf_putwhat = 2
;
  _nseg = 0
       _i0 = 1
       _i1 = 2
       _j0 = 55
       _j1 = 55
      _slf_putseg  ;{i: _{i,j}{0,1}}
       _i0 = 2
       _i1 = 3
       _j0 = 55
       _j1 = 55
      _slf_putseg  ;{i: _{i,j}{0,1}}
       _i0 = 3
       _i1 = 4
       _j0 = 55
       _j1 = 55
      _slf_putseg  ;{i: _{i,j}{0,1}}
;
```

```
;
; Lines deleted here only for brevity, traverse entire boundary.
;
;
        _i0 = 3
        _i1 = 2
        _j0 = 87
        _j1 = 87
       _slf_putseg  ;{i: _{i,j}{0,1}}
            _i0 = 2
        _i1 = 1
        _j0 = 87
        _j1 = 87
       _slf_putseg  ;{i: _{i,j}{0,1}}
end
;
```

```
; ------------------------------------
def _divcheck
;
; ------ Determines if input _ch_num can be evenly divided by _ch_div.
;        If it's not, _ch_num is increased until it passes the test.
;
; INPUT:  _ch_num  -  number to be checked
;         _ch_div  -  number to divide with
; OUTPUT: adjusted  _ch_num
;
  _ch_num = int(_ch_num)
  loop while 1 # 0
    _ch = float(_ch_num) / float(_ch_div)
    if _ch / int(_ch) = 1 then
      exit
    end_if
    _ch_num = _ch_num + 1
  end_loop
end
; ------------------------------------
def cpf_fixbdry
;
        load_vel_down = load_vel*(-1)
        command
                ;left boundary
                fix x i=1
                ;right boundary
                fix x i=201
                ;bottom boundary
```

```
                fix y j=1
                fix x j=1
                ;top boundary
                fix y j=141
        end_command
end
; ---------------------------------------
def cpf_apply_vels
        caseof flac_geom
                case 1
                        command
                                ; apply bottom gp velocities
                                ; apply yvel load_vel j 1
                                ;
                                ; apply top gp velocities
                                apply yvel load_vel_down j 141
                        end_command
        endcase
end
; ---------------------------------------
def cpf_his_set
  _hi_x1 = int((_i3_gr+_i4_gr)/2)
  _hi_x2 = int((_i2_gr+_i3_gr)/2)
  command
    history unbal
 end_command
end
;
```

```
def cpf_definegroups_BM1
  command
        group coal   i=161,201 j=55,86
        group roof   j=87,140
        group floor  j=1,54
  end_command
end
;
```

```
def cpf_matprops
;
; INPUT: cpf_emod, cpf_nu - modulus and Poisson's ratio of FLAC grid
;        cpf_dens         - density of FLAC grid
;
;  Elastic model property calcs and property definition
   cpf_dens = 2600 ; cpf_dens
```

```
  caseof flac_emod
  ;cpf_emod / (3.0*(1.0-2.0*cpf_nu))
  ;cpf_emod / (2.0*(1.0+cpf_nu))
        case 1
                _fbulk = 3.333e9    ;|5 GPa .25 nu
                _fshear = 2.0e9     ;|
        case 2
                _fbulk = 23.33e9    ;|35 GPa .25 nu
                _fshear = 14.00e9   ;|
        case 3
                _fbulk  = 33.33e9    ;|50 GPa .25 nu
                _fshear = 20.00e9    ;|
        case 4
                _fbulk = 100.00e9    ;|150 GPa .25 nu
                _fshear = 60.00e9    ;|
        case 5
                _fbulk = 166.66e9    ;|250 GPa .25 nu
                _fshear = 100.00e9   ;|
        case 6
                _fbulk = 333.33e9    ;|500 GPa .25 nu
                _fshear = 200.00e9   ;|
        case 7
                _fbulk = 500.00e9    ;|750 GPa .25 nu
                _fshear = 300.00e9   ;|
        case 8
                _fbulk = 666.66e9    ;|1000 GPa .25 nu
                _fshear = 400.00e9   ;|
        case 9
                _fbulk = 0.666e9    ;|1.0 GPa .25 nu
                _fshear = 0.4e9   ;|
  endcase
 command
        prop dens=cpf_dens bulk=_fbulk shear=_fshear group roof
        prop dens=cpf_dens bulk=_fbulk shear=_fshear group floor
 end_command

;  Mohr-Coulomb model property calcs and property definition
  cpf_dens_mo = 1313
  cpf_coh_mo  = 2.0e6
  cpf_dil_mo  = 0.0
  cpf_fric_mo = 45.0
  cpf_ten_mo  = 0.4e6
  _fbulk_mo   = 6.0e9/(3.0*(1.0-2.0*0.37)) ; cpf_emod_mo /
     (3.0*(1.0-2.0*cpf_nu_mo))
  _fshear_mo  = 6.0e9/(2.0*(1.0+0.37))     ; cpf_emod_mo / (2.0*(1.0+
     cpf_nu_mo))
 command
```

```
    prop bulk=_fbulk_mo coh=cpf_coh_mo dens=cpf_dens_mo dil=cpf_dil_mo
       &
                  shear=_fshear_mo fric=cpf_fric_mo ten=cpf_ten_mo
                     group coal
  end_command
end
; ------------------------------------
def cpf_intprops
        command
                int 1 kn 30.0e9 ks 30.0e9 fric 30 ;dil 6.0
                int 2 kn 30.0e9 ks 30.0e9 fric 30 ;dil 6.0
        endcommand
end
; ------------------------------------
def cpf_initstress
;
; INPUT: cpf_is{xx,yy,xy,zz} - initial stress in FLAC grid
;
 cpf_isxx = cpf_isxx
 cpf_isyy = cpf_isyy
  command
    initial sxx=cpf_isxx syy=cpf_isyy notnull ;j=1,73 ;sxy=cpf_isxy szz
       =cpf_iszz
  end_command
end
;
   ================================================================================

return
;EOF: cpf.fis
```

Listing F.24: FLAC ISP measurement functions and commands

```
; filename ISP_mfuncs_FLAC.dat  author EKias
;
; Measurement functions for ISP
;
; ATTENTION!!!! Lines are deleted for brevity, see comments.
; ------------------------------------------------------------
def get_Los
        array r_Yo(201,1)
        array f_Yo(201,1)
        array Lo_coal(201,1)
        array L_coal(201,1)
        array e_coal(201,1)
        array syy_r(201,1)
        array syy_f(201,1)
        loop iz(1,201)
                r_Yo(iz,1) = y(iz,87) + ydisp(iz,87)
                f_Yo(iz,1) = y(iz,55) + ydisp(iz,55)
                Lo_coal(iz,1) = r_Yo(iz,1) - f_Yo(iz,1)
        end_loop
end
get_Los

def flac_hist_function
        ; Roof and Floor dL accounting for loading velocity
        caseof flac_geom
                ;
                case 5
                        Top_yd = ydisp(1,141)
                        Bottom_yd = ydisp(1,1)
                ;
        endcase
        rdL_1 = ydisp(1,87) - Top_yd ; compression is positive
        rdL_2 = ydisp(2,87) - Top_yd
        ;
        rdL_n = ydisp(n,87) - Top_yd
        ; Lines deleted for brevity, fill in all rdL_n's
        ;
        rdL_200 = ydisp(200,87) - Top_yd
        rdL_201 = ydisp(201,87) - Top_yd
        ;
        fdL_1 = Bottom_yd - ydisp(1,55)
        fdL_2 = Bottom_yd - ydisp(2,55)
        ;
        fdL_n = Bottom_yd - ydisp(n,55)
        ; Lines deleted for brevity, fill in all fdL_n's
```

```
        ;
        fdL_200 = Bottom_yd - ydisp(200,55)
        fdL_201 = Bottom_yd - ydisp(201,55)
        ;
        ; Height of the coal layer including single zone interface
           layer
        loop iz(1,201)
                L_coal(iz,1) = Lo_coal(iz,1) - ydisp(iz,55) + ydisp(iz
                   ,87)
        end_loop
        ;
        ;  Coal layer strain, including single interface zone
        loop iz(1,161)
                e_coal(iz,1) = (Lo_coal(iz,1)-L_coal(iz,1))/Lo_coal(iz
                   ,1)
        end_loop
        ;
        e_1 = e_coal(1,1)
        e_2 = e_coal(2,1)
        ;
        e_n = e_coal(n,1)
        ; Lines deleted for brevity, fill in all e_n's
        ;
        e_200 = e_coal(200,1)
        e_201 = e_coal(201,1)
        ;
end

def get_syys
        syy_r(1,1) = syy(1,87)
        syy_f(1,1) = syy(1,54)
        loop iz(1,199)
                gp = iz+1
                syy_r(gp,1) = (syy(iz,87)+syy(gp,87))/2
                syy_f(gp,1) = (syy(iz,54)+syy(gp,54))/2
        end_loop
        syy_r(201,1) = syy(200,87)
        syy_f(201,1) = syy(200,54)
        ;
        syyr1_1 = syy_r(1,1)
        syyr3_1 = syy_r(3,1)
        ;
        syyrn_1 = syy_r(n,1)
        ; Lines deleted for brevity, fill in all syyrn_1's
        ;
        syyr191_1 = syy_r(191,1)
        syyr193_1 = syy_r(193,1) ; now single increments for
```

```
        syyr194_1 = syy_r(194,1) ; the graded area
        syyr195_1 = syy_r(195,1)
        syyr196_1 = syy_r(196,1)
        syyr197_1 = syy_r(197,1)
        syyr198_1 = syy_r(198,1)
        syyr199_1 = syy_r(199,1)
        syyr200_1 = syy_r(200,1)
        syyr201_1 = syy_r(201,1)
        ;
        syyf1_1 = syy_f(1,1)
        syyf3_1 = syy_f(3,1)
        ; Lines deleted for brevity, fill in all syyfn_1's
        ;
        syyf191_1 = syy_f(191,1)
        syyf193_1 = syy_f(193,1) ; now single increments for
        syyf194_1 = syy_f(194,1) ; the graded area
        syyf195_1 = syy_f(195,1)
        syyf196_1 = syy_f(196,1)
        syyf197_1 = syy_f(197,1)
        syyf198_1 = syy_f(198,1)
        syyf199_1 = syy_f(199,1)
        syyf200_1 = syy_f(200,1)
        syyf201_1 = syy_f(201,1)
end


history nstep = 500 flac_hist_function
history get_syys

; Syy histories
history 301 syyr1_1
history 302 syyr3_1
;
; history # syyrn_1 ; Lines deleted for brevity, fill in
;                   ; all history syyrn_1 commands
;
history 396 syyr191_1
history 397 syyr193_1
history 398 syyr194_1
history 399 syyr195_1
history 400 syyr196_1
history 401 syyr197_1
history 402 syyr198_1
history 403 syyr199_1
history 404 syyr200_1
history 405 syyr201_1
;
```

```
history 501 syyf1_1
history 502 syyf3_1
;
; history # syyrn_1 ; Lines deleted for brevity, fill in
;                    ; all history syyfn_1 commands
;
history 596 syyf191_1
history 597 syyf193_1
history 598 syyf194_1
history 599 syyf195_1
history 600 syyf196_1
history 601 syyf197_1
history 602 syyf198_1
history 603 syyf199_1
history 604 syyf200_1
history 605 syyf201_1
;
history 701 rdL_1
history 702 rdL_3
;
; history # rdL_n ; Lines deleted for brevity, fill in
;                  ; all history rdL_n commands
;
history 796 rdL_191
history 797 rdL_193
history 798 rdL_194
history 799 rdL_195
history 800 rdL_196
history 801 rdL_197
history 802 rdL_198
history 803 rdL_199
history 804 rdL_200
history 805 rdL_201
;
history 901 fdL_1
history 902 fdL_3
;
; history # fdL_n ; Lines deleted for brevity, fill in
;                  ; all history fdL_n commands
;
history 996 fdL_191
history 997 fdL_193
history 998 fdL_194
history 999 fdL_195
history 1000 fdL_196
history 1001 fdL_197
history 1002 fdL_198
```

```
history 1003 fdL_199
history 1004 fdL_200
history 1005 fdL_201
;
history 1101 e_1
history 1102 e_3
;
; history # e_n ; Lines deleted for brevity, fill in
;                    ; all history e_n commands
;
history 1196 e_191
history 1197 e_193
history 1198 e_194
history 1199 e_195
history 1200 e_196
history 1201 e_197
history 1202 e_198
history 1203 e_199
history 1204 e_200
history 1205 e_201

; ------------------------------------------------------------------------
; eof ISP_mfuncs_FLAC.dat
return
```

Listing F.25: ISP FLAC supplementary functions

```
; filename CBM_sloop_flac3.fis   author EmcK   date 11/30/12
;
;
;=============================================================================


;
def getend_solved_bdry
;ex. cp_buf(1) = 1: end loop, cp_buf(1) = 0: cont. loop
        msg = 'Reading socket message.'
        oo = out(msg)
        cp_bufn = 1
        ;
        cp_read
        msg = 'Message received. '
        oo = out(msg)
end

def isit_solved_bdry
        if cp_buf(1) = 1 then
                msg = 'Its solved'
                oo = out(msg)
                its_solved_bdry = 1
        else
                msg = 'Its not solved'
                oo = out(msg)
        endif
end

def getend_dec
;ex. cp_buf(1) = 1: end loop, cp_buf(1) = 0: cont. loop
        msg = 'Checking if fully decreased.'
        oo = out(msg)
        cp_bufn = 1
        ;
        cp_read
end

def isit_dec
        if cp_buf(1) = 1 then
                done_dec = 1
                msg = 'Its fully decreased.'
                oo = out(msg)
        else
                msg = 'Not fully decreased.'
                oo = out(msg)
```

```
        endif
end

def solve_loop_bdry
        its_solved_bdry = 0
        ;command
        ;pause
        ;end_command
        loop while its_solved_bdry # 1
                cpf_cyc  ; enter slave mode for synchronous cycling
                msg = 'Checking if its solved'
                oo = out(msg)
                getend_solved_bdry
                isit_solved_bdry
        end_loop
end

def bdry_loop
        done_dec = 0
        loop while done_dec # 1
                solve_loop_bdry
                getend_dec
                isit_dec
        end_loop
        solve_loop_bdry
        ;
        msg1 = 'flac_cmb1'
        mdf_run_name = msg1
        msg2 = '-nbdry'
    mdf_tag_name = msg2
    mdf_save_state
        ;
end
;
;To restart from saved state, you must first restore save state then
   call cpf_open
;Do this in FLAC2D first.
;
;
def slice_loop_restart
        loop while done_slice # 1
                solve_loop_slice
                getend_slice
                isit_done_slice
                ;
                get_save
                save_slice
```

```
        end_loop
end

def slice_loop
        done_slice = 0
        wzone = x(2,87)-x(1,87)
        null_znum = 1
        loop while done_slice # 1
                solve_loop_slice
                getend_slice
                isit_done_slice
                ;
                get_save
                save_slice
        end_loop
        ;solve_loop
        ;
end

def init_vars
        excav_step = 0
end
init_vars

def getend_solved_slice
;ex. cp_buf(1) = 1: end loop, cp_buf(1) = 0: cont. loop
        cp_bufn = 1
        ;
        cp_read
end

def isit_solved_slice
        if cp_buf(1) = 1 then
                its_solved_slice = 1
        endif
end

def getend_slice
        cp_bufn = 1
        ;
        cp_read
end

def isit_done_slice
        if cp_buf(1) = 1 then
                done_slice = 1
        endif
```

```
        msg = 'Read done_slice = '+string(done_slice)
        oo = out(msg)
        getw_excav
end

def getw_excav
        cp_bufn = 1
        ;
        cp_read
        wexcav = cp_buf(1)
        ;
        null_excav
end

def null_excav
        fexcav = null_znum*wzone
        if wexcav > fexcav
                command
                        model null i null_znum j 87  ;top interface
                           zone
                        model null i null_znum j 54  ;bottom interface
                           zone
                end_command
                null_znum = null_znum + 1
        endif
end

def solve_loop_slice
        its_solved_slice = 0
        loop while its_solved_slice # 1
                cpf_cyc  ; enter slave mode for synchronous cycling
                getend_solved_slice
                isit_solved_slice
        end_loop
end


def excav_loop
        done_excav = 0
        loop while done_excav # 1
                excav_step = excav_step + 1
                zonk_loop
                getend_excav
                isit_excav
        end_loop
end
```

```
def getend_excav
;ex. cp_buf(1) = 1: end loop, cp_buf(1) = 0: cont. loop
        cp_bufn = 1
        ;
        cp_read
end

def isit_excav
        if cp_buf(1) = 1 then
                done_excav = 1
        endif
end

def get_save
        cp_bufn = 1
        cp_read
        ;
        if cp_buf(1) = 1
                save_it = 1
                save_num = save_num + 1
        else
                save_it = 0
        endif
        msg = 'Read save_it = '+string(save_it)
        oo = out(msg)
end

def save_slice
        if save_it = 1
                msg1 = 'flac_cbm-ex'
                mdf_run_name = msg1
                msg2 = string(save_num)
                mdf_tag_name = msg2
                mdf_save_state
                msg = 'Saved file!'
                oo = out(msg)
        else
                msg = 'Didnt save file.'
                oo = out(msg)
        endif
end
;=============================================================================

return
;eof CBM_sloop_flac3.fis
```

Listing F.26: ISP PFC supplementary functions

```
; filename ISP_funcs_PFC.fis   author EKias
;
;
;=============================================================================

;
def free_and_appxf
        bp = ball_head
        loop while bp # null
                if b_extra(bp,2) = 5
                        bxfob = b_xfob(bp)
                        b_xfix(bp) = 0
                        b_yfix(bp) = 0
                        b_xfap(bp) = -bxfob
                endif
                bp = b_next(bp)
        end_loop
end

def replace_extra
        bp = ball_head
        loop while bp # null
                if b_extra(bp,2) = 5 then
                        b_extra(bp,2) = b_xfap(bp)
                endif
        bp = b_next(bp)
        end_loop
end

def bdry_loop
free_and_appxf
replace_extra
;command
;pause
;end_command
  dec_step = 1
  done_dec = 0
  num_decs = 25
  dec_inc = 1.0/num_decs
  dec_rat = 1.0
  loop while done_dec # 1
        dec_rat = dec_rat - dec_inc
        decrease_xf
        solve_loop_bdry
        check_dec
```

```
        put_dec
  end_loop
  free_and_zeroxf
  solve_loop_bdry ; Solve again with no applied forces
  zero_extra2
  ;
  msg1 = 'pfc_cmb1'
  md_run_name = msg1
  msg2 = '-nbdry'
  md_tag_name = msg2
  md_save_state
end

def decrease_xf
        bp = ball_head
        loop while bp # null
                if b_extra(bp,2) # 0 then
                        xfap0 = b_extra(bp,2)
                        xfap = xfap0*dec_rat
                        b_xfap(bp) = xfap
                endif
        bp = b_next(bp)
        end_loop
end

def solve_loop_bdry
  its_solved_bdry = 0
  solve_cnt_bdry = 0
  loop while its_solved_bdry # 1
        ;command
        ;pause
        ;end_command
    cpp_cyc
        cpp_cycend = 1
        cpp_cyc
        ;
        command
                hist write 1234 table 1 ; table 1 becomes hist diag smr
        end_command
        ;
        isit_solved_bdry
        put_solved_bdry
        oxo = del_table(1)
  end_loop
end

def isit_solved_bdry
```

```
        solve_cnt_bdry = solve_cnt_bdry + 1
        last_entry = table_size(1)
        cur_smr = ytable(1,last_entry) ; alternate option: table(id,
           xvalue)
        ;
        if cur_smr < 1.0e-4 then
              its_solved_bdry = 1
        endif
        msg = '------'+string(solve_cnt_bdry)+' '+'solve steps
           ----------------------------------'
        oo = out(msg)
        msg = 'Solve ratio is'+' '+string(cur_smr)
        oo = out(msg)
        msg = 'X-Force Dec. step is '+string(dec_step)+' of '+string(
           num_decs)
        oo = out(msg)
        msg = '& decrease ratio is '+string(dec_rat)
        oo = out(msg)
        msg = 'Example xforce dec.: from '+string(xfap0)+' to '+string(
           xfap)
        oo = out(msg)
        msg =
           '------------------------------------------------------------------'
        oo = out(msg)
end

def put_solved_bdry
        cp_bufn = 1
    cp_buf(1) = its_solved_bdry
        ;
        cp_write
end

def check_dec
  if dec_step = num_decs then
        done_dec = 1
  else
        dec_step = dec_step + 1
  endif
end

def put_dec
  cp_bufn = 1
    cp_buf(1) = done_dec
        ;
        cp_write
end
```

```
def zero_extra2
        bp = ball_head
        loop while bp # null
                b_extra(bp,2) = 0
        bp = b_next(bp)
        end_loop
end

def free_and_zeroxf
        bp = ball_head
        loop while bp # null
                if b_extra(bp,1) # 1
                        if b_xfap(bp) # 0.0
                                b_xfix(bp) = 0
                                b_yfix(bp) = 0
                                b_xfap(bp) = 0.0
                        endif
                endif
                bp = b_next(bp)
        end_loop
end
;
;To restart from saved state, you must first restore save state then
   call cpp_open
;Do this in FLAC2D first.
;
def slice_loop_restart
  save_pt = save_pt + save_inc
  ;
  loop while done_slice # 1
  msg = 'In done slice loop'
  oo = out(msg)
        delete_slice
        solve_loop_slice
        check_slice
        put_slice
        save_slice
  end_loop
  ;solve_loop ; Solve again with no balls present
  ;
end

def slice_loop
  w_excav = 0.0
  slice_step = 0
  done_slice = 0
```

```
  save_pt = save_inc
  ;
  loop while done_slice # 1
  msg = 'In done slice loop'
  oo = out(msg)
        delete_slice
        solve_loop_slice
        check_slice
        put_slice
        save_slice
  end_loop
  ;solve_loop ; Solve again with no balls present
  ;
end

def get_slice_range
        command
                range name slice_range x=(-10,w_excav)
        end_command
end

def delete_slice
msg = 'In delete slice.'
oo = out(msg)
        if slice_step = 0 then
                msg = 'First cycle, no slice taken.'
                oo = out(msg)
        else
                w_excav = slice_step*w_slice
                get_slice_range
                sbs_deld = 0
                ;
                bp = ball_head
                loop while bp # null
                        bnext = b_next(bp)
                        if inrange(slice_range,bp) = 1
                                ii = b_delete(bp)
                                sbs_deld = sbs_deld + 1
                        endif
                        bp = bnext
                end_loop
                msg = string(sbs_deld)+' balls deleted during slice
                   excav number '+string(slice_step)
                oo = out(msg)
        endif
        slice_step = slice_step + 1
end
```

```
def solve_loop_slice
  its_solved_slice = 0
  solve_cnt_slice = 0
  loop while its_solved_slice # 1
    cpp_cyc
        cpp_cycend = 1
        cpp_cyc
        ;
        command
                hist write 1234 table 1 ; table 1 becomes hist diag smr
        end_command
        ;
        isit_solved_slice
        put_solved_slice
        oxo = del_table(1)
        get_max_fob
        del_strays_slice
  end_loop
end

def isit_solved_slice
        solve_cnt_slice = solve_cnt_slice + 1
        last_entry = table_size(1)
        cur_smr = ytable(1,last_entry) ; alternate option: table(id,
           xvalue)
        ;
        if cur_smr < 1.0e-4 then
                its_solved_slice = 1
        endif
        msg = '------'+string(solve_cnt_slice)+' '+'solve steps
           ----------------------------'
        oo = out(msg)
        msg = 'Solve ratio is'+' '+string(cur_smr)
        oo = out(msg)
        msg = 'Excavation is '+string(w_excav)+' m after '+string(
           slice_step)+' slices.'
        oo = out(msg)
        msg =
           '------------------------------------------------------------------------'
        oo = out(msg)
end

def put_solved_slice
;  buf(1) = 1 (end loop)
        cp_bufn = 1
    cp_buf(1) = its_solved_slice
```

```
        ;
        cp_write
end

def check_slice
  if w_excav > excav_lim then
        done_slice = 1
  endif
end

def put_slice
msg = 'sending done_slice = '+string(done_slice)
oo = out(msg)
  cp_bufn = 1
  cp_buf(1) = done_slice
  cp_write
  ;
msg = 'sending wexcav = '+string(w_excav)
oo = out(msg)
  cp_bufn = 1
  cp_buf(1) = w_excav
  cp_write
end

def del_strays_slice
stray_del = 0
        bp = ball_head
        loop while bp # null
                bnext = b_next(bp)
                if inrange('brange',bp) = 0
                        ii = b_delete(bp)
                        stray_del = stray_del + 1
                endif
                bp = bnext
        end_loop
        msg = string(stray_del)+' stray ball(s) deleted!!'
        oo = out(msg)
end

def save_slice
        if w_excav > save_pt
                save_num = save_num + 1
                save_it = 1
                ;
                msg1 = 'pfc_cbm-ex'
                md_run_name = msg1
                msg2 = string(save_num)
```

```
                md_tag_name = msg2
                md_save_state
                ;
                save_pt = save_pt + save_inc
                msg = 'Saved file.'
                oo = out(msg)
        else
                save_it = 0
                msg = 'Did not save file.'
                oo = out(msg)
        endif

        put_save
end

def put_save
        cp_bufn = 1
        cp_buf(1) = save_it
        cp_write
        msg = 'Sent save_it = '+string(save_it)
        oo = out(msg)
end
;===============================================================
;eof. ISP_funcs_PFC.fis
return
```

Listing F.27: FLAC ISP excavation step driver file

```
; fname: FLAC_Ex_ISP.dvr  Author: EKias
;
; Boundary and excavation loops
;
;
   ================================================================================

restore filepath\ISP_FLAC-ini.sav

hist reset
cpf_open

call 'filepath'\ISP_mfuncs_FLAC.dat
call 'filepath'\ISP_funcs_FLAC.fis
set log FLAC_ISP_ex.log
set log on

bdry_loop
slice_loop
;
   ================================================================================

set log off
;EOF: FLAC_Ex_ISP.dvr
return
```

Listing F.28: PFC ISP excavation step driver file

```
;fname: PFC_Ex_ISP.dvr   author: EKias
;
;
   ==========================================================================

restore PFC_ISP-ini.sav

set logfile = 'PFC_ISP_Ex.log'
set log on

cpp_open

history id 1234 nstep 50 diag smr ; needed for bdry_loop and slice_loop

call %fist_emck%\2d\CM\ISP_funcs_PFC.fis
;trace energy on
;history energy kinetic

def init_vars_slice
  cpp_cycnum=500
  ex_step = 0
  excav_lim = 8.0      ;excavation limit, must be < 10.0-w_slice
  w_slice = 2*md_ravg  ;mining step width
  w_entry = 6.0        ;must be a multiple of w_slice
  save_inc = 0.5       ;excavation increment at which to save file
  ; Create range for del_strays_slice function
  command
        range name brange x -0.063 10.063 y -0.063 2.063
  end_command
end
init_vars_slice

pause 3
bdry_loop

; Assign contacts finite strength before mining
property sof_fsmax=0.65e4 &
                 sof_ftmax=0.65e4 &
                 sof_uplim=0.007

pause 3
slice_loop
;
   ==========================================================================
```

```
set log off
;EOF: PFC_Ex_ISP.dvr
return
```

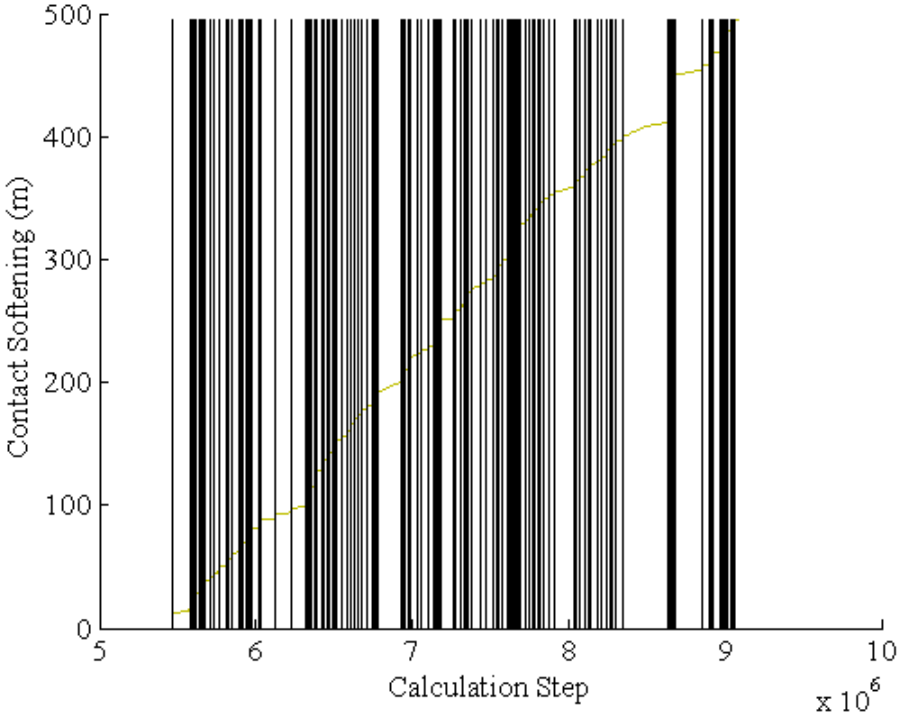

Figure G.1: Contact softening in the deep simulation

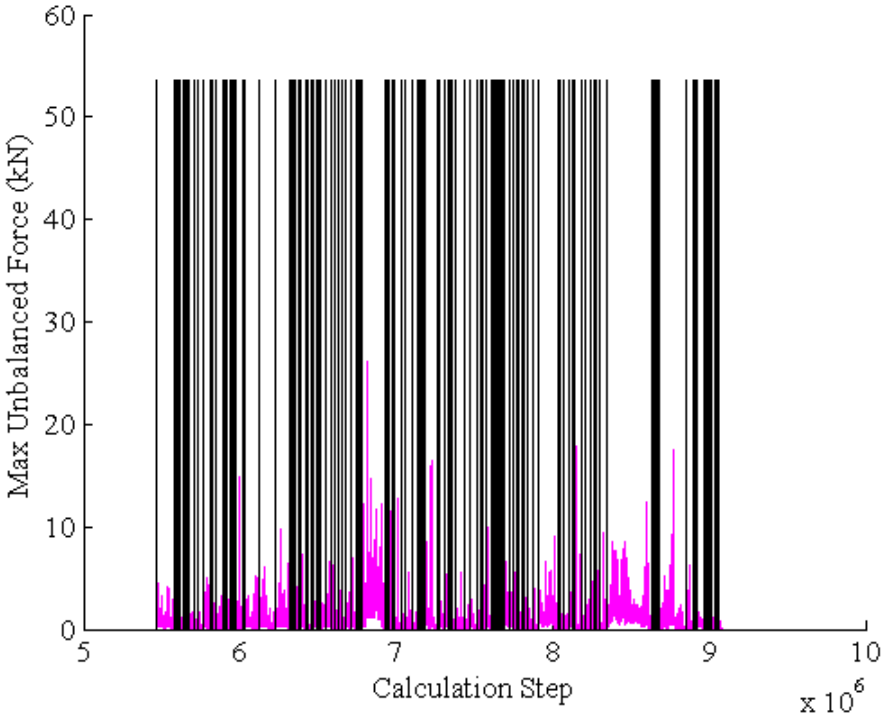

Figure G.2: Maximum unbalanced force in the deep simulation

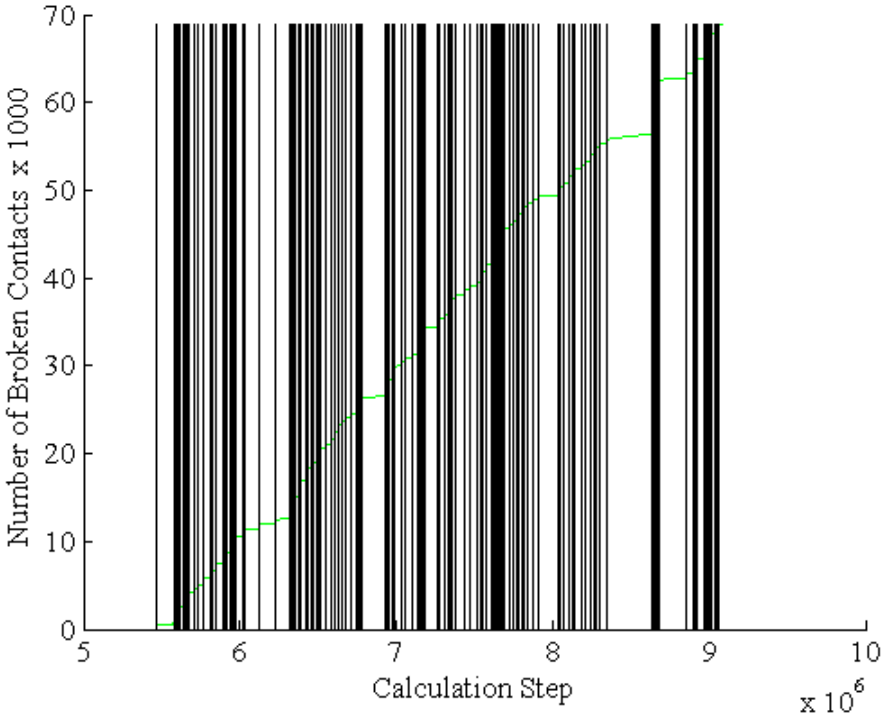

Figure G.3: Number of broken contacts in the deep simulation